INAUGURAL-DISSERTATION

zur

Erlangung der Doktorwürde

der

Gesamtfakultät für Mathematik,

Ingenieur- und Naturwissenschaften

der

Ruprecht-Karls-Universität

Heidelberg

vorgelegt von

Simon Johannes Settele

geboren in Böblingen

Tag der mündlichen Prüfung

12. April 2024

Creating Luminescent Defects in Carbon Nanotubes for Optoelectronics and Biomedical Applications

Gutachter

PROF. DR. JANA ZAUMSEIL
PROF. DR. SEBASTIAN KRUSS

Abstract

Light in the near-infrared (NIR) plays a central role in today's telecommunications systems and biomedical research as it overlaps with the transmission window of silica fibers and biological tissues. Due to their narrowband photoluminescence (PL) in the NIR, semiconducting single-walled carbon nanotubes (SWNTs) have emerged as a promising material for optoelectronic devices, bioimaging, and (bio)sensing. The covalent functionalization of SWNTs with luminescent defects enhances their optical properties, resulting in a bright red-shifted emission band with potential application as a quantum-light source. However, existing synthetic protocols offer little control over the creation of these defects and as a result emission occurs across a wide spectral range. For practical applications, it is crucial to reduce this spectral diversity and selectively introduce defects that exhibit the desired properties. Moreover, creating luminescent defects with high brightness is challenging and has impeded their application in bioimaging. Hence, their potential as biosensors is also largely unknown.

This thesis introduces a synthetic protocol for the selective creation of one specific type of luminescent sp^3 defect in polymer-sorted (6,5) SWNTs. Compared to commonly obtained defects, this type of defect emits more red-shifted light and exhibits longer PL lifetimes. The created defects exhibit single-photon emission at room temperature and the emission can be tuned further towards telecommunication wavelengths by functionalization of other SWNTs species. This new functionalization protocol relies on a base-promoted coupling approach that primarily utilizes aniline derivatives. These aniline derivatives react through nucleophilic addition with the SWNT lattice. The functionalized SWNTs exhibit excellent solution-processability, which will enable their integration into electrically-driven devices and quantum-light sources.

In a second functionalization protocol, luminescent oxygen defects were created in aqueous dispersed SWNTs through reaction with reactive oxygen species produced by Fenton-like copper redox chemistry. In the case of functionalized (6,5) SWNTs, a 5-fold brightening effect and a PL quantum yield of 3% was observed. The method employs benign and inexpensive chemicals and can be performed at high SWNT concentrations using commercially available unsorted raw material, enabling large-scale production. The excellent optical properties of functionalized SWNTs persist even after being made biocompatible through coating with biopolymers (*e.g.* DNA), making them suitable for future applications in *in vivo* NIR imaging or biosensing.

Finally, in a rational approach, sp^3-functionalized (6,5) SWNTs were designed for the optical detection of the biomarker inorganic pyrophosphate (PP_i). The detection scheme relies on a metal displacement assay, wherein copper ions reversible quench the PL of functionalized SWNTs bearing an alkyne moiety. Quenching proceeds *via* photo-induced electron transfer when Cu^{2+} ions are immobilized on the SWNT surface, facilitated by a triazole ligand and coordination to covalently attached aryl alkyne groups. PL quenching is more pronounced for defect emission, enabling the detection of PP_i in ratiometric measurements. When made biocompatible by coating with phospholipid-polyethylene glycol, this sensor is suitable for detecting PP_i released during DNA synthesis in polymerase chain reaction. This sensor design may serve as a starting point for the further rational design of biosensors based on SWNTs functionalized with luminescent defects.

ZUSAMMENFASSUNG

Licht im nahen Infrarotbereich (NIR) spielt eine zentrale Rolle in modernen Telekommunikationssystemen und in der biomedizinischen Forschung, da es mit dem Transmissionsfenster von optischen Fasern und biologischem Gewebe zusammenfällt. Aufgrund ihrer schmalbandigen Fluoreszenz im NIR haben sich halbleitende einwandige Kohlenstoffnanoröhrchen (engl. *single-walled carbon nanotubes*, SWNT) als vielversprechendes Material für Anwendungen in optoelektronischen Bauelementen, der biologischen Bildgebung und in der Sensorik etabliert. Die kovalente Funktionalisierung von SWNTs mit leuchtenden Defekten verbessert ihre optischen Eigenschaften und erzeugt eine helle, rotverschobene Fluoreszenz, die als Quantenlichtquelle genutzt werden kann. Bestehende synthetische Protokolle bieten jedoch wenig Kontrolle über die Erzeugung dieser Defekte, wodurch die Emission über einen breiten spektralen Bereich erfolgt. Für praktische Anwendungen ist es entscheidend, diese spektrale Vielfalt zu reduzieren und gezielt Defekte mit den gewünschten Eigenschaften einzuführen. Darüber hinaus ist die Herstellung von leuchtenden Defekten mit hoher Helligkeit noch schwierig, was ihre Anwendung in der biologischen Bildgebung behindert und dazu führt, dass ihr Potenzial als Biosensoren noch weitgehend unbekannt ist.

In dieser Arbeit wird ein synthetisches Protokoll vorgestellt, das die selektive Erzeugung eines bestimmten Typs leuchtender sp^3-Defekte in polymerumwickelten (6,5) SWNTs erlaubt. Im Vergleich zu sonst überlicherweiße erhaltenen Defekten emittieren diese Defekte stärker rotverschoben und zeigen längere Fluoreszenzlebensdauern. Die erzeugten Defekte zeigen Einzelphotonenemission bei Raumtemperatur und ihre Fluoreszenz kann durch Funktionalisierung anderer SWNT-Arten weiter in Richtung Telekommunikationswellenlängen verschoben werden. Dieses Funktionalisierungsprotokoll basiert auf einer basenvermittelten Kupplung, bei der in erster Linie Anilinderivate verwendet werden. Diese Anilinderivate reagieren durch nukleophile Addition mit dem SWNT-Gitter. Die funktionalisierten polymerumwickelten SWNTs zeigen eine ausgezeichnete Lösungsprozessierbarkeit und eignen sich daher gut für den Einbau in elektronische Bauelemente und Quantenlichtquellen.

In einem zweiten Funktionalisierungsprotokoll wurden leuchtende Sauerstoffdefekte in wässrig dispergierte SWNTs durch Reaktion mit reaktiven Sauerstoffspezies eingeführt, die durch Fenton-ähnliche Kupfer-Redoxchemie erzeugt wurden. Im Fall von funktionalisierten (6,5) SWNTs wurde eine 5-fache Verstärkung der Fluoreszenz und eine Fluoreszenzquantenausbeute von 3% beobachtet. Die Methode verwendet ungefährliche und kostengünstige Chemikalien und kann bei hohen SWNT-Konzentrationen mit kommerziell erhältlichem unsortierten Rohmaterial durchgeführt werden, was eine Produktion auf größerem Maßstab ermöglicht. Die hervorragenden optischen Eigenschaften von funktionalisierten SWNTs bleiben erhalten wenn sie mit Biopolymeren (z.B. DNA) umwickelt werden, um sie biokompatibel zu machen. Dies macht sie geeignet für zukünftige Anwendungen in der *in vivo* NIR-Bildgebung oder Biosensorik.

Abschließend wurden in einem rationalen Ansatz sp^3-funktionalisierte (6,5) SWNTs für die ratiometrische optische Detektion des Biomarkers anorganisches Diphosphat (Pyrophosphat, PP_i) entwickelt. Das Detektionsschema basiert auf einem Metallverdrängungstest, bei dem die

Fluoreszenz von mit Alkin-Gruppen funktionalisierten SWNTs durch Kupferionen reversibel ausgelöscht wird. Die Fluoreszenzauslöschung erfolgt durch einen photoinduzierten Elektronentransfer, wenn Cu^{2+}-Ionen auf der SWNT-Oberfläche durch Wechselwirkungen mit einem Triazol Liganden und Koordination zu kovalent gebundenen Arylalkin-Gruppen immobilisiert werden. Die Fluoreszenzauslöschung ist für die Defektemission stärker, was den Nachweis von PP_i in ratiometrischen Messungen ermöglicht. Wenn der Sensor durch Umwicklung mit Phospholipid-Polyethylenglycol biokompatibel gemacht wird, eignet er sich zur Detektion von PP_i, das während der DNA-Synthese in der Polymerase-Kettenreaktion freigesetzt wird. Dieses Sensorkonzept könnte als Ausgangspunkt für das weitere rationale Design von Biosensoren, basierend auf funktionalisierten SWNTs mit leuchtenden Defekten dienen.

ACKNOWLEDGEMENTS

This thesis would not have been possible without the fantastic support of many people.

First and foremost, I would like to thank **Prof. Dr. Jana Zaumseil** for providing me with the opportunity to work in her research group, involving me in collaborations and giving me the chance to present at conferences. Thank you for your guidance, trust in my abilities, and for pushing my ideas and projects further than I thought possible. You have taught me a lot over the last few years.

I am also grateful to **Prof. Dr. Sebastian Kruss** for sharing his expertise, allowing me to visit his group in Bochum, and kindly agreeing to review this thesis.

Furthermore, I would like to thank all my former colleagues from the **NMOE** and **PC2D** groups for the good times both in and outside the labs. I also want to thank my office mate **Daniel** for sharing a great time in San Sebastián. A special thanks goes to all members of the **TRIFECTs Team**: **Sonja**, **Ali**, **Nicolas**, **Sebastian**, **Finn**, and **Felix**. Working with you, exchanging ideas, and attending conferences together were the highlights of my PhD journey. I am especially grateful to **Nicolas** and **Felix** for their help at the beginning of my PhD and advice on completing this thesis, as well as **Finn** for proofreading.

A big thank you goes to all the students I supervised during their research projects: **Raphael Berger**, **Marco Fischer**, **Johannes Zeh**, **Simon Wald**, and **Florian Stammer**. It was a pleasure working with you.

Moreover, I would like to thank the many collaborators who contributed to this work: **Prof. Dr. Alexander Högele** and **Dr. Shen Zhao** (Ludwig-Maximilians-Universität München), **Prof. Dr. Michael Zharnikov** and **Dr. Andika Asyuda** (Heidelberg University), **Dr. Benjamin S. Flavel** and **Dr. Han Li** (Karlsruhe Institute of Technology), **Christian Scholz**, **Prof. Dr. A. Stephen K. Hashmi** and **Elena Michel** (Heidelberg University), and **Dr. Sebastian Jung** and **C. Alexander Schrage** (Ruhr University Bochum). Without your help, this work would not have been possible. I am also grateful to the other collaborators I had the pleasure to work with during my time as a PhD student: **Prof. Dr. Milan Kivala**, **Laura Brüchle**, and **Martin C. Dietl** (Heidelberg University), and **J. Alejandro de Sousa** (Institut de Ciència de Materials de Barcelona) and **Sofie Cambré** (University of Antwerp).

Ich möchte mich ebenfalls bei allen **Mitarbeiterinnen und Mitarbeitern der APC** für die Unterstützung bedanken: **Günter Meinusch**, **Peter Jeschka** und **Klaus Schmitt** sowie sein Team der **Feinmechanik-Werkstatt** für die großartige Hilfe bei technischen Fragen. Ebenso bei **Swetlana Duchnay**, **Benjamin Scherke**, **Karin Jordan**, **Isabella Haffelder** und **Anja Ihli** für die Unterstützung bei administrativen Angelegenheiten.

Ich bin besonders dankbar für alle Freundschaften, die während des Studiums entstanden sind. Danke an **Julianna**, **Michael**, **Lucas**, **Sebastian**, **Siegfried**, **Svenja** und **Elena** für all die schöne Zeit während des Studiums und der Promotion, sei es bei abendlichen Spielerunden oder dem wöchentlichem Mittagsessen. Ich hoffe, dass wir auch weiterhin in Kontakt bleiben.

Zu guter Letzt möchte ich mich bei meiner **Familie** und meiner **Freundin** bedanken. Danke, dass ihr immer für mich da seid. Ich freue mich schon auf die bevorstehende gemeinsame Zeit.

Table of Contents

Page

1 Introduction **1**

2 Background **5**

2.1 Single-walled carbon nanotubes . . . 5

2.1.1 Structure & synthesis . . . 6

2.1.2 Purification & chirality sorting . . . 8

2.1.3 Electronic structure . . . 11

2.1.4 Optical properties of SWNTs & excitons . . . 13

2.2 Luminescent defects . . . 17

2.2.1 Exciton localization & spectroscopic properties of luminescent defects . . . 18

2.2.2 Role of the defect structure . . . 22

2.2.3 Covalent functionalization of SWNTs . . . 24

2.2.4 Controlling the diversity of SWNT defect emission . . . 27

2.2.5 Luminescent oxygen defects . . . 29

2.3 SWNTs for sensing & imaging in the near-infrared . . . 30

2.3.1 SWNTs as optical biosensors . . . 32

2.3.2 Luminescent defects as recognition units . . . 35

3 Experimental Methods **37**

3.1 SWNT dispersions . . . 37

3.1.1 Selective dispersion of (6,5) SWNTs in toluene . . . 37

3.1.2 Selective dispersion of (7,5) SWNTs in toluene . . . 37

3.1.3 Selective dispersion of (10,5) SWNTs in toluene . . . 38

3.1.4 Removal of excess wrapping polymer . . . 38

3.1.5 Aqueous dispersion of (6,5) SWNTs . . . 39

3.1.6 Aqueous dispersion of (6,4), (8,3) and (7,5) SWNTs . . . 40

3.1.7 Shortening of aqueous-dispersed (6,5) SWNTs . . . 42

3.2 Covalent functionalization procedures . . . 42

3.2.1 Functionalization of polymer-wrapped SWNTs with diazonium salt . . . 42

3.2.2 Functionalization of SWNTs *via* a base-promoted coupling approach . . . 43

3.2.3 Functionalization of aqueous-dispersed (6,5) SWNTs with diazonium salts 45

3.2.4 Functionalization of SWNTs *via* Fenton-like reaction . . . 46

3.2.5 Functionalization of SWNTs with NaOCl under UV-C-light irradiation . . 47
3.3 Procedures for non-covalent functionalization 48
3.3.1 Surfactant exchange to PL-PEG$_{5000}$ 48
3.3.2 Surfactant exchange to ssDNA 48
3.4 Sensing protocol for the detection of pyrophosphates 49
3.5 Spectroscopic characterization 50
3.5.1 NIR luminescence spectroscopy setup 50
3.5.2 Time-correlated single-photon counting 52
3.5.3 PL quantum yield determination 52
3.5.4 Measurement of PL spectra at low excitation power density 53
3.5.5 Low temperature spectroscopy 53
3.5.6 Autocorrelation measurements at room temperature 55
3.5.7 Measurement of NIR-PL images 55
3.5.8 PL measurements of spiking and PCR experiments 56
3.6 Other characterization techniques 56
3.6.1 Absorption spectroscopy 56
3.6.2 Raman spectroscopy 57
3.6.3 X-ray photoemission spectroscopy 58
3.6.4 Atomic force microscopy 58
3.6.5 Inductively coupled plasma optical emission spectroscopy 59
3.6.6 Preparation of cell cultures 59
3.6.7 Polymerase chain reaction 60

4 Strongly Red-Shifted Defects in Polymer-Wrapped SWNTs 61
4.1 Introduction 61
4.2 Selective introduction of $E_{11}{}^{*-}$ defects 64
4.3 Optical properties of $E_{11}{}^{*-}$ defects 67
4.4 Temperature dependence of luminescent defects 71
4.5 Wavelength-dependent PL lifetime 74
4.6 Spectra of individual SWNTs at cryogenic temperatures 76
4.7 Single-photon emission from luminescent defects 78
4.8 Luminescent sp^3 defects in larger-diameter SWNTs 79
4.9 Mechanistic investigations 81
4.9.1 Nature of the functional group & reference experiments 81
4.9.2 Functionalization mechanism & origin of selectivity 84
4.10 Summary & conclusions 87

5 Bright Oxygen Defects in SWNTs 89
5.1 Introduction 89
5.2 Covalent functionalization *via* Fenton-like reaction 91
5.3 Optimization & optical properties of oxygen defects 93
5.4 Functionalization mechanism 98

5.5 Light-induced effects on functionalized SWNTs . . . 101
5.6 Clustering of luminescent oxygen defects . . . 104
5.7 Expanding the functionalization procedure . . . 106
5.8 Up-scaling . . . 108
5.9 Making functionalized SWNTs biocompatible . . . 109
5.10 Summary & conclusions . . . 112

6 Sensing of Pyrophosphate with Luminescent Defects 115
6.1 Introduction . . . 115
6.2 Copper-induced PL quenching . . . 117
6.3 Fluorescent probe design . . . 120
6.4 Selectivity of sp^3-functionalized SWNT probes . . . 123
6.5 PP_i sensing & PL quenching mechanism . . . 126
6.5.1 Impact of the triazole ligand . . . 126
6.5.2 Competitive complexation of Cu^{2+} ions . . . 127
6.5.3 Influence of the functional group . . . 129
6.5.4 Influence of the sp^3 defect density . . . 130
6.5.5 Origin of PL quenching . . . 131
6.5.6 Summary PP_i sensing & quenching mechanism . . . 134
6.6 Detection of PP_i in biological environments . . . 135
6.7 Detection of PP_i released from PCR . . . 139
6.8 Summary & conclusions . . . 142

7 Conclusions & Outlook 145

A Appendix: Strongly Red-Shifted Defects in Polymer-Wrapped SWNTs 153

B Appendix: Bright Oxygen Defects in SWNTs 157

C Appendix: Sensing of Pyrophosphate with Luminescent Defects 161

Bibliography 167

Abbreviations 195

Eidesstattliche Erklärung 199

CHAPTER 1

INTRODUCTION

In today's telecommunications systems and biomedical research, near-infrared (NIR) emitters have become indispensable. In standard fiber-optic communication systems, NIR-light is essential as it coincides with the transmission windows (1300-1600 nm) of silica fibers, enabling efficient high-speed transmission of digital data through modulated light pulses with minimal signal losses.[1] Currently, light-emitting diodes or lasers made from inorganic semiconductors are used as light sources in fiber-optic communication.[2] However, they fall short of meeting the demands of emerging fields such as quantum communication[3] and flexible electronics.[4] In biomedical research, *in vivo* fluorescence imaging has emerged as a powerful technique, offering significant advantages over other tomographic imaging methods.[5] These advantages include real-time wide-field imaging, non-hazardous optical radiation, and sub-diffraction-limited spatial resolution when combined with super-resolution microscopy. Yet, this technique is currently limited to fluorescent emitters in the visible range. In the NIR (*e.g.* NIR-II window, 1000-1350 nm) the transparency of biological tissues is much higher and thus allows for optical detection and imaging at deeper penetration depths with higher signal-to-noise ratio by minimizing light scattering, absorption, and autofluorescence.[5] Hence, there is a significant demand for suitable NIR emitters that meet the required criteria for a wide range of applications.

Semiconducting single-walled carbon nanotubes (SWNTs) show great promise as NIR emitters. While other NIR emitter exist, SWNTs possess a combination of various advantageous properties. They display narrowband, diameter-dependent photoluminescence (PL) in the NIR, mechanical flexibility, and solution-processability.[6–8] This allows for excellent integration into optoelectronic devices, showcasing high ambipolar charge carrier mobilities and electroluminescence upon electrical excitation.[7] Moreover, their PL is not bleached in aqueous media or by laser irradiation. However, it is highly sensitive to changes in the environment, enabling molecular recognition of biomolecules.[9] SWNTs can be made biocompatible by non-covalent coatings with biopolymers, making them a great platform as (bio)sensors for *in situ* diagnostics and agricultural plant research.[10] Despite these advantages, there are limitations such as their low PL quantum yield (PLQY) of <1% in dispersion. Additionally, the majority of accessible SWNT chiralities do not emit at telecommunication wavelengths or in the NIR-II window.

A powerful strategy to address these challenges involves the creation of luminescent defects in the SWNT lattice through controlled covalent functionalization or oxidation.[11–14] Luminescent defects are specific lattice defects wherein carbon atoms acquire significant sp^3 character within the otherwise sp^2-hybridized SWNT lattice. This leads to the creation of new localized and optically active states, which reside below the optical band gap of pristine SWNTs and give rise to an additional red-shifted emission feature. These defects not only shift SWNT emission into the NIR-II window and closer to telecom wavelengths for a given SWNT species, but can also significantly brighten the overall emission in the case of small-diameter SWNTs.[15] On top of that, SWNT excitation can be shifted into the NIR, allowing for detection and imaging with ultra-low excitation doses.[16]

The functional groups attached to the defect sites are oxygen atoms or alkyl/aryl groups and additionally offer a new level of control over the binding and interactions of the SWNT with biological analytes.[17] Due to their zero-dimensional structure, luminescent defects can also exhibit single-photon emission with high purity even at room temperature.[18,19] This unique property makes SWNTs with luminescent defects one of the very few materials that have the potential for application in fiber-based quantum information technologies.[20]

However, prior to application, significant challenges in the creation of luminescent defects must be resolved. The optical properties of these defects depend largely on their precise geometry, also referred to as the binding configuration.[21] The chemical differences between these defect configurations are subtle and currently there is limited control over their formation. As a result, defect emission occurs across a wide spectral range. Many applications cannot tolerate such high spectral diversity. Additionally, only very few defects are introduced in the configuration that exhibits strongly red-shifted emission close to or at the important telecommunication wavelengths. To overcome these challenges, new synthetic routes are necessary to selectively introduce defects in the desired binding configuration. Ideally, functionalization should be conducted with SWNTs dispersed in organic solvents to facilitate their easy implementation in electrical devices.

Furthermore, so far the reported sample quality, and thus the brightness of luminescent defects in aqueous dispersions, varies widely. This is mostly due to the high sensitivity to the reaction conditions of commonly used functionalization routes. For widespread application in *in vivo* imaging, facile, reproducible, and scalable functionalization techniques are required that can produce functionalized SWNTs with high brightness under physiological conditions.

Finally, in the majority of optical biosensors utilizing SWNTs, a single emission feature is employed for data analysis. Here, luminescent defects offer additional emission features whose potential is still largely unexplored. Only a few examples are reported in the literature, and the applied detection schemes rely on complex interactions with biopolymers that are non-covalently bound to the SWNT surface, preventing the rational design of SWNT sensors.[22,23]

This interdisciplinary thesis aims to present viable solutions to the above outlined issues by developing novel functionalization methods for SWNTs and introducing a new sensing approach using luminescent defects. First, a functionalization protocol is introduced that allows for the selectively creation of luminescent defects with a specific previously inaccessible binding configuration in polymer-wrapped SWNTs in organic solvents. The resulting optical properties

of these defects are analyzed mainly by PL spectroscopy, focusing on potential applications as a single-photon source at telecom wavelengths.
Next, chirality enriched dispersions of (6,5) SWNTs in aqueous media were used to explore the creation of luminescent oxygen defects by reaction with reactive oxygen species generated through a metal redox catalyst. Emphasis will be placed on evaluating the reproducibility and scalability of the functionalization approach and its potential applications in (bio)imaging and (bio)sensing.
Last, a novel sensor design is introduced, utilizing functionalized (6,5) SWNTs bearing an alkyne moiety for ratiometric detection of inorganic pyrophosphate in a metal displacement assay. The underlying sensing mechanism is thoroughly studied and the sensing approach was transferred to biological environments including subsequent application to track DNA synthesis during polymerase chain reaction (PCR).
The main part of this thesis begins with Chapter 2, which provides an introduction to the underlying theoretical principles and discusses the current state of research. Special emphasis is placed on the optical properties of luminescent defects in SWNTs, their synthetic incorporation, and their potential applications as imaging probes and optical biosensors.
Chapter 3 summarizes the materials and experimental methods employed in this thesis, highlighting the synthetic methods and sensing protocols developed throughout this work.
Chapter 4 introduces a functionalization method for the selective introduction of luminescent sp^3 defects with a specific binding configuration in polymer-wrapped SWNTs. The functionalization employs a base-promoted coupling approach using primarily aniline derivatives. The optical properties and decay dynamics of sp^3-functionalized SWNTs are studied in detail, along with their potential as single-photon emitters. Additionally, the functionalization approach is transferred to larger-diameter SWNTs, and the underlying chemistry is investigated.
Chapter 5 presents a method for creating luminescent oxygen defects in aqueous dispersed SWNTs. Covalent functionalization is achieved through the reaction with reactive oxygen species produced *via* Fenton-like copper redox chemistry. The influence of external factors such as reagent concentrations, choice of surfactant, and impact of light on the functionalization process are highlighted. Furthermore, the emission brightness of these defects is evaluated before and after transfer to biocompatible coatings. Lastly, the scalability of this method with unsorted SWNTs is explored.
Chapter 6 introduces a SWNT sensor design allowing for the ratiometric detection of PP_i in aqueous media. This sensing approach utilizes sp^3-functionalized (6,5) SWNTs bearing an alkyne moiety that enhances interactions with a Cu^{2+} ion/triazole complex. The strong impact of Cu^{2+} ions on defect-state PL decay dynamics enables the detection of PP_i in a metal displacement assay. The sensing mechanism is thoroughly investigated, revealing the influence of the functional group and the triazole ligand, offering guidelines for the further development of this new class of SWNT-based biosensors. Finally, this sensor is applied in biological environments to explore its potential for detecting PP_i in complex media and PP_i released during PCR.
Chapter 7 concludes the thesis, summarizing the main results and providing an interpretation within a broader context. Finally, it offers perspectives for future research in the field of luminescent defects in SWNTs.

CHAPTER 2

BACKGROUND

This Chapter provides an overview of the theoretical concepts and state-of-the-art research that are central to this thesis. First, the reader is introduced to single-walled carbon nanotubes and their electronic and optical properties. Second, the properties and underlying photophysics of luminescent defects will be discussed, with an emphasis on currently available synthetic techniques for their creation. Last, potential applications of luminescent defects as near-infrared imaging probes and optical biosensors will be reviewed.

2.1 Single-walled carbon nanotubes

In recent decades, low-dimensional materials have been the subject of intensive research in both science and industry. In particular, low-dimensional carbon allotropes have attracted great interest due to their fascinating physics and practical applications.[24,25] Among carbon-based allotropes, zero-dimensional (0D) fullerenes have demonstrated their suitability for applications in photovoltaics[26,27] and are currently being investigated for use in drug delivery systems.[28] Graphene, a two-dimensional (2D) material, is known for its exceptional thermal, mechanical, and electronic properties.[29–31] Within this category, carbon nanotubes represent the corresponding one-dimensional (1D) analogue and are characterized by a high aspect ratio with diameters of ~1 nm and lengths up to several µm.[32–34] In particular, single-walled carbon nanotubes (SWNTs) are attractive due to their exceptional mechanical properties,[35] ballistic transport capabilities,[36,37] and structure-dependent electronic and optical characteristics.[6,38] Over the past decade, their application potential has been further enhanced by rapid progress in growth[39–41] and purification,[42–44] as well as various other advancements, such as the ability to manipulate their optoelectronic properties through covalent functionalization.[15,45]

2.1.1 Structure & synthesis

SWNTs are hollow tubular structures consisting of sp^2-hybridized carbon atoms organized in a hexagonal lattice. To describe their intriguing structure-dependent properties, it is advantageous to conceptualize SWNTs as a rolled-up sheet of graphene, as shown in Figure 2.1.[46] Depending on the orientation of this theoretical roll-up process, different structurally distinct SWNT species are obtained. Each species is uniquely defined by its circumferential roll-up vector ($\vec{C}_h$), which connects pairs of carbon atoms that coincide in the resulting SWNT lattice. $\vec{C}_h$ can be expressed mathematically as a linear combination according to:[47]

$$\vec{C}_h = n\vec{a}_1 + m\vec{a}_2\,, \tag{2.1}$$

where n and m are integers, and $\vec{a}_1$ and $\vec{a}_2$ denote the primitive lattice vectors of graphene. Their length is the Bravais lattice constant a ($a = \sqrt{3}\,a_{C\text{-}C} = 0.246\,\text{nm}$), where $a_{C\text{-}C}$ is the carbon-carbon bond length (~0.142 nm). The integer pair (n,m) is commonly referred to as chirality, irrespective of the actual stereochemistry. This integer pair correlates directly with the SWNT diameter (d_t) and the chiral angle (α) between $\vec{C}_h$ and $\vec{a}_1$:[48,49]

$$d_t = \frac{|\vec{C}_h|}{\pi} = \frac{a}{\pi}\sqrt{n^2 + nm + m^2}\,, \tag{2.2}$$

$$\cos(\alpha) = \frac{2n + m}{2\sqrt{n^2 + nm + m^2}}\,. \tag{2.3}$$

Finally, the translation vector $\vec{T}$ can be introduced as the smallest graphene lattice vector orthogonal to $\vec{C}_h$, which defines the periodicity of the SWNT along the axis. The length L_t of the SWNT can be expressed as a multiple of $|\vec{T}|$ and, together with d_t, $\vec{T}$ defines the unit cell of a SWNT. Although the size of the unit cell can vary significantly between chiralities with similar chiral angles and diameters, SWNTs are typically modeled with infinitely repeating units because $L_t \gg d_t$ and tube ends are neglected. Figure 2.1 illustrates the exemplary construction of a (6,5) (red arrow) and a (6,6) SWNT (grey arrow).

As a result of the symmetric hexagonal lattice, only chiral angles in the range of $0° \leq \alpha \leq 30°$ give unique values for n and m. The overall SWNT structure can therefore be divided into three categories: Zigzag, armchair and chiral SWNTs. Zigzag SWNTs, characterized by a chiral angle of $\alpha = 0°$ and the index pair (n,0), along with armchair SWNTs, characterized by a chiral angle of $\alpha = 30°$ and the index pair (n,n), are achiral SWNTs due to their mirror symmetry. All other species are considered chiral SWNTs, denoted as (n,m).[46] Chiral SWNTs exist in enantiomeric pairs, represented as (n,m) and (m,n) = (n + m,−m), which have the same diameter and properties, but show opposite circular dichroism.[50]

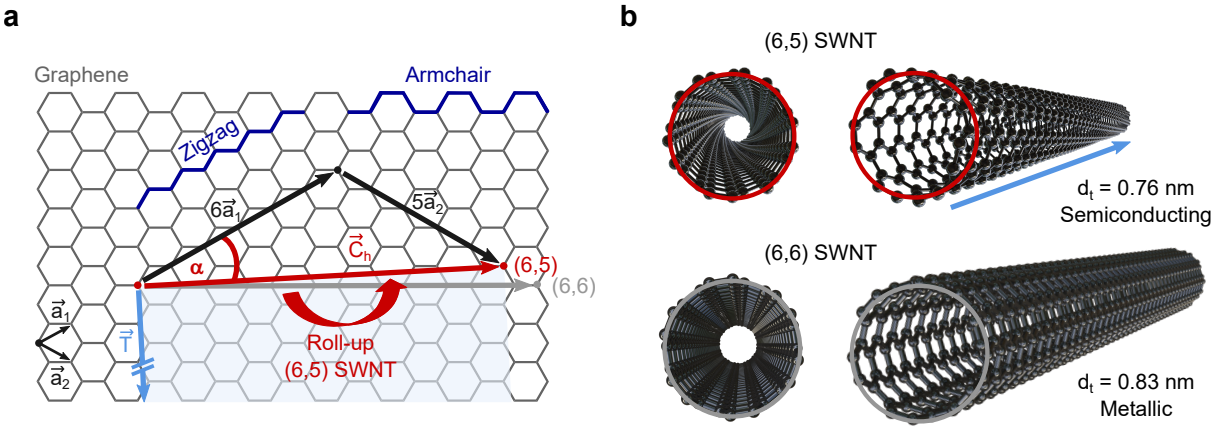

Figure 2.1: a) Illustration of the theoretical roll-up process of graphene forming a (6,5) SWNT. The roll-up vector $\vec{C}_h$ (red), constructed from the graphene lattice vectors $\vec{a}_1$ and $\vec{a}_2$ (black), defines the (6,5) SWNT's circumference. The translational vector $\vec{T}$ (light blue) indicates the SWNT axis and its length. Blue carbon bonds signify the roll-up direction of achiral zigzag and armchair SWNTs. The chiral vector of an armchair (6,6) SWNT is depicted in grey. b) Molecular structures of the chiral (6,5) SWNT (top) and achiral (6,6) SWNT (bottom), with a view from the front on the left. Despite similar $\vec{C}_h$, (6,5) SWNTs are semiconducting, while (6,6) SWNTs exhibit metallic characteristics.

In reality, SWNTs can have hemispherical end caps and their cylindrical structure is formed during growth from a metal catalyst.[46,51] Commercial production of raw SWNT material has already been achieved, employing various techniques to vary the diameter distribution. Large-diameter nanotubes (d_t~1-2 nm) can be obtained by methods such as laser ablation[52] or arc-discharge,[53] while the plasma-torch process yields high-quality SWNTs with diameters between 0.9-1.5 nm.[54] This method involves the decomposition of carbon precursors (*e.g.*, carbon black) and transition metal catalyst particles in an argon plasma-torch. However, the most cost-effective and widely adopted method due to its mild conditions, is chemical vapor deposition (CVD).[55] In the CVD process, gaseous carbon precursors like CH_4 undergo catalytic decomposition, leading to carbon precipitation at catalyst particles.[56] The diameter of the resulting SWNT is significantly influenced by catalyst size, composition, and melting point.[39,57] The most relevant CVD synthesis routes for this thesis include the CoMoCAT (cobalt-molybdenum catalyst) and HiPCO (high-pressure carbon monoxide) processes.

The CoMoCAT process is the preferred method for producing small-diameter SWNTs (d_t ~ 0.7-1.0 nm) with a narrow diameter distribution. It yields predominantly (6,5) and (7,5) SWNTs along with smaller species such as (6,4) and (8,3) SWNTs.[58–60] SWNT growth is initiated by carbon monoxide decomposition on a cobalt-molybdenum catalyst at temperatures between 700 °C and 950 °C on a SiO_2 support substrate. Post-growth, the support substrate is dissolved by acid treatment with hydrofluoric or sulfuric acid.[58,61] In HiPCO synthesis, carbon monoxide serves as the carbon feedstock, mixed at high pressure (1-10 bar) and high temperature (800-1200 °C) with $Fe(CO)_5$ catalysts.[62] Under these conditions, $Fe(CO)_5$ decomposes, and carbon nucleation is initiated at the newly formed iron catalyst particles, resulting in SWNTs with an average diameter between 0.8-1.3 nm (*e.g.* (10,5) SWNTs).[62,63]

Currently, commercial synthesis methods yield mixtures of SWNTs that include both semiconducting and metallic types with varying diameters, and contain impurities such as amorphous carbon or residual catalyst particles. Despite advances in selective growth methods for specific SWNT chiralities,[41] the purification and sorting of SWNT raw material remains indispensable. Obtaining chirality-pure SWNTs and separating semiconducting from metallic SWNTs are prerequisites for realizing their full potential in (opto)electronic applications and as optical (bio)sensors.[64]

2.1.2 Purification & chirality sorting

The currently available purification and chirality sorting techniques are designed exclusively for solution-processed SWNTs. The first step is to separate aggregated, as-grown SWNT bundles. To overcome the strong van der Waals interactions between SWNT sidewalls, intense sonication methods such as tip sonication or bath sonication are typically required.[65] Since the entropy of mixing is small for SWNTs, they are practically insoluble in most solvents with only a few exceptions such as cresols.[66] Most commonly dispersants are employed to stabilize the colloidal dispersion and prevent re-aggregation. In the next step, centrifugation is used to remove bulk impurities and remaining bundled SWNTs.[65] The resulting supernatant containing individualized SWNTs can be used for further chirality sorting. Depending on the separation technique, chirality selectivity may already be achieved in this step.

Various chirality sorting techniques, including ultracentrifugation (both density gradient (DGU)[67] and rate-zonal methods[68]), electrophoresis,[69] ion-exchange chromatography,[42] gel chromatography,[70] aqueous two-phase extraction (ATPE),[43,71] and selective polymer-wrapping in organic solvents[72] have been developed. Chirality sorting *via* ATPE and polymer-wrapping will be discussed further, as they were specifically employed in this thesis to obtain nearly monochiral SWNT dispersions. Notably, ATPE separation driven by selective DNA wrapping is a distinct process not covered here.[73,74]

In ATPE (see Figure 2.2a), two water-soluble polymers with different densities, typically polyethylene glycol (PEG) and dextran, are mixed together. Upon exceeding a critical concentration threshold, the homogeneous mixture undergoes a thermodynamic phase separation, yielding two phases. To aid this separation process, low-speed centrifugation is typically performed for a few minutes. When surfactant-dispersed SWNTs are introduced, selective partitioning depends on the chemical potential differences for each chirality between the two phases. The partition coefficient K_i for each chirality is defined as its concentration ratio in the upper phase ($c_{T,i}$) and the bottom phase ($c_{B,i}$). In a simplified model, this ratio can be expressed in correlation with the standard chemical potential and is given by:[43]

$$K_i = \frac{c_{T,i}}{c_{B,i}} = \exp\left(-\frac{\mu^0_{T,i} - \mu^0_{B,i}}{k_B T}\right), \tag{2.4}$$

where $\mu^0_{T,i}$ and $\mu^0_{B,i}$ are the standard chemical potentials of the chirality in the upper and lower phases, T is the absolute temperature, and k_B is the Boltzmann constant. Small changes in the chemical potential of a chirality in the two phases can lead to significant differences in

the partition coefficient, causing transitions between phases. This effect is exploited in ATPE to separate a single chirality from a mixed population. To control (small-diameter) SWNT partitioning in the phases, commonly the surfactants sodium deoxycholate (DOC) and sodium dodecyl sulfate (SDS) are used.[43] Increasing the coverage of the SWNT sidewall with the bile salt DOC leads to partitioning into the bottom dextran-rich phase, while coverage with SDS results in partitioning into the top PEG-rich phase.

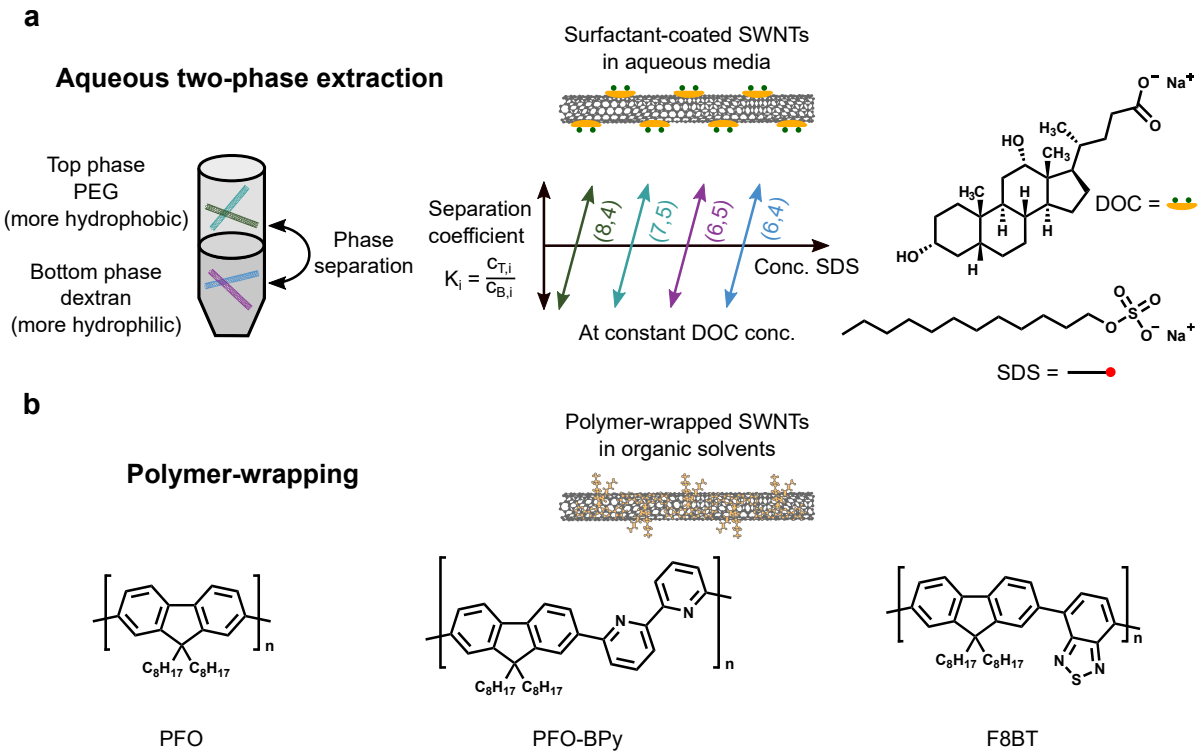

Figure 2.2: a) Schematic of aqueous two-phase extraction: Poly(ethylene glycol) (PEG) and dextran undergo phase separation in an aqueous solution, forming two phases. Surfactant-dispersed SWNTs partition between these phases, governed by the separation coefficient. The separation coefficient is illustrated for (n,m) SWNTs in an SDS/DOC competitive separation. At constant DOC concentrations and increasing SDS concentrations, SWNTs transition to the upper phase, mainly based on their diameter. Molecular structures of DOC and SDS are on the right. b) Molecular structures of polyfluorene polymers used for chirality-selective polymer-wrapping used in this thesis.

DOC possesses a rigid structure and is a planar amphiphile with a charged face.[67] Its planar structure is expected to enhance the formation of densely packed monolayers on the hydrophobic SWNT surface.[75,76] Empirically, it has been found that DOC preferentially interacts with small-diameter semiconducting SWNTs.[77] In contrast to DOC, the anionic alkyl amphiphile SDS forms more disordered sparse coatings and preferentially interacts with larger diameters, as its hydrophobic tail is oriented along the SWNT axis to maximize van der Waals interactions.[78] For orientation along the circumferential direction, a significant energetic barrier exists for small-diameter SWNTs.[75,78] Hence, DOC and SDS show opposing trends concerning SWNT diameter which enables the separation of small-diameter SWNTs in ATPE when DOC and SDS serve as

surfactants. However, the separation of larger-diameters is more complicated as differences in affinity towards a specific surfactant are small. The interactions are much more complex in detail. At commonly used SDS concentrations, micellar assembly occurs, which further stabilizes the SWNT and changes the surface morphology.[78] Radial and half-cylindrical structures of SDS micelles have been observed, but this depends on the symmetry and diameter of the SWNT.[35,79]
In a standard diameter sorting protocol, chirality separation occurs in three steps. First, the SDS concentration is increased at a constant DOC concentration, causing SWNTs with diameters larger than the target species to partition into the top PEG-rich phase. The top phase is then replaced with a new PEG phase and SDS is added until the target species has partitioned into the top phase. Finally, a semiconducting-metallic separation step is performed, typically with the aid of sodium cholate (SC) and an oxidant such as sodium hypochlorite (NaOCl).
In an alternative approach, the effective DOC concentration is gradually decreased at a constant SDS concentration by acid addition, inducing protonation and DOC aggregation. Various other sorting protocols exist, including separation based on enantiomeric handedness and sorting of large-diameter SWNTs.[43,80] For further details, the readers are referred to an excellent review of ATPE by Jeffrey Fagan.[43]
While ATPE allows for the selection of various chiralities and achieves a purity of up to 99.5% for semiconducting SWNTs, the challenge of residual metallic SWNTs persists in many applications.[81] For device integration, an exceptionally high purity of semiconducting SWNTs is indispensable, making polymer-wrapping in organic solvents the preferred method.[44] Introduced by Nish *et al.*, this approach relies on the chirality-selective adsorption of conjugated polymers onto the SWNT sidewall.[72] This straightforward method can yield dispersions with very high selectivity toward semiconducting chiralities (>99.7%) in a single step, as chirality sorting occurs during the initial exfoliation.[82] By mixing the SWNT raw material with a conjugated polymer in solvents like toluene or *ortho*-xylene and applying sonication, the polymer wraps around its preferred chiralities in the mixture. Additionally, the polymer stabilizes the wrapped species, preventing re-aggregation, while other SWNTs and bulk impurities can be sedimented and removed through centrifugation.
Fluorene-based polymers and copolymers, in particular, exhibit high selectivity.[72,83–85] Figure 2.2b illustrates the molecular structures of polymers used for chirality sorting in this thesis. They feature a π-conjugated backbone, which enables strong adsorption to the SWNT sidewall through π-π interactions, and a long alkyl chain that improves the polymer's solubility, enhancing colloidal stability in non-polar solvents. Molecular dynamics (MD) simulations and transmission electron microscopy analysis suggest that the polymer can align along the nanotube axis or form helices around the SWNT.[86–89] For (6,5) SWNTs wrapped with poly[(9,9-dioctylfluorenyl-2,7-diyl)-*alt*-(6,6'-2,2'-bipyridine)] (PFO-BPy), simulations show helical wrapping as the energetically favored geometry.[90] However, the exact nature of their interactions with the SWNT sidewall, contributing to observed high selectivity, remains elusive.[91] Empirically, various polymer parameters (*e.g.*, molecular weight, concentration, alkyl chain length),[85,92] solvent factors (*e.g.*, viscosity),[85,93] and sonication conditions (*e.g.*, time, temperature)[85,94] can influence wrapping yield and selectivity. Samanta *et al.*[44] and Fong *et al.*[95] extensively reviewed parameters affecting the wrapping process.

Polymer-wrapping is particularly effective when performed with SWNT raw material that is already enriched in the target chirality. A good example represents the extraction of (6,5) SWNTs from CoMoCAT raw material using PFO-BPy, as demonstrated by Ozawa *et al.* in 2011.[96] Alternatively, the extraction of (7,5) SWNTs and (10,5) from CoMoCAT and HiPCO raw material can be achieved using poly(9,9-dioctylfluorene) (PFO) or poly[(9,9-di-*n*-octylfluorenyl-2,7-diyl)-*alt*-(benzo[2,1,3]thiadiazol-4,8-diyl)] (F8BT), respectively.[84,85]
Additionally, polymer-sorting can be paired with mild exfoliation techniques, which leads to long SWNTs with low lattice defect concentrations. Harsh sonication conditions can reduce the average SWNT length,[97] introduce lattice defects, and create open tube ends susceptible to solvent intercalation.[98] Graf *et al.* introduced shear-force mixing as a mild and scalable exfoliation method that enables the production of large quantities of nearly monochiral PFO-BPy-wrapped (6,5) SWNTs with average tube lengths of 1-2 µm.[83,99] In contrast, aqueous dispersions for ATPE typically require harsh tip sonication, resulting in SWNTs with a length of approximately 0.5 µm. The difference in exfoliation methods is likely a key factor contributing to the significantly different photoluminescence quantum yields of aqueous ATPE-sorted (6,5) SWNTs (~0.5%) compared to PFO-BPy-wrapped (6,5) SWNTs in toluene (~2%), both of which will be utilized in this thesis.

2.1.3 Electronic structure

Similar to the geometrical structure of SWNTs, their electronic properties can be derived from those of graphene. Graphene possesses a flat hexagonal structure of sp^2-hybridized carbon atoms, resulting in delocalized π-electrons formed by the interacting $2p_z$ orbitals above and below the graphene plane. The graphene lattice is highly symmetrical, with two carbon atoms per primitive unit cell leading to the formation of two π-bands: A bonding π-band and an anti-bonding π*-band (also referred to as the conduction band and valence band). These bands dominate the electronic properties near the Fermi level ($\pm$ 3 eV), and thus govern the electronic charge transport and optical transitions in the UV-Vis-NIR region.[48] Utilizing tight-binding approximations and assuming electron-hole symmetry, the valence and conduction bands in reciprocal space are given by:[100]

$$E(\vec{k}) = \pm\gamma\sqrt{1 + 4\cos\frac{\sqrt{3}\,k_x a}{2}\cos\frac{k_y a}{2} + 4\cos^2\frac{k_y a}{2}}\,, \tag{2.5}$$

where $\vec{k}$ is the wave vector, γ is the nearest-neighbor carbon-carbon interaction energy (typically taken to be 3.1 eV), and the Fermi level was set to zero. When plotting the valence band in the first Brillouin zone, points with high symmetry are revealed, known as K and K' (see Figure 2.3a,b). They correspond to neighboring atoms in the real space lattice. These points constitute two non-equivalent sets of three points and thus a valley degeneracy of two is obtained. This characteristic sets graphene apart from traditional semiconductors, where Γ is typically the primary point of interest. The valence and conduction bands meet at the K-points and the energy dispersion close to the Fermi energy is linear. Consequently, graphene is termed a semi-metal or zero-band gap semiconductor.

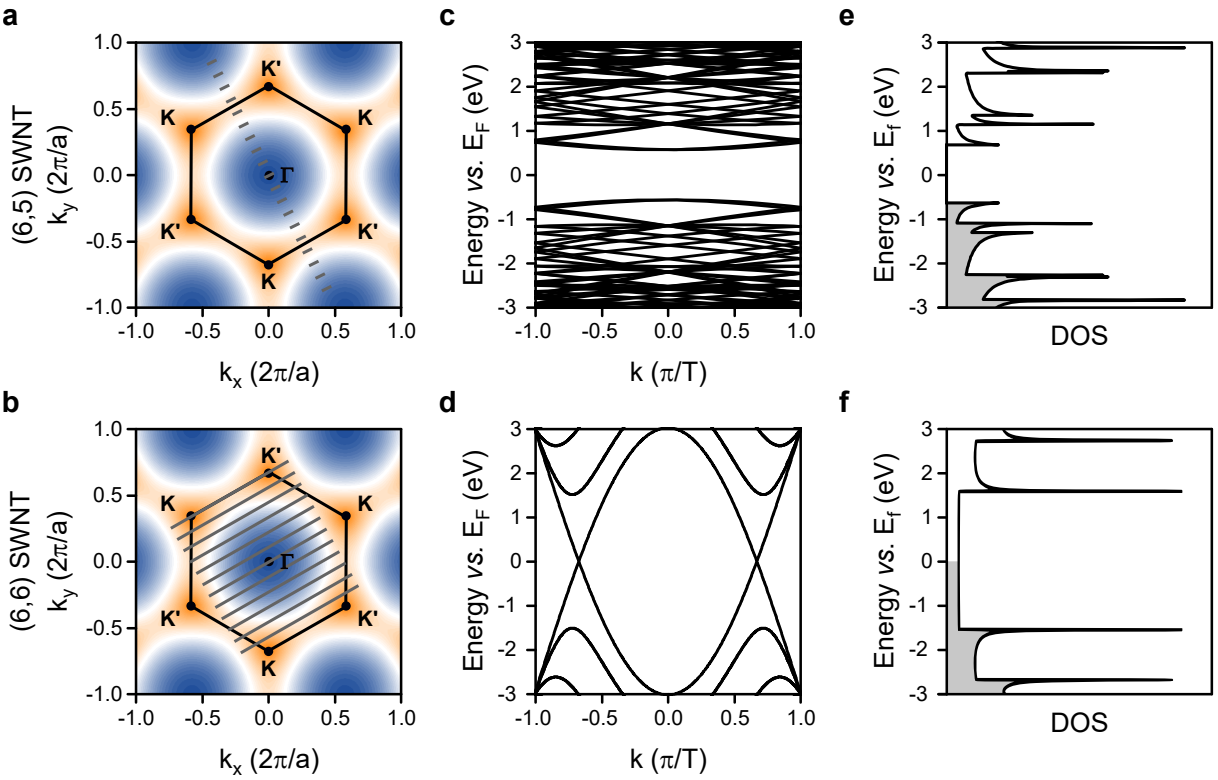

Figure 2.3: Electronic structures of (6,5) SWNTs (top row) and (6,6) SWNTs (bottom row) calculated within the tight-binding and zone-folding formalisms. a,b) Contour plot of the valence band structure of graphene in the first Brillouin zone. The allowed wave vectors of (6,5) and (6,6) SWNTs are shown as cutting lines through the band structure. Energy band structure (c,d) and DOS (e,f) are presented for both chiralities. The DOS at the Fermi energy (E_F) is zero for semiconducting (6,5) SWNTs but finite for metallic (6,6) SWNTs.

The electronic properties of SWNTs can now be derived from those of graphene using the so-called zone-folding model.[101] First, the real-space structure of SWNTs needs to be converted to its reciprocal lattice, following the reciprocity condition specified by:[46]

$$\exp[i(\vec{K}_a + \vec{K}_c) \cdot (\vec{C}_h + \vec{T})] = 1\,. \tag{2.6}$$

Hence, the nanotube Brillouin zone is defined by the reciprocal lattice vectors $\vec{K}_a$ along the nanotube axis and $\vec{K}_c$ in the circumferential direction. Rolling up a graphene sheet to form a SWNT introduces additional periodic boundary conditions on the wave vectors $\vec{K}_a$ and $\vec{K}_c$. Due to the high aspect ratio of SWNTs ($L_t \gg d_t$), axial wave vectors k are closely spaced and treated as quasi-continuous, while circumferential wave vectors q become quantized according to:[46,48]

$$q = j|\vec{K}_c| = \frac{2\pi j}{|\vec{C}_h|} = \frac{2j}{d_t}\,, \qquad \text{with } j = 0, 1, ..., j_{max}\,. \tag{2.7}$$

This quantization results in 1D SWNT sub-bands, depicted as cutting lines through the band structure of graphene. The band structure of a SWNT is then given as the sum of all these 1D sub-bands.[101] Figure 2.3a-d illustrates the cutting lines and band structures of the chiral (6,5) and armchair (6,6) SWNTs. Depending on the boundary conditions, the cutting lines may intersect or not intersect with a K point. SWNTs with an intersection at the K point (*e.g.*, (6,6) SWNTs)

lack a band gap, exhibiting metallic properties, while other SWNTs (*e.g.*, (6,5) SWNTs) possess a band gap, displaying semiconducting properties. Consequently, the chiral vector $\vec{C}_h$, and thus the chiral indices (n,m), determine the electronic type of a SWNT. Further analysis reveals that if (n-m) is zero or an integer multiple of 3, they are metallic, while all other chiralities are semiconducting.[46,101] The band gap E_g can be estimated by $E_g = 2\gamma\frac{a_{C\text{-}C}}{d_t}$ and is primarily determined by the tube diameter, showing an inverse correlation.[46] This diameter–transition energy dependency is often visualized in a Kataura plot.[6,102]
Furthermore, the total density of states (DOS) distribution, $g_{tot}(E)$, can be derived from the sum over the sub-bands with index j of the SWNT, as follows:

$$g_{tot}(E) = \sum_j g(E, j) = \sum_j \frac{1}{\pi}\left|\frac{\partial k}{\partial E}\right|. \tag{2.8}$$

As characteristic for electrons in a 1D solid, the DOS distribution exhibits van Hove (vH) singularities, illustrated in Figure 2.3e,f for (6,5) and (6,6) SWNTs. At the Fermi level, the DOS is finite for metallic (6,6) SWNTs and zero for semiconducting (6,5) SWNTs. The presence of a direct band gap should allow for the observation of luminescence in semiconducting SWNTs upon optical (and electrical) excitation, a topic explored further in the following section.

2.1.4 Optical properties of SWNTs & excitons

In the preceding section, the DOS was derived from the tight-binding model, providing a convenient way to estimate the energy of optical transitions in semiconducting SWNTs. In a single-particle model framework, the optical absorption transition in SWNTs involves electronic transitions between the valence band and the conduction band. According to Fermi's golden rule, the transition rate is proportional to the DOS in both the initial and final energy levels.[103] Consequently, transitions primarily occur between the van Hove (vH) singularities of the valence band (v_1, v_2...) and the vH singularities of the conduction band (c_1, c_2...).[6] Upon closer inspection, only transitions between the ith vH singularity of the valence band and the conduction band (E_{ii}) are prominent, with E_{ij} transitions appearing but being weak (~5% of E_{ii}).[104] This observation can be rationalized by highly polarized absorption along the SWNT axis. Considering SWNT symmetry and the dipole selection rule, E_{ij} transitions are allowed for excitation perpendicular to the SWNT axis, while E_{ii} transitions are allowed for excitation parallel to the SWNT axis.[105] However, significantly higher oscillator strengths are obtained when the electric field polarization is parallel, as opposed to perpendicular to the SWNT axis, where it is suppressed by depolarization effects (antenna effect of the 1D structure of SWNTs).[106] Hence, only E_{ii} transitions are observed, and the energy of the E_{11} transition should correspond to the absorption or luminescence across the band gap energy (E_g) (see Figure 2.4a).

However, the optical properties as described by tight-binding models fall short in explaining the observed transition energies, as they overlook many-body effects arising from photo-excited electrons and holes.[6,107,108] The low dimensionality of SWNTs results in reduced dielectric screening of charge carriers, as the electric field lines between the electron and hole predominantly pass through vacuum or a medium with low dielectric constant (see

Figure 2.4b).[109] This leads to strong electrostatic interactions between photo-excited electrons and holes, forming tightly bound electron-hole pairs known as (Frenkel) excitons. Many-body interactions of excitons can shift the transition energy in two ways. First, attractive Coulomb interactions between the electron and hole lower the effective band gap energy. Due to the poor dielectric screening in SWNTs, these exciton binding energies (E_b) are on the order of several hundred meVs,[110,111] significantly larger than in conventional three-dimensional inorganic semiconductors (few meV),[103] making them stable at room temperature. Conversely, the repulsive interaction between the excited electron and electrons in the valence band effectively increases the band gap energy through the self-energy term (E_{self}). In summary, the E_{11} transition can be described by $E_{11} = E_g + E_{self} - E_b$, and an overall increase in transition energy compared to the single-particle band gap E_g is obtained, as E_{self} exceeds E_b in SWNTs.[107,108]

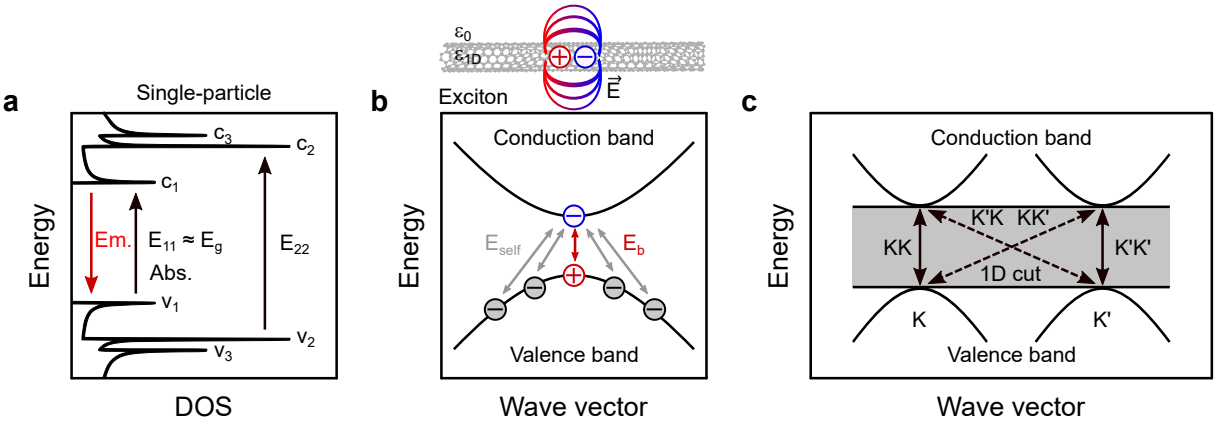

Figure 2.4: a) Within the single-particle picture, optical transitions in semiconducting SWNTs can be described as transitions (absorption black; emission red) between van Hove singularities of the valence band (v_1,...) and the conduction band (c_1,...). The E_{11} transition corresponds to the band gap E_g. b) Illustration of many-body interactions in SWNTs: The low dimensionality in SWNTs leads to reduced dielectric screening, as electric field ($\vec{E}$) lines pass primarily through areas with low ε_0. Attractive electron-hole interactions (exciton binding energy E_b, red arrow) and repulsive electron-electron interactions (self-energy E_{self}, grey arrows) lead to changes in E_{11} compared to the single-particle picture. c) Illustration of the two-fold valley (K and K') degeneracy in SWNTs, resulting in a four-fold degeneracy of each excitonic level.

Taking into account the K- and K'-point degeneracy in the graphene unit cell, SWNTs demonstrate a two-fold valley degeneracy, resulting in a four-fold degeneracy for each excitonic level. Hence, one excitonic level corresponds to four singlet excitons, accommodating the electron and hole in either the K or K'-valley. The individual configurations include KK, K'K', KK', or K'K, as depicted in Figure 2.4c. Additionally, considering the spin of the involved charge carriers, each configuration further splits into one singlet and three triplet states. Consequently, each E_{ii} state encompasses a total of 16 excitons, of which only one is optically active, as will be detailed in the following.

Out of the 16 excitons, 12 represent triplet excitons, which are considered dark due to the requirement of spin conservation and low intersystem crossing yields caused by weak spin-orbit coupling in SWNTs. Additionally, of the four singlet excitons, the KK' and K'K intervalley

excitons (E_{11}(K)) have a finite center-of-mass momentum, formally making them dark as well. Finally, the remaining two intravalley zero-momentum singlet excitons split into a bonding and an antibonding linear combination with even parity (E_{11}(D)) and odd parity (E_{11}(B)), respectively.[112] The selection rules further necessitate the initial and final states to have opposite parity, categorizing the even-parity singlet exciton (E_{11}(D)) as dark as well.[113] Consequently, only the odd-parity, zero-momentum singlet exciton is optically active and accessible through a one-photon absorption or emission process.

A summary of the described model for singlet E_{11} excitons is shown in Figure 2.5a. The parity-forbidden E_{11}(D) state can be found a few meV below the bright E_{11}(B) state, and non-radiative decay to the E_{11}(D) state yields reduced E_{11} photoluminescence (PL) intensity at low temperatures (< 50 K).[114] The K-momentum dark excitons are degenerate and located ~25 meV above the E_{11}(B) state.[115] Their population is assumed to occur *via* exciton scattering at lattice defects.[116,117] K-momentum dark excitons can be brightened under absorption (emission) by coupling with a D-phonon with a momentum of K as will be outlined below.

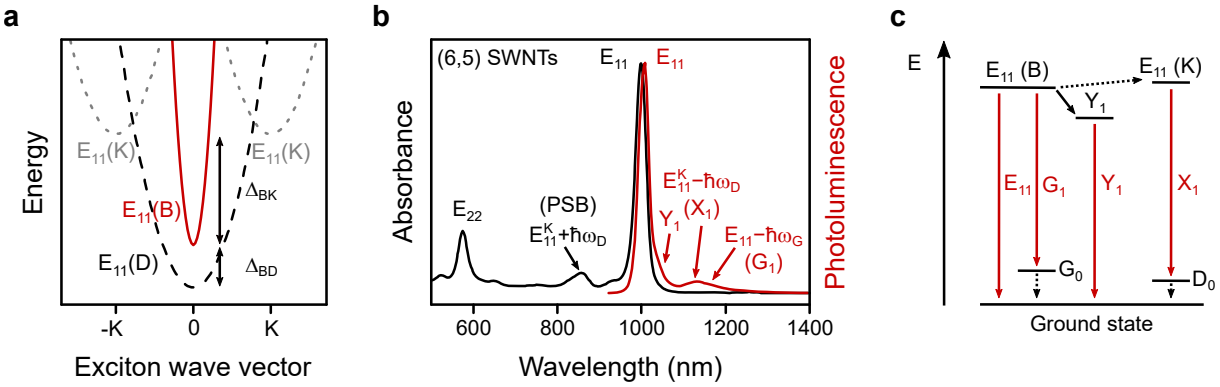

Figure 2.5: a) Schematic energy dispersion of singlet E_{11} states. Variations in exciton wave vector and parity give rise to three distinct dark excitons ($2 \times E_{11}$(K), grey-dotted line; E_{11}(D), black-dashed line) and one bright exciton (E_{11}(B), red solid line). The effective mass is lower for bright excitons compared to dark excitons, explaining the steep dispersion of bright E_{11}(B) excitons.[118] b) Exemplary absorption (black) and photoluminescence spectra (red) of polymer-wrapped (6,5) SWNTs with the assignment of main excitonic transitions and sidebands. For the assignment of SWNT sub-species see Figure 3.11. c) Schematic energy level diagram of the main excitonic transitions from the E_{11} state. Red arrows represent emissive transitions. Phonon-mediated transitions are shown as dashed arrows. Energy axis and arrows are not to scale.

This knowledge of the exciton manifold allows for a discussion of absorption and PL spectra, using solution-dispersed (polymer-wrapped) (6,5) SWNTs as an example (see Figure 2.5b). The absorption spectrum shows the E_{11} transition in the near-infrared (NIR) at ~1000 nm and the E_{22} transition in the visible at ~575 nm. Furthermore, a pronounced sideband of the E_{11} transition arises from the absorption of an additional D phonon (also referred to as phonon sideband, PSB).[115] Upon absorption at the E_{22} transition (or higher transitions), efficient coupling of excitons to lattice vibrations leads to fast internal relaxation (100 fs) to the E_{11} band-edge exciton.[119] Radiative recombination gives then rise to E_{11} PL with a narrow linewidth (~22 meV). For simplicity, in this thesis, the energy of the transition as well as its optical transition will

always be referred to as E_{ii}. E_{11} PL displays a very small Stokes shift (<8 meV) in respect to the E_{11} absorption feature and is attributed to the rigid structure of the SWNT with small reorganization energy.[120] SWNTs are frequently associated with large Stokes shifts, however, this exclusively refers to the detection of E_{11} PL upon E_{22} excitation. Emission from the K-momentum dark exciton state by coupling with the D phonon gives rise to a pronounced sideband, also referred to as the X_1 band.[116] A second weaker side-band (G_1) is associated with the bright E_{11}(B) exciton coupled to the G phonon.[115,116] Lastly, E_{11} PL exhibits a low-energy shoulder (Y_1) attributed to lattice defects introduced during SWNT production. They act as shallow excitonic traps similar to luminescent defects (to be explored in the next section).[116,121] A schematic overview of the discussed radiative emission transitions is shown in Figure 2.5c.

The overall PL quantum yield (PLQY) is very low in SWNTs (<1%) and typically attributed to the rapid decay of bright excitons into the lower-lying dark singlet or triplet states, from which excitons decay non-radiatively.[112] Furthermore, in the NIR, emission efficiencies are typically low because non-radiative recombination is more likely to occur between the higher vibration levels of the ground state and the lowest vibration level of the excited state ("energy-gap law").[122] However, several other extrinsic factors can influence the decay dynamics and thus optical properties of SWNTs. With the exception of CVD grown air-suspended SWNTs with almost no lattice defects, these extrinsic factors can play a more important role at room temperature than lower-lying dark states.

The exciton dynamics in SWNTs are highly sensitive to the surrounding environment[105] and in solution can be discussed within a solvatochromic model.[123,124] The dielectric environment around the SWNT is directly altered upon exposure to surfactants and solvents. An increase in the dielectric constant is typically associated with a redshift in the optical transition energy and a decrease in exciton oscillator strength. Conversely, SWNTs dispersed in solvents with a low dielectric constant have been shown to exhibit higher PLQY and induce a blueshift in the optical transition energy.[123] However, the correlation between PLQY and the local dielectric constant is not consistently observed. The PLQY of SWNTs in solvents with similar dielectric constants is further influenced by the electrophilicity of the solvent, which can extract electron density from the SWNT.[123] In addition to solvents, surfactants, or polymers adsorbed to the SWNT surface play a crucial role in affecting the optical properties of excitons.[105] The specific interactions between the surfactant and the SWNT strongly impact its interactions with the solvent, and a high surface coverage can protect the SWNT from quenching molecules.[125]

One important property of excitons in SWNTs is their high diffusion constant, typically on the order of 1-10 cm^2s^{-1}.[105,126,127] This enables excitons to diffuse over hundreds of nanometers or more during their lifetime (10-100 ps).[126,128] Consequently, before returning to the ground state radiatively, excitons are highly likely to interact with entities such as charge carriers, other excitons, tube ends, or lattice defects. Lattice defects can be introduced during SWNT growth, chemical treatment, or sonication and may manifest as five- or seven-membered rings, Stone-Wales defects, vacancies, sp^3-hybridized carbon atoms, or oxidation.[129] Tube ends and a majority of lattice defects have been found to efficiently quench bright excitons upon diffusive encounters. This diffusive quenching has been identified as one of the primary sources of non-radiative decay in solution-processed SWNTs, contributing to the observed low intrinsic PLQY.[126,130]

2.2 Luminescent defects

Following the initial reports on luminescence originating from dispersed semiconducting-SWNTs[131] and ongoing improvements in purification methods (see Section 2.1.2), the desire arose to customize and tailor their optical characteristics. Modifications of SWNTs can be broadly classified into three categories: a) Non-covalent functionalization through the adsorption or wrapping of functional molecules or polymers; b) endohedral functionalization by filling the inner empty cavity and c) covalent functionalization of the sp^2-hybridized SWNT lattice, forming new σ-bonds.[132] The latter approach is particularly attractive due to the high stability of the newly formed SWNT-hybrids and considerable synthetic flexibility. However, it introduces the uncontrolled formation of lattice defects. As outlined above, these defects were identified as causing non-radiative exciton quenching, thus affecting the optical (and electronic) properties.[126,130] A significant paradigm shift occurred with discoveries by Ghosh *et al.* and Piao *et al.*, indicating that not all lattice defects lead to non-radiative exciton quenching.[11,15] The emergence of a new bright red-shifted emission features was reported when oxygen and aryl sp^3 defects where introduced *via* covalent functionalization under highly controlled conditions. These new defect sites serve as localization sites for mobile E_{11} excitons, facilitating radiative relaxation of excitons from a lower energy level. The competitive diffusion (see Figure 2.6) of mobile E_{11} excitons toward such luminescent defects (L) instead of non-radiative quenching sites (Q) represents a key aspect in their ability to increase the overall emission brightness in SWNTs.[133,134] Luminescent defects have been given various names in literature, such as "quantum defects", signifying a 0D emitter within a 1D material. In the context of oxygen defects and sp^3 defects with variable functional groups, the terms "oxygen doping" and "organic color centers" have been established. Their remarkable ability to significantly enhance the PLQY[15] and even exhibit single-photon emission in the NIR at room temperature[18,19] has led to extensive research over the past decade, summarized in comprehensive reviews.[12–14,21,135]

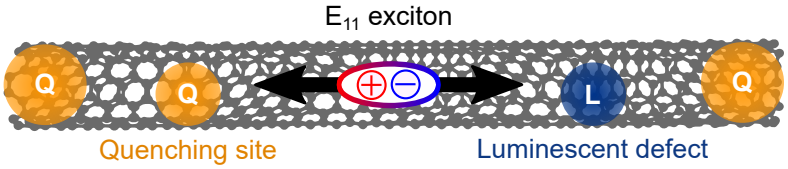

Figure 2.6: Schematic illustration of E_{11} exciton diffusion in a SWNT. During diffusion along the SWNT axis, E_{11} excitons can encounter quenching sites (Q, orange) or luminescent defects (L, blue).

The following sections provide a brief overview of the optical properties of luminescent defects in SWNTs, the experimental methods for their controlled introduction, and synthetic approaches to fine-tune their properties. Since (aryl) sp^3 defects are the most extensively studied defect type, the general concept of luminescent defects will be discussed using this specific type. A brief introduction to luminescent oxygen defects follows.

2.2.1 Exciton localization & spectroscopic properties of luminescent defects

When performing covalent functionalization of SWNTs, carbon atoms attached to functional groups, with some exceptions,[45] acquire significant sp^3 character in the otherwise sp^2-hybridized SWNT lattice. This introduces a perturbation in the π-conjugated electronic system at defect sites, a common feature in luminescent defects. The degree of this perturbation largely determines the properties of the resulting luminescent defect.[136] Importantly, the local symmetry and degeneracy of the K and K' valleys are lifted at the defect site, giving rise to a new optically-allowed excitonic state below the E_{11} exciton (see Figure 2.7a).[11] More precisely, the linear combinations of the nearly degenerate (Δ_{BD} ~5 meV) KK and K'K' excitonic states,[114] which contribute to the zero-momentum E_{11}(B, odd parity) and E_{11}(D, even parity) excitons, undergo a split. This leads to a two-level system containing a stabilized bright E_{11}* state and a destabilized E_{11}^{up} state (see Figure 2.7b).

As the newly formed emissive E_{11}* state resides energetically below the E_{11}(B) state, mobile E_{11} excitons encountering a sp^3 defect site can become trapped and strongly confined (size ~2-8 nm).[137] Due to the substantial energy difference between the E_{11}* and E_{11} excitonic states (~100 meV), the trapped exciton remains localized even at room temperature.[134] Radiative relaxation of E_{11}* excitons then leads to a red-shifted E_{11}* emission feature, while simultaneously the E_{11} emission intensity is reduced (see Figure 2.7c). The energy difference between the E_{11} and E_{11}* emissions is commonly referred to as the optical trap depth, denoted as $\Delta E_{optical}$ ($\Delta E_{optical} = E_{11} - E_{11}$*), and is expected to be proportional to the depth of the exciton trap. Typically, an inverse correlation of $\Delta E_{optical}$ with the SWNT diameter is observed and rationalized by a weaker splitting of the frontier orbital due to the reduction in strain of the sp^2-hybridized lattice and, consequently, lattice deformation upon sp^3 functionalization.

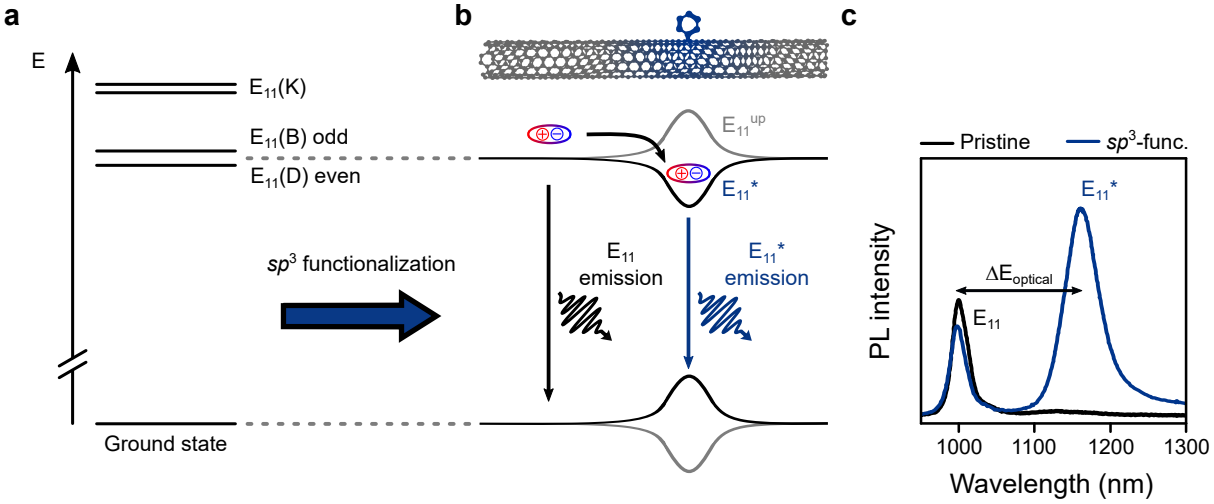

Figure 2.7: a) Schematic energy level diagram of singlet E_{11} excitons in pristine SWNTs. b) Upon sp^3 functionalization, the local symmetry is broken, leading to an energetic splitting of the E_{11}(B) and E_{11}(D) states. A low-lying bright E_{11}* state is formed that can trap mobile E_{11} excitons. Parity-allowed radiative relaxation from this state gives rise to E_{11}* emission. Unfunctionalized segments still yield E_{11} emission upon radiative relaxation from the bright E_{11}(B) state. Energy axis and arrows are not to scale. c) PL spectra of pristine (black) and sp^3-functionalized (blue) (6,5) SWNTs.

Density functional theory (DFT) calculations suggest comparable radiative lifetimes in the range of 1-10 ns for both intrinsic E_{11} excitons[118,138] and trapped E_{11}* excitons.[139] This stands in stark contrast to the apparent lifetimes of E_{11} excitons in solution-processed SWNTs, which are on the order of 1-10 ps due to efficient diffusion-limited contact quenching.[126] For trapped excitons at sp^3 defect sites, the limitation of diffusive quenching is alleviated, resulting in defect-state lifetimes on the order of a few hundred ps (see Figure 2.8a).[139] As trapping on defect sites occurs on similar time scales as diffusive contact quenching,[126,140] substantially brighter emission compared to intrinsic E_{11} emission can be obtained.[15]
An important consequence of this is the strong correlation between the brightening effect and both the initial length of SWNTs and the density of quenching sites.[141] Ultra-short SWNTs ($L_t < 80$ nm) display a significant brightening upon sp^3 functionalization.[142] In contrast, CVD-grown, air-suspended SWNTs even exhibit a decrease in PLQY when covalently functionalized with aryl halides in the vapor phase.[143] Furthermore, although sp^3 defects can be emissive, they still disrupt the sp^2-hybridized lattice. At high sp^3 defect densities, the lattice may become too perturbed for the radiative relaxation of excitons to occur, leading to a decrease in PLQY. At the optimal defect density (4-8 sp^3 defects per µm in solution-processed SWNTs),[144] an ensemble PLQY of up to 16% has been reported,[15] but several other studies suggest that the PLQY is more likely to be distributed between 1-4%.[141,145]
Despite exciton localization preventing diffusive contact quenching, the observed lifetimes of defect states (100-200 ps) remain considerably shorter than the predicted intrinsic radiative lifetimes (1-10 ns).[139] Consequently, additional non-radiative decay pathways for localized excitons must exist that determine the defect-associated PLQY. Three main non-radiative relaxation paths have been identified as dominant factors in the decay dynamics of trapped excitons: Thermal detrapping, multi-phonon decay, and electronic-to-vibrational energy transfer (see Figure 2.8b, orange arrows).[139] The relative contributions of these pathways to the overall decay highly depend on nanotube chirality, exciton trapping potential, temperature, and solvent environment and will be discussed in the following.[133,139,146]

Thermal detrapping (TD):

TD refers to the thermally induced back promotion of trapped excitons to mobile E_{11} excitons. The rate of TD is assumed to be correlated with the exciton trapping potential and is lower for deeper exciton traps. This reduction is evident through an increase in PL lifetime for defect emissions at longer wavelengths relative to the E_{11} transition (of the respective chirality).[139] Temperature-dependent PL measurements revealed that the TD energy (*i.e.* thermal trap depth; $\Delta E_{thermal}$, 80-100 meV) is substantially smaller than the extracted $\Delta E_{optical}$ (160-180 meV). This mismatch has been interpreted as a reorganization energy resulting from the deformation of the SWNT lattice upon exciton trapping.[146] However, this contradicts the small measured Stokes shifts (<20 meV)[141] of defect states, which instead suggest an energy splitting of the ground state at the defect site as displayed in Figure 2.7b.[11] A conclusive explanation of this discrepancy is still missing and will be discussed in more detail in Section 4.4.

Multi-phonon decay (MPD):

MPD refers to a process in which an exciton decays non-radiatively under additional emission of multiple phonons. In contrast to mobile E_{11} excitons, MPD is accelerated for trapped excitons due to enhanced exciton-phonon coupling.[147] MPD is expected to exhibit an opposing dependence on the defect emission wavelength compared to TD, and MPD rates increase when the number of phonons needed to bridge the gap to the ground state decreases. This is expected to be the primary reason for the observation of shorter defect-state lifetimes and lower emission efficiencies for larger-diameter SWNTs,[133] assuming chirality-independent radiative relaxation rates and similar exciton trap depths.

Electronic-to-vibrational energy transfer (EVET):

EVET can be conceptualized as a Förster-type resonant energy transfer mechanism from the defect to the surrounding environment.[148,149] This phenomenon occurs when the environment possesses broad absorption bands with high absorption coefficients across the spectral range of defect emission. EVET is particularly prominent in polar solvents like water, where the energy of the defect (donor) state aligns with combinations of vibrational bands of the solvent (acceptor).[139] Non-radiative decay *via* EVET is therefore especially pronounced for aqueous-dispersed functionalized SWNTs, leading to significantly reduced PL lifetimes.[139] Consequently, SWNTs dispersed in D_2O are expected to exhibit a higher PLQY compared to those in water, as EVET does not occur in the former case.

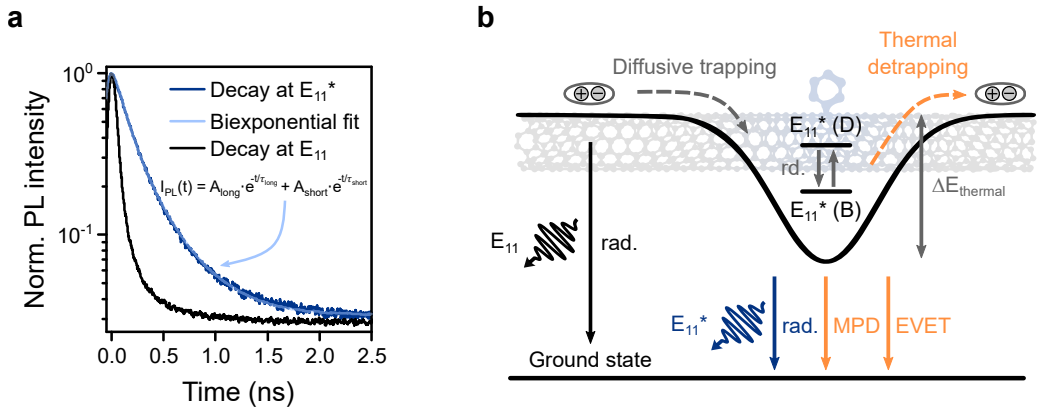

Figure 2.8: a) Exemplary time-resolved PL decay recorded at the E_{11} (black) and E_{11}* (blue) emission of sp^3-functionalized (6,5) SWNTs. As diffusive contact quenching is ruled out for E_{11}* excitons, the E_{11}* lifetime is significantly longer than the E_{11} lifetime (here limited by the instrument response). The decay of E_{11}* excitons follows a biexponential model (light blue) with a long and short decay component. b) Schematic representation of exciton dynamics at sp^3 defects, adapted from the model by He *et al.*[139] The process involves the trapping of mobile E_{11} excitons at the defect site, followed by the redistribution of the exciton population between the bright E_{11}*(B) state and dark E_{11}*(D) states. Non-radiative decay paths are depicted in orange, while radiative decay paths of mobile E_{11} and trapped E_{11}* excitons are illustrated in black and blue, respectively.

In addition to the detailed non-radiative relaxation paths, localized E_{11}* excitons are similar to E_{11} excitons associated with only one bright singlet state and several optically dark states.[150,151] Theoretical computations predict that, in the case of aryl- and alkyl-functionalized sp^3 defects, the lowest-energy singlet state is bright, while dark states reside at energies close to it.[139] At room temperature these dark states can drain the population of bright E_{11}* excitons and rapid exciton redistribution among the bright and dark states can occur at any time. For this reason, a biexponential PL decay model is used to described the decay dynamics of E_{11}* excitons. In this model according to He *et al.*, the long component of the decay (τ_{long}^{-1}) can be expressed as the sum of all of the above discussed decay paths:[139]

$$\tau_{long}^{-1} = \tau_{TD}^{-1} + \tau_{MPD}^{-1} + \tau_{EVET}^{-1} + k_{other}\,, \tag{2.9}$$

with k_{other} denoting all remaining decay paths, including radiative recombination. The decay rate of the short component (τ_{short}^{-1}) is determined by adding the rate constant of exciton redistribution ($\tau_{rd.}^{-1}$) between bright and dark states:

$$\tau_{short}^{-1} = \tau_{rd.}^{-1} + \tau_{long}^{-1}\,. \tag{2.10}$$

Furthermore, the normalized amplitude of the long decay component (A_{long}) is directly correlated with the initial total population of bright states immediately after trapping.[139]

One of the most outstanding features of luminescent defects is their ability to exhibit single-photon emission (SPE). Single-photon sources operating at both room temperature and telecom wavelengths are highly desired for fiber-based quantum information technology. Luminescent defects represent one of the very few materials that fulfill this requirement.[152] Their capability to demonstrate SPE at room temperature stems from the creation of a deep excitonic trapping potential at the defect site. The 0D luminescent defect functions as a two-level system, capable only of transitioning between a singly occupied and an unoccupied state, thus emitting single photons. By introducing luminescent defects into (10,3) SWNTs, He *et al.* were able to demonstrate SPE at room temperature in the telecom C-Band (emission maxima at 1550 nm) with a high single-photon purity of 99%.[19]
Another consequence of the described two-level system is the saturation of defect emission at significantly lower excitation densities compared to E_{11} emission. This saturation is attributed to state-filling and arises from the faster population of the defect state (~10 ps)[126] compared to its depopulation (~100-200 ps).[139] Hence, the measured E_{11}*/E_{11} emission ratios are highly dependent on the excitation densities used and, therefore, on experimental conditions.[153] Under identical measurement conditions, the E_{11}*/E_{11} emission ratios can be used to qualitatively compare the defect density. However, for reliable quantification, determination of the Raman D/G^+ ratio is required (see Section 3.6.2).

In summary, the decay dynamics of luminescent defects can be characterized in the following steps:

1. Upon optical excitation of the SWNT species, fast internal conversion (~100 fs) occurs from higher exciton states to the band-edge E_{11} exciton level before exciton diffusion ensues.
2. The mobile E_{11} exciton quickly diffuses to the luminescent defect site within ~10 ps, and as the E_{11}* state lies below the bright E_{11}(B), becomes trapped and strongly localized.
3. Upon trapping, redistribution of exciton population between a low-lying bright state and several energetically higher dark states ($\tau_{rd} = 60$ - 100 ps) occurs.
4. Recombination takes place ($\tau_{long} = 200$ - 500 ps), which can proceed radiatively, resulting in the emission of a single E_{11}* photon, or non-radiatively *via* TD, MPD or EVET. While TD is expected to be dominant for shallow trapping potentials and at elevated temperatures, MPD increases for SWNT chiralities with larger-diameters and potentially with increasing exciton trap depth. In polar solvents such as water, efficient EVET dominates the non-radiative decay of E_{11}* excitons.

2.2.2 Role of the defect structure

The defect emission wavelength depends on several factors like the dielectric environment and the attached functional group.[154] Electron-withdrawing functional groups were found to enhance electrostatically induced exciton localization, leading to further red-shifted emission bands (Figure 2.9a).[137] This effect can be viewed as similar to the influence of an auxochrome attached to a chromophore. Furthermore, the sp^3 character of the defect site has a significant impact on the emission wavelength. Divalent functional groups introduce additional strain, reducing the *s* character of the carbon atom at the defect site and leading to an redshift of the emission wavelength.[137,155] Conversely, defects with higher *s* character posses shallower traps with a blue-shifted emission.[156] Although both effects, the sp^3 character at the defect site and electrostatically induced exciton localization, can be used to fine-tune the defect emission wavelength, the emission spectra of luminescent defects are dominated by their so-called 'binding configuration' (see Figure 2.9b).[21]

The current depiction of a single luminescent sp^3 defect remains inconclusive. Covalent attachment of a functional group (*e.g.*, aryl group) to an sp^2-hybridized lattice results in an SWNT intermediate with radical or charged character. This intermediate can delocalize to carbon atoms in the *ortho* (blue) or *para* (red) positions relative to the initial group. The secondary reaction site quickly captures an auxiliary group (X), forming a closed-shell system with six possible, topologically distinct configurations in chiral SWNTs. Theoretical and experimental studies indicate that each binding configuration is associated with a different energy and thus different exciton trap depth.[21] This results in a high spectral diversity of defect emission features, observable in the PL spectra of individual functionalized nanotubes at cryogenic temperatures.[157] It is noteworthy that binding configurations exist where the sp^3 carbon atoms are not on the same carbon ring, however, these configurations are not optically active.[136]

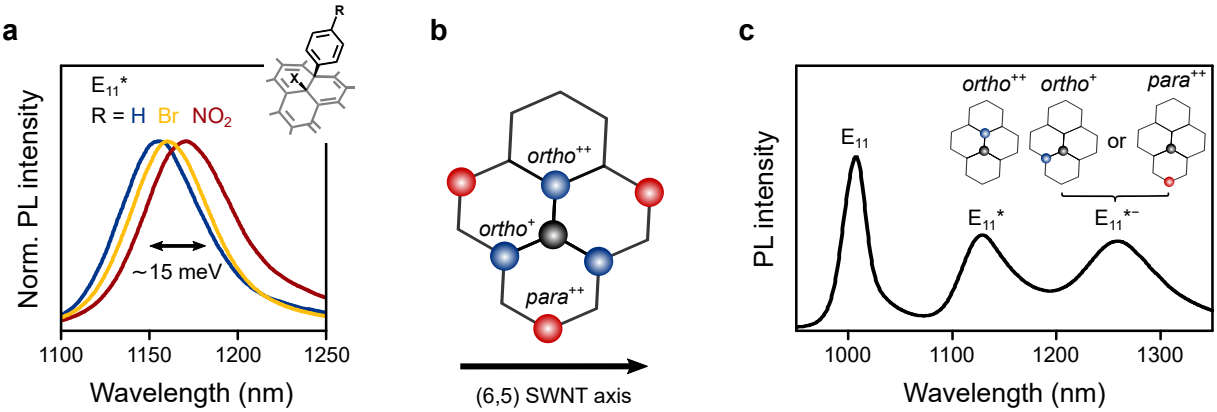

Figure 2.9: a) PL spectra of (6,5) SWNTs with phenyl, 4-bromophenyl, and 4-nitrophenyl functional groups. Defect emission (E_{11}*) redshifts with increasing electron-withdrawing character of the functional group. b) Schematic representation of potential sp^3 defect binding configurations in a (6,5) SWNT, where a first functional group (black) is added, and a second auxiliary (X) group may bind to carbon atoms in the *ortho* (blue) or *para* (red) position. The orientation of the SWNT axis is indicated by the arrow. c) PL spectrum of (6,5) SWNTs displaying E_{11}* and E_{11}*$^-$ emission. The proposed origin of E_{11} emission is the *ortho*$^{++}$ configuration, while E_{11}*$^-$ emission may arise from either an *ortho*$^+$ or *para*$^{++}$ configuration.

According to Saha *et al.*, among the six optically active configurations, the *ortho* configurations dominate the emission spectra for luminescent defects generated *via* diazonium salt chemistry.[158] More precisely, the *ortho*$^{++}$ (along the circumference of the SWNT tube) and *ortho*$^+$ (along the SWNT axis) configurations are predominantly obtained. These two binding configurations give rise to the typically observed E_{11}* (1100-1200 nm) and E_{11}*$^-$ (1200-1350 nm) emission features, respectively (see Figure 2.9c). Recent results also suggest that in some cases, E_{11}*$^-$ emission originates from the *para*$^{++}$ configuration.[159,160] As the precise assignment of defect emission bands remains an open debate and may vary depending on the chosen functionalization approach, in this thesis, the assignment of E_{11}* and E_{11}*$^-$ emission is conducted according to their emission wavelength rather than the assumed binding configuration. The energies of E_{11}* and E_{11}*$^-$ defects further exhibit a dependence on the mod(n-m,3) SWNT class, as the binding configurations change along with the angle of each C-C bond with respect to the SWNT axis.[158,161]

The auxiliary group that pairs with the functional group is assumed to be either a second functional group or solvent molecules. Changing the solvent system has been shown to induce additional small wavelength shifts, similar to the observed shifts upon variation in the functional group.[159] The difference between the optical transitions induced by all substituent-related shifts can accumulate up to 70 meV, however, it still remains smaller than the difference in optical transition energies between the *ortho*$^{++}$ and *ortho*$^+$/*para*$^{++}$ configurations (>80 meV).

2.2.3 Covalent functionalization of SWNTs

Since the discovery of luminescent defects, a large variety of synthetic methods have been reported. They most commonly rely on decade-old types of carbon nanotube chemistry,[132,162,163] but conducted under tightly controlled conditions. Luminescent defects are only formed when sp^3 defects are sparsely introduced into the SWNT lattice and well-separated. Once too many defects are introduced, the conjugated π-system becomes too disordered, leading to the disappearance of all emission features.[15,164] Hence, for each reaction system, a window must be found where this is achieved, explaining why luminescent defects were not discovered earlier. The reactivity of SWNTs is largely governed by two components: The surface coverage and thus accessibility of the SWNT lattice, and the intrinsic reactivity of the C-C bonds, which depends on the curvature-induced pyramidalization and misalignment of the π-orbitals.[158,165] For this reason, most functionalization methods were developed for aqueous-dispersed small-diameter SWNTs (*e.g.*, (6,5) SWNTs) in SDS. Such conditions are ideal for introducing luminescent defects, as small-diameter SWNTs possess high strain-induced reactivity, and SDS micelles form a sparsely disordered coating on the surface, facilitating the introduction of randomly distributed sp^3 defects.[78] However, the introduction of luminescent defects in the presence of other surfactants (*e.g.*, cholates), larger-diameter SWNTs, polymer-wrapped SWNTs in organic solvents, or SWNTs deposited on substrates has also been reported.[12,135,141,166,167]
The following section shall provide a brief overview of commonly employed functionalization methods for solution-processed SWNTs, as illustrated in Figure 2.10.

Diazonium chemistry (Figure 2.10a,b) is the most widely used approach for introducing luminescent defects. Its reaction mechanism with SWNTs was investigated in some detail in the past and involves fast non-covalent adsorption to the SWNT sidewall,[168,169] followed by the release of N_2 and radical formation initiated by electron transfer from the SWNT. Alternatively, aryl radicals may be formed *via* the Gomberg-Bachmann reaction.[170] The formed (aryl) radicals then undergo covalent functionalization with the carbon lattice, yielding a stochastically distributed number of sp^3 defects per SWNT.[171] One significant drawback is its long reaction times (several days), and physisorption of diazonium salts on semiconducting SWNTs was shown to induce strong reversible PL quenching.[15,130,141] For this reason, reaction rates are often accelerated by additional light irradiation,[172,173] and excess diazonium salt needs to be removed from the SWNT surface by vacuum filtration or surfactant transfer. Notably, SWNT dispersion and the introduction of luminescent defects can be combined by *in situ* diazotation of anilines with sodium nitrite in the presence of chlorosulfonic acid in a one-pot reaction. This allows for functionalization on a large scale (mg scale), a requirement for applications in biomedical research. However, no data is available on the achieved brightness after processing.[174] A large variety of functional groups have already been attached to sp^3 defects, enabling their potential application as optical sensors or biosensors (see Section 2.3.2). Considering the wide variety diazonium salts offer, further expansion is expected in the future.[175]

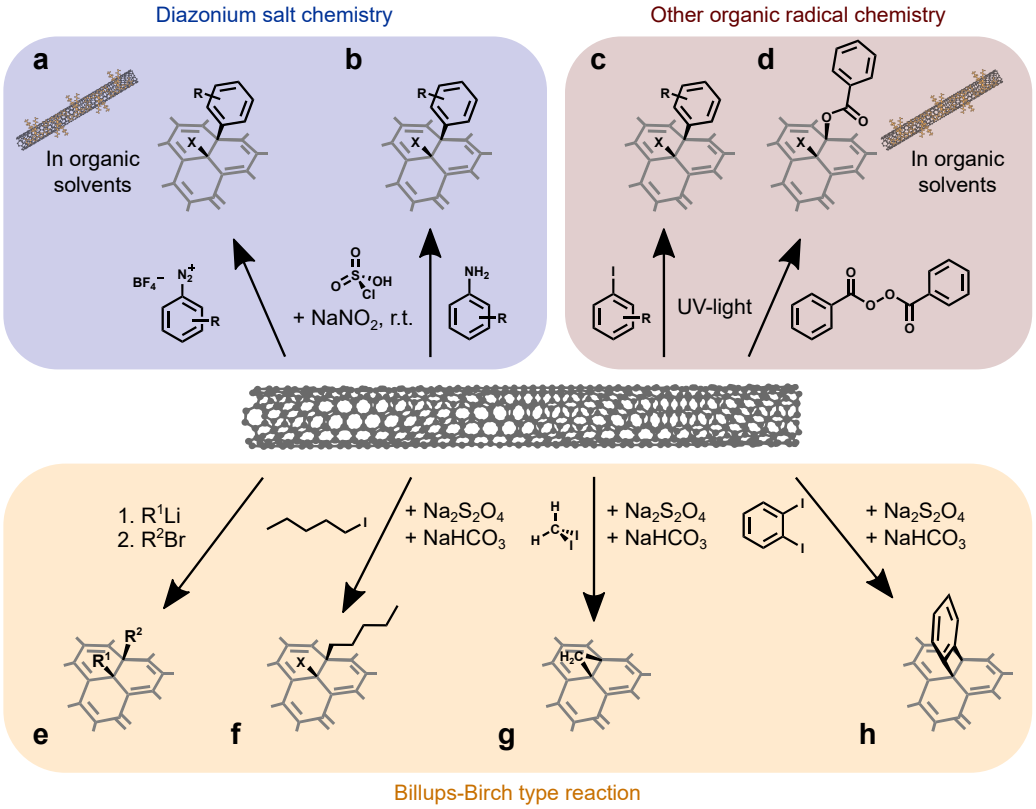

Figure 2.10: Selection of possible synthetic routes to create luminescent sp^3 defects with suggested defect structure. a, b) Most commonly diazonium salt chemistry is applied, which can be conducted with isolated[15] (a) or *in situ* generated (b) diazonium salts.[174] Isolated diazonium salts can also be used to functionalize polymer-wrapped SWNTs.[141] *In situ* generation of diazonium salts in the presence of a superacid is suitable to perform covalent functionalization on a milligram scale.[174] c) Aryl radical addition *via* UV-light activation of aryl halides.[176] d) Reaction of polymer-wrapped SWNTs with benzoyl radicals upon the thermal decomposition of benzoyl peroxides.[177] e-h) Billups-Birch type reactions with SWNTs: Reaction with organolithium compounds and subsequent addition of alkyl bromides (e);[178] coupling with alkyl iodides (f), alkylene diiodides (g), or arylene diiodides (h) under the addition of sodium dithionite as a mild reducing agent.[154]

The Billups-Birch reduction (Figure 2.10e-h) represents one of the first functionalization approaches where luminescent defects were observed.[179] Originally, this reaction involves the solvation of electrons by the addition of sodium to liquid ammonia at low temperatures. Upon reduction of the SWNT, alkyl iodides are added, generating reactive alkyl radicals through electron transfer from the SWNT and dehalogenation.[180] As shown by Deng *et al.*, this alkylation process is propagative in nature and is driven by preferable accumulation of charge carriers at existing defect sites.[181] While this reaction is rarely used anymore, its concept has been transferred to other synthetic approaches where milder reducing agents are used. For instance, organolithium compounds combined with alkyl bromides enable alkylation with control over both introduced functional groups.[178] Maeda *et al.* significantly expanded this method, demonstrating the covalent attachment of even highly sterically demanding molecules like dendrimers.[182] However, limited information is available on the brightness of the resulting alkyl-functionalized SWNT.

A similar chemistry was employed by Kwon *et al.*, using the mild reducing agent sodium dithionite in the presence of sodium bicarbonate to enhance control over the SWNT reduction step.[154] Although functionalization is confined to alkyl iodides, it offers considerable tuneability with over 30 reported functional groups, extendable to divalent alkylene diiodides and arylene diiodides.[154] In both approaches by Maeda *et al.* and Kwon *et al.*, charge accumulation is expected to be localized around existing defects, and clustering of luminescent defects is highly likely, as indicated by studies by Danné *et al.*[142] To address this, Maeda *et al.* introduced a thermal treatment step, partially recovering and enhancing the PL properties as functional groups detach from the SWNT lattice, likely reducing defect clustering.[178]
Beyond diazonium salt chemistry and reductive alkylation, other functionalization techniques have been explored and are mostly based on organic radical formation (Figure 2.10c,d). Wu *et al.* demonstrated functionalization using photo-activated aryl halides with UV-light, a process that can even be performed in the gas phase to functionalize air-suspended SWNTs.[143,176] Additionally, to introduce a stable polymer coating to the SWNT surface, alongside luminescent defects, Nagai *et al.* employed radical polymerization reactions.[183]

The majority of reactions so far have been conducted in aqueous surfactant-stabilized dispersions. However, functionalizing SWNTs in organic solvents offers significant advantages for incorporating luminescent defects in (opto)electronic applications, owing to enhanced processability (high viscosity and vapor pressure) and more uniform film formation. As discussed in Section 2.1.2, dispersions of SWNTs in organic solvents like toluene are easily achieved through polymer sorting, yielding large quantities and high purity (almost monochiral). Up to this point, only two functionalization protocols have been reported for introducing luminescent defects in polymer-wrapped SWNTs in organic solvents. Berger *et al.* achieved covalent functionalization *via* diazonium salt chemistry by enhancing the solubility of small aryl diazonium salts by adding polar solvents (*e.g.*, acetonitrile) and a phase-transfer agent.[141] Alternatively, functionalization can be conducted using benzoyl radicals formed *in situ* through the thermal decomposition of benzoyl peroxides.[177]

It is worth mentioning that other covalent functionalization techniques exist, which cannot be strictly categorized as sp^3 functionalization, as described above. Covalent functionalization of ssDNA-wrapped SWNTs with guanine nucleotides under singlet oxygen exposure enables controlled defect patterning in the SWNT lattice, causing a redshift (~60 nm) in the E_{11} emission without introducing the previously mentioned E_{11}* emission.[184] A [2+1] reaction with azidodichlorotriazine, as demonstrated by Setaro *et al.*, results in sp^2-hybridized binding sites that do not impact the carbon lattice conjugation.[45] However, the outcomes of this technique seem to rely heavily on the functional group attached to the azide moiety. Simple aryl azides were also found to form sp^2-hybridized binding sites but induce sufficient sp^3 character for E_{11}* emission to occur.[156]

2.2.4 Controlling the diversity of SWNT defect emission

Despite the diverse synthetic approaches highlighted above, the introduced luminescent defects exhibit emission over a broad spectral range (1100-1350 nm), with a predominant emission feature typically centered around 1150 nm for (6,5) SWNTs. As discussed in Section 2.2.2, this spectral diversity mainly arises from the presence of *ortho*$^{++}$ (E_{11}*) and *ortho*$^{+}$/*para*$^{++}$ (E_{11}*$^{-}$) configurations. To gain control over defect emission features, two strategies can be pursued: One involves selecting reaction conditions favoring a specific configuration, and the other entails altering the SWNT species. The selective introduction of the *ortho*$^{++}$ configuration was rationalized through alkylene diiodide functionalization, favoring configurations along the circumference due to bond angle constraints.[137] While this reduces spectral diversity, it results in prevalent E_{11}* emission. The controlled introduction of E_{11}*$^{-}$ emission is more sought after, given its suitability for SPE at room temperature and its proximity to relevant telecommunication bands.[18,21] The presumably easiest approach involves functionalizing achiral zigzag SWNTs, where the energetic states of the *ortho*$^{++}$ and *ortho*$^{+}$ configurations collapse, resulting in a single narrow emission feature.[158] However, this approach is currently impractical due to the rarity of zigzag SWNTs in raw materials.[185]

To enhance the selectivity towards *ortho*$^{+}$ defects in chiral SWNTs, Shiraki *et al.* employed functional groups with 'bridging' moieties that enforce the introduction of two pairs of sp^3 defects in close proximity.[186] The initial sp^3 defect increases the π-orbital mismatch of adjacent C-C bonds, favoring functionalization of the second sp^3 defect in *ortho*$^{+}$ configuration.[137] While this approach achieved notable selectivity towards *ortho*$^{+}$ defects, a considerable amount of *ortho*$^{++}$ defects persisted. In Chapter 4, the first synthetic approach to achieve selectively E_{11}*$^{-}$ emission in chiral nanotubes in organic solvents will be presented. In the following, other promising routes for aqueous-dispersed SWNTs, published since then (see Figure 2.11) are presented.

Yu *et al.* employed covalent functionalization with *ortho*-substituted aryl diazonium salts having π-conjugated substituents to selectively introduce *ortho*$^{+}$ configurations.[145] Experimental efforts and computational simulations suggest that π-electrons from the π-conjugated substituent stabilize radical formation at the *ortho*$^{++}$ carbon, facilitating saturation in this configuration. Bright E_{11}*$^{-}$ emission around 1260 nm for (6,5) SWNTs was observed with PLQYs of up to 2%. This method has since then been extended to heterocycle-substituted aryl diazonium salts with pyridine, furan, and thiophene units. The electron-withdrawing effect of pyridine led to an even further red-shifted emission around 1274 nm.[187]

A different approach was chosen by Wang *et al.*, where control over the defect configuration was achieved by increasing the steric size of the *ortho* substituent of the functional group.[159] During covalent functionalization with 3,4,5-trifluoro-2-sulfonate-aniline *via in situ* diazotation, the bulky sulfonate functional group inhibits the formation of *ortho* configurations due to its large steric hindrance. Instead, it was suggested that the *para*$^{++}$ configuration was formed, which, like *ortho*$^{+}$ configurations, has its emission band around 1260 nm. Importantly, this approach can be extended to (10,5) and (8,7) SWNTs, where defect emission falls within the telecom C-band (1530-1565 nm), with emission bands around 1536 nm and 1527 nm, respectively.

Lastly, Zheng *et al.* introduced a spin-state-controlled approach to determine the binding configuration of sp^3 defects, involving the covalent functionalization of aniline derivatives under UV-light.[160,188] Conducting this reaction under an inert gas atmosphere initiates a triplet-state mechanism, leading to the preferential formation of the *para*$^{++}$ configuration. Spin-constrained DFT results indicated that binding to SWNTs *via* aniline triplet states exhibits a lower energy barrier for *para* configurations than *ortho* configurations. This finding was rationalized by the Pauli exclusion principle, which favors the spatial separation of reactive electrons in the triplet state. In contrast to that, reactive aniline singlet states prefer binding to the *ortho*$^{++}$ configuration. As both singlet and triplet anilines are present in the reaction mixture, the simultaneous introduction of two emission bands ($E_{11}{}^{*-}$ and $E_{11}{}^{*}$), assigned to *para*$^{++}$ and *ortho*$^{++}$ configurations, was observed. Even achiral zigzag (11,0) SWNTs exhibited two emission features, supporting the hypothesis that both *ortho* and *para* configurations are introduced in this reaction scheme. This also reinforces the previous hypothesis by Saha *et al.* that diazonium salts preferably lead to *ortho* configurations.[158]

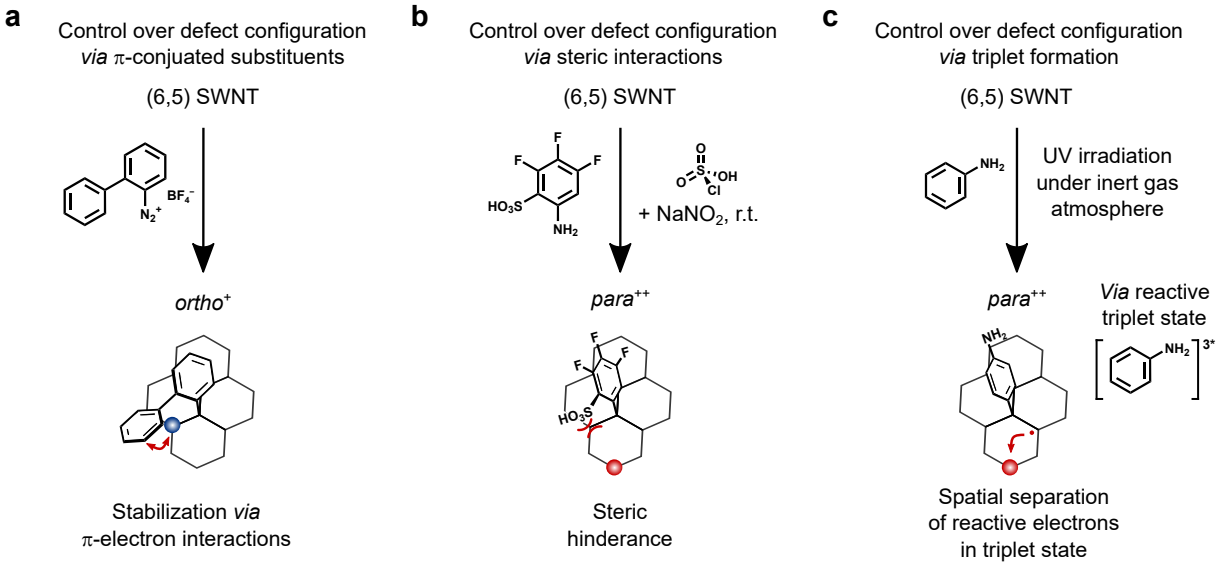

Figure 2.11: Synthetic methods for introducing $E_{11}{}^{*-}$ defects in aqueous-dispersed SWNTs. a) Covalent functionalization with π-conjugated substituents in the *ortho* position to the functional group yields defects in the *ortho*$^{+}$ configuration due to the stabilization of reactive SWNT intermediates in the *ortho* position. b) Bulky, sterically demanding substituents in the *ortho* position to the functional group prevent saturation in *ortho* configuration and thus lead to defects in the *para*$^{++}$ configuration. c) Photo-induced reactions under inert gas with aryl triplet states favor defects in the *para*$^{++}$ configuration.

2.2.5 Luminescent oxygen defects

As discussed above, luminescent sp^3 defects have been extensively studied since their discovery. However, the first deliberate introduction and observation of luminescent defects occurred for the incorporation of oxygen atoms into the SWNT lattice.[11] This process creates oxygen defects which, like sp^3 defects, act as deep exciton traps for mobile E_{11} excitons and share many properties with sp^3 defects. Oxygen defects were initially introduced by adding ozonated water to a dispersion of SWNTs and subsequent irradiation with a desk lamp or LED for several hours (Figure 2.12a).[11] Since then, various functionalization techniques have been developed, typically involving oxidants such as hydrogen peroxide or potassium chromate (K_2CrO_4) under prolonged illumination.[11,189] Alternatively, oxides such as Al_2O_3 or SiO_2 have been deposited onto SWNTs using electron beam evaporation.[190] Modern approaches employ NaOCl under UV-B-light irradiation in a continuous flow reactor to scale up the production process[189] or polyunsaturated fatty acids that react after autoxidation under E_{22} irradiation with the SWNT lattice (Figure 2.12b,c).[191]

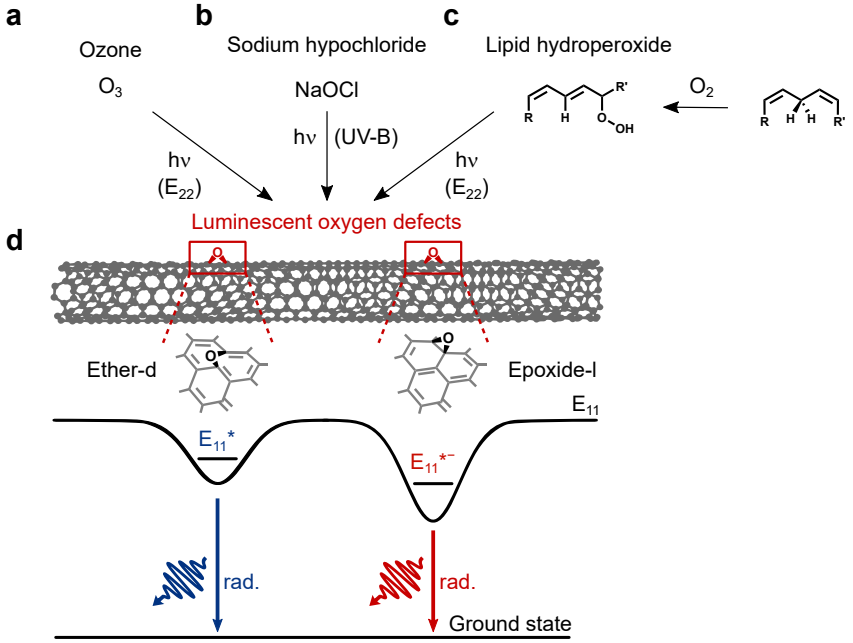

Figure 2.12: Introduction and properties of luminescent oxygen defects. a-c) Luminescent oxygen defects are introduced *via*: (a) Ozonolysis under visible light irradiation (presumably SWNT excitation, *e.g.*, at the E_{22} transition);[11] (b) reaction with reactive oxygen species upon the photolysis of sodium hypochlorite (NaOCl) under UV-B irradiation[189] or (c) autoxidation of polyunsaturated fatty acids and subsequent reaction under E_{22} excitation.[191] d) Oxygen defects appear in either ether-d or epoxide-l configuration and give rise to low-lying bright states. Ether-d defects are associated with E_{11}^* emission (blue arrow), while epoxide-l configurations are expected to yield E_{11}^{*-} emission (red arrow) upon radiative relaxation.

Similar to sp^3 defects, luminescent oxygen defects in (6,5) SWNTs primarily exhibit two emission bands at ~1120 nm (E_{11}^*) and ~1240 nm (E_{11}^{*-}), representing exciton traps with distinct trapping potentials. Through combined experimental and theoretical efforts, these defects have been assigned to ether-d (d-bonds perpendicular to the SWNT axis) and epoxide-l (l-bonds parallel

to the SWNT axis) configurations (Figure 2.12d).[192] For ozone-treated SWNTs, the formation of oxygen defects is rationalized by the initial creation of a short-lived Criegee ozonide, which decomposes to epoxide-l and epoxide-d configurations.[11,193] Typically, hydrolysis of epoxides to 1,2-diols would occur in aqueous media, however, this ring opening is likely sterically prohibited or very slow.[135] Instead, the highly strained epoxide-d configuration rearranges quickly to a seven-membered ring in ether-d configuration, giving rise to E_{11}* emission. This rearrangement partly restores the sp^2 character of the carbon atoms, likely explaining why E_{11}* emission for oxygen defects (~1120 nm) is blue-shifted compared to E_{11}* emission of sp^3 defects (~1160 nm). The remaining epoxide-l configuration gives rise to E_{11}^{*-} emission. However, the epoxide-l configuration was estimated to be less stable compared to the ether-d configuration and typically only represents a minority species.[189,193] It has been suggested that epoxide-l defects isomerize upon light irradiation, and isomerization is accelerated in aqueous media by protonation of the expoxide.[11,135] This is supported by the finding that when oxygen defects are created in SWNT thin films, a higher E_{11}^{*-} contribution is typically observed.[194,195]
Even though room temperature SPE from SWNTs was first demonstrated with oxygen defects,[18] they have received less attention compared to sp^3 defects due to their previously observed lower emission brightness. DFT calculations suggest that the lowest-energy singlet state in oxygen defects is likely dark (bright in case of sp^3 defects).[146,196] While this could explain the observed lower emission brightness, other effects might have a stronger impact. The controlled creation of luminescent oxygen defects is more difficult to achieve compared to sp^3 defects. Oxygen defects are expected to be preferably created near pre-existing oxygen defects and can be further oxidized to presumably non-radiative carboxylate/ketone defects.[197,198] Consequently, the introduction of oxygen defects in a well-separated manner becomes less likely, and functionalization can rapidly lead to severe oxidative damage to the SWNT lattice. Recent improvements in the brightness of oxygen defects, achieved by fine-tuning the reaction conditions, support this hypothesis.[199] Nevertheless, due to the easy implementation of oxygen defects, they have attracted significant attention for *in vivo* imaging by the group around Okazaki.[194,200]

2.3 SWNTs for sensing & imaging in the near-infrared

Several properties of SWNTs make them exceptionally suitable as sensors and contrast agents in biomedical research, right up to *in vivo* applications. When excited at the E_{22}, (6,5) SWNTs exhibit a large Stokes shift with emission falling within the second biological window (1000–1350 nm, NIR-II). Emitted light in this region provides numerous advantages for detection and imaging applications compared to the visible range (400-700 nm) and the first biological window (700-1000 nm, NIR-I). Unlike visible and NIR-I-light, which only penetrates tissue for micrometers to ~3 mm at most, NIR-II-light can pass multiple millimeters to centimeters through biological tissues (see Figure 2.13).[201–203] Light absorption by most tissues and water is significantly reduced,[203,204] and less scattering occurs at longer wavelengths ($\propto \lambda^{-a}$, a = 0.7-1.6).[205] Additionally, low autofluorescence is observed in the NIR-II,[206] and detection can be performed with commercially available InGaAs detectors, enabling imaging with ultra-low background noise and high spatial resolution.

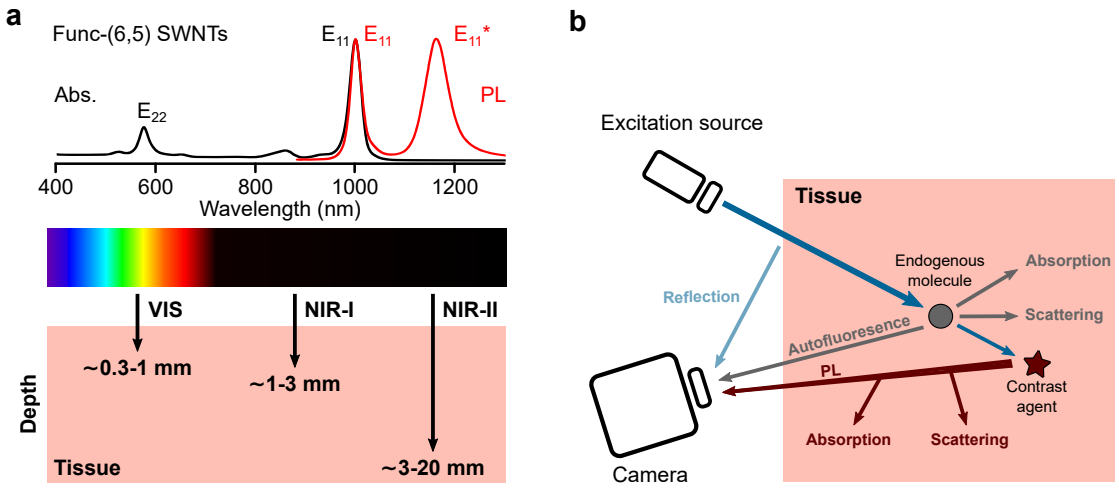

Figure 2.13: a) Schematic illustration of the penetration depth of light with different wavelengths in biological tissues. Exemplary absorption (black) and PL (red) spectra of functionalized (6,5) SWNTs are provided above. b) Schematic interactions of light with biological tissue. Light from an excitation source (blue) can be reflected (light blue) when entering tissue, be absorbed or scattered by an endogenous molecule (grey). Emitted light from the contrast agent (red) can again be absorbed or scattered. Schematics are adapted from He *et al.*[207] and Chen *et al.*[5]

The first use of *in vivo* imaging with SWNTs in mice in the NIR-II range was reported in 2009.[208] While other NIR-II emitters exist (see Table 2.1 for a brief overview), SWNTs remain highly attractive as they combine multiple desirable properties. In contrast to most organic dyes[209,210] SWNTs do not photobleach even under high fluence ($1 \cdot 10^7$ Wcm^{-2}).[211,212] On the other hand, lanthanide nanoparticles (LaNPs) possess good photostability but have lower absorption coefficients (10^3 M^{-1}cm^{-1}).[213,214] Quantum dots (QD) exhibit a high PLQY, but their toxicity, attributed to the presence of transition metals such as Pb and Cd, poses a major issue in biological applications.[215,216] There are several comprehensive reviews on this topic for more information.[5,204,207,217,218]

Table 2.1: Comparison of the properties of selected NIR-II emitting materials suitable for *in vivo* imaging. Only properties reported in aqueous media were considered. Adapted from Jackson *et al.*[217] and Chen *et al.*[5] *Length of the SWNT. †Contain heavy metals.

Fluorophore	Photostability	Size (nm)	Emission (nm)	QY (%)	Lifetime	Ref.
SWNTs	++++	100-1000*	950-1800	<1	~10 ps	38,126,211
Func-SWNTs	++++	100-1000*	1000-1600	1-2	~150 ps	12,139,145
LnNPs	+++	10-100	1000-1700	0.1-10	µs-ms	219–221
QDs†	++	2-10	900-2000	1-30	ns-µs	222–225
AuNPs	++	2-3	800-1200	0.1-4	ns-µs	226,227
Organic dyes	+	~1	900-1300	0.1-5	ns	228–230

SWNTs can be made biocompatible through non-covalent functionalization with DNA and phospholipid–polyethylene glycol (PL-PEG), where they remain stable in lysosomes and serum for months.[208,231,232] The long-term biocompatibility of SWNTs depends on various factors such as length, impurities, aggregation state, surface coating, and functional groups. Therefore, biocompatibility should ideally be evaluated individually for each type of SWNT sensor.[233] Nevertheless, SWNTs have shown promising results thus far. When wrapped with DNA, they do not trigger inflammatory, cytotoxic, or genotoxic responses in cells and mice at time points less than four months[232] and even add sensing capabilities.[10,234]
One fundamental drawback of SWNTs is their low PLQY (<1%) in aqueous dispersion. The introduction of luminescent defects offers a promising solution to enhance the optical properties of SWNTs, as defect emission is further red-shifted into the NIR and significantly boosts the PLQY. While there is limited reported data on functionalized SWNTs in aqueous dispersion, it is anticipated that the PLQY for (6,5) SWNTs could increase to 1-2%.[144,145] Luminescent defects also enable the utilization of the strong absorption band of the E_{11} transition (at 990 nm) for efficient excitation in the NIR-I, thereby reducing phototoxicity. The bright defect-induced emission band in the NIR-II (E_{11}*, 1160 nm) can be detected and is almost re-absorption-free due to the very low defect absorption band. By making functionalized SWNTs biocompatible with PL-PEG, Mandel *et al*. were able to demonstrate the imaging of single functionalized (6,5) SWNTs in live brain tissue with ultra-low excitation doses, an order of magnitude lower than typically necessary for pristine SWNTs.[16] Luminescent defects are particularly useful to brighten even ultra-short SWNTs (<80 nm),[142] allowing for their detection with potential applications in super-resolution microscopy of SWNTs within living tissue or cells.[235,236] Although this research field is still small, its expansion is expected as luminescent defects become more readily available in larger quantities (mg scale) with reproducible brightness.

2.3.1 SWNTs as optical biosensors

An optical biosensor is a device designed to identify chemicals (analytes) or other substances in a biological environment. Typically, it comprises a biological recognition unit interacting with the target analyte and a transduction unit converting the binding event into an optical signal proportional to the analyte's quantity.[237] Since the discovery of band gap emission from stable SWNT dispersions, SWNTs have been recognized as promising transduction units due to the strong dependence of their PL on the local dielectric environment.[123,124] Recognition units such as antibodies, aptamers, DNA sequences, or lectins can be employed in combination with SWNTs.[238] This field has seen substantial progress, as indicated by various comprehensive reviews.[10,212,239–241] Here, only a select analyte recognition concept will be briefly discussed.
This concept is based on a screening approach where various biopolymers wrapped around the SWNT are screened against different analytes (see Figure 2.14a). Molecular interactions between (macromolecular) analytes and the biopolymer can be highly selective, inducing specific changes in the immediate environment of the SWNT and, consequently, modulating SWNT emission.[242,243]

In particular single-stranded DNA-wrapped (ssDNA) SWNTs have attracted attention as they can exhibit highly selective molecular interactions with analytes.[10,234] Unlike other biopolymers, ssDNA allows for easy and almost limitless variation in its sequence, with each sequence exhibiting a slightly different response upon interaction with an analyte. When bundled SWNTs are sonicated with ssDNA, they become effectively dispersed through the helical wrapping of the ssDNA around the SWNT surface.[244] This self-assembly is driven by π-stacking of the aromatic nucleotide bases with the hydrophobic sidewall of the SWNT, while the hydrophilic backbone of the nucleobase faces outward towards the aqueous surroundings.

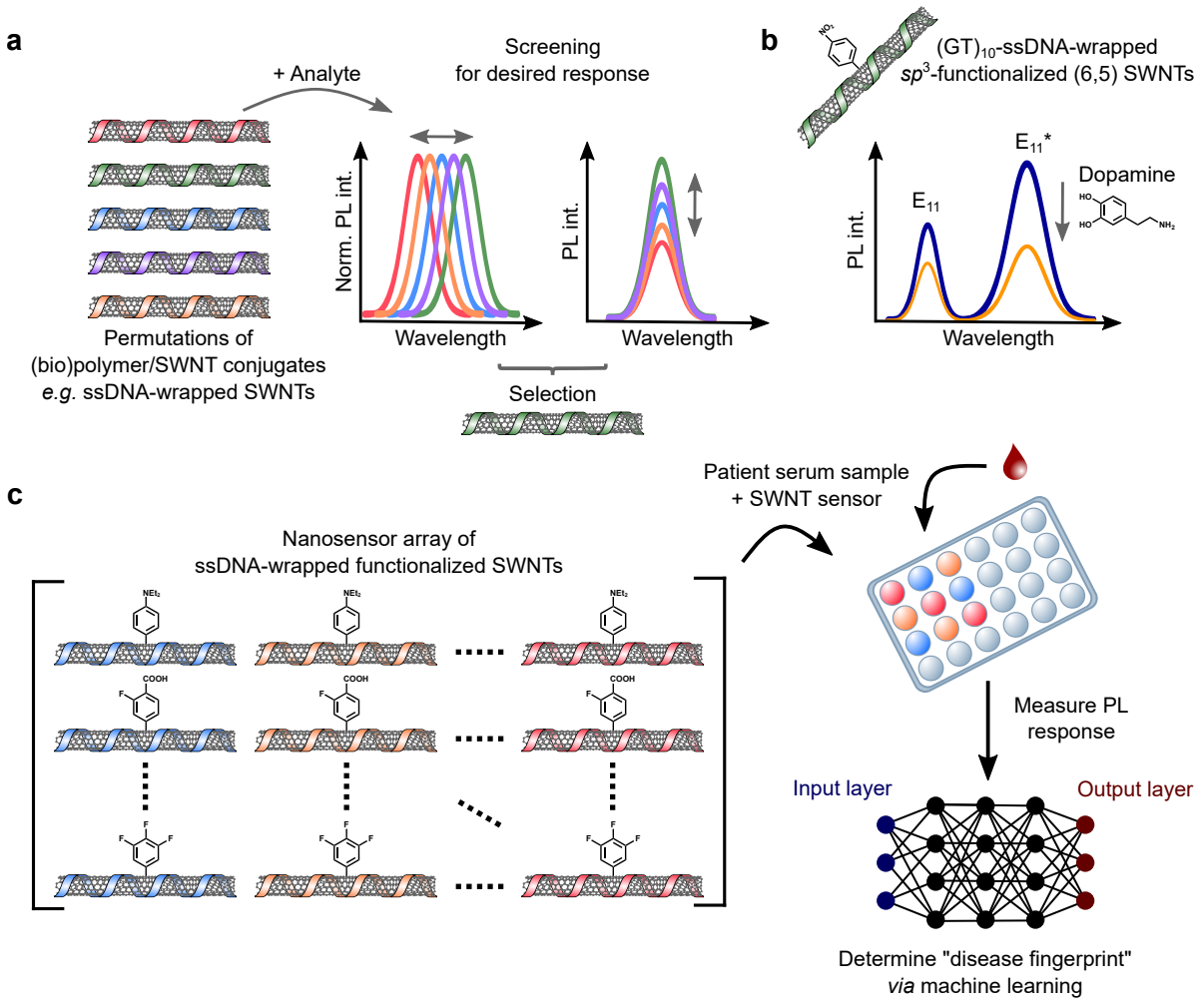

Figure 2.14: a) Concept of a biosensor designed through screening of permutations of (bio)polymer/SWNT conjugates, such as ssDNA-wrapped SWNTs, with an analyte. The permutation exhibiting the desired response in PL peak positions or PL intensity is chosen as the biosensor for the target analyte. b) $(GT)_{10}$-ssDNA-wrapped sp^3-functionalized (6,5) SWNTs show a reversed response upon the addition of dopamine. In contrast to pristine SWNTs, a decrease in E_{11} and E_{11}* emission is observed.[23] c) Perception-based sensing scheme for the detection of ovarian cancer from patient serum. The constructed nanosensor array consists of ssDNA-wrapped functionalized SWNTs with different ssDNA sequences and functional groups. The PL response of each SWNT sensor is measured upon the addition of a patient serum sample and used as input to determine a "fingerprint" of the disease *via* machine learning.[22]

Among the many available ssDNA sequences, various lengths of the $(GT)_x$ sequence are commonly employed due to their ability to demonstrate high selectivity towards catecholamine neurotransmitters such as dopamine.[245,246] The interactions of $(GT)_x$-wrapped SWNTs with dopamine are comparably well-studied, and based on molecular dynamics, it was hypothesized that dopamine binds to the phosphate backbone of the DNA *via* its two hydroxy groups.[247] This pushes the phosphate backbone closer to the SWNT surface, potentially shielding the system from quencher molecules and altering the dielectric environment across the entire SWNT surface.[247] Even moderate changes in this dielectric environment can lead to significant alterations in PL intensity and peak position, as outlined in Section 2.1.4. Furthermore, the exciton diffusion dynamics of dispersed SWNTs are dominated by scattering on disordered surface potentials and thus are altered upon recognition of analytes.[240,248,249] Hence, complex conformational changes to the three-dimensional structure around the SWNT lead to analyte-specific responses in the optical properties of SWNTs. In the case of $(GT)_x$-wrapped SWNTs, a selective turn-on response towards dopamine is obtained, resulting in a strong increase in PL emission (20% - 350%).

The above-outlined recognition concept has already been applied to SWNTs with luminescent defects, which not only increases the sensor brightness but also allow the study of exciton dynamics in such SWNT-based biosensors. Surprisingly, when (6,5)-enriched SWNTs are functionalized with 4-nitrophenyl diazonium tetrafluoroborate and wrapped by $(GT)_{10}$-ssDNA, the optical response towards dopamine was found to be reversed, leading to an overall decrease in E_{11} (-35%) and E_{11}* (-50%) emission (see Figure 2.14b).[23] Monte Carlo simulations of exciton diffusion suggest a decrease in the non-radiative decay from the E_{11} states, while the exciton diffusion constant and non-radiative decay of E_{11}* states increased upon the addition of dopamine.[23] However, a conclusive understanding of how defects alter the decay dynamics upon molecular recognition of analytes with ssDNA-wrapped SWNTs is still missing. Nevertheless, this study demonstrates that luminescent defects may facilitate the assembly of new SWNT-based sensors with distinct responses compared to pristine SWNTs.

Furthermore, luminescent defects were found to exhibit slightly different responses depending on the attached functional group during the molecular recognition of biomarkers with ssDNA-wrapped SWNTs. By varying the functional group and applying ssDNA-wrapped SWNTs with varying sequences, Kim *et al.* were able to build a powerful optical nanosensor array capable of detecting ovarian cancer from patient serum samples (Figure 2.14c). In this perception-based detection scheme, the response of each functionalized SWNT sensor within the nanosensor array to over 200 different patient serum samples was used to train several machine learning models.[22] When trained with the changes in E_{11} and E_{11}* intensity, as well as changes in E_{11} and E_{11}* peak position, the classification model showed the best performance. Through this machine learning approach, a "disease fingerprint" was acquired, capable of detecting high-grade serous ovarian carcinoma in serum samples with higher sensitivity than other available clinical screening tests. Furthermore, it was found that the best classifier was not correlated with known biomarkers that are part of conventional screening approaches, indicating that ssDNA-wrapped SWNTs with luminescent defects are sensitive to previously unidentified serum biomarkers for ovarian cancer.[22]

2.3.2 Luminescent defects as recognition units

It is not just the remarkably high sensitivity of luminescent defects to the local chemical environment that can be harnessed in the design of new SWNT-based biosensors. The ability to modify the functional group attached to luminescent defects has created opportunities to design optical probes, wherein analytes selectively interact with the functional group, thus predominantly influencing the intensities and wavelengths of defect emission. This enables the design of ratiometric detection schemes, wherein alterations in defect emission are measured relative to E_{11} emission. Relative changes provide a more robust metric and are less susceptible to external noise.

Several optical probes with luminescent defects, suitable for this approach, have been previously reported and extensively reviewed.[10,13,14,250] In the following, a few examples where analyte-specific responses were observed are presented (see Figure 2.15). In all cases, luminescent defects were introduced *via* diazonium salt chemistry, and the optical response of defect emission typically involves inductively-induced PL shifts upon a binding event to the defect site. These shifts in defect emission are influenced by the electron-withdrawing nature of the functional group (compare to Figure 2.9a).

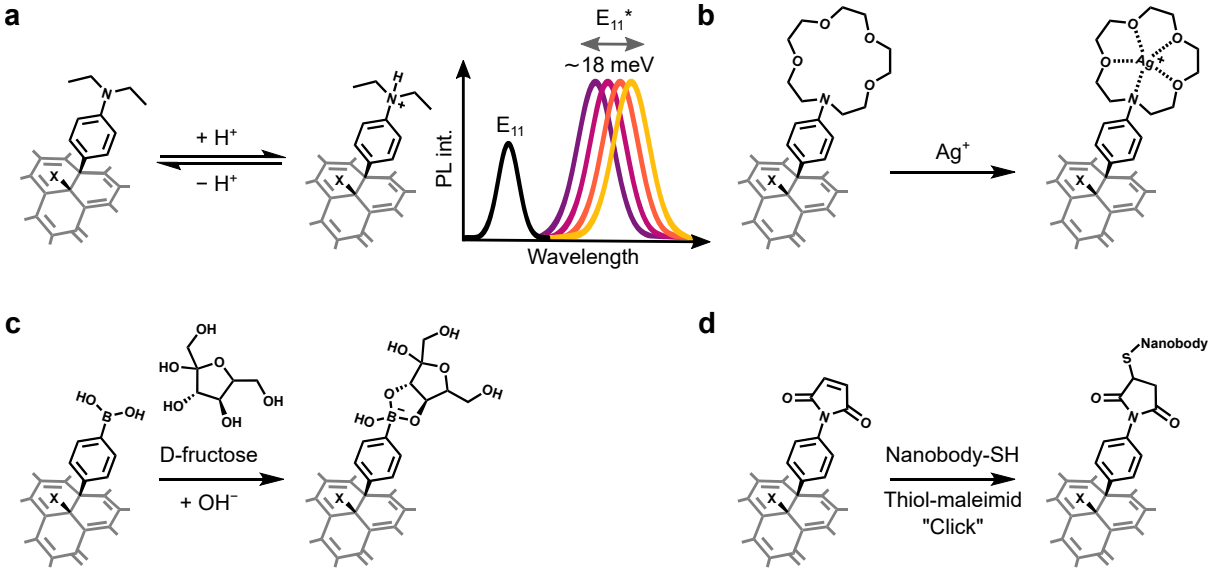

Figure 2.15: a) Reversible protonation of *N*,*N*-diethyl-4-aminobenzene-functionalized (6,5) SWNTs induces a significant E_{11}* emission shift (18 meV) over a pH range of 3.97 to 9.02, while E_{11} emission remains constant.[251] b) SWNTs functionalized with *N*-phenylaza-15-crown-5-ether defects exhibit E_{11}* emission redshift upon Ag^+ ion complexation, attributed to increased electron-withdrawing character through metal coordination.[252] c) Phenyl boronic acid groups on SWNTs form boronate complexes with saccharides, leading to an increase in electron-donating of the functional group and results in a blue-shift in defect emission.[253] d) Post-functionalization of SWNTs with (*N*-maleimido)phenyl moieties through thiol-maleimide click reaction with thiol-nanobodies.[17]

A good example are *N,N*-diethylamino-substituted aryl defects, where protonation of the functional group enhances the electron-withdrawing properties of the aryl defect (Figure 2.15a). This induces selective redshifts in E_{11}* emission up to 18 meV while the E_{11} peak position remains constant.[251] Such defects are well-suited for use as pH-sensitive probes, capable of detecting changes in pH down to 0.2 units within a working range covering the physiological pH range. These pH-dependent PL shifts have been employed in the same perception-based approach as illustrated in Figure 2.14c to detect lysosomal acidification.[254] In the future, this approach could be further enhanced by employing *ortho*-pyridine aryl functional groups, which enable pH-responsive PL shifts further red-shifted in the NIR with presumably different sensitivity towards pH compared to *N,N*-diethylamino substituents.[187]
A similar recognition concept was developed by Shiraki *et al.*, employing *N*-phenylaza-15-crown-5-ether defects for the detection of Ag^+ ions in aqueous solution (Figure 2.15b).[252] Upon the inclusion of Ag^+ ions at the aza crown ether rings, a pronounced redshift in E_{11}* emission occurred and was rationalized by the decrease in electron density at the nitrogen atom due to coordination with the metal ion. A similar shift was observed upon the inclusion of potassium cations, but to a lesser extent due to their lower binding affinity compared to Ag^+.[252,255] The same research group also reported optical probes with functional groups that can directly interact with biomolecules. For example, SWNTs functionalized with phenyl boronic acid groups can bind to saccharides like D-fructose, causing a blueshift in defect emission due to the increasing electron-donating properties of the boronate (Figure 2.15c).[253] Alternatively, small redshifts in defect emission were observed for functionalized SWNTs with palmitic acid groups, selectively binding to serum albumin.[256]
Many more optical sensors based on molecular recognition directly at the defect site are likely to be developed in the future. However, eventually, the limit of molecular tuneability of functional groups for which sp^3 functionalization can be performed is reached. To expand the scope of possible functional groups, "click" chemistry has been recently explored.[17,145] For example, maleimide defects were used to link nanobodies, such as peptides and proteins, to the defect site *via* a thiol-maleimide click reaction, enabling the synthesis of peptides directly at the defect site (Figure 2.15d).[17]

An ideal optical biosensor must have many properties such as high brightness, sensitivity, selectivity, biocompatibility, and robustness. Additionally, it should be cost-effective and simple in its operation. Luminescent defects have the potential to enhance SWNT-based biosensors in several areas. They can increase brightness, improve selectivity through defect-specific molecular recognition, and enhance robustness by enabling ratiometric detection schemes.

CHAPTER 3

EXPERIMENTAL METHODS

This Chapter describes the materials, functionalization procedures, sample fabrication procedures, and characterization techniques used in this thesis.

3.1 SWNT dispersions

3.1.1 Selective dispersion of (6,5) SWNTs in toluene

Highly purified dispersions of (6,5) SWNTs in toluene were prepared by selective polymer-wrapping *via* shear force mixing (SFM) of SWNT raw material.[83,99] For this, CoMoCAT nanotube raw material (Chasm Advanced Materials, batch SG65i-L63 and Sigma-Aldrich, batches MKCJ7287 and MKCR4865) was dried at 130 °C overnight. Dried raw material (0.38 mg mL^{-1}) was then added to a solution of the fluorene-bipyridine copolymer poly[(9,9-dioctylfluorenyl-2,7-diyl)-*alt*-(6,6′-2,2′-bipyridine) (PFO-BPy, American Dye Source, $M_W = 40\,\mathrm{kg\,mol^{-1}}$, 0.5 g L^{-1}) in toluene (ca. 250 mL). De-bundeling was achieved by SFM (Silverson L2/Air) at maximum speed (10 230 rpm) for 72-92 h while the temperature was kept at ~20 °C using a water-cooling bath. Unexfoliated material was removed from the obtained dispersion by two consecutive centrifugation steps at 60 000 *g* for 45 min (Beckman Coulter Avanti J-26S XP). The supernatant, containing PFO-BPy-wrapped (6,5) SWNTs, was collected and passed through a poly(tetrafluoroethylene) (PTFE) syringe filter (Whatman, 5 µm pore size) to remove larger aggregates.

3.1.2 Selective dispersion of (7,5) SWNTs in toluene

(7,5) SWNTs were selectively dispersed in toluene by the same process as described above under adjustment of the wrapping polymer and its respective concentration. Poly(9,9-dioctylfluorene) (PFO, Sigma-Aldrich, $M_W > 20\,\mathrm{kg\,mol^{-1}}$) was used as wrapping polymer and dissolved in toluene at a concentration of 0.9 g L^{-1}. CoMoCAT nanotube raw material from Chasm Advanced Materials (batch SG65i-L63) and Sigma-Aldrich (batch MKCJ7287) was used.

3.1.3 Selective dispersion of (10,5) SWNTs in toluene

Dispersions of (10,5) SWNTs in toluene were prepared by Sebastian Lindenthal. For the selective dispersion of (10,5) SWNTs, HiPCO raw material (Unidym, Inc., batch No. 2172) was dried at 130 °C overnight and added to a solution of poly[(9,9-di-*n*-octylfluorenyl-2,7-diyl)-*alt*-(benzo[2,1,3]thiadiazol-4,8-diyl)] (F8BT, American Dye Source, $M_W = 59\,\mathrm{kg\,mol^{-1}}$, $4\,\mathrm{g\,L^{-1}}$) in toluene (10 mL). Exfoliation was achieved by tip sonication for 30 min using a Sonics VibraCell VCX500 (40 % amplitude, 8 s on : 2 s off cycles) equipped with a tapered microtip. The temperature was maintained at ~10 °C using a water-cooling bath. Unexfoliated material was removed by centrifugation at 30 000 *g* for 5 min (Beckman Coulter Avanti J-26S XP). Lastly, the extracted supernatant was passed through a PTFE syringe filter (Whatman, 5 µm pore size) to remove larger aggregates, yielding F8BT-wrapped (10,5) SWNTs.

3.1.4 Removal of excess wrapping polymer

Prior to covalent functionalization the concentration of unbound polymer in the dispersion was reduced. In case of (6,5) and (7,5) SWNTs, as-prepared dispersions by SFM were passed through a PTFE membrane filter (Merck Millipore, JVWP, 25 mm diameter, 0.1 µm pore size), washed with toluene (5-10 mL) and the SWNT-coated membrane was re-dispersed in fresh toluene by bath sonication (10-15 min). Typically, the obtained polymer-depleted dispersion of (6,5) and (7,5) SWNTs was diluted with toluene to an optical density (OD) of $1\,\mathrm{cm^{-1}}$ at the respective E_{11} transition. To remove excess of free F8BT polymer, (10,5) SWNTs were pelletized by ultracentrifugation (Optima XPN-80 centrifuge, 284 600 *g*, 24 h) and the polymer-rich supernatant was discarded. Obtained SWNT pellets were washed with THF and re-dispersed in a diluted solution of F8BT ($0.4\,\mathrm{mg\,mL^{-1}}$) in toluene by bath sonication (10-15 min). This centrifugation and re-dispersion process was repeated three times. Representative absorption spectra after removal of excess wrapping polymer are shown in Figure 3.1.

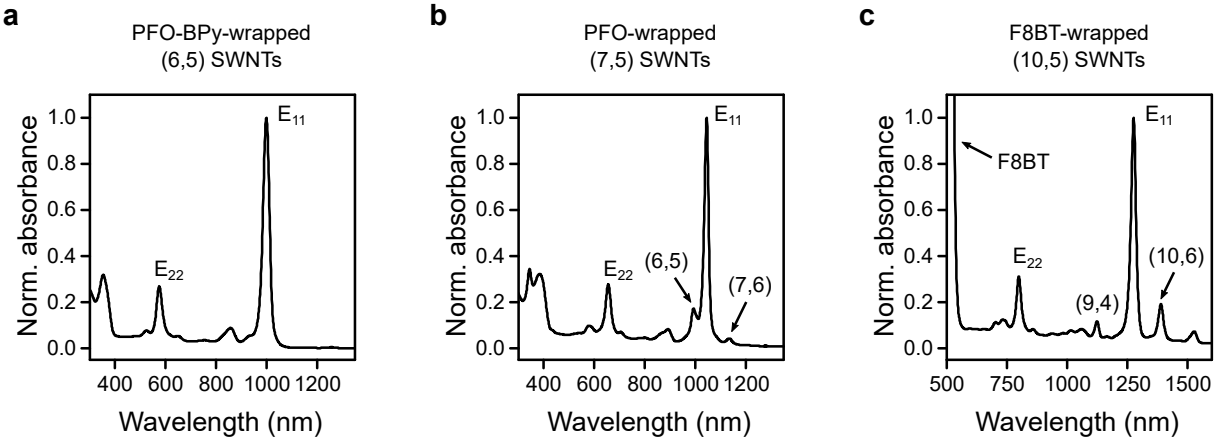

Figure 3.1: a-c) Representative absorption spectra in the UV-Vis-NIR spectral range of (a) PFO-BPy-wrapped (6,5) SWNTs, (b) PFO-wrapped (7,5) SWNTs and (c) F8BT-wrapped (10,5) SWNTs after removal of excess wrapping polymer with peak assignment. For assignment of most commonly observed sub-species in PFO-BPy-wrapped (6,5) see Figure 3.6.1.

3.1.5 Aqueous dispersion of (6,5) SWNTs

Preparation of aqueous-dispersed (6,5) SWNTs was performed by Dr. Han Li and Dr. Benjamin S. Flavel (Institute of Nanotechnology, Karlsruhe Institute of Technology) *via* aqueous two-phase extraction (ATPE).[43,144] CoMoCAT SWNT raw material (Chasm Advanced Materials, batch SG65i-L58) was dispersed in deoxycholate (DOC, BioXtra) and mixed in a two-phase system composed of dextran ($M_W = 70$ kDa, TCI) and poly(ethylene glycol) (PEG, $M_W = 6$ kDa, Alfa Aesar). (6,5) SWNTs were extracted according to a diameter sorting protocol at a fixed DOC concentration of 0.04% (w/v) and gradual increase of the concentration of sodium dodecyl sulfate (SDS, Sigma-Aldrich). To push all species with diameter larger than (6,5) SWNTs from the dextran-rich bottom phase into the PEG-rich top phase, the SDS concentration was adjusted to 1.1% (w/v). After removal of the top phase and addition of a new top phase the SDS concentration was further increased to 1.5% (w/v) and the (6,5) SWNT enriched top-phase was collected. To facilitate separation of semiconducting and metallic SWNT species of similar diameter, sodium cholate (SC, Sigma-Aldrich) and sodium hypochlorite (NaClO, 5 µL mL^{-1} of the 1/100th concentration, Sigma-Aldrich) as an oxidant was added so that the final surfactant concentrations were 0.9% SC, 1% SDS and < 0.02% (w/v) DOC . The sorted (6,5) SWNTs were diluted with an aqueous solution of DOC and concentrated using a pressurized ultrafiltration stirred cell (Millipore) with 300 kDa molecular weight cut-off (MWCO) membrane (polyehtersulfon Biomax, Millipore). Using iterative concentration dilution cycles, a highly concentrated dispersion of (6,5) SWNTs in 0.1% (w/v) DOC was obtained and transferred to SDS by dilution with 1% (w/v) SDS. Obtained dispersions of selected (6,5) SWNTs in 1% (w/v) SDS were stored for several months without noticeable changes in material properties. The residual DOC concentration was ~0.002% (w/v). Representative absorption spectra of unsorted DOC-coated CoMoCAT SWNTs and ATPE-sorted SDS-coated (6,5) SWNTs are shown in Figure 3.2.

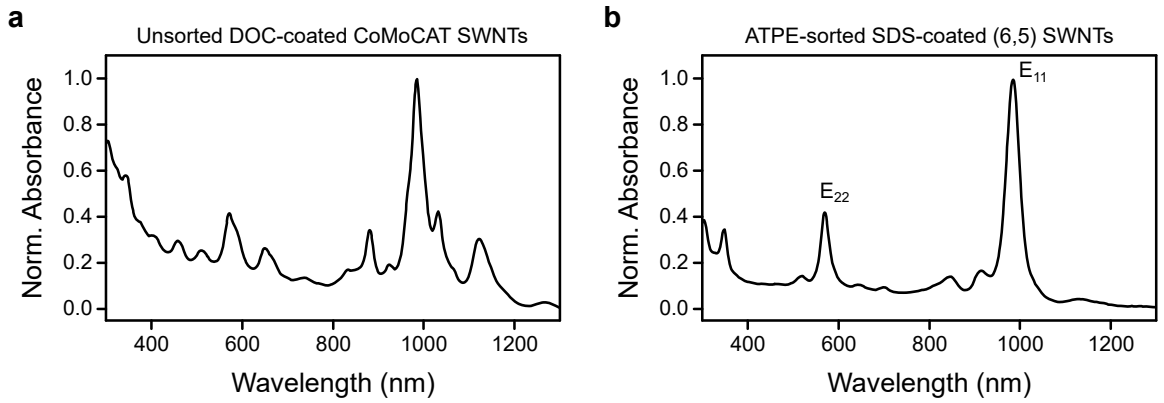

Figure 3.2: Representative absorption spectra in the UV-Vis-NIR spectral range of (a) unsorted DOC-coated CoMoCAT SWNTs and (b) ATPE-sorted SDS-coated (6,5) SWNTs. For assignment of most commonly observed sub-species after ATPE-sorting see Figure 3.6.1.

3.1.6 Aqueous dispersion of (6,4), (8,3) and (7,5) SWNTs

Preparation of aqueous-dispersed (6,4), (8,3) and (7,5) SWNTs was performed by Simon R. Wald *via* acid addition ATPE based on a modified protocol by Li *et al.*[257] CoMoCAT SWNT raw material (Sigma-Aldrich, batch MKCR4865) was mixed with 1% (w/v) DOC so that the final concentration of the raw material was 1 mg mL^{-1}. Dispersion was achieved by tip sonication for 75 min (Sonic Vibra Cell VCX500) while the sample was immersed in a 5 °C water cooling bath. Unexfoliated material and aggregates were removed by centrifugation at 46 000 *g* for 1 h (Beckman Coulter Avanti J-26S XP) and collection of 2/3 of the supernatant, yielding individualized DOC-coated SWNTs for ATPE.

ATPE was performed at a concentration of 4% (w/w) dextran (M_W = 70 kDa, TCI), 8% (w/w) PEG (M_W = 6 kDa, Sigma-Aldrich) and 0.5% (w/v) SDS (Sigma-Aldrich). The concentration of DOC varied depending on the target species and was 0.025% (w/v) for (6,4) SWNTs, 0.05% (w/v) for (8,3) SWNTs and 0.08% (w/v) for (7,5) SWNTs. The concentration of DOC was adjusted by appropriate addition of CoMoCAT SWNTs dispersed in 1% (w/v) DOC, thus lower/higher SWNT concentrations in the two-phase system depending on the used concentration of DOC are obtained. To enhance the sensitivity of the SWNT separation towards the chiral angle, 0.5% (w/v) SC (Sigma-Aldrich) was added for the separation of (6,4) SWNTs. A mimic suspension was prepared in the same way except for the addition of 1% (w/v) DOC instead of DOC-dispersed SWNTs. The resulting suspension with a total volume of 4 mL was mixed for 30 s (VWR Analog Vortex Mixer) and centrifuged at 4 140 *g* for 2 min at 15 °C (Hettich Micro 220R) to accelerate phase separation. This process was repeated after each separation step.

ATPE was conducted in a three-step procedure by pH modulation through addition of 0.5 M or 0.25 M hydrochloric acid (HCl). In a first step HCl was added until the SWNT species with larger-diameters than the target species transitioned to the top phase (T1). The same amount of HCl was also added to the mimic suspension. Following the removal of T1 the top phase of the mimic suspension was added. In a second step HCl was added until the target species transitioned to the top phase (T2). The extracted T2, containing the target species, was subsequently mixed with the leftover bottom phase of the mimic suspension and separation of metallic and semiconducting SWNTs was achieved by further addition of HCl and aided by addition of NaOCl (10-15% available chloride, Carl Roth). The purified target species was extracted from the top phase (T3, in case of (8,3) and (7,5) SWNTs) or bottom phase (B3, in case of (6,4) SWNTs). Exact volumes of added HCl and NaOCl are shown in Table 3.1. Finally, ATPE-polymers and surfactants were removed *via* multiple spin-filtration cycles (Amicon Ultra-4, 100 kDa) and purified chirality enriched SWNTs were re-suspended in 0.33% (w/v) SDS. Representative absorption spectra of selected SDS-coated SWNTs are shown in Figure 3.3a. Corresponding PLE maps of the obtained dispersions are shown in Figure 3.3b-d.

Table 3.1: Exact volumes of added HCl and NaOCl used for the separation of (6,4), (8,3) and (7,5) SWNTs from CoMoCAT raw material by acid addition ATPE.

Separated species	Step 1	Step 2	Step 3
(6,4) SWNTs	10 µL HCl (0.5 M)	20 µL HCl (0.5 M)	40 µL HCl (0.5 M)
			20 µL NaOCl
(8,3) SWNTs	4 µL HCl (0.5 M)	6 µL HCl (0.5 M)	5 µL HCl (0.5 M)
			10 µL NaOCl
(7,5) SWNTs	8.5 µL HCl (0.5 M)	2.5 µL HCl (0.5 M)	5 µL HCl (0.5 M)
			10 µL NaOCl

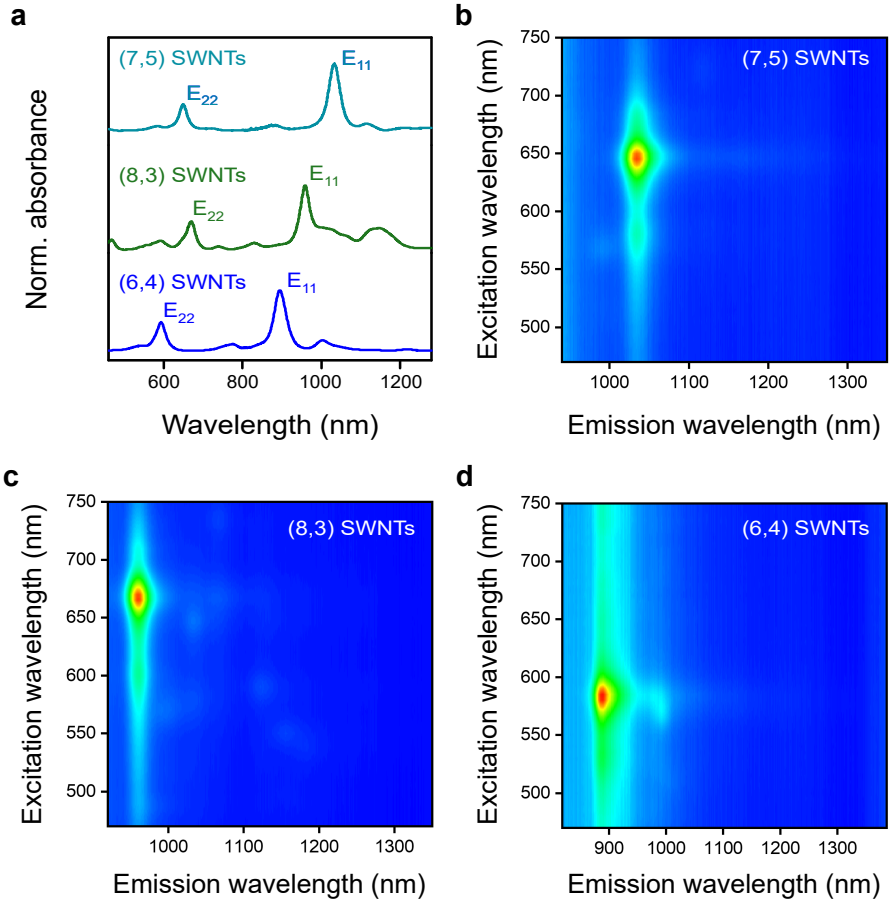

Figure 3.3: Optical characterization of ATPE-sorted SDS-coated (7,5), (8,3) and (6,4) SWNTs. a) Recorded absorption spectra of sorted (7,5), (8,3) and (6,4) SWNTs. b) PLE map of sorted (7,5) SWNTs. c) PLE map of sorted (8,3) SWNTs. d) PLE map of sorted (6,4) SWNTs.

3.1.7 Shortening of aqueous-dispersed (6,5) SWNTs

SDS-coated (6,5) SWNTs in 1% (w/v) SDS obtained by ATPE as described above were diluted with ultra-pure water to achieve an OD of $0.33\,\mathrm{cm}^{-1}$ at the E_{11} transition. The dispersion was subsequently tip-sonicated stepwise for 4 h (Sonics VibraCell VCX500) using a tapered microtip (25% amplitude, 8 s on : 2 s off cycles) while immersed in a 5 °C cooling bath. After sonication, the dispersion was centrifuged at 60 000 g for 30 min (Beckman Coulter Avanti J-26S XP) and the supernatant was used for further covalent functionalization. Note, that after successful functionalization spin-filtration with a 10 kDa cut-off membrane was employed (Amicon Ultra-4).

3.2 Covalent functionalization procedures

This section briefly summarizes all the procedures carried out for the covalent functionalization of SWNTs in organic solvents and in aqueous dispersion.
The carbon concentrations of SWNT dispersions used in the functionalization procedures were estimated based on the OD of the E_{11} transition of the respective species. For this, the absorption spectra were fitted according to Pfohl *et al.*[258] and the spectrally integrated molar absorptivity of the E_{11} transition as determined by Streit *et al.* and Sanches *et al.* was used.[259,260] The integrated molar absorptivity instead of the peak molar absorptivity was chosen to account for the higher full width at half maximum (FWHM) of SDS-coated SWNTs compared to polymer-wrapped SWNTs. Thus, a higher SWNT concentration is obtained for SDS-coated SWNTs at the same peak absorbance. The carbon concentration of (10,5) SWNTs was estimated based on the following equation as proposed by Sanches *et al.* where d_t is the diameter:[260]

$$\mathrm{OD}_{E_{11}}(\text{(10,5) SWNTs}) = 0.183 + 0.163\left(\frac{0.85 - d_t}{0.158}\right)\left(\frac{\mu g}{mL}\right)^{-1}\mathrm{cm}^{-1}. \tag{3.1}$$

3.2.1 Covalent functionalization of polymer-wrapped SWNTs with diazonium salt

Polymer-wrapped SWNTs were covalently functionalized with commercially available aryl diazonium salts following a protocol by Berger *et al.*[141]

General remarks. This functionalization procedure utilizes acetonitrile (MeCN) as a co-solvent (volumetric fraction, 20 vol-%) and crown ether (18-crown-6, $2\,\mathrm{mg\,mL}^{-1}$) as a phase-transfer agent to increase the solubility of aryl diazonium salts in organic solvents. Prior to functionalization, excess wrapping polymer was removed as described in Section 3.1.4. The OD at the E_{11} transition of the polymer-wrapped SWNTs was $0.3\,\mathrm{cm}^{-1}$ (corresponding to $0.55\,\mathrm{mg\,L}^{-1}$ for (6,5) SWNTs and $0.77\,\mathrm{mg\,L}^{-1}$ for (7,5) SWNTs) in the final reaction mixture. The degree of covalent functionalization was controlled by the concentration of the diazonium salt and the respective reaction time. In case of PFO-BPy-wrapped (6,5) SWNTs the diazonium salt concentration was $300\,\mu\mathrm{g\,L}^{-1}$ and $600\,\mu\mathrm{g\,L}^{-1}$ with a reaction time of 16 h. Due to the higher concentration and lower reactivity of PFO-wrapped (7,5) SWNTs, functionalization was performed at a diazonium salt concentration of $700\,\mu\mathrm{g\,L}^{-1}$ and a reaction time of 14 days.

Reagents. 4-Nitrobenzenediazonium tetrafluoroborate ($DzNO_2$) and 18-crown-6 (18C6) were purchased from Sigma-Aldrich and used without further purification.

Reaction protocol. Briefly, 18C6 was dissolved in toluene and added to a polymer-depleted dispersion of polymer-wrapped SWNTs. $DzNO_2$ was dissolved in MeCN (5 mg mL^{-1}) and an appropriate aliquot of $DzNO_2$ stock solution as well as pure MeCN was added to the reaction mixture. The reaction mixture was thoroughly mixed and kept in the dark for the desired reaction time.

Workup. The reaction was stopped by vacuum filtration through a PTFE membrane filter (Merck Millipore, JVWP, 0.1 µm pore size) to collect the SWNTs. After thorough washing with MeCN (20 mL) and toluene (10 mL) to remove unreacted diazonium salt, re-dispersion of functionalized SWNTs in pure toluene was achieved by bath sonication (15-30 min).

3.2.2 Covalent functionalization of polymer-wrapped SWNTs *via* a base-promoted coupling approach

Luminescent defects were introduced in polymer-wrapped SWNTs *via* a base-promoted coupling approach using potassium *tert*-butoxide (KO^tBu) and aniline derivatives (later also indoles/thiols/phenols/phenantrolines). As will be discussed in detail in Chapter 4, luminescent $E_{11}{}^{*-}$ defects are selectively obtained when the functionalization was performed under exclusion of light. Additionally, functionalization may be performed under UV-light irradiation, yielding luminescent $E_{11}{}^{*}$ and $E_{11}{}^{*-}$ defects simultaneously.

General remarks. Prior to functionalization, excess wrapping polymer was removed as described in Section 3.1.4. The removal of excess wrapping is not mandatory when functionalization is performed in the dark and the concentration of the wrapping polymer is low (< 0.3 g mL^{-1}). However, it is strongly recommended as it increases reproducibility and avoids light attenuation by the wrapping polymer when UV-light irradiation is performed. Functionalization was typically performed at an OD of 0.3 cm^{-1} or 0.5 cm^{-1} at the E_{11} transition of the SWNT corresponding to 0.55 mg L^{-1} and 0.91 mg L^{-1} (6,5) SWNTs, respectively. Functionalization of (7,5) and (10,5) SWNTs were performed at an OD of 0.3 cm^{-1} at the E_{11} transition which corresponds to 0.77 mg L^{-1} and 0.90 mg L^{-1}, respectively. As will be discussed in Chapter 4, functionalization was performed in a solvent mixture composed of toluene, dimethyl sulfoxide (DMSO) and tetrahydrofuran (THF). The degree of functionalization can be controlled by multiple reaction parameters, yet most commonly variation of the reaction time at otherwise fixed reagent concentrations was utilized.

Reagents. Covalent functionalization was primarily performed with aniline derivatives, but was also extended to other coupling reagents such as 1,10-phenantroline-5-amine, 2-iodophenol, thiophenol and indole (see Figure 3.4). The following chemicals were used for the described covalent functionalization of polymer-wrapped SWNTs: 2-Iodoaniline, 2-bromoaniline,

2-fluoroaniline, 4-ethynylaniline, aniline, 1,10-phenantroline-5-amine, 2-iodophenol, thiophenol, indole, KO^{t}Bu, DMSO (anhydrous), THF (anhydrous, inhibitor free). They were purchased from Sigma-Aldrich and used without further purification. The quality of used chemicals was found to have a significant impact on the overall reactivity as well as selectivity of the functionalization process. In this regard, the quality of DMSO was primarily found to influence the overall reactivity (presumably due to decomposition of DMSO over time and water content), while the quality of the used aniline reagent can influence the overall selectivity. It is therefore recommended to use freshly dried DMSO and perform additional purification of the aniline derivative (*e.g.* re-crystallization) if necessary. For this reason, DMSO, KO^{t}Bu and THF were stored under inert gas atmosphere, however, the functionalization process itself was performed in an open flask if not stated otherwise.

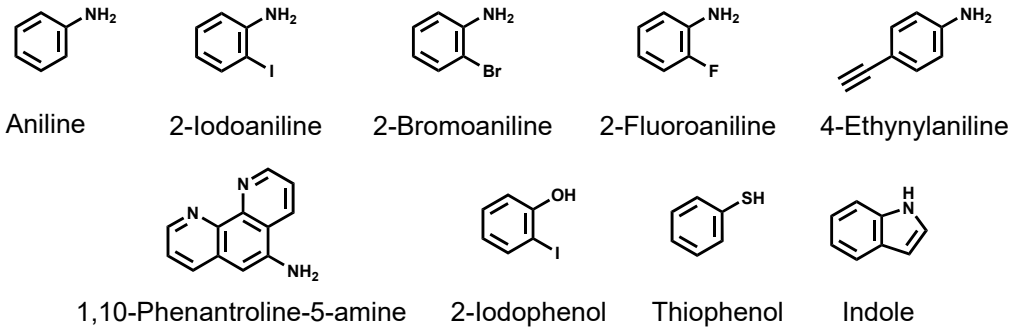

Figure 3.4: Moleculare structures of used coupling reagents.

Reaction protocol. First, the desired coupling reagent (*e.g.* aniline derivative) was dissolved in toluene in a reaction vial equipped with a stirring bar so that the final reagent concentration was 29.30 mM. DMSO and KO^{t}Bu dissolved in THF were added to this solution. Lastly, a concentrated polymer-depleted SWNT dispersion was added to the reaction mixture. The final volumetric fractions of the solvents were 83.3 : 8.3 : 8.3 vol-% toluene/DMSO/THF. The reaction mixture was either stirred under exclusion of light or irradiated with UV-light (365 nm, SOLIS-365C, Thorlabs, 1.9 mW mm^{-2}) for the desired period of time at room temperature.

Workup. The reaction was stopped by vacuum filtration through a PTFE membrane filter (Merck Millipore, JVWP, 0.1 µm pore size) to collect the SWNTs. After washing with MeOH (5 mL) and toluene (5 mL) to remove unreacted reagents and side-products, the SWNTs were re-dispersed in pure toluene by bath sonication (15-30 min). To increase the stability of the dispersion, fresh wrapping polymer was added when necessary (0.1 g L^{-1}).

3.2.3 Covalent functionalization of aqueous-dispersed (6,5) SWNTs with diazonium salts

Covalent functionalization of SDS-coated (6,5) SWNTs with diazonium salts was performed following a modified procedure as reported by Piao *et al.*[15]

General remarks. SDS-coated (6,5) SWNTs were used as obtained by ATPE selection (see Section 3.1.5) and adjusted to an OD of $0.33\,\mathrm{cm}^{-1}$ at the E_{11} transition (corresponding to $0.63\,\mathrm{mg\,L}^{-1}$) with ultra-pure water. Thus, functionalization was performed at a SDS concentration of 0.33% (w/v). Diazonium salts strongly interact with the electronic structure of the SWNT leading to efficient PL quenching. Thus, great care was taken to ensure the full decomposition of the diazonium salt prior to optical characterization (*e.g.* by application of long reaction times). The degree of covalent functionalization was controlled by the concentration of the diazonium salt, which was typically between $0.005\,\mu\mathrm{g\,L}^{-1}$ and $0.025\,\mu\mathrm{g\,L}^{-1}$.

Reagents. Functionalization was performed with 4-ethynyl benzene diazonium tetrafluoroborate (Dz-Alkyne) and benzene diazonium tetrafluoroborate (DzBenzene, for moleculare structures see Figure 3.5). Arenediazonium tetrafluoroborates were synthesized by Elena Michel under the supervision of A. Stephen K. Hashmi (Organisch-Chemisches-Institut, Heidelberg University) according to an optimized general procedure as reported by Zhang *et al.* from the corresponding anilines.[261] The obtained diazonium salts were stored at $-20\,^{\circ}\mathrm{C}$.

Dz-Alkyne Dz-Benzene

Figure 3.5: Moleculare structures of the diazonium salts Dz-Alkyne and Dz-Benzene.

Reaction protocol. Briefly, an aqueous stock solution of the desired diazonium salt was prepared ($10\,\mu\mathrm{g\,mL}^{-1}$) and an appropriate amount was added to a dispersion of SDS-coated (6,5) SWNTs (5-15 mL). The reaction mixture was stored in the dark for 7 days until no further change in the PL spectra was observed.

Workup. Multiple spin-filtration cycles (Amicon Ultra-4, 100 kDa) were performed to remove excess diazonium salt and functionalized SWNTs were re-suspended in 0.33% (w/v) SDS. All dispersions were subjected to bath sonication before further characterization (15 min).

3.2.4 Covalent functionalization of aqueous dispersions of SWNTs *via* Fenton-like reaction

This functionalization procedure is subject of discussion in Chapter 5. Introduction of luminescent oxygen defects to SWNTs is based on the efficient generation of hydroxyl radicals during a Fenton-like reaction of Cu(I) ions in the presence of oxygen in an aqueous dispersion. Cu(I) ions are generated *in situ* by the reduction of Cu(II) ions by a reducing agent.

General remarks. Aqueous-dispersed SWNTs as obtained from ATPE (see Sections 3.1.5 and 3.1.6) were used as starting material and covalent functionalization was performed in 0.33% (w/v) SDS if not stated otherwise. Prior to functionalization with other surfactants (DOC, SC or sodium dodecyl benzene sulfonate (SDBS)), SDS-coated (6,5) SWNTs were transferred to the respective surfactant (0.33% (w/v)) by multiple spin-filtration cycles (Amicon Ultra-4, 100 kDa). Functionalization of (6,5) and (6,4) SWNTs was performed at an OD of 0.33 cm^{-1} at the E_{11} transition (corresponding to 0.63 mg L^{-1} of (6,5) SWNTs and 0.77 mg L^{-1} of (6,4) SWNTs) and in case of (7,5) and (8,3) SWNTs at an OD of 0.2 cm^{-1} (corresponding to 0.54 mg L^{-1} of (7,5) SWNTs and 0.49 mg L^{-1} of (8,3) SWNTs).
For functionalization of unsorted SWNTs, CoMoCAT raw material was dispersed in 1% (w/v) DOC as described in Section 3.1.6. Surfactant transfer to 0.33% (w/v) SDS was achieved by multiple spin-filtration cycles (Amicon Ultra-4, 100 kDa). Functionalization was again performed at an OD of 0.33 cm^{-1} at the E_{11} transition of (6,5) SWNTs. In case of functionalization of unsorted SWNTs at a high SWNT concentration (OD ~55 at the E_{11} transition of (6,5) SWNTs corresponding to ~100 mg L^{-1}), functionalization was performed directly after surfactant transfer to 0.33% (w/v) SDS. This is necessary due to the instability of the dispersion over long periods of time. The degree of covalent functionalization can be controlled by various reaction parameters as discussed in Chapter 5. Among others, variation of the concentration of $CuSO_4(H_2O)_5$ (25 µM - 250 µM) and the respective concentration of sodium-L-ascorbate (12 eq. with respect to $CuSO_4(H_2O)_5$, 0.3 mM - 3 mM) were suitable parameters to adjust the degree of functionalization.

Reagents. The following chemicals were used in the described functionalization procedure. They were purchased from Sigma-Aldrich and used without further purification: Copper(II) sulfate pentahydrate ($CuSO_4(H_2O)_5$, trace-metal basis), sodium-L-ascorbate (NaAsc), ethylenediaminetetraacetic acid tetrasodium salt hydrate (EDTA). The purity of $CuSO_4(H_2O)_5$ and NaAsc was found to have a significant impact on the result of the functionalization. Thus, fresh stock solutions of said compounds were always used to achieve optimal and reproducible results.

Reaction protocol. First, stock solutions of $CuSO_4(H_2O)_5$ and NaAsc were prepared with concentrations of 6.25 mg mL^{-1} and 40 mg mL^{-1}, respectively. Aliquots of the as-prepared stock solutions were added to the SWNT dispersion and the reaction mixture was stored in the dark for ~16 h. For functionalization under E_{22} excitation (570 nm, (6,5) SWNTs) the reaction

mixture (1 mL) was filled in a quartz cuvette (StarnaGmbH, Spectrosil material) and placed in a Fluorolog-3 spectrometer (Horiba Jobin-Yvon, see Section 3.5.4). Illumination of the reaction mixture was performed with the spectrally filtered output of a 450 W xenon arc-discharge lamp. For functionalization under UV-light irradiation the filled cuvette (1 mL) was placed under a high-power UV-LED (365 nm, SOLIS-365C, Thorlabs, 1.9 mW mm^{-2}). Please note that the functionalization does not proceed under UV-C irradiation (< 280 nm) due to absorption by and hence decomposition of NaAsc.

Workup. The reaction was stopped by addition of aliquots (20 µL per 1 mL reaction volume) of a 1.4 M EDTA solution and 10% (w/v) DOC solution. For the elimination of quenching effects and re-organization of the defect configurations the reaction mixture was irradiated with UV-light (365 nm, SOLIS-365C, Thorlabs, 1.9 mW mm^{-2}) for 2 h. Alternatively, the reaction mixture was exposed to daylight for more than 4 days. Required irradiation times vary depending on excitation wavelength, excitation power, SWNT concentration as well as total reaction volume. Lastly, to remove side-products and additives, the reaction mixture was filtered *via* spin-filtration (Amicon Ultra-4, 100 kDa) and functionalized (6,5) SWNTs were re-suspended in 1% (w/v) DOC.

3.2.5 Functionalization of SWNTs with NaOCl under UV-C-light irradiation

Luminescent oxygen defects were introduced following a procedure adapted from Lin *et al.*[189]

General remarks. SDS-coated (6,5) SWNTs were used as obtained by ATPE selection (see Section 3.1.5) and adjusted to an OD of 0.1 cm^{-1} at the E_{11} transition (corresponding to 0.19 mg L^{-1}) with ultra-pure water. Thus, functionalization was performed at a SDS concentration of 0.1% (w/v), which is below its critical micelle concentration (CMC). This leads to increased instability of the SWNT dispersion and thus dispersions were prepared shortly before the actual functionalization process. The degree of functionalization was controlled by the concentration of NaOCl in the reaction mixture and ranged between 0.025 mM and 1.5 mM. Please note that significant SWNT PL quenching can be observed during the functionalization process. Surfactant transfer to DOC reverses this PL quenching effect.

Reagents. NaOCl (10-15% available chloride) was purchased from Carl Roth and used without further purification. To prevent photo-induced decomposition of NaOCl prior to functionalization, stock solutions were prepared under exclusion of light.

Reaction protocol. Aliquots of NaOCl (15.15 mM) in ultra-pure water were added to 3 mL of a diluted SWNT dispersion. The reaction mixture was irradiated with UV-C-light (254 nm, VL-215.LC, Vilber Lourmat, 15 W) for 45 min.

Workup. The reaction was stopped *via* surfactant exchange by addition of 20 µL of 10% (w/v) DOC.

3.3 Procedures for non-covalent functionalization

3.3.1 Surfactant exchange to PL-PEG$_{5000}$

Surfactant exchange of functionalized SDS-coated (6,5) SWNTs to PL-PEG$_{5000}$ was based on a kinetic surfactant exchange *via* dialysis. For this, an adapted procedure reported by Welsher *et al.* was used.[208] An appropriate amount of 1,2-distearoyl-*sn*-glycero-3-phosphoethanolamine-*N*-[methoxy(polyethylene glycol)-5000] (ammonium salt, 18:0 PEG5000 PE, PL-PEG$_{5000}$, $M_W = 5801.071\,g\,mol^{-1}$, see Figure 3.6) was added to 4-15 mL of dispersion of functionalized (6,5) SWNTs so that the final concentration of PL-PEG$_{5000}$ was $2\,mg\,mL^{-1}$. This mixture was dialyzed against ultra-pure water for 7 days (1 kDa dialysis bag, Spectra/Por, Spectrum Laboratories Inc.) in a 500 mL beaker. Ultra-pure water was exchanged twice a day. After successful transfer the obtained dispersion of functionalized PL-PEG$_{5000}$-coated (6,5) SWNTs was briefly sonicated for 15 min.

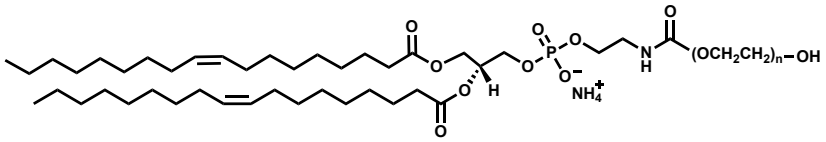

PL-PEG$_{5000}$

Figure 3.6: Moleculare structure of PL-PEG$_{5000}$.

3.3.2 Surfactant exchange to ssDNA

Surfactant exchange of functionalized SDS-coated (6,5) SWNTs to ssDNA was carried out according to a protocol by Ackermann *et al.*[262] First, the functionalization and workup process for the functionalization of (6,5) SWNTs *via* Fenton-like reaction as described in Section 3.2.4 was followed. After transfer to 1% (w/v) DOC an additional concentration step was performed by spin-filtration (Amicon Ultra-4, 100 kDa) such that an OD at the E_{11} transition of 2.0 was obtained. For dialysis, $(GT)_{10}$-ssDNA (Sigma-Aldrich) was dissolved in phosphate buffered saline (PBS, Carl Roth) and 100 µL were mixed with 1 mL of the concentrated dispersion of functionalized (6,5) SWNTs. The mixture was transferred to a 1 kDa dialysis bag (Spectra/Por, Spectrum Laboratories Inc.) and dialyzed for 4 days against PBS in a 500 mL beaker. PBS was renewed daily. After dialysis the SWNT dispersion was sonicated for 15 min by bath sonication and subsequently centrifuged for 20 min at 20 000 *g* (Hettich Micro 220R). The supernatant was used for further characterization.

3.4 Sensing protocol for the detection of pyrophosphates

This Section briefly summarizes the sensing protocol as applied and described in Chapter 6. This protocol can be used for the detection of pyrophosphates in a surfactant solution as well as in a biocompatible buffer solution. Functionalized SDS-coated (6,5) SWNTs were used in this process and obtained as described in Section 3.1.5.

Reagents. Chemicals used in this sensing protocol were purchased from commercial suppliers and used without further purification: Copper(II) sulfate pentahydrate ($CuSO_4(H_2O)_5$, trace-metal basis, Sigma-Aldrich), tris(3-hydroxypropyltriazolylmethyl)amine (THPTA, TCI), tetrasodium pyrophosphate (PP_i, Alfa Aesar), EDTA-free morpholinopropane sulfonic acid buffer (MOPS, Serva).

Reagents for reference experiments. Additionally the following chemicals were used in reference experiments: Nickel(II) sulfate hexahydrate ($NiSO_4(H_2O)_6$), cobalt(II) sulfate heptahydrate ($CoSO_4(H_2O)_7$), adenosine 5'-diphosphat sodium salt (ADP, bacterial, HPLC), sodium carbonate (Na_2CO_3), potassium nitrate (KNO_3), potassium iodide (KI), calcium dichloride hexahydrate ($CaCl_2(H_2O)_6$), sodium citrate tribasic dihydrate ($Na_3C_6H_5O_7(H_2O)_2$), L-cysteine and ethylenediaminetetraacetic acid tetrasodium salt hydrate (EDTA) were all purchased from Sigma-Aldrich. Adenosine 5'-triphosphate disodium hydrate (ATP, HPLC) was purchased from TCI.

Pyrophosphate sensing protocol in surfactant solution. Sensing of PP_i with SDS-coated functionalized (6,5) SWNTs was performed according to the following procedure. First, fresh stock solutions of $CuSO_4(H_2O)_5$ (12 mM) and THPTA (12 mM) in ultra-pure water were prepared and mixed in a 1:1 ratio. This yields an equimolar (1:1) solution of $CuSO_4(H_2O)_5$ and THPTA. The previously pale blue solution turns deep blue and indicates successful complex formation. For sensing with different $CuSO_4(H_2O)_5$:THPTA ratios the concentration of the THPTA stock solution was increased accordingly. Small aliquots of the obtained solution were added to 1 mL of SDS-coated functionalized (6,5) SWNT dispersion an OD of 0.1 cm^{-1} at the E_{11} transition (corresponding to 0.19 mg L^{-1}). Typically, 2.5 µL were added, which leads to a final concentration of the copper complex of 15 µM. After 15 min of incubation time aliquots of a stock solution of PP_i in ultra-pure water were added.

Pyrophosphate sensing protocol in biocompatible buffer solution. For sensing of PP_i with biocompatible SWNTs, first surfactant transfer of SDS-coated functionalized (6,5) SWNTs to PL-PEG_{5000} was performed as described above. To facilitate the adsorption of the copper complex onto the SWNT surface typically 2 mL of PL-PEG_{5000}-coated functionalized (6,5) SWNTs were concentrated *via* spin-filtration (Amicon Ultra-4, 100 kDa) to approximately 100 µL. Briefly, a stock solution of $CuSO_4(H_2O)_5$ (12 mM) was mixed in a 1:1 ratio with a stock solution of THPTA (60 mM) and 20 µL were added to the concentrated dispersion. Following 15 min of incubation time the dispersion was diluted with 2 mL of ultra-pure water. To remove excess

copper complex, spin-filtration (Amicon Ultra-4, 100 kDa) was performed and the SWNTs were re-suspended in a 10 mM EDTA-free MOPS buffer solution that was adjusted to a pH of 7.4. The obtained SWNT dispersion was adjusted to an OD of 0.1 cm^{-1} at the E_{11} transition (corresponding to 0.19 mg L^{-1}) and 1 mL of dispersion was used for PP_i sensing. An overview of the described workflow is displayed in Figure 3.7. To detect PP_i in spiked cell lysate and PP_i released during polymerase chain reaction (PCR), the SWNT dispersion was adjusted to an OD of 0.02 cm^{-1} at the E_{11} transition (corresponding to 0.04 mg L^{-1}) and PL measurements were performed in a total volume of 100 µL.

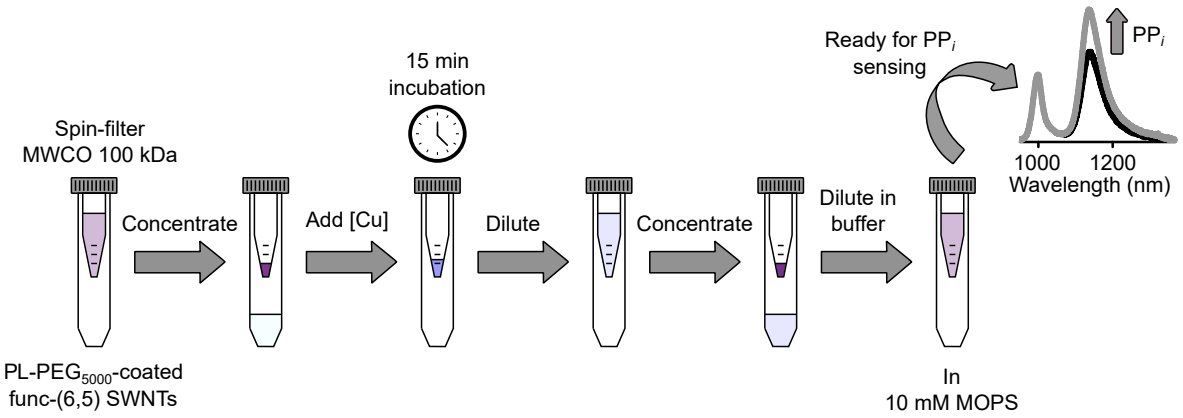

Figure 3.7: Sample preparation of functionalized (6,5) SWNTs dispersed in PL-PEG_{5000} for the detection of PP_i in a buffer solution.

3.5 Spectroscopic characterization

3.5.1 NIR luminescence spectroscopy setup

If not stated otherwise all PL spectra recorded at high excitation density and room temperature were obtained in a home-built setup as schematically illustrated in Figure 3.8. This includes all PL quantum yield (PLQY) and time-resolved PL measurements.

The **excitation source** was a picosecond-pulsed supercontinuum laser (**SCL**, Chapter 4: Fianium WhiteLase SC400, 20 MHz repetition rate; Chapters 5 and 6: NKT Photonics SuperK EXTREME, 19.5-78.1 MHz repetition rate) coupled to a tuneable band-pass filter (**BPF**, Photon etc. LLTF Contrast vis). The excitation wavelength was tuned to the corresponding E_{22} transition of the investigated SWNT chirality (*e.g.* 575 nm for PFO-BPy-wrapped (6,5) SWNTs). To block unwanted NIR-laser light, two short-pass filters (**SP**, cut-off 750 nm and 1000 nm) were placed in the excitation path. The excitation beam was guided *via* silver mirrors (**M1**) and a dichroic long-pass filter (**DMLP**, cut-on 875 nm) to a NIR-optimized 50× objective (**OBJ1**, Olympus, N.A. 0.65). A small volume (400-500 µL) of dispersion was filled in a quartz cuvette (Hellma Analytics, QX material) and placed on top of a sample holder located on a piezo stage (**PS**, Mad City Labs, Nano-LPS200). The filled cuvette was sealed with a PTFE stopper and tilted on its side with the clear surface facing down. Focusing of the laser beam was achieved by approaching the objective (**OBJ1**) until the PL signal of the E_{11} emission feature reached its maximum. Typically,

the excitation power recorded at the top of the sample holder was ~0.0125 mJ cm^{-2}. Scattered laser light and sample emission were collected by the same objective (**OBJ1**) and separated by the **DMLP**. Residual laser light was blocked by an additional long-pass filter (**LP**, cut-on 830 nm). Sample emission was focused by a tube lens (**TL**) onto the slit of a grating spectrograph (**GS**, Princeton Instruments Acton SpectraPro SP2358). For acquisition of PL spectra, sample emission was spectrally dispersed using a grating with 1200 nm blaze and 150 grooves mm^{-1}. For detection a liquid nitrogen-cooled InGaAs line camera (**NIR LC**, Princeton Instruments OMA V:1024-1.7 LN) was used. In case of time-resolved PL measurements (**TCSPC**, see Section 3.5.2) the spectrally selected output of the spectrograph was collected by a collimation lens (**CL**) and focused onto a gated InGaAs/InP single-photon avalanche diode (**NIR SPAD**, Micro Photon Devices) *via* a NIR-optimized 20× objective (**OBJ2**, Mitutoyo, N.A. 0.40).
For PLQY measurements (see Section 3.5.3) a different configuration of the setup was used and the excitation beam was guided by an additional silver mirror (**M2**) onto a filled quartz cuvette placed inside an integrating sphere (**IS**). Light from the **IS** was guided through an optical fiber (**OF**) and coupled to an optical cage in front of the spectrograph. The isotropic light exiting the **OF** was re-focused by a **TL** and laser signal was filtered by a **LP** (cut-on 950 nm).

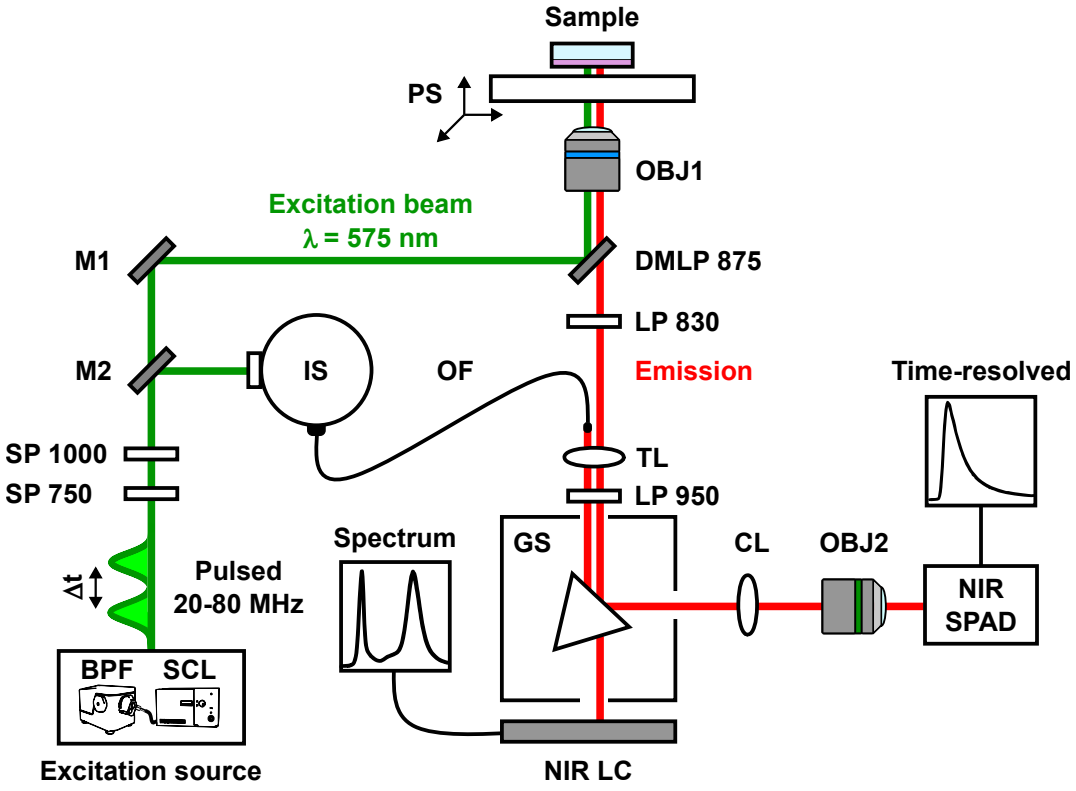

Figure 3.8: Schematic of the NIR luminescence spectroscopy setup employed in this thesis. The excitation (laser) and detection paths are indicated by green and red lines, respectively.

Spectral correction. A background spectrum was recorded under dark conditions and substracted from all spectra to account for the thermal noise of the detector. Additionally, the wavelength-dependent detection efficiency as well as other optical losses due to absorption by optical components was accounted for by acquisition of a calibration spectra ($I_{exp,lamp}(\lambda)$)

using a stabilized tungsten halogen light source (Thorlabs SLS201/M, 300-2600 nm) with known spectral power distribution ($I_{theo,lamp}(\lambda)$). A transfer function $t(\lambda) = I_{exp,lamp}(\lambda)/I_{theo,lamp}(\lambda)$ was computed and raw spectra were corrected according to $I_{corr}(\lambda) = I_{raw}(\lambda)/t(\lambda)$.

3.5.2 Time-correlated single-photon counting

Wavelength-dependent PL lifetime measurements were recorded in a time-correlated single-photon counting scheme (TCSPC) using the pulsed output of a supercontinuum laser as excitation source (19.5 or 20 MHz repetition rate) as described in Section 3.5.1. Histograms of photon arrival times were recorded with a counting module (PicoQuant PicoHarp 300) with the laser providing electrical trigger signals to the counting module and the gated NIR-SPAD. Time-tagging of detected photons was performed by the controller of the piezo stage. The obtained histograms where fitted with a biexponential reconvolution fit using the SymPhoTime 64 software. The short decay of E_{11} excitons of a drop-cast (6,5) SWNT film with a FWHM of ~78-90 ps served as the instrumental response function (IRF).

3.5.3 PL quantum yield determination

The PLQY represents the absolute efficiency of an emitter and can be experimentally determined by the ratio of emitted (N_{em}) and absorbed photons (N_{abs}):

$$PLQY = \frac{N_{em}}{N_{abs}}. \tag{3.2}$$

To obtain these values, integrating sphere measurements of SWNT dispersions were performed following an adapted method by de Mello *et al.*[83,263] An overview of this measurement technique can be found in Figure 3.9. First, a quartz cuvette (Hellma Analytics, QX material) was filled (1 mL) with the respective solvent (toluene or surfactant in water) and placed in the center of the integrating sphere (LabSphere, Spectralon coating). As the excitation source the output of a supercontinuum laser (270 µW) tuned to the E_{22} transition of the respective SWNT chirality (*e.g.* 575 nm for (6,5) SWNTs) was used. Light leaving the integrating sphere was guided to the spectrometer *via* an optical fiber and the laser signal (red lines) was recorded at the respective excitation wavelength in the Vis (Figure 3.9b) and emission wavelength of the SWNT in the NIR (Figure 3.9c). The same measurement was performed for the SWNT dispersion, which was adjusted to an OD of 0.1-0.2 cm^{-1} at the E_{11} transition to avoid re-absorption effects.[264] Again, the laser signal was measured and the PL spectrum in the NIR was recorded (black lines). Due to absorption by the SWNTs an attenuated laser signal is obtained. After multiplication of the detected intensity with the respective wavelength the number of absorbed (emitted) photons can then be calculated from the difference in integrated laser signal (PL emission). Prior to integration all spectra were corrected for the wavelength-dependent detection efficiency and other optical losses as described in Section 3.5.1. To account for absorption by the respective solvent a solvent-filled cuvette was placed in the integrating sphere and a calibration spectrum in the NIR range was recorded.

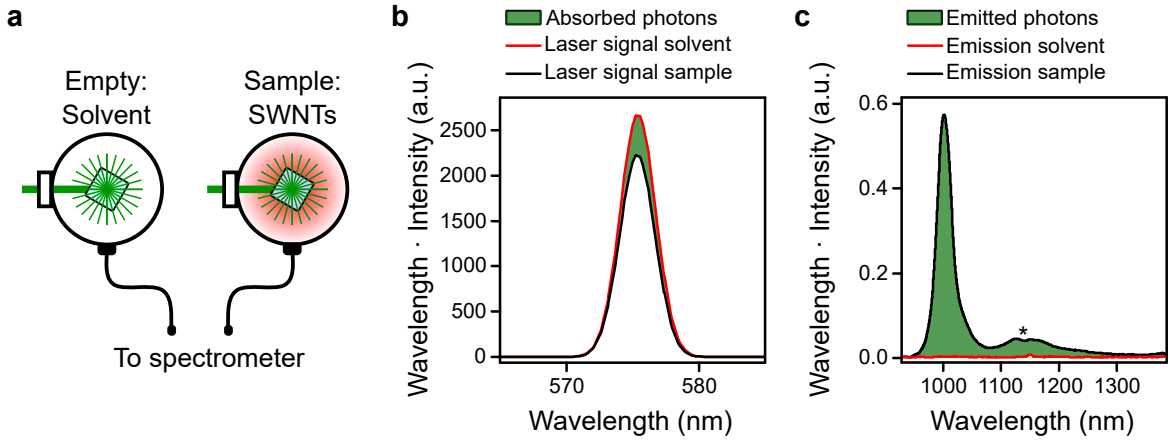

Figure 3.9: Photoluminescence quantum yield measurement as conducted in this thesis. a) Schematic of the absolute PLQY measurement in an integrating sphere. b) Exemplary measurement of the laser signal of the pure solvent without any SWNTs (red) and with SWNTs (black). The integrated area is indicated in green and is proportional to the number of absorbed photons. c) Exemplary measurement of the PL emission of the pure solvent without any SWNTs (red) and with SWNTs (black). The integrated area is indicated in green and is proportional to the number of emitted photons. The asterisk marks an artificial dip in the PL spectra that originates from an imperfect lamp correction due to strong absorption by the solvent (here toluene).

3.5.4 Measurement of PL spectra at low excitation power density

PL spectra as well as PL emission-excitation (PLE) maps that were recorded at low excitation density were obtained with a Fluorolog-3 spectrometer (Horiba Jobin-Yvon) equipped with a 450 W xenon arc-discharge lamp and a liquid nitrogen-cooled InGaAs line camera (Symphony II). Residual excitation light was blocked by an additional 850 nm or 780 nm long-pass filter. For temperature-dependent PL measurements of dispersions between 293 K and 353 K a Peltier-based temperature-controlled cuvette holder was used.
In Chapter 6, the unfocused wavelength-filtered output of a picosecond-pulsed supercontinuum laser (NKT Photonics SuperK EXTREME) was used as excitation source occasionally. For this a quartz cuvette (Hellma Analytics, QX material) was filled (1 mL) with the SWNT dispersion and placed inside an integrating sphere. PL spectra were recorded using an Acton SpectraPro SP2358 spectrograph (grating blaze 1200 nm, 150 lines mm^{-1}) and a liquid nitrogen-cooled InGaAs line camera (Princeton Instruments, OMA-V:1024) as described in Sections 3.5.1 and 3.5.3.

3.5.5 Low temperature spectroscopy of individual SWNTs and variable temperature spectroscopy of SWNTs in a polystyrene matrix

Low-temperature PL spectra of individual SWNTs were recorded in a home-built laser setup equipped with a closed-cycle liquid helium optical cryostat (Montana Instruments Cryostation s50) with an adjustable temperature between 3.8 K and 330 K. A schematic illustration of this setup is displayed in Figure 3.10.
For sample preparation, a dispersion of functionalized PFO-BPy-wrapped (6,5) SWNTs was mixed with a solution of polystyrene (PS, Polymer Source, Inc., $M_W = 230\,kg\,mol^{-1}$) in toluene.

The PS concentration in the final mixture was 20 g L^{-1}. To achieve individual SWNTs in a PS matrix, the OD was adjusted to 0.005 cm^{-1} at the E_{11} transition of (6,5) SWNTs. For variable temperature spectroscopy the OD was adjusted to 2 cm^{-1}. The obtained PS-SWNT mixture was spin-coated (2000 rpm) onto glass slides (Schott AF32eco) coated with 150 nm of gold (thermal evaporation) to suppress PL from the glass.

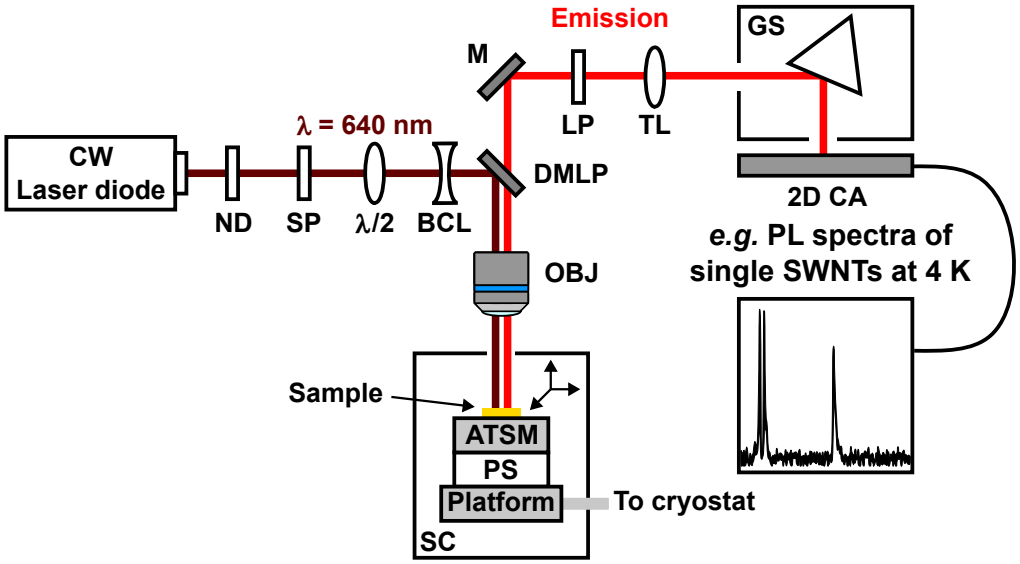

Figure 3.10: Schematic of the employed luminescence spectroscopy setup for low temperature spectroscopy of individual SWNTs and variable temperature spectroscopy. The excitation (laser, $\lambda = 640$ nm) path and the detection path are indicated by burgundy red and red lines, respectively.

The **samples** were mounted inside the sample chamber (**SC**) of the cryostat on an agile temperature sample mount (**ATSM**) connected to a piezo stage (**PS**, attocube ANC350 piezo controller). High-vacuum was applied to the **SC** ($< 10^{-5}$ mbar) using a turbopump (Pfeiffer Vacuum). The nanotube samples were excited with the output of a **continuous wave laser diode** (CW, OBIS, Coherent Inc., 640 nm) which was passed through a neutral density filter (**ND**) and a short pass filter (**SP**, cut-off 750 nm). A laser power of typically ~100 µW was used. In case of single-SWNT measurements, the polarization of the excitation source was adjusted with a half-wave plate (**λ/2**) to match the orientation of the SWNT. The excitation beam was guided to the sample chamber *via* a dichroic long-pass filter (**DMLP**, cut-on 875 nm) and focused onto the sample through the window (uncoated fused silica) of the **SC** with a NIR-optimized 50× objective (**OBJ**, Mitutoyo, N.A. 0.42).

For spectra acquisition, PL was guided by gold mirrors (**M**) and focused by a tube lens (**TL**) onto the entrance slit (100-200 µm width) of a grating spectrograph (**GS**, Princeton Instruments IsoPlane SCT-320). Residual laser light was blocked by the **DMLP** and a long-pass filter (**LP**). Luminescence was dispersed using a grating with 85 grooves mm^{-1} and 1200 nm blaze and detected with a thermoelectrically-cooled 2D InGaAs camera array (**2D CA**, NIRvana 640ST). For the identification of single SWNTs the PL signal of a large sample area was imaged using the mirror grating of the **GS** and expansion of the excitation beam with a biconcave lens (**BCL**).

The base temperature for spectroscopy of individual SWNTs was 3.8 K. In case of variable temperature spectroscopy the temperature was adjusted using the temperature controller (Lakeshore Model 335) of the **ATSM** and spectra were recorded after complete thermal equilibration. After each temperature step the focus was re-adjusted by using the z-controller of the **PS**.

3.5.6 Room-temperature spectroscopy of individual SWNTs and autocorrelation measurements

Room-temperature PL and autocorrelation measurements on individual functionalized (6,5) SWNTs (Chapter 4) were performed by Dr. Shen Zhao under the supervision of Prof. Alexander Högele (Fakultät für Physik, Ludwig-Maximilians-Universität München). For sample preparation, functionalized (6,5) SWNTs were embedded in a PS matrix on top of a glass substrate covered with a gold layer as described above. A home-built confocal microscope equipped with slip-stick positioners (ANPxy101 and ANPz102, attocube systems) was used. The wavelength-tuneable output of a Ti:sapphire laser (Mira, Coherent) in continuous wave mode was employed as the excitation source. The excitation wavelength was tuned to 995 nm corresponding to the E_{11} transition of (6,5) SWNTs and focused onto the sample through an apochromatic objective (LT-APO/IR/0.81, attocube systems). The collected PL was spectrally filtered by a tuneable long-pass filter (TLP01-1116, Semrock) and focused onto a spectrometer (Acton SP2500, Roper Scientific) equipped with a liquid nitrogen-cooled InGaAs camera (OMA V: 1024-1.7, Roper Scientific).
For time-resolved PL measurements and autocorrelation measurements a supercontinuum laser (NKT Photonics, SuperK EXTREME, 78 MHz repetition rate) tuned to 995 nm served as excitation source. The second-order photon-correlation function $g^{(2)}(t)$ of individual SWNTs at room temperature was measured in a standard Hanbury-Brown and Twiss geometry. Emission was guided through a 50:50 beam splitter on a pair of superconducting single-photon detectors (TCOPRS-CCR-SW-85, Scontel). Photon detection events were recorded and correlated using a TCSPC module (PicoHarp300, PicoQuant).

3.5.7 Measurement of NIR-PL images

For macroscopic imaging of the NIR-PL (950-1600 nm) of SWNT dispersions (Chapter 5), pristine and functionalized SWNTs were filled in Eppendorf tubes and placed in a fixed sample holder to ensure imaging under identical conditions. An expanded beam of a 785 nm laser diode (Alphalas Picopower-LD-785-50) operated in continuous wave mode was used as the excitation source and the NIR-PL was imaged by focusing emitted light with a tube lens on a thermoelectrically cooled InGaAs camera (Xenics XEVA-CL-TE3, 252×320 pixels). Residual laser light was blocked by a 950 nm long-pass filter.

3.5.8 PL measurements of spiking and PCR experiments

PL measurements of spiking and PCR experiments (see Chapter 6) were performed with the help of C. Alexander Schrage under the supervision of Prof. Sebastian Kruss at the Department of Chemistry and Biochemistry, Ruhr-Universität Bochum. Typically, 100-200 µL of a SWNT dispersion were placed in 96 well plates and the output of a continuous wave laser diode (561 nm, Laser Quantum, Gem 561) operated at 100 mW was used as excitation source. PL spectra were recorded with a spectrometer (Shamrock 193i, Andor Technology Ltd.) coupled to a microscope (IX73, Olympus).

3.6 Other characterization techniques

3.6.1 Absorption spectroscopy

Absorption spectra in the UV-Vis-NIR spectral range (300-1400 nm) were recorded with a Varian Cary6000i UV-Vis-NIR spectrometer equipped with a silicon and InGaAs detector. All samples were measured in a quartz glass cuvette (Hellma Analytics, QS material) with 1 cm path length and background corrected by baseline measurement of the cuvette with pure solvent prior to the sample measurement. Figure 3.11 shows a representative absorption spectrum of a polymer-depleted dispersion of PFO-BPy-wrapped (6,5) SWNTs (a) and an aqueous dispersion of SDS-coated (6,5) SWNTs (b). Each SWNT chirality possesses a unique set of transition energies labelled as E_{11}, E_{22}, E_{33} and E_{44} which display an additional PSB (see Section 2.1.4). Main excitonic transitions of (6,5) SWNTs, most commonly observed sub-species and polymer absorption bands for PFO-BPy-wrapped and SDS-coated (6,5) SWNTs, as observed in this work, are displayed in Figure 3.11. Background scattering occurs from high energy π-plasmon interactions as well as scattering from residual amorphous carbon, catalyst particles and bundled SWNTs.[265,266] As suggested by Pfohl *et al*. a background profile in the form of $Ae^{(-\lambda/t)}$ was subtracted from all spectra prior to evaluation (red dotted lines).[258]

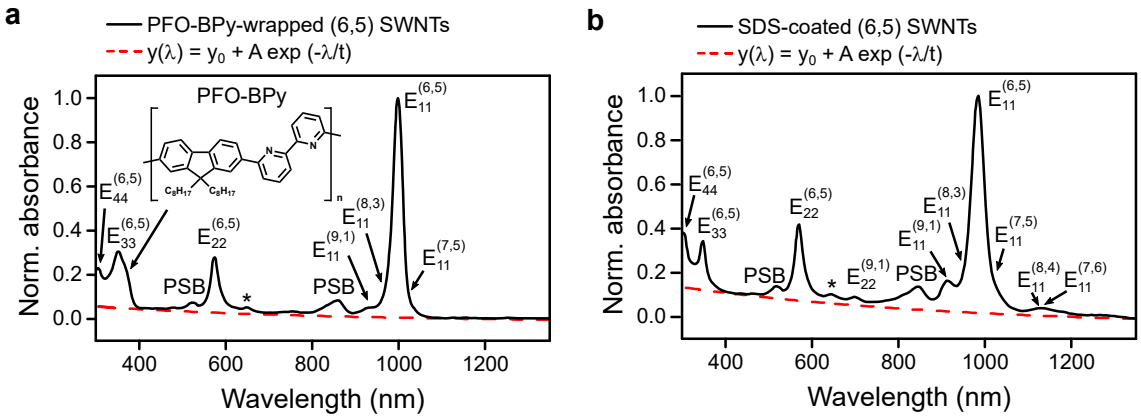

Figure 3.11: Representative absorption spectra in the UV-Vis-NIR spectral range of PFO-BPy-wrapped (6,5) SWNTs (a) and SDS-coated (6,5) SWNTs (b). Main excitonic transitions of (6,5) SWNTs, most commonly observed sub-species and polymer absorption bands are assigned according to Graf *et al.* and Weisman *et al.*[6,83] The asterisks mark the overlapping E_{22} transitions of (7,5) and (8,3) SWNTs.

3.6.2 Raman spectroscopy

Raman spectroscopy was performed with a Renishaw inVia Reflex confocal Raman microscope equipped with a 50× long-working distance objective (Olympus, N.A. 0.5). Samples were prepared by drop-casting of the respective SWNT dispersion onto glass slides (Schott AF32eco) and gently rinsed with THF or water to remove excess wrapping polymer or surfactants. Raman spectra of drop-cast SWNT films were obtained upon 532 nm laser excitation in StreamLine mode and mapping of an area of >80×80 µm^2 (grating 2400 lines mm^{-1}). This results in >1000 individual measurements that where averaged and baseline corrected prior to further analysis. A representative Raman spectrum of PFO-BPy-wrapped (6,5) SWNTs is displayed in Figure 3.12. The grey area indicates the section typically displayed in this work.

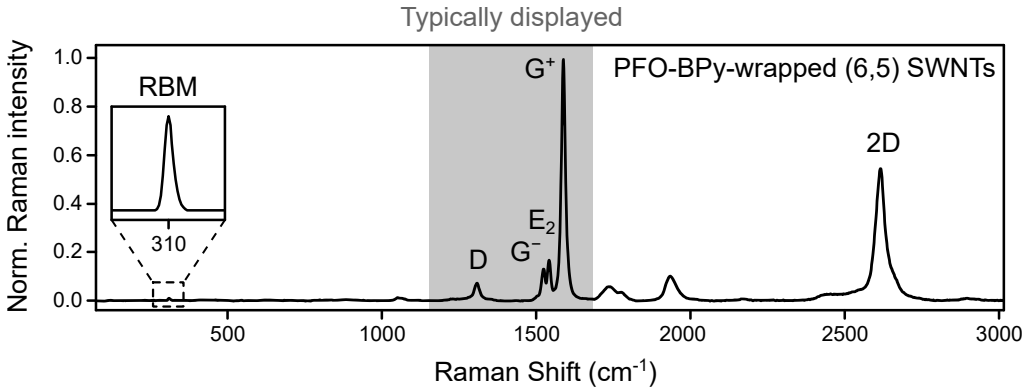

Figure 3.12: Exemplary Raman spectra of PFO-BPy-wrapped (6,5) SWNTs with inset on the RBM mode at ~310 cm^{-1}. The grey area indicates the spectral range typically shown in this thesis.

Multiple characteristic Raman modes can be identified in SWNTs. The most commonly discussed bands are labeled in Figure 3.12 and are:

- The radial breathing mode (RBM, 100-350 cm^{-1}) corresponds to the in-phase expansion and compression of the nanotube in the radial direction. Its wavenumber scales with the tube diameter and is frequently used for the identification of SWNTs chiralities under resonant excitation.[267,268]

- The D mode (1300-1350 cm^{-1}) is a breathing mode of the carbon honeycomb lattice that originates from a double-resonant Raman scattering event activated by defects.[269]

- The G modes (1500-1600 cm^{-1}) are C-C bond stretching modes in longitudinal (G^+) and axial direction (G^-) due to symmetry-breaking effects resulting from the curvature of the tube.[268] Their intensities and peak positions correlate strongly with the doping level of the SWNT.[270] The additional E_2 mode has been described in the past as an intermediate mode of the G^+ and G^- mode.[271,272]

- The 2D mode (or G' mode, 2600-2700 cm^{-1}) is an overtone of the D mode originating from the same scattering event, but is not activated by defects. Its intensity and peak position strongly shift with the charge density.[273]

In this thesis the focus will be on the G^+ and D mode. As the intensity of the G^+ mode is directly correlated to the number of sp^2-hybridized carbon atoms and the D mode is activated by defects, its integrated intensity ratio (D/G^+) is frequently used to quantify the degree of disorder in the SWNT lattice.[269] The change in D/G^+ area ratio ($\Delta D/G^+$) upon introduction of luminescent defects can be used to determine the absolute number of defects in small-diameter SWNTs considering the excitation wavelength, as shown by Sebastian *et al.*[144,274]

3.6.3 X-ray photoemission spectroscopy

X-ray photoemission spectroscopy (XPS) was performed by Dr. Andika Asyuda under the supervision of Prof. (apl.) Michael Zharnikov. For sample preparation, a concentrated dispersion of pristine (6,5) SWNTs or (6,5) SWNTs functionalized with 2-fluoroaniline was drop-cast on gold-coated silicon substrates and rinsed with THF multiple times. The sample was placed in the sample chamber and measurements were carried out under ultra-high vacuum conditions ($\sim 3 \times 10^{-9}$ mbar). A Mg K_α X-ray source (260 W; ~1.5 cm distance) was focused onto the sample and photo-emitted electrons were collected with a MAX 200 (Leybold-Heraeus) spectrometer equipped with a hemispherical analyzer (EA 200; Leybold-Heraeus). F1*s* XPS spectra were recorded in normal emission geometry with an energy resolution of ~0.9 eV. The Au $4f_{7/2}$ signal of the gold-coated silicon substrate at 84.0 eV was used for calibration of the binding energy scale.

3.6.4 Atomic force microscopy

For nanotube length measurements of shortened DOC-coated (6,5) SWNTs, atomic force micrographs were recorded with a Bruker Dimension Icon atomic force microscope in tapping mode under ambient conditions. Adhesion between SWNTs and Si/SiO_2 substrates was enhanced by incubation with aqueous solution of poly-L-lysine hydrobromide (PLL, 0.1 g L^{-1}, Sigma-Aldrich) for 10 min. The incubated substrates were carefully washed with ultra-pure water and blow-dried with nitrogen. The PLL-coated substrates were incubated for 10 min with a diluted dispersion of shortened (6,5) SWNTs with an OD of 0.2 cm^{-1} at the E_{11} transition. After incubation the SWNT dispersions were carefully removed and the substrates were rinsed with ultra-pure water and blow dried with nitrogen. Data was visualized and analyzed using Gwyddion software. The length distribution of shortened DOC-coated (6,5) SWNTs was determined from 150 SWNTs.

3.6.5 Determination of copper concentration by inductively coupled plasma optical emission spectroscopy

The copper concentration of aqueous-dispersed (6,5) SWNTs functionalized *via* a Fenton-like reaction was determined by inductively coupled plasma optical emission spectroscopy (ICP-OES) and was performed by Christian Scholz (Institut für Geowissenschaften, Heidelberg University, see Chapter 5). SDS-coated ATPE-sorted (6,5) SWNTs as well as SDS-coated unsorted CoMoCAT SWNTs with a total volume of 4 mL were functionalized *via* Fenton-like reaction and processed as described in Section 3.2.4. A concentration of 63 µM $CuSO_4(H_2O)_5$ and 750 µM sodium-L-ascorbate was chosen for functionalization. The reaction mixtures were spin-filtered (four cycles, Amicon Ultra-4, 100 kDa) and re-suspended in 1 mL 0.1% (w/v) DOC. The SWNT concentration was estimated to be ~2.4 mg L^{-1} with respect to (6,5) SWNTs. Subsequently, 1 mL H_2O_2 (30%, Sigma Aldrich) were added to the dispersions and the mixtures were heated to 80 °C until complete digestion of SWNTs was achieved and the solutions became transparent (~3 h). The solutions were acidified by addition of 50 µL nitric acid (65%, Suprapur) and passed through a PTFE syringe filter (Whatman, 5 µm pore size). Samples were topped-up with ultra-pure water until a total volume of approximately 4 mL was obtained. For reference measurements identical processing was performed for (6,5) SWNTs as well as unselected CoMoCAT SWNTs without prior functionalization steps. An additional reference sample was prepared without SWNTs with identical laboratory equipment, solvents and additives. All samples were prepared in duplicate. Copper concentrations were determined with a ICP-OES spectrometer by Agilent (ICP-OES 720) at $\lambda = 327.395$ nm. A copper single element solution from Ultra Scientific (1000 mg L^{-1}) was used for calibration.

3.6.6 Preparation of cell cultures

Preparation of cell cultures was performed by Dr. Sebastian Jung with the help of C. Alexander Schrage under the supervision of Prof. Sebastian Kruss (Department of Chemistry and Biochemistry, Ruhr-Universität Bochum). HEK293 cells (ACC 305, DSMZ German Collection of Microorganisms and Cell Cultures) were cultivated in T-75 flasks (Sarstedt) in a humidified 5% CO_2 atmosphere at 37 °C with a sub-cultivation ratio of 1:5 every 3-4 days. Fetal bovine serum (FBS) (10%), penicillin (100 units mL^{-1}) and streptomycin (100 µg mL^{-1}, Thermo Fisher Scientific) was supplemented to achieve cell growth in 16 mL of Dulbeccos modified eagle medium (DMEM, Thermo Fisher Scientific). At a density of $2.2 \cdot 10^6$ cells in 100 mm dishes (Sarstedt), cells were grown for 4 days until confluency. Cells were washed two times with ultra-pure water to remove the cultivation medium and harvested by scraping in 200 µL ultra-pure water. Harvested cells were immediately transferred to 1.5 mL Eppendorf cups and shock-frozen in liquid nitrogen. Pulsed sonication (Qsonica Model Q700 with cuphorn attachment) was performed for 2 min (50% amplitude, 1 s on : 1 s off cycles) to achieve lysis and cell debris was removed by centrifugation at 21 000 g for 2 min. The supernatant was used immediately for spiking experiments (see Chapter 6).

3.6.7 Polymerase chain reaction

Polymerase chain reaction (PCR) was performed by Dr. Sebastian Jung under the supervision of Prof. Sebastian Kruss (Department of Chemistry and Biochemistry, Ruhr-Universität Bochum). PCR constructs were generated by standard PCR techniques. In a total volume of 150 µL, the PCR reaction mixture was assembled on ice according to the Q5 High-Fidelity DNA polymerase manufacturer's (New England BioLabs) instructions. As such, deoxynucleotide triphosphates (NTPs, 10 mM dNTP mix, Promega) with a final concentration of 200 µM and 0.5 µM of forward (T7pro-fwd TAATACGACTCACTATAGGGG) and reverse (T7term-rev TGCTAGTTATTGCTCAGCGG) primer (Eurofins Genomics). 150 ng of pET27b(+) vector with *E. coli OmpC* gene served as template DNA. The reaction mixture was divided into three individual sets and PCR-cycling was performed in an Eppendorf Mastercycler for 12 cycles and 24 cycles. One set was kept on ice (*i.e.* 0 cycles). For each cycle initial denaturation was conducted at 98 °C for 30 s and was followed by 30 s annealing at 50.9 °C and elongation at 72 °C for 35 s. Successful amplification of the parent DNA of the same molecular weight was determined by gel electrophoresis (5 V cm^{-1} for 45 min) on a 1% agarose TAE gel containing 1X GelRed (Biotium) and visualized under UV-light with the help of a Bio-Rad ChemiDoc gel imaging system (see Chapter 6).

CHAPTER 4

SELECTIVE INTRODUCTION OF STRONGLY RED-SHIFTED LUMINESCENT sp^3 DEFECTS IN POLYMER-WRAPPED SWNTS

This Chapter introduces a new method to create luminescent defects in polymer-wrapped SWNTs in organic solvents and discusses the ensuing optical properties. In contrast to previous methods, the obtained luminescent defects exhibit a deeper optical trap depth, and the emitted light is stronger red-shifted and confined to a narrower wavelength range.

The results of this Chapter are published in Settele *et al.*, *Nat. Commun.* **12**, 2119 (2021) and *ACS Appl. Opt. Mater.* **1**, 1706–1714 (2023). Modified reprints are presented with permission of Springer Nature and the American Chemical Society and have been licensed under a Creative Commons CC BY license. Room-temperature PL and autocorrelation measurements on individual functionalized (6,5) SWNTs (see Section 4.7) were performed by Dr. Shen Zhao under the supervision of Prof. Alexander Högele (Fakultät für Physik, Ludwig-Maximilians-Universität München). Sebastian Lindenthal (Heidelberg University) performed the selective dispersion of (7,5) and (10,5) SWNTs, as well as the covalent functionalization and characterization of (10,5) SWNTs. XPS was performed by Dr. Andika Asyuda under the supervision of Prof. (apl.) Dr. Michael Zharnikov (Heidelberg University). Parts of the data shown in Figure 4.19 were collected by Raphael Berger and Johannes Zeh under my supervision.

4.1 Introduction

As outlined in Chapter 2, luminescent defects in semiconducting SWNTs represent emissive states at lower energies than mobile E_{11} excitons, featuring attractive properties. Exciton localization at these defect sites prevents non-radiative decay of mobile E_{11} excitons and gives rise to red-shifted defect-state emission with a prolonged PL lifetime.[15,139] This funneling of mobile excitons to luminescent defects enhances the PLQY of SWNTs in an ensemble.[15,141] Also,

trapped excitons can show single-photon emission even at room temperature.[18,19] For practical applications, narrow defect emission should ideally occur within one of the telecommunication bands, namely the O-band (1260-1360 nm) or the C-band (1530-1565 nm). For this reason, a desire emerged to selectively introduce luminescent defects with deep optical trap depth, where emission is strongly red-shifted and thus in closer proximity to relevant telecommunication bands. Additionally, due to the deeper exciton trapping potential, non-radiative decay of localized excitons *via* thermal detrapping is reduced, yielding higher defect-related emission efficiencies, and achieving higher single-photon purity at room temperature.[18,141]

Luminescent defects can be created through a variety of different functionalization techniques, including ozonation,[11] diazonium salt chemistry,[15,141] aryl/alkyl halide chemistry,[154,176] or Billups-Birch reduction.[179,275] However, emission typically occurs over a wide spectral range (*e.g.*, from 1100 to 1350 nm for (6,5) SWNTs) with the main emission feature, labeled as E_{11}^{*}, located at ~1150 nm. The emission wavelength of luminescent defects is not expected to be governed by the functional group attached to the SWNT but rather by the precise defect binding configuration.[21,150] For luminescent sp^3 defects, the addition of a functional group to the sp^2-hybridized SWNT lattice (typically radical addition) generates a highly reactive SWNT intermediate, which must be saturated with a second functional group or substituent from the solvent (*e.g.*, OH group). Following delocalization of the unpaired electron, saturation is assumed to occur either in the *ortho* or *para* position with respect to the initial functional group. In the case of chiral SWNTs, this results in six possible binding configurations obtained during covalent functionalization (see Section 2.2.2).

Experimental results corroborated by density functional theory (DFT) calculations suggest that each binding configuration is associated with a distinct defect-state energy and therefore emission wavelength.[21,150] Typically, a mixture of two defect emission bands, labeled as E_{11}^{*} (1100-1200 nm) and E_{11}^{*-} (1200-1350 nm), is obtained in (6,5) SWNTs. These defect species are expected to originate from $ortho^{++}$ (circumferential direction) and $ortho^{+}$ (orientation along the nanotube axis) configurations of the two sp^3 carbons, respectively.[158] Recent results also suggested that in some cases E_{11}^{*-} emission originates from the $para^{++}$ configuration.[159,160] Due to the reasons outlined above, E_{11}^{*-} defects are more suitable to achieve high single-photon purity at telecommunication wavelengths. However, E_{11}^{*-} defects represent a minority in most functionalization procedures. Consequently, a higher level of control over the binding configuration needs to be achieved synthetically to introduce E_{11}^{*-} defects into chiral SWNTs and reduce overall spectral diversity.

When this work was conducted in 2021, various functionalization strategies had already been explored to achieve the selective introduction of E_{11}^{*-} defects. These strategies include the use of achiral zigzag SWNTs to reduce the symmetry in SWNTs[158] or covalent functionalization with bisdiazonium salts with methylene linkers.[186] However, zigzag nanotubes are a very rare species in typical nanotube raw materials,[185] and bisdiazonium salts still produce a mixture of E_{11}^{*} and E_{11}^{*-} defects, albeit with higher selectivity for E_{11}^{*-} defects. Since then, Yu *et al.*[145] and Wang *et al.*[159] reported two functionalization strategies in 2022 that result in high selectivity towards E_{11}^{*-} defects. While Yu *et al.* utilized intermolecular interactions between the reagent and SWNT sidewall, Wang *et al.* found that the steric influence of the functional group can be

used to introduce E_{11}^{*-} defects. Importantly, both functionalization protocols are restricted to aqueous dispersions of SWNTs in surfactant solutions. Surfactant-dispersed SWNTs limit the processability of functionalized SWNTs, and residual metallic SWNTs impair integration into optoelectronic devices.[276,277]

In contrast, polymer-sorted SWNTs, especially (6,5) SWNTs, are available with high semiconducting purity[44] and can be integrated into high-quality optoelectronic devices, even when covalently functionalized.[278] Additionally, when selected *via* mild exfoliation methods such as shear-force mixing, long SWNTs (1-2 µm) with a high PLQY (~2%) are obtained.[83] Hence, a functionalization protocol for the selective introduction of E_{11}^{*-} defects in polymer-wrapped SWNTs could also enable their integration into optoelectronic devices.

In the author's master thesis, a functionalization approach based on a photo-induced base-promoted homolytic aromatic substitution reaction (photo-BHAS) was developed, enabling the covalent functionalization of polymer-wrapped (6,5) SWNTs in toluene with aryl halides.[279] In this functionalization scheme, potassium *tert*-butoxide (KO^{t}Bu) in the presence of excess dimethyl sulfoxide (DMSO) and tetrahydrofuran (THF), was used to induce an electron transfer to the aryl halide under UV-light (~350 nm) illumination. As suggested by Buden *et al.*, deprotonation of DMSO and electron transfer of the formed dimsyl anion to the aryl halide upon UV-light illumination are assumed (see Figure 4.1).[280] Subsequently, the reduced aryl halide undergoes dehalogenation and forms a reactive aryl radical, which can perform covalent functionalization of the SWNT sidewall.

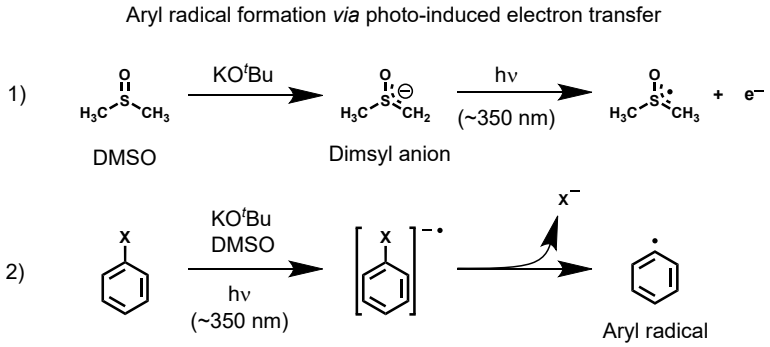

Figure 4.1: Aryl radical formation in a photo-BHAS reaction scheme as proposed by Buden *et al.*[280] 1) Upon deprotonation of DMSO by KO^{t}Bu, the formed dimsyl anion can perform electron-transfer upon UV-light illumination at ~350 nm. 2) This electron transfer leads to a reduction of an aryl halide, which can undergo aryl radical formation through dehalogenation.

Surprisingly, when this reaction was performed with 2-iodoaniline (I*o*NH$_2$) at low concentrations of KO^{t}Bu (<1.0 eq., always noted in respect to I*o*NH$_2$), simultaneous introduction of E_{11}^* (~1130 nm) and E_{11}^{*-} (~1250 nm) emission was observed (see Figure 4.2). Furthermore, when covalent functionalization was performed at higher concentrations of KO^{t}Bu in relation to I*o*NH$_2$ (>1.0 eq.), a shift towards the introduction of the E_{11}^{*-} emission band was noted (see Figure 4.2c,d). While E_{11}^* defects, which are the majority product for covalent functionalization with *e.g.* diazonium salts, are still evident, their relative emission is greatly reduced. This fascinating result sparked further investigations of the described reaction system.

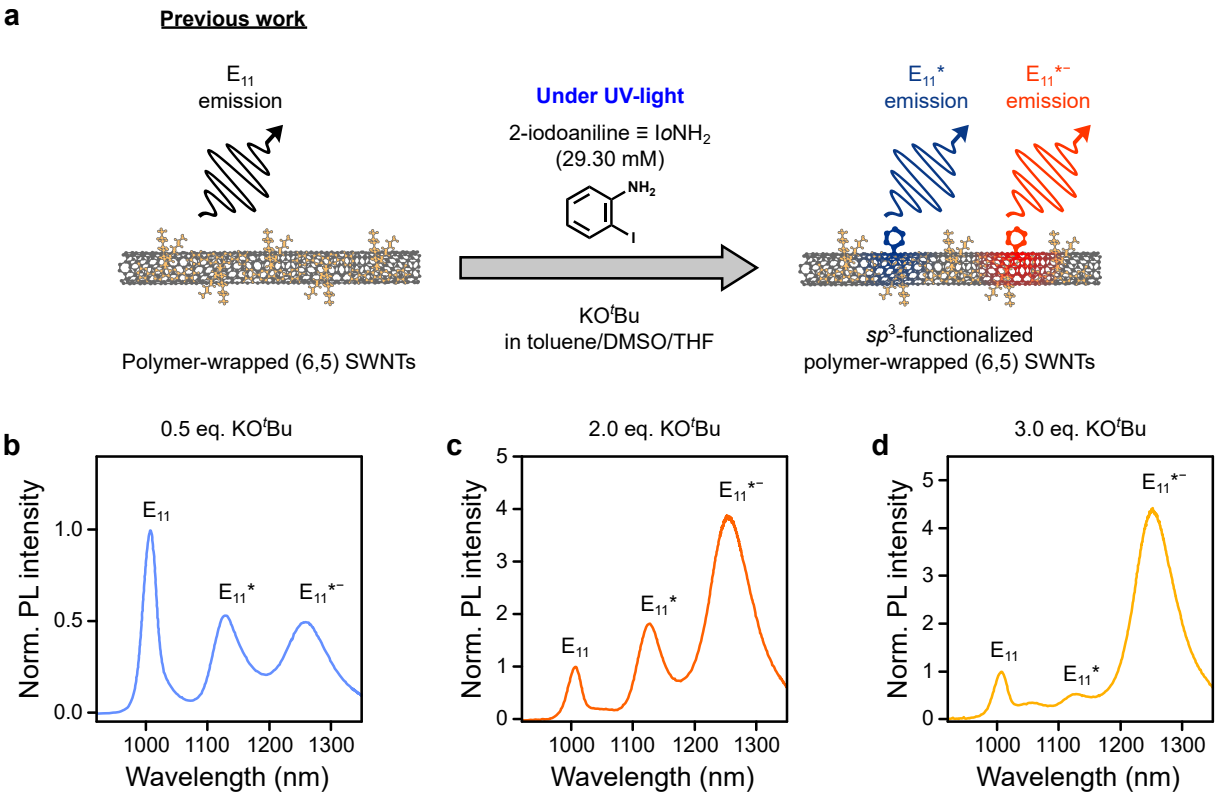

Figure 4.2: a) Scheme for the previously conducted functionalization of polymer-wrapped (6,5) SWNTs with 2-iodoaniline ($IoNH_2$) and KO^{t}Bu in toluene, DMSO and THF under UV-light illumination.[279] b-d) Normalized PL spectra of (6,5) SWNTs functionalized with $IoNH_2$ and varying concentrations of KO^{t}Bu under UV-light illumination. Two red-shifted emission bands are obtained and labeled as E_{11}^* (~1130 nm) and E_{11}^{*-} (~1250 nm). Higher concentrations of KO^{t}Bu lead to a relative increase in defect emission and an increased selectivity towards E_{11}^{*-} emission.

Based on the apparent possibility to tune the relative emission of E_{11}^* and E_{11}^{*-} defects, this Chapter explores the development of a functionalization method to selectively introduce E_{11}^{*-} defects in polymer-wrapped SWNTs. An in-depth investigation of the optical properties of E_{11}^{*-} defects and the functionalization mechanism are performed.

4.2 Selective introduction of E_{11}^{*-} defects

To explore the aforementioned functionalization approach in greater detail, the previously established reaction conditions were adapted. Long, polymer-wrapped (6,5) SWNTs (length 1-2 µm) served as a model system and were selectively dispersed *via* shear-force mixing from CoMoCAT raw material by polymer-wrapping with a polyfluorene copolymer (poly[(9,9-dioctylfluorenyl-2,7-diyl)-*alt*-(6,6′)-(2,2′-bipyridine)] (PFO-BPy, see Figure 4.3a for molecular structure and Section 3.1). Excess wrapping polymer was removed through vacuum filtration, and the collected PFO-BPy-wrapped (6,5) SWNTs were re-dispersed in fresh toluene. Covalent functionalization was performed through the addition of $IoNH_2$ (29.3 mM) and KO^{t}Bu, a strong organic base. THF (8.3 vol%) was added to increase the solubility of KO^{t}Bu in toluene and DMSO (8.3 vol%) was

added as a co-solvent. The functionalization process was carried out in an open flask at room temperature with reaction times ranging from 10 min to 180 min. Following functionalization, side-products and co-solvents were removed through filtration/washing, and the collected functionalized SWNTs were re-dispersed in fresh toluene. Due to the low concentration of wrapping polymer in the solution after two consecutive filtration steps, fresh PFO-BPy was added prior to optical characterization to enhance the colloidal stability of the SWNT dispersions.
In a classical photo-BHAS, photo-induced electron transfer from the dimsyl anion to I*o*NH_2 would be expected, initiating dehalogenation and subsequent aryl radical formation. While this reaction path could still proceed thermally, its activation would be significantly suppressed in the absence of UV-light. To investigate the impact of UV illumination, covalent functionalization was conducted as described above but under exclusion of UV-light, *i.e.* in the dark. The concentrations of KO^{t}Bu (0.5-2.0 eq.) was varied and functionalization proceeded at a fixed reaction time of 30 min at room temperature. Surprisingly, in contrast to functionalization under UV illumination, a high selectivity towards the introduction of E_{11}^{*-} defects was observed regardless of the chosen concentration of KO^{t}Bu (see Figure 4.3b).

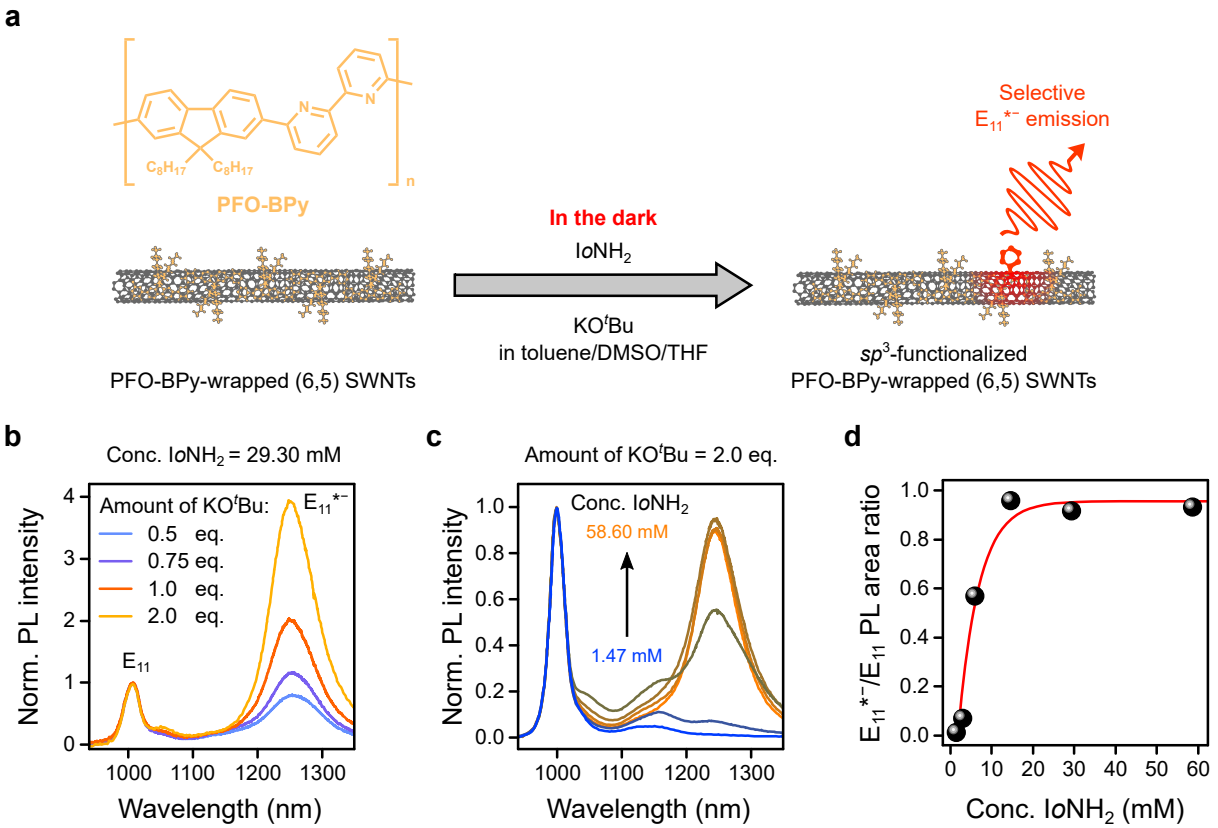

Figure 4.3: a) Scheme for functionalization of PFO-BPy-wrapped (6,5) SWNTs with 2-iodoaniline (I*o*NH_2, 29.30 mM) and KO^{t}Bu in toluene, DMSO and THF in the dark. b) Normalized PL spectra of (6,5) SWNTs functionalized with I*o*NH_2 and varying concentrations of KO^{t}Bu. c) Normalized PL spectra of (6,5) SWNTs functionalized with varying concentrations of I*o*NH_2 and KO^{t}Bu (2.0 eq. in relation to I*o*NH_2). d) Plot of the extracted E_{11}^{*-}/E_{11} PL intensity ratio against the concentration of I*o*NH_2.

Evidently, the introduction of E_{11}^* defects can be attributed to an UV-light induced reaction pathway, while E_{11}^{*-} defects are related to a thermally activated reaction. Thus, higher selectivity towards the formation of E_{11}^{*-} defects is observed when functionalization was conducted in the dark. A potential reaction mechanism will be discussed in Section 4.9.
To further investigate this reaction, the total reagent concentrations (*i.e.*, I*o*NH_2 and KO^{t}Bu) were varied while maintaining a fixed relative ratio of 2.0 eq. KO^{t}Bu. Based on the extracted E_{11}^{*-}/E_{11} PL intensity ratio, a sharp rise in reactivity was observed for concentrations (with respect to I*o*NH_2) between 1.5 mM and 15 mM, saturating for concentrations exceeding 15 mM. Notably, the selectivity towards E_{11}^{*-} defects was reduced at low concentrations (<15 mM) and improved at higher concentrations. Consequently, functionalization was typically carried out at a concentration of 29.3 mM I*o*NH_2 to ensure the selective introduction of E_{11}^{*-} defects while minimizing the formation of side-products.
In addition to varying the base concentration, adjusting the reaction time was identified as an effective tool to control the number of defects and, consequently, E_{11}^{*-}/E_{11} emission ratios. The E_{11}^{*-}/E_{11} emission ratio steadily increased for reaction times spanning 15-180 min, allowing for precise tuning of the defect density (see Figure 4.4a,b). A high selectivity towards the introduction of E_{11}^{*-} defects was maintained even for extended reaction times and no additional emission bands (such as E_{11}^*) were observed.
To unambiguously confirm that the observed E_{11}^{*-} emission originates from the introduction of sp^3 defects into the sp^2-hybridized SWNT carbon lattice, Raman spectra were recorded and are displayed in Figure 4.4c. Clearly, there is a noticeable increase in the Raman D mode, and the integrated D/G^+ area ratio ($\Delta D/G^+$) was found to linearly increase with the reaction time (see Figure 4.4d). Furthermore, a new absorption band located around ~1247 nm is evident in the absorption spectra (Figure 4.4e). This absorption feature was absent in the pristine sample and was assigned to E_{11}^{*-} defects due to the strong correlation between the observed E_{11}^{*-}/E_{11} absorption and E_{11}^{*-}/E_{11} PL area ratio (Figure 4.4f). Similar to E_{11}^* defects obtained through diazonium salt chemistry for polymer-wrapped (6,5) SWNTs, a small Stokes shift of 9-16 meV was observed for E_{11}^{*-} defects. DFT calculations predicted a reduced oscillator strength for sp^3 defects with a greater redshift (*i.e.*, E_{11}^{*-} defects),[150,158] which was experimentally confirmed by Sebastian *et al.*[144] A reduced oscillator strength of 1.1 per defect site was reported for E_{11}^{*-} defects, in contrast to 3.5 per defect site in the case of E_{11}^* defects. As a result, only negligible E_{11}^{*-} absorption bands are visible in Figure 4.4e at low to medium defect density (*i.e.*, PL intensity ratios below three in Figure 4.4a).

In summary, the base-mediated functionalization scheme established here facilitates the selective introduction of E_{11}^{*-} defects with emission at 1250 nm, which is further red-shifted compared to the emissions typically observed in sp^3-functionalized SWNTs (E_{11}^* emission at 1150 nm). The introduction of sp^3 defects was confirmed *via* Raman spectroscopy and the obtained defect density can be modulated easily by adjusting the reaction time.

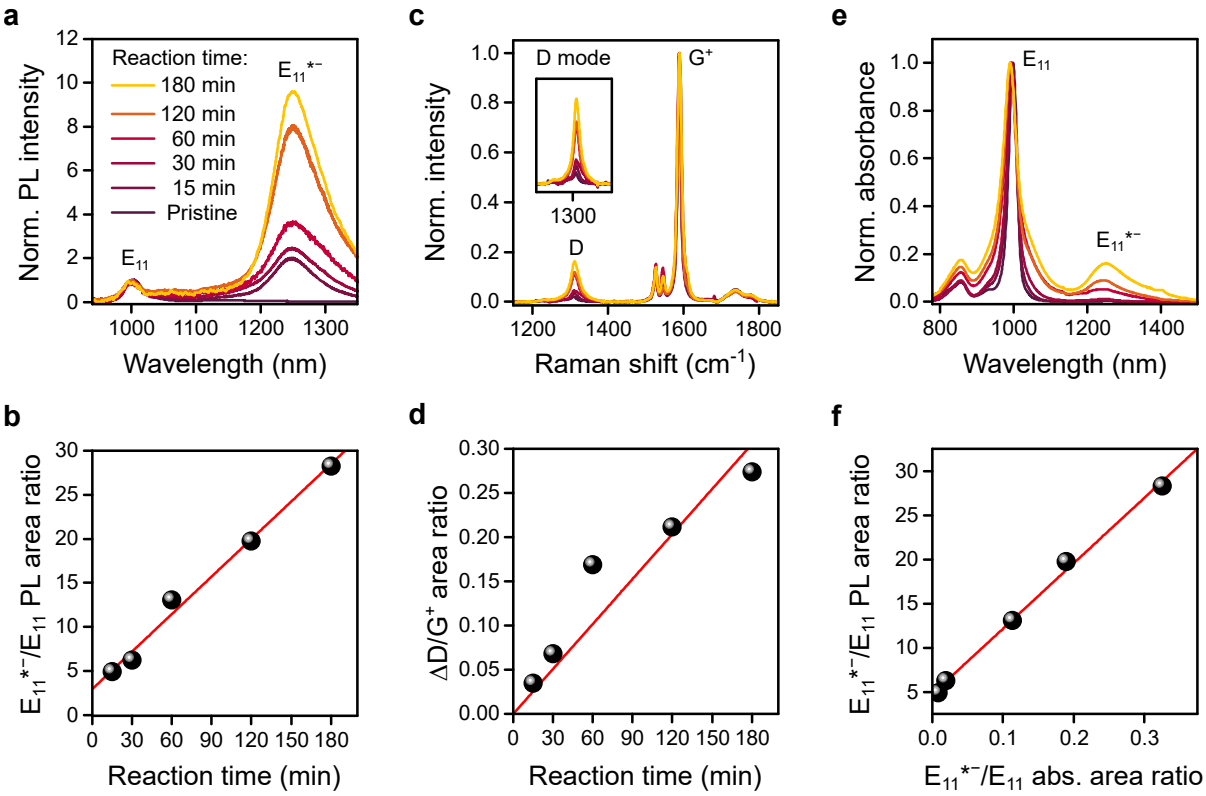

Figure 4.4: a) Normalized PL spectra of (6,5) SWNTs functionalized at a fixed concentration of I*o*NH_2 (29.30 mM) and 2.0 eq. of KO^{t}Bu for increasing reaction times. b) Plot of the extracted E_{11}^{*-}/E_{11} PL area ratio against the reaction time with a linear fit to the data (red line). c) Corresponding normalized Raman spectra with a zoom-in on the D mode. d) Plot of the extracted $\Delta D/G^+$ area ratio against the reaction time with a linear fit to the data (red line). e) Corresponding normalized absorption spectra. f) Plot of the extracted E_{11}^{*-}/E_{11} area ratio against the E_{11}^{*-}/E_{11} PL area ratio with a linear fit to the data (red line).

4.3 Optical properties of functionalized (6,5) SWNTs

When luminescent defects are introduced into small-diameter SWNTs, such as (6,5) SWNTs, a significant enhancement of their ensemble PLQY has been reported.[15,141] To determine the ensemble PLQY of functionalized PFO-BPy-wrapped (6,5) SWNTs, absolute PL measurements were conducted utilizing an integrating sphere (see Section 3.5.3). The total PLQY of the sample is then correlated with the integrated emission across the entire spectral range. However, to gain further insight into the respective contributions of E_{11} and E_{11}^{*-} emission, integration was performed separately for each emission band.

Figure 4.5a illustrates the determined total PLQY and the spectral contributions of E_{11} and E_{11}^{*-} emission as functions of the respective defect density of the sample, expressed in the form of the $\Delta D/G^+$ area ratio. As is characteristic of luminescent sp^3 defects, a continuous decline in E_{11} PLQY was observed with increasing defect density. This phenomenon can be attributed to the trapping of E_{11} excitons at luminescent sp^3 defect sites. Simultaneously, a sharp increase in E_{11}^{*-} PLQY starts, reaching a maximum and then declining as the sp^2 lattice becomes too disrupted for radiative relaxation of excitons to occur. To identify the defect density at which

this maximum appears, absolute quantification of sp^3 defect sites was performed based on Raman measurements according to Sebastian *et al.*[144] When the PLQY is plotted against the obtained absolute number of defect sites (n_d) per µm (see Figure 4.5a), the maximum PLQY is found at ~10-15 μm^{-1}. This value is slightly higher than typically observed for E_{11}^* defects (4-8 μm^{-1}).[144] As we will see in the Section below, E_{11}^{*-} defects exhibit more efficient radiative relaxation compared to E_{11}^* defects. Thus, the introduction of additional E_{11}^{*-} defects outweighs the downside of the introduced disorder in the sp^2 lattice, even for higher defect densities. At optimal defect density, a strong brightening effect compared to pristine (6,5) SWNTs (PLQY ~2%) is observed, with the PLQY reaching up to 5.1%.

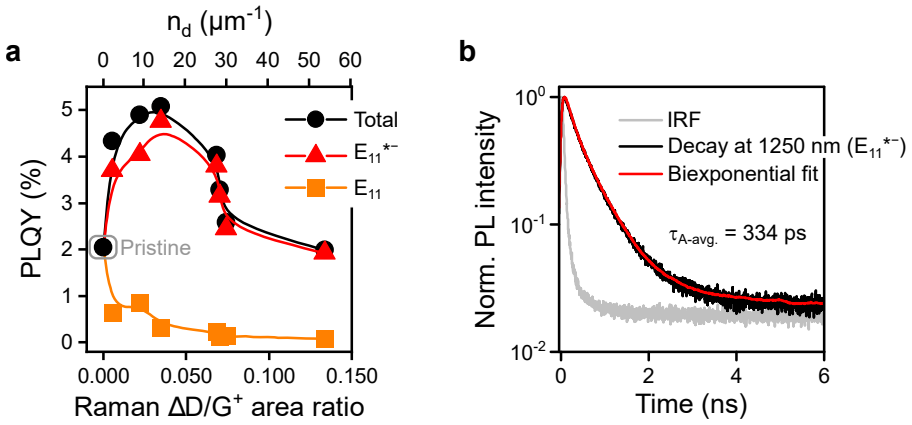

Figure 4.5: a) Determined PLQY (total and separated into contributions of E_{11}^{*-} and E_{11} emission) plotted *versus* the $\Delta D/G^+$ area ratio and corresponding absolute number of defects per µm (lines are guides to the eye). b) PL decay trace (black) recorded for the spectrally selected E_{11}^{*-} emission around 1250 nm. The red line represents a biexponential fit that takes into account the instrument response function (IRF, grey).

The obtained PLQY values are significantly higher than the values determined for polymer-wrapped (6,5) SWNTs functionalized with diazonium salts (mainly E_{11}^* defects). This observation aligns with the expected correlation of the PLQY with the optical trap depth ($\Delta E_{optical}$, $\Delta E_{optical} = E_{11} - E_{11}^*$) as described by Berger *et al.*[141] E_{11}^{*-} defects exhibit a significantly deeper $\Delta E_{optical}$ of 247 meV compared to E_{11}^* defects (130-170 meV). The overall brightening effect and observed higher PLQY for E_{11}^{*-} defects compared to E_{11}^* defects is best understood when considering defect-state relaxation dynamics.

For this reason time-resolved PL measurements were conducted at the E_{11}^{*-} peak emission wavelength of I*o*NH_2-functionalized (6,5) SWNTs using time-correlated single-photon counting (TCSPC). The recorded PL decay is shown in Figure 4.5b, and a biexponential model was reconvolution-fitted to the data (see Table 4.1 for extracted components). The two extracted short and long decay times (τ_{short} and τ_{long}) are commonly understood as the fast redistribution of trapped excitons between dark and bright states (τ_{short}) and the slow radiative and non-radiative recombination (τ_{long}). A long component of 568 ps was found for E_{11}^{*-} defects, which represents a significant increase compared to reported values for E_{11}^* defects (τ_{long} ~250 ps). This finding agrees well with PL lifetime measurements on (6,5) SWNTs functionalized *via* diazonium salt chemistry, where E_{11}^{*-} represented a minority species.[139]

For E_{11}^{*-} defects, an amplitude-averaged PL lifetime ($\tau_{A\text{-}avg.}$) of 334 ps was extracted, which is over an order of magnitude larger than reported values for E_{11} excitons (~10 ps).[126] DFT calculations suggest comparable radiative lifetimes in the range of 1-10 ns for both intrinsic E_{11} excitons[118,138] and trapped excitons.[139] Hence, the observed strong brightening effect upon introduction of E_{11}^{*-} defects is rationalized by trapping of mobile E_{11} excitons at E_{11}^{*-} defect sites, which prevents non-radiative decay by fast diffusive contact quenching at quenching sites.

Table 4.1: Extracted PL lifetime components (τ_{long}, τ_{short}) with the corresponding normalized amplitudes (A_{long}, A_{short}) and the amplitude-averaged PL lifetime ($\tau_{A\text{-}avg.}$).

Sample	τ_{long}	τ_{short}	A_{long}	A_{short}	$\tau_{A\text{-}avg.}$
Functionalized PFO-BPy-wrapped (6,5) SWNTs (measured at 1250 nm)	568 ps	134 ps	0.46	0.54	334 ps

A characteristic consequence of the presence of a limited number of defect states with long lifetime is strong non-linear behavior at high excitation power.[153] In a simplified picture, this can be understood as a state-filling effect, which occurs when the filling of defect states by mobile E_{11} excitons outcompetes their respective depopulation. Excitation power-dependent PL measurements were performed for functionalized PFO-BPy-wrapped (6,5) SWNTs (see Figure 4.6), revealing a pronounced non-linear behavior even at low excitation power. E_{11}^{*-} emission decreased significantly in relation to E_{11} emission, and almost full saturation of the E_{11}^{*-} transition was observed at high pump power. This makes the obtained E_{11}^{*-} defects potentially interesting for applications where population inversion is required, such as optical gain measurements.[281]

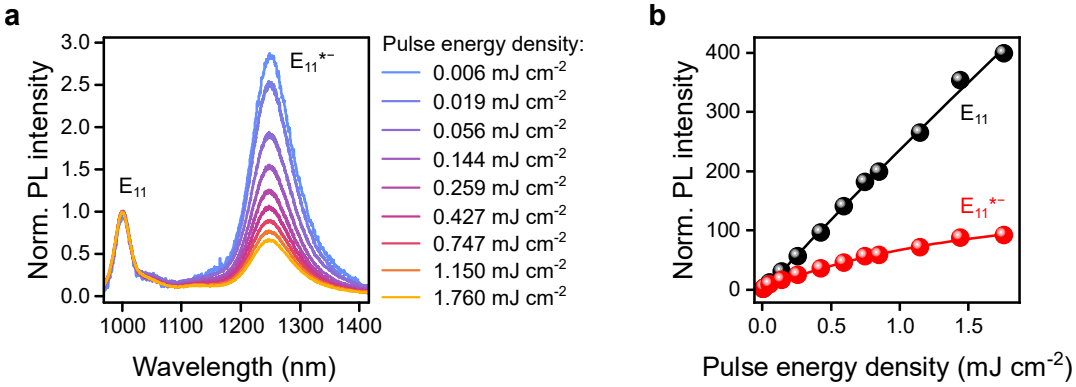

Figure 4.6: a) Normalized PL spectra of functionalized (6,5) SWNTs recorded at varying excitation pulse energy densities. b) PL intensity of E_{11}^{*-} (red) and E_{11} (black) emission plotted against the pulse energy density. PL intensities were normalized to their initial values at the lowest excitation power. E_{11}^{*-} emission shows a strong non-linear behavior and approaches saturation at high excitation power. Note that weak non-linear behavior also occurs for E_{11} emission due to exciton-exciton annihilation.[282,283]

Without the limitation of diffusive contact quenching, the emission efficiency of defect-state emission is governed by the radiative and non-radiative decay rates of localized excitons. More precisely, for the same chirality, the PLQY of the defect-associated transition is determined by the non-radiative decay rates of the localized excitons, as the radiative lifetime of trapped excitons is assumed to be independent of the defect configuration. The defect-state lifetime of E_{11}^{*-} excitons is significantly longer than that reported for E_{11}^{*} excitons.[141] Thus, the stronger brightening effect of E_{11}^{*-} defects can be rationalized by slower non-radiative decay paths compared to E_{11}^{*} defects. The most important non-radiative decay path, which is slowed down, was suggested to be thermal detrapping due to the strong correlation of increasingly long defect-state lifetimes with $\Delta E_{optical}$.[139] For deeper excitonic trapping potentials, the thermally activated back promotion of trapped excitons is reduced, and thus, the defect-state lifetime is increased. In the case of E_{11}^{*} excitons, thermal detrapping rates were found to be accelerated at elevated temperatures, leading to a significant decrease in the E_{11}^{*}/E_{11} emission ratio.[146]
In clear contrast to E_{11}^{*} emission, negligible temperature-dependent changes in the relative E_{11}^{*-} emission were observed in the probed temperature range between 5 and 35 °C, as shown in Figure 4.5a for (6,5) SWNTs functionalized with I*o*NH_2. Kim *et al.* suggested that the thermal trap depth ($\Delta E_{thermal}$) can be extracted from a Van't Hoff plot constructed using the ratio of the integrated PL intensities at different temperatures (T):[146]

$$\frac{E_{11}}{E_{defect}} \propto \exp\left(-\frac{\Delta E_{thermal}}{kT}\right), \tag{4.1}$$

$$\ln\left(\frac{E_{11}}{E_{defect}}\right) = -\frac{\Delta E_{thermal}}{kT} + A, \tag{4.2}$$

where k is the Boltzmann constant, and A is a correction factor. While the constructed Van't Hoff plot displays a good linear fit for E_{11}^{*-} defects (see Figure 4.7b), the extracted $\Delta E_{thermal}$ of 23 meV is significantly lower than for E_{11}^{*} defects (~80-100 meV). This observation was also found to be largely independent of the defect density, as $\Delta E_{thermal}$ increased only marginally for functionalized (6,5) SWNTs at a higher defect density ($\Delta E_{thermal}$ = 27,meV; see Appendix A, Figure A.1).

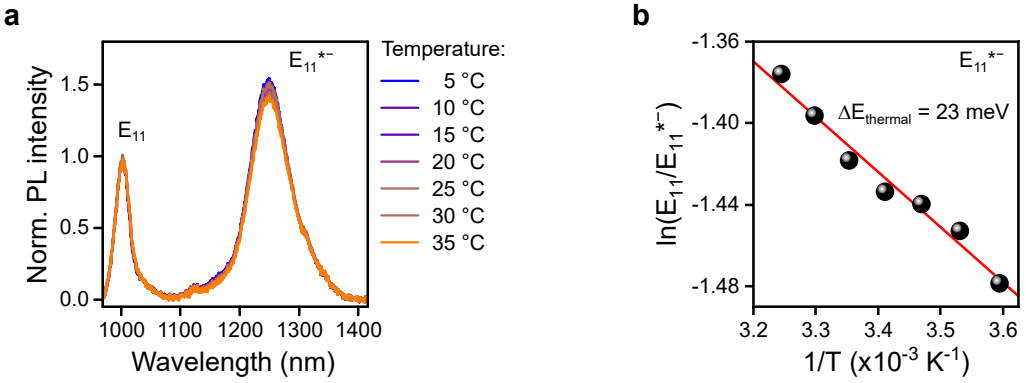

Figure 4.7: a) Recorded temperature-dependent normalized PL spectra of functionalized (6,5) SWNTs in dispersion between 5 °C and 35 °C. c) Computed Van't Hoff plot for the E_{11}^{*-} emission band and linear fit to the data (red line). E_{11} and E_{11}^{*-} represent integrated PL areas.

A small $\Delta E_{thermal}$ should result in fast detrapping rates and directly contradicts the above described model that was applied to rationalize the observed long defect-state lifetime. To better understand this mismatch, the temperature dependence of luminescent defects will be further investigated in the following section.

4.4 Temperature dependence of luminescent defects

To investigate the impact of temperature on E_{11}^* and E_{11}^{*-} defect population more comprehensively, the simultaneous presence of both emission features is advantageous. This approach mitigates the influence of effects associated with the defect density, which has been previously identified as a significant factor affecting the observed temperature dependence. Largely isolated sp^3 defects are assumed, where E_{11}^* and E_{11}^{*-} defects do not interact with each other, and the possibility of one exciton being trapped at multiple defect sites is estimated to be negligible.[142] Functionalized PFO-BPy-wrapped (6,5) SWNTs bearing both E_{11}^* and E_{11}^{*-} defects were produced through covalent functionalization with I*o*NH_2 under UV illumination and the addition of 0.75 eq. of KO^{t}Bu, as detailed in Section 4.1. The PL spectrum of the resulting dispersion is presented in Figure A.1 in the Appendix A. To study the temperature dependence over a wide temperature range, functionalized SWNTs were mixed with polystyrene (PS) and spin-coated onto a glass slide coated with 150 nm of gold. Temperature-dependent PL spectra between 80 K and 330 K were recorded in a home-built optical setup equipped with a closed-cycle liquid helium optical cryostat with adjustable temperature.

Recorded normalized PL spectra measured at 80-200 K and 200-330 K are shown in Figure 4.8a and b, respectively. In agreement with observations made by Kim *et al.*,[284] the temperature dependence of E_{11}^* and E_{11}^{*-} emission can be separated into two parts: First, an overall increase in the defect/E_{11} PL ratio was observed for temperatures <200 K, followed by a steady decrease at temperatures >200 K. This leads to a maximum in the defect/E_{11} PL ratio around 160-220 K. The decrease in relative E_{11}^* emission for temperatures >200 K can be described as the thermal detrapping of localized E_{11}^* excitons, and the constructed Van't Hoff plot displayed in Figure 4.8d shows a good linear fit at high temperatures (>240 K). In this Section, the term ΔE_{detrap} will refer to the thermal trap depth (previously $\Delta E_{thermal}$). Similar to the measurements in dispersion for the same sample, a ΔE_{detrap} of 74 meV was extracted (79 meV in dispersion) for E_{11}^* defects.

As typically noted for sp^3 defects, the observed ΔE_{detrap} is significantly smaller than the extracted $\Delta E_{optical}$ ($E_{11} - E_{11}^* = 132$ meV). Kim *et al.* proposed vibrational reorganization of the excited state upon exciton trapping to cause this mismatch, yet observations of small Stokes shifts by Berger *et al.* for E_{11}^* defects indicate a significant perturbation of the sp^3 defect ground state.[141] As the latter is also observed in this thesis for E_{11}^{*-} defects (as well as luminescent oxygen defects, see Chapter 5), ground state perturbation at the defect sites is assumed, as initially proposed by Ghosh *et al.*[11] In this model, equal perturbation for the excited state and ground state is proposed, and the extracted ΔE_{detrap} could be described as:

$$\Delta E_{detrap} = \frac{\Delta E_{optical}}{2}. \tag{4.3}$$

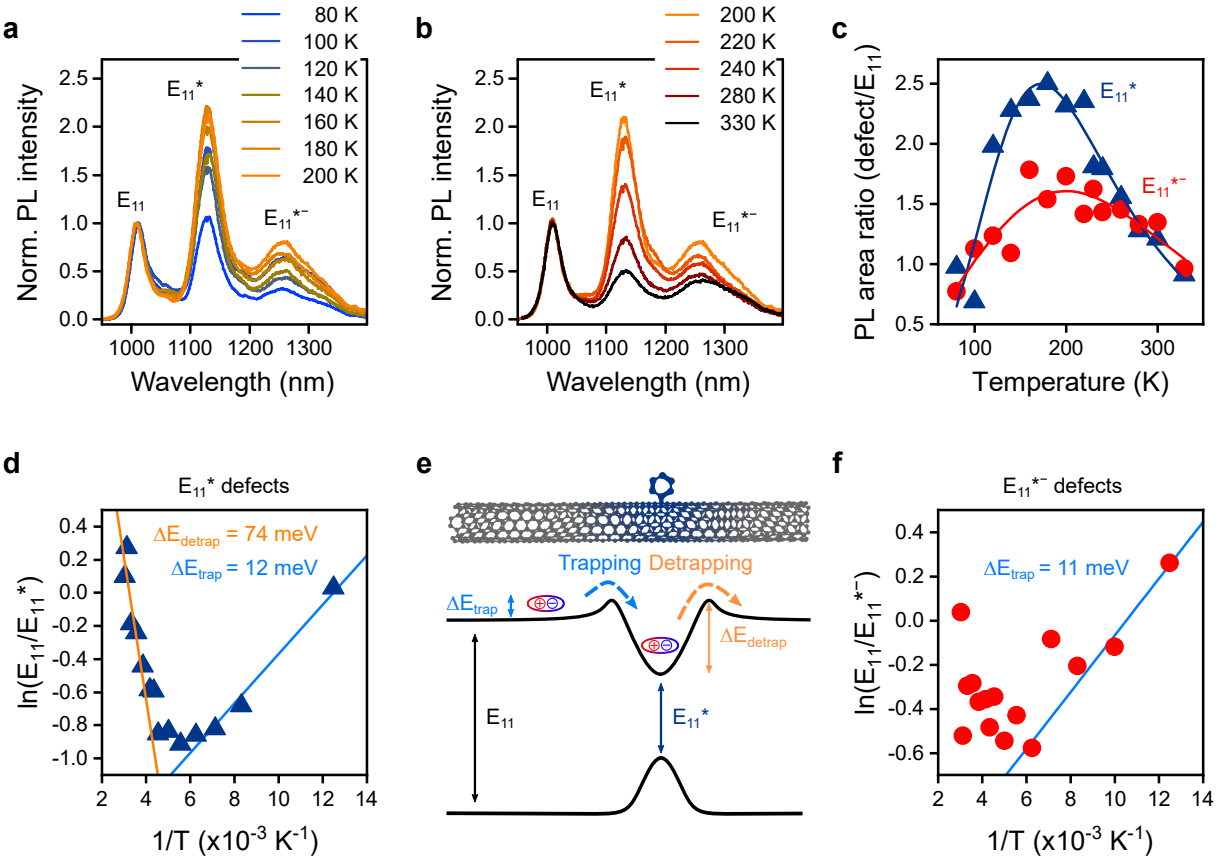

Figure 4.8: Temperature dependence of (6,5) SWNTs embedded in a polystyrene matrix, which were functionalized with I*o*NH_2 and 0.75 eq. KO^{t}Bu under UV-light illumination. a-b) Normalized PL spectra recorded at (a) 80-200 K and (b) 200-330 K. c) E_{11}^*/E_{11} (blue) and E_{11}^{*-}/E_{11} (red) PL area ratios plotted against temperature. Solid lines serve as guides to the eye. d) Computed Van't Hoff plot for the E_{11}^* emission band with linear fits to the data at higher temperatures (>240 K, orange line) and at low temperatures (80-140 K, light blue line). e) Schematic of temperature-dependent exciton dynamics at sp^3 defects. Mobile E_{11} excitons have to overcome a trapping potential (ΔE_{trap}) before being trapped at the defect site. Trapped excitons can be detrapped (ΔE_{detrap}) at elevated temperatures, leading to the regeneration of mobile E_{11} excitons. f) Computed Van't Hoff plot for the E_{11}^* emission band with a linear fit to the data at low temperatures (80-140 K, light blue line). E_{11}, E_{11}^*, and E_{11}^{*-} represent integrated PL areas.

Yet, this model also fails to sufficiently explain the extracted ΔE_{detrap} (74 meV), which is higher than the estimated 66 meV based on Equation 4.3. This discrepancy appears universally for sp^3 defects and is also apparent in reported values from Kim *et al.* and Danné *et al.*[142,146]
The offset between the calculated and the extracted ΔE_{detrap} could be rationalized by the presence of a trapping barrier (ΔE_{trap}) in the vicinity of the sp^3 defect, as proposed in the literature.[18,142,284] Such a potential barrier needs to be overcome prior to exciton trapping. This is expressed in an increase in relative defect emission at temperatures between 80-180 K. Kim *et al.* estimated the height of the potential barrier to be 3-22 meV based on a kinetic model.[284] A similar value of 12 meV can be obtained in this study for E_{11}^* defects when a linear fit is applied to the constructed Van't Hoff plot at low temperatures (80-140 K).

Consequently, when considering an additional potential barrier around the defect site, Equation 4.3 has to be corrected according to:

$$\Delta E_{detrap} = \frac{\Delta E_{optical}}{2} + \Delta E_{trap} \,. \tag{4.4}$$

Based on this, a ΔE_{detrap} of 78 meV can be computed, which closely matches the experimentally extracted ΔE_{detrap} (74 meV, see Figure 4.8d, and 79 meV, see Appendix A, Figure A.1). Hence, this model sufficiently explains the observed ΔE_{detrap} for E_{11}* emission. An overview of the proposed trapping and detrapping mechanisms is given in Figure 4.8e.
In this context, the previously observed dependence of ΔE_{detrap} on the defect density might correlate with changes in the height of the trapping potential ΔE_{trap}. Changes in ΔE_{trap} would influence experimentally determined ΔE_{trap} while $\Delta E_{optical}$ remains constant. Thus, further investigations should focus on possible defect density-dependent changes in the described trapping potential. A fundamental understanding of this process would be particularly useful in the design of single-photon emitters based on functionalized SWNTs, as large trapping potentials are expected to lead to undesired fluctuations in defect-state emission.[284]
Next, the temperature dependence of E_{11}^{*-} defects will be analyzed in more detail. The observed changes in the PL spectra of E_{11}^{*-} defects largely mirror the trends for E_{11}* defects, but with noteworthy differences. Similar to E_{11}* defects, a trapping barrier can be assumed, leading to an increased population of E_{11}^{*-} defect states when the temperature is increased from 80 K to 200 K. A ΔE_{trap} was estimated from a Van't Hoff plot and found to be approximately 11 meV, similar in scale to E_{11}* defects (see Figure 4.8f). However, in clear contrast to E_{11}* defects, an attenuated reduction in relative E_{11}^{*-} PL intensity was observed for temperatures >200 K.
E_{11}^{*-} defects are considered to be deep exciton traps with a $\Delta E_{optical}$ of 247 meV. According to Equation 4.4, this would result in ΔE_{detrap} of approximately 135 meV, nearly twice as large as the observed ΔE_{detrap} for E_{11}* defects. This estimated exciton trap depth is on the same scale as the electrochemical band gap ($\Delta E_{electro}$ = 163 meV) of E_{11}^{*-} defects originating from oxygen defects as estimated by Shiraishi *et al.*[285] A potential explanation for the reduced correlation of E_{11}^{*-} PL intensity with the applied temperature could be the absence of sufficient thermal detrapping within the chosen temperature range. Consequently, considerably higher temperatures might be necessary to induce significant thermal detrapping. Hence, the observed temperature dependence may arise mainly from a different non-radiative decay channel. This assumption is supported by the extracted E_{11}^{*-} defect-state lifetime shown in Figure 4.5. He *et al.* estimated the detrapping rate of E_{11}^{*-} defects to be on the order of several nanoseconds. However, the observed τ_{long} (568 ps) for E_{11}^{*-} defects was found to be significantly shorter. This strongly suggests that for E_{11}^{*-} defects, another non-radiative decay channel becomes more dominant, which exhibits a reduced temperature dependence within the probed temperature range.

4.5 PL lifetime dependence on defect-state emission wavelength

To gain insight into the dependence of non-radiative decay channels in sp^3 defects, wavelength-dependent lifetime measurements were conducted on sp^3-functionalized SWNTs. For this purpose, polymer-wrapped (6,5) SWNTs were functionalized with I*o*NH_2 in the dark, resulting in the selective introduction of E_{11}^{*-} defects (see Figure 4.9a). The defect-state lifetime of E_{11}^{*-} emission was probed using TCSPC, and spectrally-resolved PL decays were recorded for emission wavelengths ranging from 1180 nm to 1340 nm. Extracted $\tau_{A\text{-}avg.}$ are plotted as a function of the emission wavelength in Figure 4.9b.

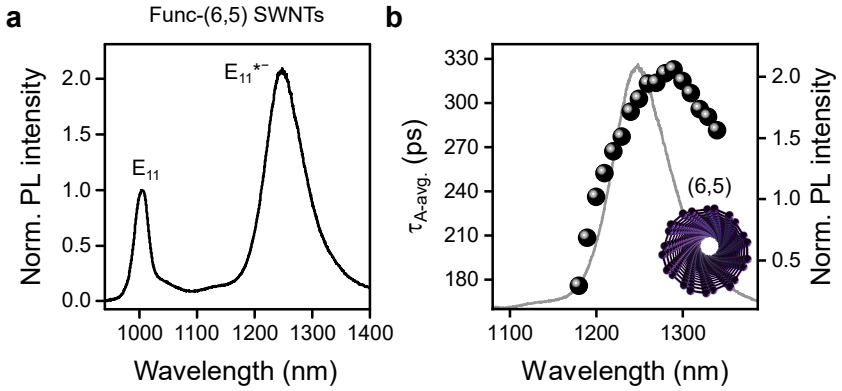

Figure 4.9: a) Normalized PL spectrum of functionalized (6,5) SWNTs. b) A-avg. PL lifetime depending on defect-state emission wavelength for (6,5) SWNTs. The corresponding PL spectrum is shown in grey.

In agreement with the results by He *et al.*,[139] the defect-state lifetime steadily increased for longer emission wavelengths up to 1280 nm. This increase can be rationalized by decreasing thermal detrapping rates with increasing $\Delta E_{optical}$. Surprisingly, for wavelengths beyond 1280 nm, a steady decrease in $\tau_{A\text{-}avg.}$ was observed. The presence of such a maximum in defect-state lifetime is also indicated in the results by He *et al.*, however, as only E_{11}^* defects could be probed, their study was restricted to emission wavelengths <1270 nm.

Decay rates of thermal detrapping (k_{detrap}) are expected to decrease further with increasing emission wavelength and therefore $\Delta E_{optical}$. Thus, the observed reduction in $\tau_{A\text{-}avg.}$ is anticipated to be correlated with a different second non-radiative decay rate that increases for longer wavelengths. At the maximum $\tau_{A\text{-}avg.}$, the increase in lifetime due to the reduction in k_{detrap} is fully compensated by an increase in this second non-radiative decay. This second non-radiative decay is presumably multi-phonon decay (MPD), which is one of the main non-radiative relaxation pathways for trapped excitons. Perebeinos and Avouris modeled MPD decay rates depending on the respective SWNT diameter and predicted MPD rates (k_{MPD}) for localized excitons for SWNT diameters matching the (6,5) SWNT chirality to be ~1 ns.[147] Hence, k_{MPD} roughly equals k_{detrap} (also on the nanosecond scale) for E_{11}^{*-} defects. As the number of phonons needed to bridge the optical gap decreases for longer wavelengths, the MPD rate is expected to further increase for deeper $\Delta E_{optical}$ leading to a decrease in $\tau_{A\text{-}avg.}$. An overview of the proposed trends in decay rates with $\Delta E_{optical}$ is given in Figure 4.10.

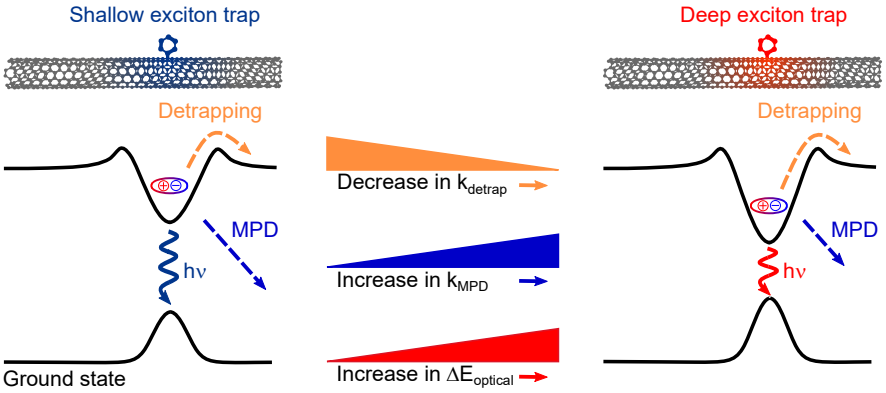

Figure 4.10: Schematic of the exciton dynamics of trapped E_{11}^{*-} excitons for shallow (left) and deep (right) exciton traps. E_{11}^{*-} excitons can decay non-radiatively through thermal detrapping (orange), MPD (blue), or decay under E_{11}^{*-} emission (red). For decreasing optical trap depth ($\Delta E_{optical}$), a decrease in detrapping rate (k_{detrap}) and an increase in MPD (k_{MPD}) are expected. All elements (*e.g.* arrows) are not to scale.

To corroborate this hypothesis, (7,5) SWNTs were selected from CoMoCAT raw material *via* polymer-wrapping with poly(9,9-dioctylfluorene) (PFO) (see Section 3.1), and covalently functionalized with $IoNH_2$ in the dark. The recorded normalized PL spectra of functionalized PFO-wrapped (7,5) SWNTs is displayed in Figure 4.11a. The optical properties of functionalized (7,5) SWNTs will be discussed in more detail in Section 4.8. Due to the smaller band gap in (7,5) SWNTs compared to (6,5) SWNTs, faster defect-state decay rates are typically observed and rationalized by a faster MPD.[133] Surprisingly, a longer PL lifetime of functionalized PFO-wrapped (7,5) SWNTs with E_{11}^{*-} defects was found in comparison to (6,5) SWNTs in this specific case. Nevertheless, an overall faster k_{MPD} is expected.
PL lifetime measurements on functionalized (7,5) SWNTs revealed a similar dependence on the emission wavelength as observed for (6,5) SWNTs, and a PL lifetime maximum can be found at 1300 nm. As thermal detrapping correlates with the trap depth rather than emission wavelength, extracted PL lifetimes were plotted as a function of $\Delta E_{optical}$. This analysis reveals that the maximum in defect-state lifetime is shifted towards lower $\Delta E_{optical}$ for functionalized (7,5) SWNTs. The observed trends were found to be independent of the defect density and defect species, as they are also observed for (6,5) and (7,5) SWNTs, that were functionalized *via* diazonium salt chemistry, yielding E_{11}^{*} defects (see Appendix A, Figure A.2 and Table A.1).
Considering an equally fast k_{detrap} for the same $\Delta E_{optical}$, the shift of the maximum towards shallower $\Delta E_{optical}$ for (7,5) SWNTs can be rationalized by an increase in MPD. Hence, this finding strongly suggests that MPD becomes the dominant non-radiative decay rate for defect-state emission with deep $\Delta E_{optical}$. To further confirm this observation, covalent functionalization of even larger-diameter SWNTs would be necessary. However, achieving sp^3 defects with deep $\Delta E_{optical}$ in such species is challenging, as will be discussed in Section 4.8. To conclude, it is reasonable to assume that the observed temperature dependence of E_{11}^{*-} defects, as shown in Section 4.3 and 4.4, is an effect of temperature-enhanced MPD rather than thermally induced detrapping of localized excitons.

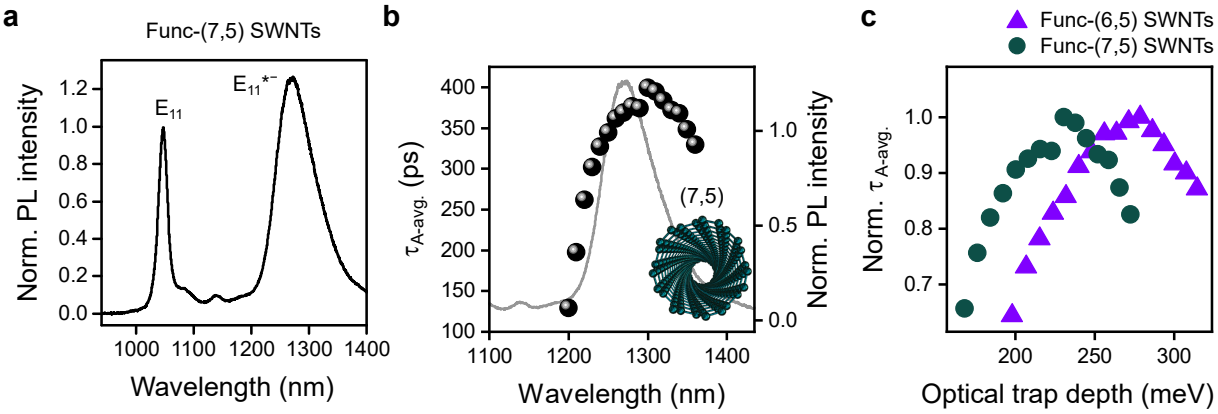

Figure 4.11: a) Normalized PL spectrum of functionalized (7,5) SWNTs. b) A-avg. PL lifetime depending on defect-state emission wavelength for (7,5) SWNTs. The corresponding PL spectra are shown in grey.

In summary, E_{11}^{*-} defects in polymer-wrapped (6,5) SWNTs represent deep exciton traps that exhibit a long defect-state lifetime and induce a strong brightening effect. According to Equation 4.4 an exciton trap depth of 135 meV can be estimated. As a result, depopulation of E_{11}^{*-} defect states by thermal detrapping is weak in the investigated temperature range (up to ~35 °C) and the observed temperature dependence of E_{11}^{*-} emission can be assigned to a different non-radiative decay path. This non-radiative decay path is probably MPD.

4.6 Spectra of individual SWNTs at cryogenic temperatures

Achieving a uniform response from luminescent defects is vital for their effectiveness in various applications such as quantum information technologies. Previously, PL from luminescent defects in (6,5) SWNTs appeared over a broad spectral range (1100 to 1350 nm). With the functionalization approach described in Section 4.2, this broad emission range is significantly reduced, and E_{11}^{*-} emission is confined to a narrow window (peak width ~65 meV). However, for practical applications, it is essential that this narrowing is reflected in the single-tube spectra.
To verify this, PL spectra of individualized functionalized (6,5) SWNTs with E_{11}^{*-} defects were recorded at 4 K. For this, covalent functionalization was performed with I*o*NH_2 so that a low sp^3 defect density was obtained, and a diluted SWNT dispersion was embedded in a PS matrix to increase the probability of measuring an individual SWNT. Figure 4.12a presents a confocal scanning PL map (measured at room temperature) of individual functionalized (6,5) SWNTs, confirming their spatial separation. In total, 62 spots were recorded at 4 K, of which 12 individual SWNTs are shown in Figure 4.12b. The majority of defect emission peaks were observed within a narrow spectral range of 80 meV, with peak widths ranging from 2.9-5 meV. The heterogeneous distribution over this spectral range likely originates from variations in the distinct dielectric environments of individual defects.[19,158] As characteristic for polymer-wrapped SWNTs at cryogenic temperatures, each emission feature is accompanied by a weak phonon sideband, resulting in an asymmetric line shape.[286] The strong segmentation of E_{11} is expected to result from random localization of excitons in long polymer-wrapped SWNTs.[287,288]

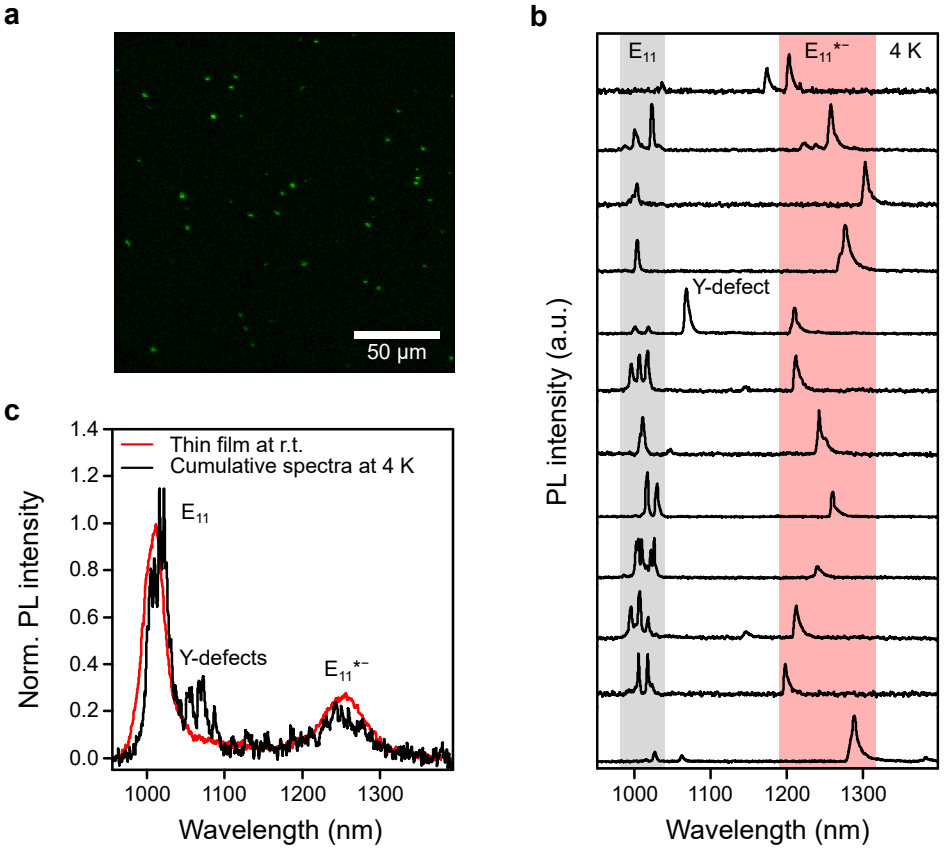

Figure 4.12: a) Scanning confocal PL map (acquired at room temperature) of individual functionalized (6,5) SWNTs in a polystyrene matrix. b) PL spectra of 12 individual (6,5) SWNTs functionalized with I*o*NH_2 recorded at 4 K. The spectral ranges of the E_{11} (grey) and $E_{11}{}^{*-}$ (red) emission peaks are highlighted. c) The cumulative PL spectrum of all 62 spots at 4 K (black) representing the average signal of a large number of functionalized (6,5) SWNTs, fits the spectrum measured for a thin film of the same sample at room temperature (r.t., red line). Emission at ~1060 nm at low temperatures can be assigned to Y-defects.[116]

When all 62 spots are spectrally integrated, the cumulative spectrum matches the thin-film spectrum of the same sample at room temperature (see Figure 4.12c). Surprisingly, a prominent emission band at ~1060 nm is observed, which is absent at room temperature. This emission band has been labeled as Y-band in the past and was connected to sidewall defects with shallow excitonic trapping potentials. These defects are expected to be introduced during the initial processing or through interactions with groups on the substrate surface and are also present in unfunctionalized SWNTs.[116,121]

Overall, the emission from $E_{11}{}^{*-}$ defects in polymer-wrapped (6,5) SWNTs is confined to a narrow spectral range between 1200 nm and 1300 nm even on a single-nanotube level. Crucially, these results show that the reaction conditions can be tuned so that there is a high probability that only a single $E_{11}{}^{*-}$ defect is incorporated in a single SWNT. The presence of a single $E_{11}{}^{*-}$ defect on a single SWNT is an important requirement for their potential application as a single-photon emitter, a topic that will be explored in the following section.

4.7 Single-photon emission from luminescent defects

The ability to exhibit single-photon emission (SPE) in the near-infrared is one of the most exciting properties of luminescent defects, making them a suitable material for potential applications in fiber-based quantum information technologies.[289] Achieving SPE requires a quantum mechanical two-level system, where a single emitter can transition exclusively between a singly occupied and an unoccupied state. In the case of SWNTs, such a system can be realized by trapping excitons in zero-dimensional localized states. While cryogenic temperatures are necessary for achieving this localization in unfunctionalized SWNTs, luminescent defect sites offer deep trapping potentials (exceeding k_BT), enabling exciton localization at higher temperatures. Luminescent defects with deep potential traps (*e.g.* E_{11}^{*-} defects in (6,5) SWNTs) were shown to achieve SPE with high purity even at room temperature.[19]

To assess the suitability of the selectively introduced E_{11}^{*-} defects in polymer-wrapped SWNTs, Hanbury Brown-Twiss experiments were conducted on individualized (6,5) SWNTs with a low concentration of E_{11}^{*-} defects embedded in a polystyrene matrix at room temperature (same sample as seen in Figure 4.12). Figure 4.13a displays the room temperature (298 K) PL spectrum recorded for a single functionalized (6,5) SWNT bearing one defect with a deep potential well (emission at 1258 nm). The corresponding recorded (pulsed) second-order photon correlation ($g^{(2)}$) for defect emission is shown in Figure 4.13b.

The $g^{(2)}(t)$ trace represents the probability of two consecutive photon detection events to occur within a specific time frame and is used to benchmark single-photon sources. In the case of pulsed optical excitation, photon antibunching is indicated by the absence of the peak at zero time delay in the $g^{(2)}(t)$ trace. The $g^{(2)}(t)$ trace for E_{11}^{*-} defects exhibits clear photon antibunching, as evidenced by the negligible number of correlation events at zero time delay. Its degree of photon antibunching is defined as the area of the center peak normalized to one of the side peaks. When normalized to the side peak at a 26 ns time delay, a $g^{(2)}$ value of 0.07 was extracted, indicating photon antibunching with single-photon purity of 93%.

Histograms of PL count rates collected over a time period of 23 min further revealed high count rates (~60 kHz, Figure 4.13c) and demonstrated low long-timescale fluctuations. To quantify these fluctuations, the deviation of the PL intensity distribution of the emitter (σ_{QE}) from the Poisson distribution of the detector shot noise (σ_{SN}) was determined according to:

$$\frac{\sigma_{QE}}{\sigma_{SN}} = \sqrt{\frac{\langle n^2 \rangle - \langle n \rangle^2}{\langle n \rangle}}, \tag{4.5}$$

where n is the number of PL counts per 100 ms time bin. This analysis indicates that E_{11}^{*-} emission is mostly free of long-timescale fluctuations, as a σ_{QE}/σ_{SN} ratio of 1.2 was obtained (where 1 represents the shot noise limit). Comparable values in single-photon purity and PL fluctuation were reported by He *et al.* for polymer-wrapped (6,5) SWNTs with E_{11}^{*-} (at 1280 nm).[19] However, only few SWNTs had E_{11}^{*-} defects and luminescent defects were spread over a large spectral range (1100–1350 nm) due to the presence of additional E_{11}^{*} defects. Narrowing down the spectral range to a distinct emission band where high single-photon purity can be achieved represents a significant advancement.

Single-photon purity and count rate fluctuations are currently not the main issues for application. Homogeneous emission line broadening is a major limitation to photon indistinguishability. To improve the photon indistinguishability, by bringing the homogeneous linewidth closer to the Fourier-transform limit, cavity enhancement of the radiative emission rate *via* the Purcell effect has emerged as the most promising approach.[290,291] However, optimal cavity performance is confined to a finite spectral band. Here, the selective introduction of E_{11}^{*-} defects allows for better matching with such cavities, as defect emission originates from a narrower wavelength window.

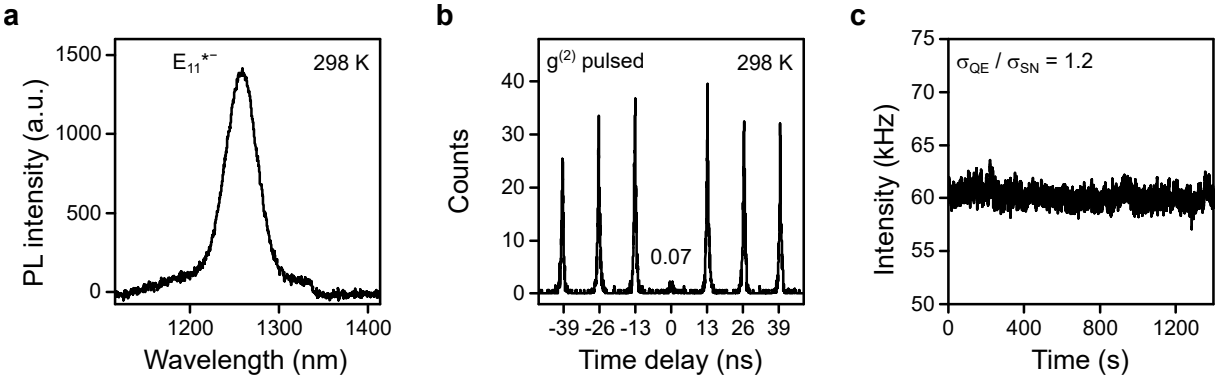

Figure 4.13: a) Zoom-in on the E_{11}^{*-} emission band of a single functionalized (6,5) SWNT embedded in a polystyrene matrix at room temperature (298 K). b) Second-order photon-correlation function $g^{(2)}(t)$ of E_{11}^{*-} emission at room temperature. The absence of a peak at zero time delay indicates photon antibunching with high single-photon purity (93%). c) Histogram of PL count rates collected over a time period of 23 min showing a count rate fluctuation near the shot-noise limit.

In summary, E_{11}^{*-}defects in individual polymer-wrapped (6,5) SWNTs exhibit single-photon emission with high purity at room temperature within a narrow spectral range between 1200 nm and 1300 nm. However, for real applications, emission should fall within one of the standard telecommunication bands (O-band or C-band). A significant portion of E_{11}^{*-} defects does not fulfill this requirement, as their emission does not fall within the O-band (1260-1360 nm).

4.8 Luminescent sp^3 defects in larger-diameter SWNTs

The introduction of luminescent defects is frequently conducted on (6,5) SWNTs, which serve as a model system due to their abundance in CoMoCAT raw material and high reactivity towards covalent functionalization. However, to achieve defect emission in the relevant telecommunication bands, ideally in the C-band (1530-1565 nm), the conceptual transition to larger-diameter SWNTs with smaller optical band gaps is necessary.

To address this, polymer-wrapped (7,5) SWNTs (diameter 0.83 nm, E_{11} transition at 1047 nm) and (10,5) SWNTs (diameter 1.05 nm, E_{11} transition at 1276 nm) were selectively dispersed in toluene using the polyfluorene derivatives PFO and poly[(9,9-di-*n*-octylfluorenyl-2,7-diyl)-*alt*-(benzo[2,1,3]thiadiazol-4,8-diyl)] (F8BT), respectively.

The nearly monochiral dispersions (see Section 3.1.3 and 3.1.4) were then functionalized in the dark with I*o*NH_2, resulting in new red-shifted emission bands in PFO-wrapped (7,5) (see Figure 4.14a) and F8BT-wrapped (10,5) SWNTs (see Figure 4.14b). In both cases, very long reaction times (2.5-5.0 h) were required, due to a reduced curvature-induced local strain on the carbon bonds.[165] Nevertheless, Raman spectroscopy revealed significant introduction of sp^3 defects in (7,5) SWNTs with defect densities up to 13 µm^{-1}.[144,274] Hence, extended reaction times are sufficient to achieve defect densities where maximum PLQY is reached (~4-8 µm^{-1} for (6,5) SWNTs).

Narrow defect emission was observed for functionalized (7,5) and (10,5) SWNTs at 1270 nm and 1474 nm, respectively. While PL emission can be achieved in the O-band by functionalizing (7,5) SWNTs, emission in the C-band remains elusive. Achieving further red-shifted defect emission becomes increasingly challenging for larger-diameter SWNTs,[12] as $\Delta E_{optical}$ steadily decreases with increasing diameter (see Figure 4.14c). However, in contrast to E_{11}^* defects on (7,5) SWNTs (uncertain in case of (10,5) SWNTs), E_{11}^{*-} emission is still significantly more red-shifted, making it more suitable. Still, the obtained E_{11}^{*-} defects in (7,5) and (10,5) SWNTs represent significantly shallower traps compared to E_{11}^{*-} defects in (6,5) SWNTs, resulting in shorter defect-state PL lifetimes and the absence of PL brightening.[133,292]

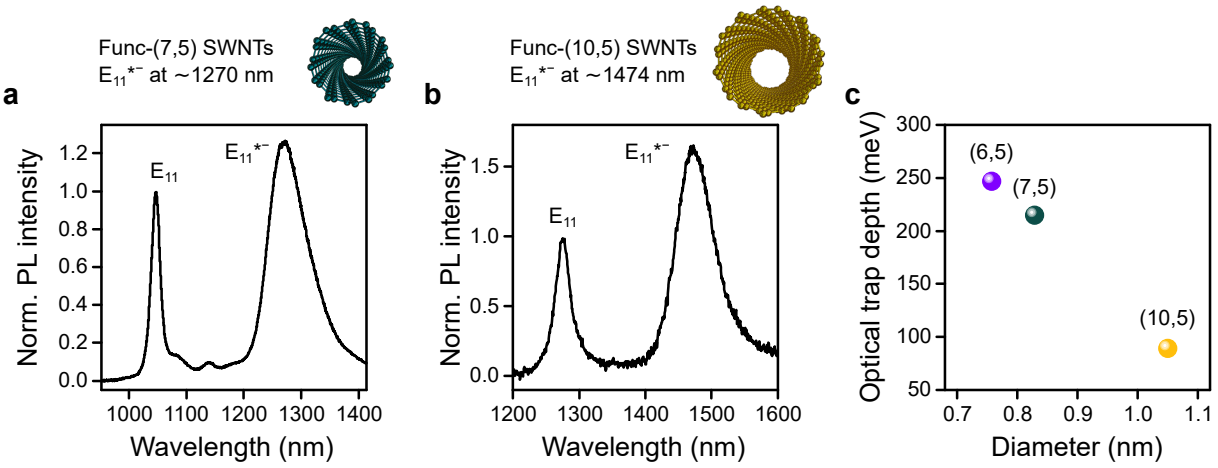

Figure 4.14: a) PL spectra of PFO-wrapped (7,5) SWNTs functionalized with I*o*NH_2 for 5 h showing a pronounced E_{11}^{*-} emission band at ~1270 nm. b) PL spectra of F8BT-wrapped (10,5) SWNTs functionalized with I*o*NH_2 for 2.5 h with pronounced E_{11}^{*-} emission band at ~1474 nm. Note that the average length of (7,5) and (10,5) is expected to be different due to different exfoliation methods (shear-force mixing in case of (7,5) SWNTs and tip sonication in case of (10,5) SWNTs). c) Optical trap depth of E_{11}^{*-} defects plotted against the respective SWNT diameter.

The functionalization of multiple SWNT chiralities can further be utilized to gain insights into the defect binding configuration. Initially, E_{11}^{*-} defects in (6,5) SWNTs were assumed to originate from an *ortho*$^+$ configuration, however, Wang *et al.* and Zheng *et al.* suggested that in some cases E_{11}^{*-} defects may originate from a *para*$^{++}$ configuration.[159,160] While, in the case of (6,5) and (7,5) SWNTs, E_{11}^{*-} emission from both configurations occurs at a similar wavelength, a clear difference is observed for (10,5) SWNTs. Functionalized (10,5) SWNTs with E_{11}^{*-} defects

which are expected to result from *para*$^{++}$ configuration appear significantly more red-shifted at 1527 nm.[159] Hence, based on this comparison and the observed similar spectral behavior across the tested (n,m) range, $E_{11}{}^{*-}$ emission will be assigned to an *ortho*$^{+}$ configuration in this work.

In summary, covalent functionalization using the presented base-promoted coupling approach is highly suitable for introducing $E_{11}{}^{*-}$ defects in polymer-wrapped larger-diameter SWNTs, shifting defect emission further towards telecom wavelengths. However, achieving even further red-shifted emission with the presented functionalization approach remains a challenging task and will require the functionalization of even larger-diameter and less reactive SWNTs.

4.9 Mechanistic investigations

4.9.1 Nature of the functional group & reference experiments

In Section 4.2, the selectivity of the reaction of I*o*NH$_2$ with SWNTs, leading to $E_{11}{}^{*}$ or $E_{11}{}^{*-}$ defects, was attributed to divergent reaction paths. The introduction of $E_{11}{}^{*}$ defects was associated with a reaction path proceeding under UV-light illumination, while the introduction of $E_{11}{}^{*-}$ was assigned to a thermally activated process.
Under UV-light illumination, dehalogenation and aryl radical formation of I*o*NH$_2$ *via* photo-BHAS is expected (see Figure 4.1) and $E_{11}{}^{*}$ introduction *via* a similar reaction path has been demonstrated in the past.[176] However, when covalent functionalization was performed with 2-fluoroaniline under UV-light and at low concentrations of KO^{t}Bu (0.75 eq. with respect to the aniline), $E_{11}{}^{*}$ and $E_{11}{}^{*-}$ emission were observed (see Figure 4.15a). The C-F bond represents one of the strongest single bonds, and aryl radical formation *via* dehalogenation is highly unlikely.[293] When the reaction with 2-fluoroaniline proceeded in the dark in the presence of high base concentrations (2.0 eq.), selective introduction of $E_{11}{}^{*-}$ was observed. Therefore, the introduction of both $E_{11}{}^{*}$ and $E_{11}{}^{*-}$ is not expected to occur *via* a dehalogenation process.

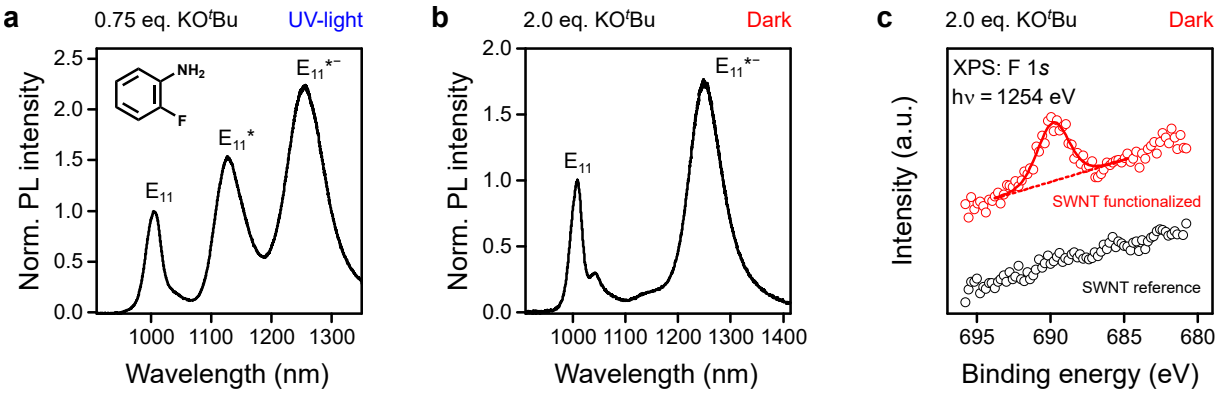

Figure 4.15: a) PL spectrum of (6,5) SWNTs functionalized with 2-fluoroaniline and 0.75 eq. KO^{t}Bu under UV-light illumination. b) PL spectrum of (6,5) SWNTs functionalized with 2-fluoroaniline and 2.0 eq. KO^{t}Bu in the dark. c) F 1*s* XPS spectra of (6,5) SWNTs after reaction with 2-fluoroaniline in the dark with (red circles including peak fit; red line) and without (black circles; reference) addition of 2.0 eq. of KO^{t}Bu.

To confirm the chemical group attached to the SWNT, X-ray photoemission spectroscopy (XPS) measurements were performed on thin films of (6,5) SWNTs functionalized (in the dark) with 2-fluoroaniline. In a reference experiment, pristine (6,5) SWNTs were processed similarly, but no base was added. Figure 4.15c clearly shows a strong signal from the F 1*s* core level with an extracted binding energy of 689.5 eV, which agrees with reported values for aryl and alkyl C-F bonds.[294,295] This demonstrates that 2-fluoroaniline is covalently bound to polymer-wrapped (6,5) SWNTs, and no dehalogenation occurred.

Before formulating a reaction mechanism, further experiments are required. Such mechanistic studies represent a challenging task. Only very few luminescent defects are created in the presented reaction scheme at extremely high reagent concentrations (*e.g.*, aniline, 29.30 mM), in contrast to the SWNT concentration (0.55 mg L^{-1}, corresponding to ~0.4 nM). Hence, even at high defect concentrations (>20 µm^{-1}), only 1 of 10^6 aniline reagent molecules reacts with the SWNT sidewall. Minor side reactions may also lead to the formation of the observed luminescent defects. For this reason, mechanistic studies were restricted to variations in the reaction conditions and simple PL measurements, with the aim to correlate the chosen conditions with the introduction of luminescent defects.

First, a large number of reference and control experiments were conducted in toluene and THF. Notably, covalent functionalization and pronounced defect emission bands were observed even in the absence of halo anilines, as illustrated in Figure 4.16 (black spectra). While defect emission is absent under pure UV-light illumination (see Appendix A, Figure A.3), E_{11}^* emission is evident when functionalization took place in THF and DMSO (Figure 4.16a). Elevated concentrations of KO^{t}Bu under UV-light illumination resulted in the generation of both E_{11}^* and E_{11}^{*-} defects (Figure 4.16b). Conversely, under dark conditions in the presence of DMSO, selective introduction of E_{11}^{*-} defects occurred (Figure 4.16c). Importantly, the introduction of defect emission bands is greatly accelerated and displays a change in selectivity towards E_{11}^* and E_{11}^{*-} defects when halo anilines were added (PL spectra in red in Figure 4.16d-f, see also Appendix A, Figure A.3). Consequently, covalent functionalization is anticipated to proceed through reactive aniline intermediates.

Considering all conducted experiments, an interesting correlation between the introduction of E_{11}^* and E_{11}^{*-} defects and the chosen reaction conditions can be established. E_{11}^* emission occurs only in the absence of DMSO or under UV-light illumination. Both, the dimsyl anion under UV-light exposure and KO^{t}Bu can serve as electron donors in the presence of suitable electron acceptors.[296] Thus, the formation of E_{11}^* defects can be correlated with a reaction path involving electron transfer and possibly leading to radical formation. Currently available functionalization methods largely rely on the covalent functionalization of SWNTs *via* reactive radical species and yield E_{11}^* emission.[15,154,176,183] This strongly implies that the covalent functionalization of SWNTs by radicals primarily induces E_{11}^* emission.

In contrast to this, the appearance of E_{11}^{*-} emission bands can be directly linked to the basicity of the system and occurs exclusively in the presence of KO^{t}Bu. When DMSO is added as a co-solvent, the basicity of KO^{t}Bu is known to increase[297] due to formation of dimsyl anions.[280] These conditions resulted in selective E_{11}^{*-} emission and suggest that nucleophilic intermediates are involved in the covalent functionalization mechanism leading to E_{11}^{*-} defects.

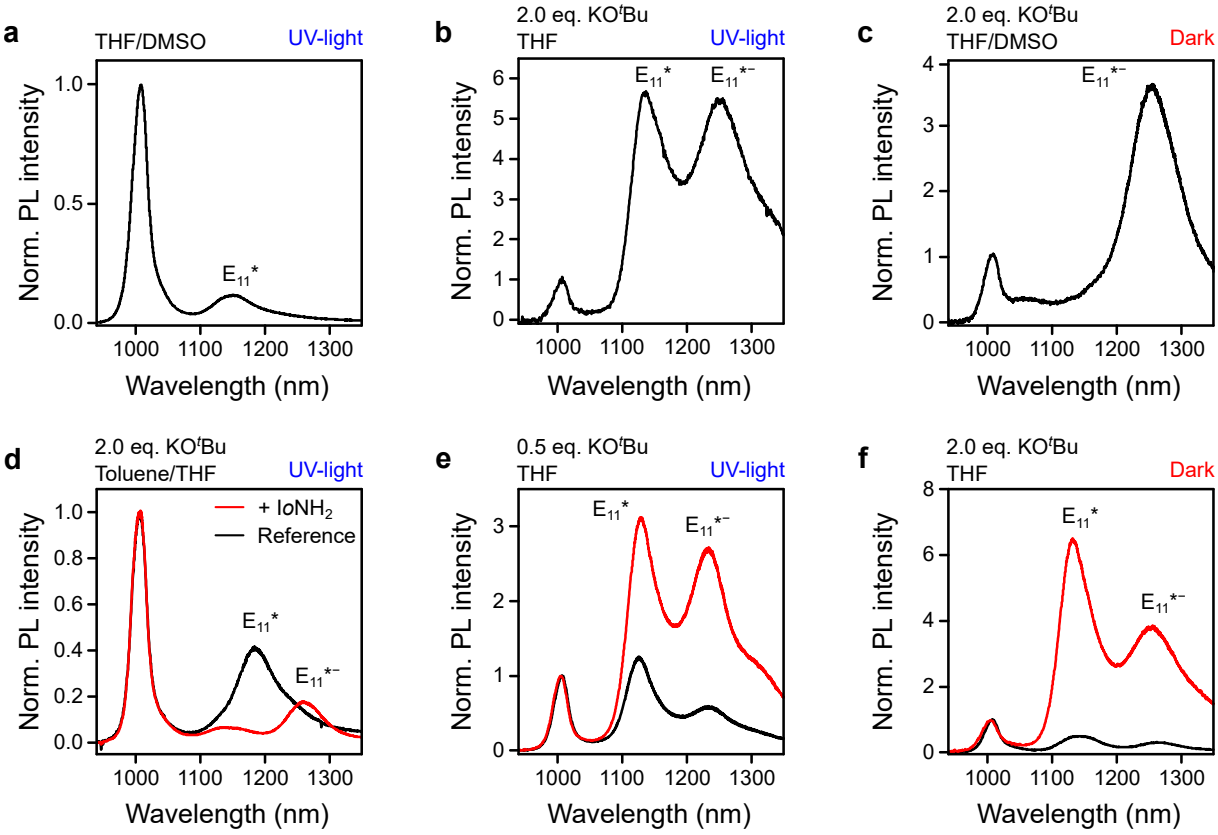

Figure 4.16: PL spectra of control and reference reactions (black) performed under various conditions with (6,5) SWNTs in THF and toluene with and without UV-light. Reactions in which 29.30 mM I*o*NH$_2$ was added are shown in red.

To explore this hypothesis further, functionalization with I*o*NH$_2$ in toluene in the dark was performed at varying reaction temperatures. A pronounced temperature dependence was noted, wherein the introduction of E_{11}^{*-} defects was enhanced at elevated temperatures and inhibited at 0 °C (Figure 4.17a). Consequently, the reaction path leading to E_{11}^{*-} defects exhibits the typical temperature dependence of a thermally activated reaction, resembling that of a nucleophilic addition reaction. The observed temperature dependence follows the Arrhenius equation when the rate constant is assumed to be proportional to the change in the E_{11}^{*-}/E_{11} PL area:

$$\ln\left(\frac{E_{11}^{*-}}{E_{11}}\right) = -\frac{E_A}{RT} + \ln A\,, \tag{4.6}$$

with A the pre-exponential factor, and R representing the universal gas constant. The activation energy (E_A) was derived from the Arrhenius plot presented in Figure 4.17b, yielding a value of 40 kJ mol^{-1}. For radical reaction pathways, a significantly lower temperature dependence and, hence, activation energy would be expected. Furthermore, when covalent functionalization is performed under inert conditions (*via* freeze-pump-thaw technique), an increase in E_{11}^{*-} emission was observed. This increase suggests that the oxidation of carbanion intermediates, such as the dimsyl anion, by oxygen inhibits the formation of E_{11}^{*-} defects. Zheng *et al.* previously reported a functionalization approach using aniline derivatives under UV-light illumination. In their case, the introduction of E_{11}^{*-} defects was only observed under inert conditions, and the

reaction was proposed to occur *via* reactive triplet intermediates.[160,188] Hence, the here observed increase in E_{11}^{*-} emission under inert conditions could indicate the presence of triplet intermediates. Yet this seems unlikely as E_{11}^{*-} emission occurs also under atmospheric conditions and no light irradiation was used.

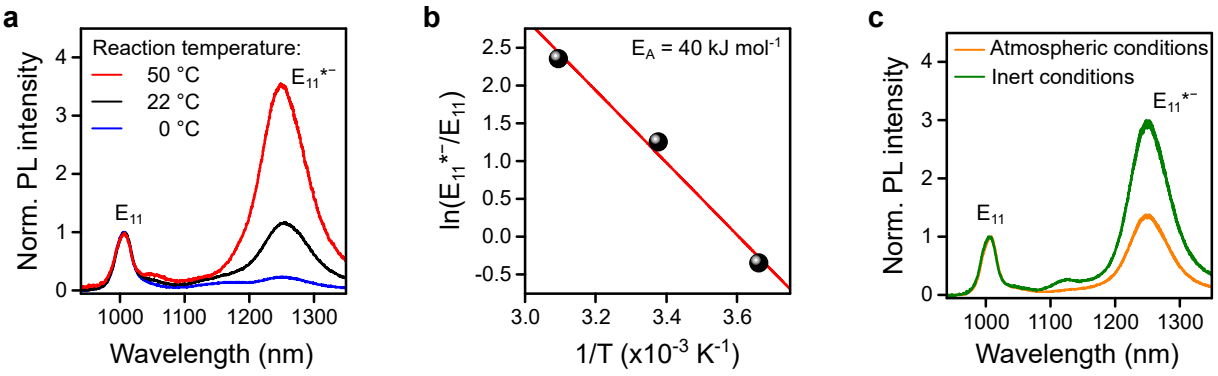

Figure 4.17: a) PL spectra of (6,5) SWNTs functionalized with I*o*NH_2 at various reaction temperatures in the dark. b) Computed Arrhenius plot with linear fit to the data (red line). E_{11} and E_{11}^{*-} represent integrated PL areas. c) Normalized PL spectra of (6,5) SWNTs functionalized under atmospheric conditions (orange) and under inert conditions (green). Prior to functionalization PFO-BPy-wrapped (6,5) SWNTs in toluene were degassed *via* the freeze-pump-thaw technique.

4.9.2 Functionalization mechanism & origin of selectivity

Overall, the collected results strongly suggest that E_{11}^* defects are associated with a radical reaction pathway, while E_{11}^{*-} defects are linked to a nucleophilic reaction path, both proceeding through the respective (halo) aniline derivative. Based on these findings, two plausible functionalization mechanisms can be formulated.

The E_{11}^* emission band is often attributed to the *ortho*$^{++}$ configuration, which is oriented in the circumferential direction for (6,5) SWNTs (see Figure 4.18, blue carbon atom). Consequently, radical addition is expected to occur on the carbon bond in the circumferential direction, leading to the formation of *ortho*$^{++}$ defects (E_{11}^*) upon saturation of the reactive radical SWNT intermediate. Radical formation in this reaction scheme is anticipated to occur upon electron transfer to the (halo) aniline and assisted by UV-light illumination in the presence of DMSO. The one-electron reduction of aniline is expected to favor the imine tautomer, and thus, addition presumably occurs *via* a carbon-centered aryl radical anion, resulting in C-C bond formation with the SWNT lattice followed by oxidative re-aromatization of the aniline.[298] In this case, covalent functionalization with the SWNT would occur in *meta* position to the amine group. The reason for the intrinsic preference for radicals to add to carbon bonds in the circumferential direction remains elusive, as C-C bonds in the axial direction were predicted to exhibit higher reactivity due to higher π-orbital misalignment. Results by Gifford *et al.* indicate that in radical reactions, addition at bonds along the SWNT axis only occurs when these C-C bonds are further activated (*e.g.* when other sp^3 defects are located in close proximity).[137]

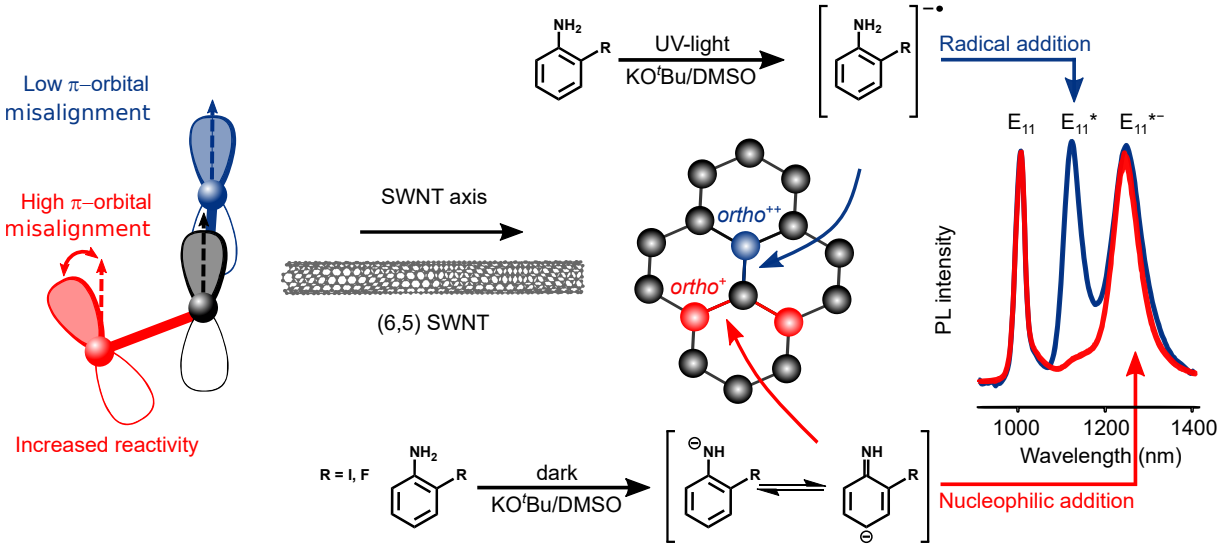

Figure 4.18: Proposed functionalization mechanism for the introduction of E_{11}* and E_{11}*$^-$ defects in (6,5) SWNTs. Functionalization with aniline derivatives proceeds *via* two reaction paths in the presence of KO^{t}Bu and DMSO. Under UV-light illumination, electron transfer to the aniline derivative leads to a radical anion that attacks the C-C bonds in the circumferential direction (blue bond). Upon oxidative re-aromatization of the aniline and saturation of the reactive SWNT intermediate, an *ortho*$^{++}$ configuration is formed, leading to E_{11}* emission (blue path). When the reaction is performed in the dark, deprotonation of the amine group by KO^{t}Bu/DMSO occurs, and charge delocalization takes place. Nucleophilic addition presumably occurs in the *para* position to the amine group, and a C-C bond is attacked with increased π-orbital misalignment (red bonds). Upon saturation of the negatively charged SWNT intermediate, the *ortho*$^+$ configuration is formed, leading to E_{11}*$^-$ emission (red path). Note that the deprotonated aniline species is in equilibrium with its protonated form.

Reactive nucleophilic intermediates are expected to possess lower reactivity than radical intermediates and may thus exhibit a higher intrinsic preference for carbon bonds with higher π-orbital misalignment. Hence, nucleophilic addition occurs on C-C bonds in the axial direction of the SWNT, resulting in *ortho*$^+$ (E_{11}*$^-$) defects after saturation of the reactive charged SWNT intermediate (*e.g.* by a proton from the solvent). Nucleophilic intermediates can be formed after deprotonation of the halo aniline (pK_a of 2-fluoroaniline in DMSO 28.7) by KO^{t}Bu (pK_a of KO^{t}Bu in DMSO 32.2).[299] Subsequent delocalization of the negative charge, a soft nucleophilic carbanion is formed.[300] Nucelophilic addition may preferably occur in the *para* position to the amine group due to steric interactions. However, the precise structure of the fragment attached to the SWNT remains unclear. The noted increase in E_{11}*$^-$ emission at elevated concentrations of the base can thus be attributed to a shift in favor of the deprotonated aniline species (see Figure 4.3b). Lastly, it should be mentioned that nucleophilic addition as well as electron transfer to the polyfluorene backbone of the wrapping polymer cannot be excluded.

Nucleophilic addition reactions with SWNTs have been known for decades but have never been utilized for the introduction of sp^3 defects at low concentrations.[132,301] Hence, it was previously unknown whether they have the ability to form luminescent defects. Very similar nucleophilic reaction mechanisms were reported for the functionalization of C_{60}-fullerenes. In that case, a KO^{t}Bu-promoted coupling approach was employed to achieve covalent functionalization with

indoles[302] and phenols.[303] Based on these reactions and the proposed mechanism, functionalization was conducted with a total of nine different reagents, including six aniline derivatives, 1,10-phenantroline-5-amine, thiophenol, 2-iodophenol, and indole (see Figure 4.19). In all cases, strong E_{11}^{*-} emission was observed, although the highest selectivity was obtained for aniline derivatives. Significant variations in reactivity and selectivity can be expected due to different structures of the carbanion intermediate. Thus, when the introduction of E_{11}^{*-} is hindered, other functionalization processes (*e.g.*, radical reactions) might become more kinetically favored. Nevertheless, the base-promoted coupling approach provides access to functionalized SWNTs with a large library of different functional groups that may be difficult to obtain *via* other functionalization approaches (*e.g.*, diazonium salt chemistry in the case of thiophenols).

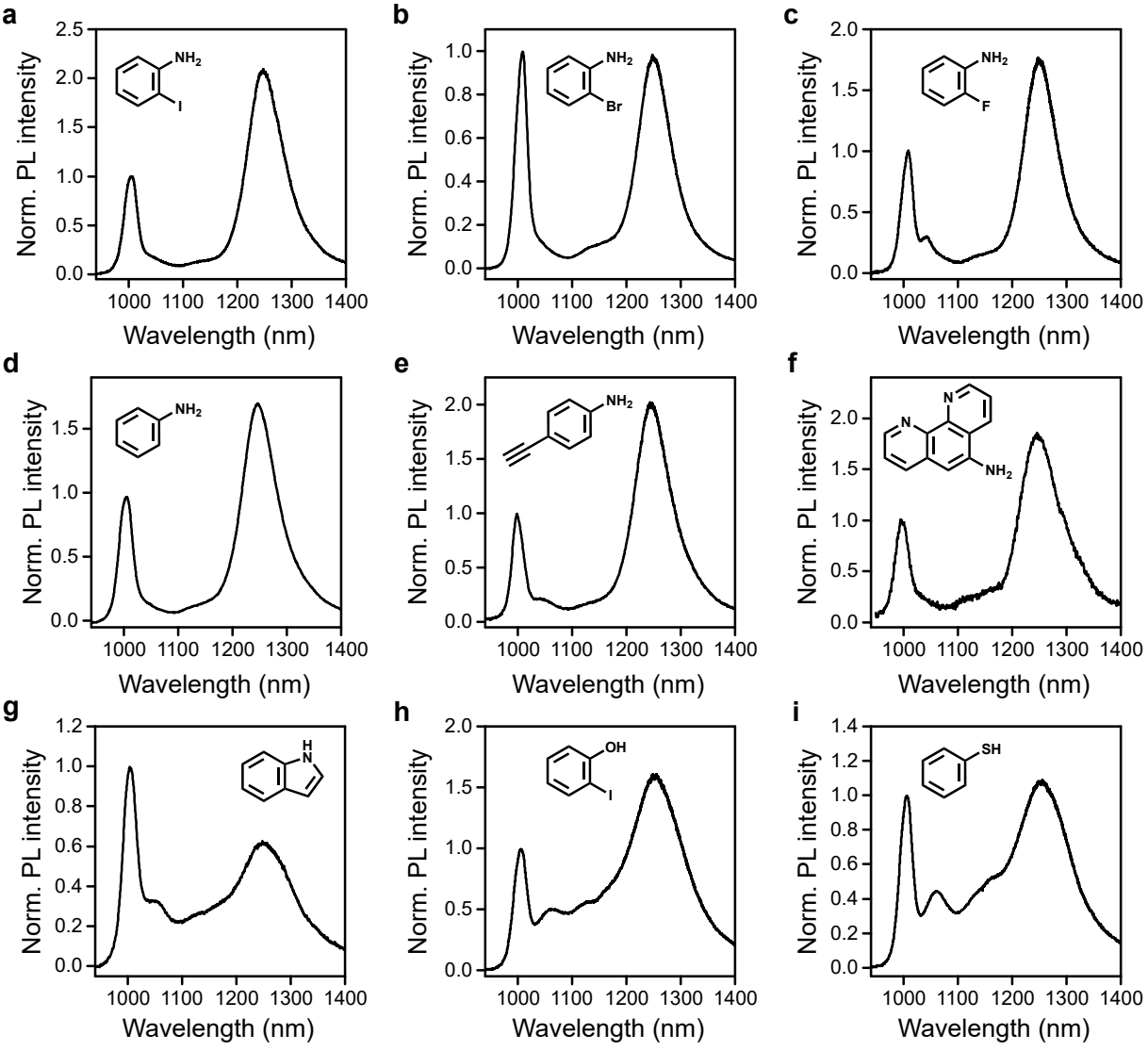

Figure 4.19: PL spectra of (6,5) SWNTs functionalized in the dark with 2.0 eq. KO^{t}Bu and addition of 29.30 mM I*o*NH_2 (a), 2-bromoaniline (b), 2-fluoroaniline (c), aniline (d), 4-ethynylaniline (e), 1,10-phenantroline-5-amine (f), indole (g), 2-iodophenol (h) and thiophenol (i). Note that for the functionalization with 4-ethynylaniline heating to 50 °C was necessary due to increased steric interactions. Functionalization is expected to occur in *ortho* position to the amine. Reaction times varied between 20-40 min.

4.10 Summary & conclusions

In summary, this Chapter presented the first functionalization protocol for the selective introduction of luminescent sp^3 defects with strongly red-shifted $E_{11}{}^{*-}$ emission in chiral small-diameter SWNTs. This facile method relies on a base-promoted coupling between primary aniline derivatives and polymer-wrapped SWNTs in organic solvents. The reaction can be performed in an open flask at room temperature and the final defect density is tuneable by adjusting the concentration of the base KO^{t}Bu or the reaction time. Red-shifted $E_{11}{}^{*-}$ emission is associated with a different sp^3 defect binding configuration on the SWNT lattice and occurs at 1250 nm for (6,5) SWNTs, with a PLQY of up to 5% for optimized defect densities.
Analysis of the temperature dependence of defect emission indicated that the previously observed mismatch between optical trap depth and thermal trap depth could be rationalized by considering an exciton trapping barrier. Based on this analysis, $E_{11}{}^{*-}$ defects were estimated to possess deep excitonic trapping potentials of ~135 meV. At this potential depth, depopulation *via* thermal detrapping was found to be greatly reduced. Instead, MPD was proposed as the dominant non-radiative decay mechanism for $E_{11}{}^{*-}$ defects in (6,5) SWNTs, leading to a reduced temperature dependence. MPD rates are expected to increase for even further red-shifted emission, and in agreement with this, a reduction in defect-state lifetime was found for longer emission wavelengths. This result also suggests that the introduction of even deeper optical traps will not further enhance the radiative efficiency from defect sites, and an optimal trap depth exists for which maximum PLQY is obtained (around 1280 nm for (6,5) SWNTs). This maximum is shifted towards shallower trap depths for chiralities with smaller band gaps, such as (7,5) SWNTs, indicating an optimal emission wavelength that is also chirality-dependent.
The deep trapping potentials and long fluorescence lifetimes ($\tau_{\text{A-avg.}}$ of 334 ps) of $E_{11}{}^{*-}$ defects in (6,5) SWNTs further enabled their application as near-infrared single-photon emitters at room temperature. Single-photon emission was demonstrated to occur with high purity (93%) at room temperature. This makes it one of the very few materials, besides nitrogen-vacancy centers in SiC, to exhibit single-photon emission in the near-infrared at room temperature with high purity.[152,304] High photon count rates ($6 \cdot 10^5$ photons s^{-1}) were achieved and in contrast to previously reported SWNT single-photon emitters with luminescent defects, defect emission originated from a smaller wavelength window. This represents a significant practical advancement, as the incorporation of functionalized SWNTs in optical cavities with finite spectral width will be required to achieve the necessary brightness (10^9 photons s^{-1}) and photon indistinguishability for application.[290,291,305]
The functionalized polymer-wrapped SWNTs exhibited excellent solution-processability, which might further facilitate device integration to achieve electrically-pumped single-photon emission. Their integration in light-emitting field-effect transistors was already demonstrated in collaboration with Zorn *et al.* and resulted in NIR electroluminescence, which was tuneable up to the telecommunication O-band through $E_{11}{}^{*-}$ functionalization of PFO-wrapped (7,5) SWNTs.[306] Further red-shifting of the defect emission into the C-band proved to be a challenging task due to the strong reduction in the optical trap depth of $E_{11}{}^{*-}$ defects with increasing SWNT diameter. While luminescent defects could be introduced even in large SWNT diameters, $E_{11}{}^{*-}$ emission

in polymer-wrapped (10,5) SWNTs only occurred at 1474 nm. To achieve emission ideally at 1550 nm, functionalization of larger-diameter SWNTs, such as PFO-wrapped (9,7) SWNTs, will be required.[84]

A large set of reference and control experiments confirmed that the high selectivity toward a defect binding configuration leading to E_{11}^{*-} emission was related to reactive nucleophilic species. In contrast to the commonly found (aryl) radical addition to the SWNT lattice, nucleophilic addition of an aryl carbanion was proposed, which shows a higher affinity towards addition to C-C bonds with larger π-orbital misalignment. As a result, nucleophilic addition may lead primarily to E_{11}^{*-} defects, while radical addition leads to E_{11}^{*} defects.

Covalent functionalization was performed with five different anilines, as well as with amino-phenantroline, thiophenol, and indole. Hence, this functionalization approach greatly expands and complements available methods, enabling the introduction of luminescent sp^3 defects with functional groups that are currently not easily accessible (*e.g.*, thiols in the case of diazonium salt chemistry). Specifically, covalent functionalization with ethynylanilines, amino-phenantrolines, and thiophenols could open new routes to achieve additional functionalities at the defect site.[17,145] However, further post-functionalization may be challenging due to limitations in the usable solvent system, steric hindrance of the wrapping polymer, and a lack of suitable techniques for reaction control so far.

Overall, the selective introduction of further red-shifted E_{11}^{*-} defects in polymer-wrapped SWNTs paves the way for integrating luminescent defects into electrically driven quantum-light sources with emission close to telecommunication bands.

CHAPTER 5

CREATING BRIGHT OXYGEN DEFECTS IN SINGLE-WALLED CARBON NANOTUBES

This Chapter describes a novel approach to create luminescent oxygen defects in aqueous-dispersed SWNTs and investigates the resulting optical properties with potential applications as biosensors or fluorescent probes within the second biological window.

The results of this Chapter are subject of a patent application (Settele *et al.* 2024. Method for preparing single-walled carbon nanotubes having luminescent oxygen defects. EP24158317.8). Parts of the data presented in this Chapter were collected by Florian Stammer under my supervision. Dr. Han Li and Dr. Benjamin S. Flavel (Institute of Nanotechnology, Karlsruhe Institute of Technology) provided ATPE-sorted (6,5) SWNTs. Simon R. Wald prepared ATPE-sorted (6,4), (8,3) & (7,5) SWNTs and Christian Scholz performed inductively coupled plasma optical emission spectroscopy (both Heidelberg University).

5.1 Introduction

As described in Section 2.2 and demonstrated in Chapter 4, the incorporation of luminescent sp^3 defects in semiconducting SWNTs is emerging as a potent strategy to enhance their optical properties. This includes the generation of a new red-shifted emission feature that can significantly increase the PLQY in dispersion and exhibit high single-photon purity at room temperature. While a high PLQY of up to 5% has been achieved with the functionalization method for polymer-wrapped (6,5) SWNTs presented in Chapter 4, its applicability is limited to organic solvents. The obtained bright defect-induced emission of (6,5) SWNTs is well within the second biological window (NIR-II, 1000-1350 nm) and therefore of particular interest for luminescence imaging in biomedical research. In this spectral region, light attenuation in biological tissues is greatly reduced, resulting in increased optical penetration depth (mm to cm), while interference from autofluorescence is minimized.[5,204]

Over the past decade, various synthetic methods have been developed to generate luminescent sp^3 defects in aqueous-dispersed SWNTs, with aryl diazonium salt chemistry being the most popular due to its synthetic flexibility.[186,187,307] However, the reported sample quality and thus brightness scatter widely, and so far reported up-scaling techniques require highly toxic solvents such as chlorosulfonic acid.[174] In addition to sp^3 defects, luminescent oxygen defects also have attracted considerable attention for *in vivo* imaging.[194,200] They were originally introduced by light-induced reaction with ozone.[11] For several years, it was thought that luminescent oxygen defects exhibit lower brightness due to a dark state that is energetically below the bright defect state.[146,196] However, Chiu *et al*. in 2016 and Lin *et al.* in 2019 showed that bright defect-state emission can be obtained upon reaction of SWNTs with polyunsaturated fatty acids or NaOCl under (UV-)light irradiation.[189,191] The latter approach was further improved by Eremin *et al.* by optimizing the intensity of UV-light illumination.[199] Thus, the main obstacle has been the efficient introduction of luminescent oxygen defects rather than their expected lower intrinsic brightness. To obtain luminescent oxygen defects, precise control over the reaction of reactive oxygen species (ROS) with the SWNT sidewall is required. Typically, ROS are generated through the photolysis of *e.g.* ozone or NaOCl.

One of the most important processes to generate ROS and a major cause of oxidative stress under physiological conditions is the so-called Fenton reaction.[308] The Fenton reaction describes the decomposition of hydrogen peroxide (H_2O_2) by Fe(II) ions and was discovered by H.J.H. Fenton in 1894.[309] In acidic media, a simplified mechanism as proposed by Haber and Weiss in 1932 is usually assumed, involving the oxidation of Fe(II) ions to Fe(III) ions to facilitate the decomposition of H_2O_2 into hydroxyl ions (OH^-) and hydroxyl radicals ($OH^\bullet$, see Figure 5.1, Reaction 1).[310–312] Since then, the name "Fenton reaction" has been used as a generic term, and related reactions involving other transition metals such as Cu(I) ions with peroxides have been called "Fenton-like reactions".[313]

Fe(II/III) salts in the presence of H_2O_2 have been employed in the past for the covalent functionalization of carbon nanotubes.[314,315] However, due to the harsh reaction conditions and the resulting excessive functionalization, the observation of potential luminescent defects was prevented. A potential way to perform covalent functionalization under controlled conditions could be the use of Cu(I) ions, which are expected to decompose H_2O_2 into $OH^\bullet$ analogous to the Fenton reaction (Figure 5.1, Reaction 2). In addition, the combination of Cu(II) salts with a reducing agent eliminates the need for large amounts of H_2O_2. In this Fenton-like reaction, the regeneration of the active Cu(I) species takes place through the reaction of Cu(II) ions with H_2O_2 or superoxide anions ($O_2^{-\bullet}$, Figure 5.1, Reaction 3 & 4), which are in equilibrium with their protonated form as hydroperoxyl radicals ($HOO^\bullet$, $pk_a(O_2^{-\bullet}) = 4.8$).[316] This regeneration cycle can be bypassed by adding a reducing agent such as L-ascorbate (Asc^-), which outcompetes the reduction of Cu(II) by $H_2O_2/O_2^{-\bullet}$ (Figure 5.1, Reaction 5). The formed monodehydroascorbic acid ($NaAsc^\bullet$) is expected to be further oxidized and finally hydrolyzed to 2,3-diketogulonic acid.[317] Lastly, due to the steady regeneration of Cu(I), small amounts of H_2O_2 are produced *in situ* by the stepwise reduction of dissolved oxygen (see Figure 5.1, Reaction 6+7). Hence, the combination of Cu(II) salts with a reducing agent such as L-ascorbate in the presence of dissolved oxygen is a promising tool to generate ROS under well-controlled conditions.

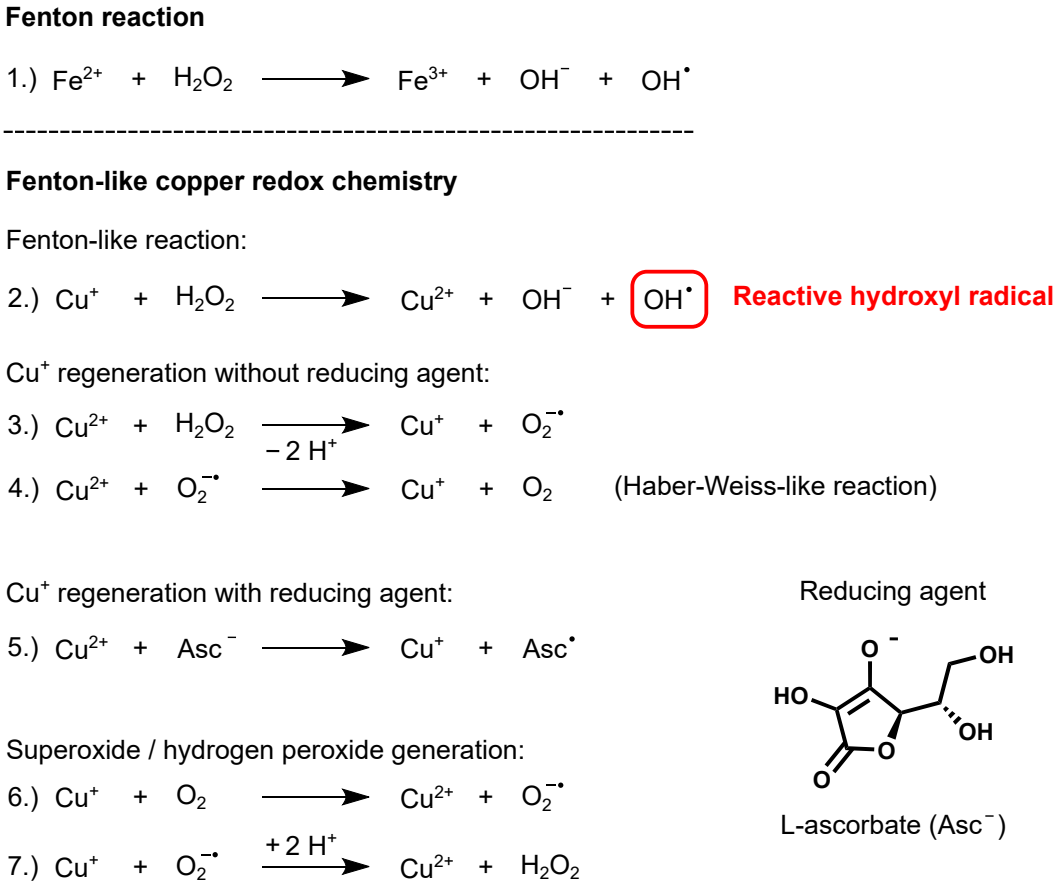

Figure 5.1: Schematic representation of the sequence of steps involved in the Fenton reaction and Fenton-like copper redox chemistry.

In this Chapter, a functionalization method is described that enables the scalable creation of luminescent oxygen defects into aqueous-dispersed SWNTs by utilizing ROS production *via* Fenton-like copper redox chemistry.

5.2 Covalent functionalization *via* Fenton-like reaction

To achieve covalent functionalization of the SWNT sidewall by ROS in aqueous dispersion, SDS-coated (6,5) SWNTs were chosen as a model system due to their high strain-induced reactivity and their sparse, disordered coating by SDS micelles.[78] SDS-coated (6,5) SWNTs were sorted from CoMoCAT raw material by aqueous two-phase extraction (ATPE) as described in Section 3.1.5.[43,257] The production of ROS is initiated by the addition of $CuSO_4(H_2O)_5$ (250 µM, hereafter referred to as $CuSO_4$) and the subsequent reduction of solvated Cu(II) by the addition of 12 equivalents (eq.) of sodium-L-ascorbate (12 mM, NaAsc, eq. with respect to $CuSO_4$). The reduction of Cu(II) to Cu(I) triggers several oxidation-reduction cycles in which dissolved oxygen is reduced to H_2O_2, while the Cu(I) catalyst is regenerated by an excess of NaAsc. Finally, the formed H_2O_2 decomposes in a Fenton-like reaction to OH^- and $OH^\bullet$. These highly reactive $OH^\bullet$ then undergo covalent functionalization of the SWNT sidewall (see Figure 5.2).

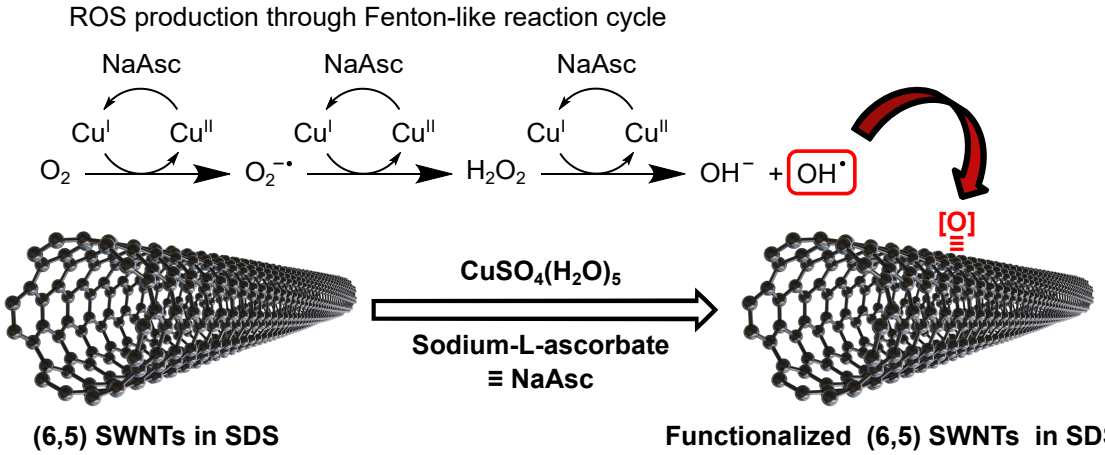

Figure 5.2: Schematic representation of the covalent functionalization of SDS-coated (6,5) SWNTs by reaction with ROS generated in Fenton-like reaction cycles. The formation of ROS is initiated by addition of $CuSO_4(H_2O)_5$ and sodium-L-ascorbate (NaAsc) and results in the creation of oxygen defects.

The progress of covalent functionalization of SDS-coated (6,5) SWNTs can be monitored by recording PL spectra upon E_{22} excitation at 570 nm as shown in Figure 5.3a. Within a few minutes after the addition of $CuSO_4$ and NaAsc, a new emission feature (E_{11}*) can be observed around 1105 nm, which is 115 nm (ΔE = 131 meV) red-shifted with respect to the original E_{11} emission. This E_{11}* emission increases strongly over the course of 2.8 h until it reaches a maximum PL intensity that is 3.2 × higher than the initial E_{11} intensity. Simultaneously, the E_{11} emission decreases steadily during the reaction time. After a reaction time of 2.8 h, the E_{11}* PL intensity decreases again until both emission features finally stabilize at a constant value after 14 h (see Figure 5.3b,c). The recorded PL spectra clearly indicate the formation of luminescent defects and can be rationalized by the localization of mobile E_{11} excitons at newly introduced defect sites from where they can emit as E_{11}* emission features. This funneling of mobile excitons to luminescent defect sites is reflected in the constant increase of the integrated E_{11}*/E_{11} PL emission ratio until no further change of the PL ratio can be observed after about 12 h of reaction time. This suggests that within 12 h, the entirety of added NaAsc is consumed and no further regeneration of the Cu(I) catalyst and thus no $OH^\bullet$ generation occurs. After long reaction times and thus high defect density, the efficient generation of mobile excitons is also reduced because the carbon lattice is highly damaged leading to a decrease in total PL intensity.
In addition to the formed E_{11}* emission, a second, further red-shifted emission feature occurs around 1240 nm (E_{11}*$^-$) and becomes significantly blue-shifted with increasing reaction time. Instead of a blueshift, an emerging third emission feature which appears at ~1200 nm (E_{11}**) could also explain the latter observation. These emission features will be discussed in more detail in Section 5.5. In the following sections the focus will be exclusively on the predominant E_{11}* emission feature. Note that the emission features described here are expected to originate from defect sites that are fundamentally different in their chemical structure (here oxygen defects, see Section 2.2.5) to the defects described in Chapter 4 (sp^3 defects).

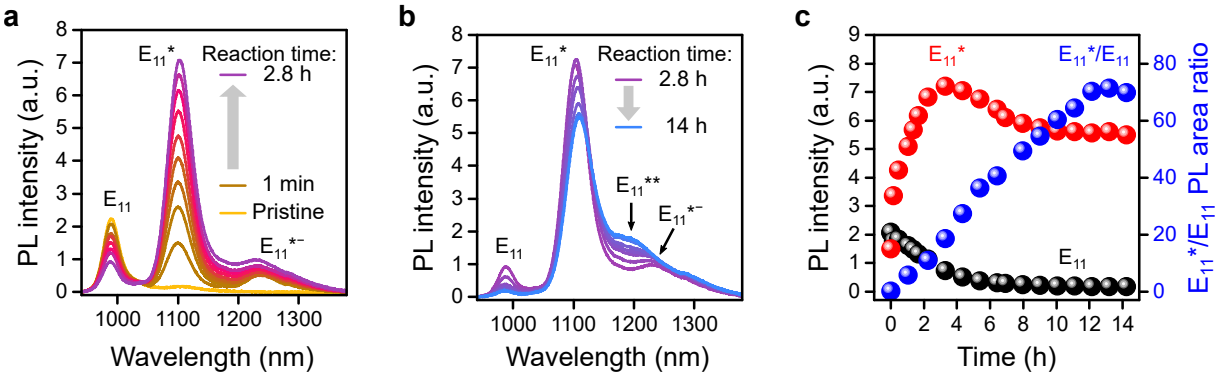

Figure 5.3: a) Evolution of the PL spectra of (6,5) SWNTs under E_{22} excitation after addition of 250 µM $CuSO_4$ and 3 mM NaAsc for reaction times between 1 min and 2.8 h, where a strong increase in E_{11}* PL intensity is observed. b) Recorded PL spectra with possible peak assignment for reaction times between 2.8 h and 14 h. A slow decrease increase in E_{11}* PL intensity is observed. c) Evolution of the absolute E_{11}* and E_{11} PL intensities as well as the E_{11}*/E_{11} PL area ratio. A constant value of the E_{11}*/E_{11} PL area ratio after 12 h indicates that the functionalization has stopped.

To confirm that the covalent functionalization is initiated by the reduction of Cu(II) species, reference experiments were performed (see Appendix B, Figure B.1). When NaAsc (3 mM) is added to SDS-coated (6,5) SWNTs, no significant change in the PL spectra can be observed over a period of 16 h. In this context, the here occurring thermal decomposition of NaAsc to a potentially reactive NaAsc$^{\bullet}$ should reflect its decomposition by reaction with Cu(II) in the Fenton-like reaction. When only $CuSO_4$ (250 µM) is added to SDS-coated (6,5) SWNTs, a slight copper-induced PL quenching is observed, as previously reported by Wulf *et al.* and described in detail in Chapter 6.[318] After successful functionalization, this quenching effect by residual Cu(II) species remains small and a negligible change in PL spectra can be observed upon addition of 1.4 mM of tetrasodium ethylenediaminetetraacetic acid (EDTA), a strong metal ion chelating ligand. However, due to the additional spectral overlap of the broad absorption band of solvated Cu(II) ions in the visible with the E_{22} transition of (6,5) SWNTs, Cu(II) ions were always removed by the addition of 1.4 mM EDTA followed by filtration in future experiments. Finally, the obtained functionalized (6,5) SWNTs were re-suspended in 1% (w/v) DOC to increase the stability of the dispersion.

5.3 Optimization of the functionalization process & optical properties of luminescent oxygen defects

Figure 5.3c clearly shows that the degree of functionalization must be controlled to obtain functionalized (6,5) SWNTs with maximum brightness. Two approaches can be taken depending on the desired application. When extremely high precision and only small sample quantities are required, the most practical approach is to control the defect density by quenching the reaction at the desired reaction time. This is done by first performing the reaction as shown in Figure 5.2 and monitoring the evolution of the PL spectra (see Figure 5.4a,b). When the desired absolute

PL intensity or E_{11}^*/E_{11} PL intensity ratio is reached, the reaction can be stopped by addition of DOC, which initiates surfactant transfer from SDS-coated (6,5) SWNTs to DOC-coated (6,5) SWNTs. After the surfactant transfer, the dense DOC coverage of the SWNT surface inhibits the reaction and no further change in the PL spectra can be observed.[15,76] This is best illustrated by following the E_{11}^*/E_{11} PL intensity ratio, which increases linearly with reaction time (black dots, Figure 5.4c) until surfactant transfer occurs and a constant PL intensity ratio can be observed for the remaining monitored time (red dots). Interestingly, the PL intensity ratio is reduced for DOC-coated functionalized (6,5) SWNTs, suggesting that the surfactant primarily affects the decay and diffusion dynamics of mobile E_{11} excitons (see inset in Figure 5.4b).

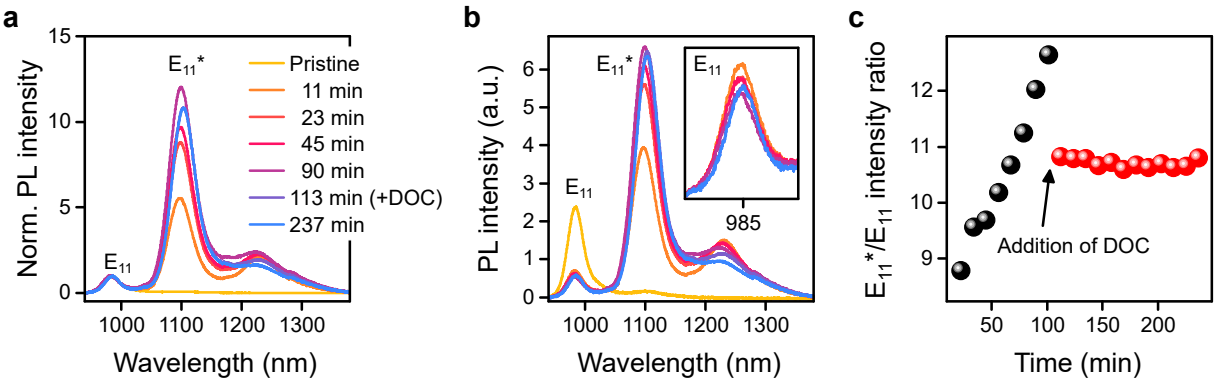

Figure 5.4: Control over the degree of functionalization can be achieved by *in situ* monitoring of the PL spectra upon E_{22} excitation and stopping the reaction by addition of DOC. Normalized (a) and absolute (b) PL spectra measured at different reaction times before and after addition of DOC after 113 min. The inset shows the change in the E_{11} PL emission and shows that the E_{11} emission increases slightly with the addition of DOC. c) E_{11}^*/E_{11} PL intensity ratios extracted from the PL spectra measured before (black dots) and after the addition of DOC (red dots).

A more practical strategy for controlling the density of introduced luminescent defects is to vary the reagent concentration. In this case no additional optical SWNT excitation will take place during the functionalization process. Figure 5.5a shows normalized PL spectra of SDS-coated (6,5) SWNTs after functionalization for 16 h in the absence of light at different reagent concentrations. Note that the reagent concentration refers to the concentration of added $CuSO_4$, while the NaAsc concentration (12 eq.) was increased accordingly. Clearly, the E_{11}^*/E_{11} PL ratios increase with increasing $CuSO_4$ (and NaAsc) reagent concentrations, and variation of the reagent concentrations enables precise tuning of the defect density. This is in agreement with the absorption spectra, where besides the pronounced E_{11} absorption at ~988 nm originating from intrinsic band-edge excitons, a red-shifted absorption band appears with increasing reagent concentration. This new absorption band is assigned to the absorption of E_{11}^* defect states due to the linear correlation of the integrated E_{11}^*/E_{11} absorption area ratios with the reagent concentration. Interestingly, as observed by Berger *et al.* for sp^3 defects, a very small E_{11}^* Stokes shift of about 10 meV can be extracted. This indicates that luminescent oxygen defects, similar to sp^3 defects, create a substantial deformation of the SWNT ground state structure at the defect site and do not show a large vibrational reorganization of the nanotube geometry upon exciton trapping, as previously suggested by Kim *et al.*[146]

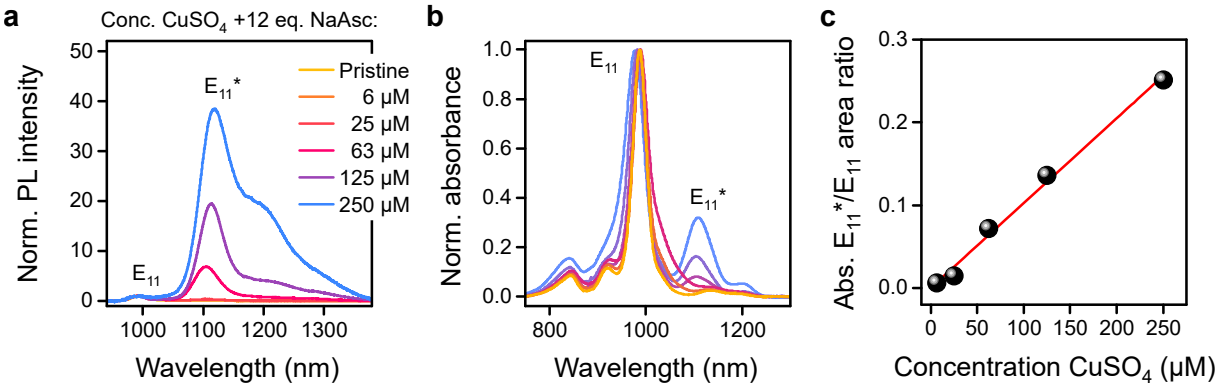

Figure 5.5: a) Normalized PL spectra of DOC-coated (6,5) SWNTs that were previously functionalized with different concentrations of $CuSO_4$ and 12 eq. of NaAsc in the dark. b) Corresponding normalized absorption spectra. c) Extracted E_{11}^*/E_{11} absorption area ratios as a function of the concentration of $CuSO_4$. The red line is a linear fit to the data.

To confirm that the observed E_{11}^* PL emission and absorption are correlated to structural defects in the sp^2-hybridized SWNT lattice, Raman spectra were recorded under near-resonance excitation and are shown in Figure 5.6a. A continuous relative increase in the D mode and thus the D/G^+ area ratio is observed, which has been used in the past to qualitatively and quantitatively determine the defect density in SWNTs (see Section 3.6.2). In agreement with the recorded absorption spectra, again a linear correlation with the reagent concentration can be seen in Figure 5.6b.

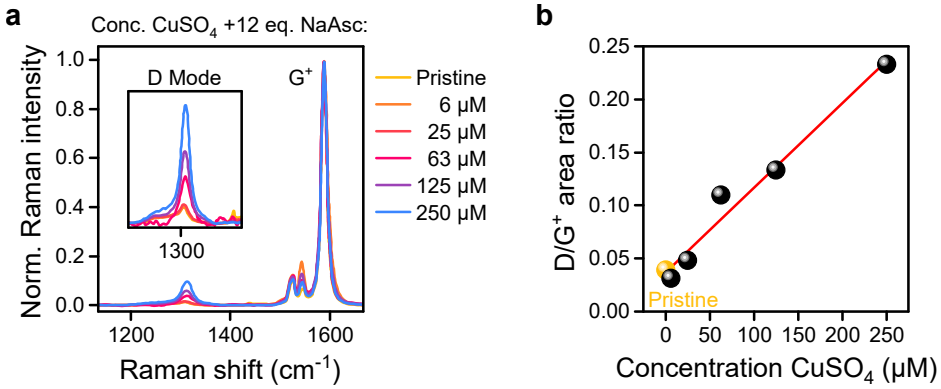

Figure 5.6: a) Normalized Raman spectra with a zoom-in on the defect-related D mode (inset) of DOC-coated (6,5) SWNTs that were previously functionalized at different concentrations of $CuSO_4$ and 12 eq. of NaAsc in the dark. b) Extracted Raman D/G^+ area ratio as a function of the concentration of $CuSO_4$. The red line is a linear fit to the data.

In the *in situ* monitored PL spectra in Figure 5.3, a strong brightening effect at optimum defect density can be observed, where the E_{11}^* PL intensity is about 3.2 × higher than the initial E_{11} PL intensity. This relative increase in E_{11}^* PL intensity represents a significant improvement over previous reports on luminescent oxygen defects and rivals the PL enhancements observed for sp^3 defects.[15,189,199] However, it is important to note that this brightening effect should not be interpreted as the actual brightness of the sample. The observed brightening upon functionalization depends highly on the used reference system and surfactant (see Figure 5.4) as well as the

quality of the starting material, *e.g.* tube length.[141] The most practical metric for determining the brightness of a material is the PLQY, as defined in Section 3.5.3. To determine the PLQY, SDS-coated (6,5) SWNTs were functionalized at varying concentrations of $CuSO_4$/NaAsc and processed as described above. From the absolute PL measurement of the obtained functionalized DOC-coated (6,5) SWNTs, the PLQY was determined and plotted as a function of defect density given by the change in the D/G$^+$ area ratio (ΔD/G$^+$) in Figure 5.7a. Compared to DOC-coated (6,5) SWNTs (average PLQY ~0.64%, SWNT length ~500 nm), a strong brightening effect is observed for functionalized DOC-coated (6,5) SWNTs with a PLQY up to 3.6% at optimal defect density. This ~5.6-fold increase in PLQY is in good agreement with the ~6-fold increase in integrated PL area observed upon functionalization in SDS. Importantly, the determined PLQY was obtained for SWNTs dispersed in H_2O in contrast to the commonly used D_2O, where the non-radiative decay of defect-state emission by electronic-to-vibrational energy transfer (EVET) is strongly suppressed.[139] The pronounced enhancement in brightness can be visualized by NIR-PL images of said dispersions when placed in Eppendorf cups (Figure 5.7b).

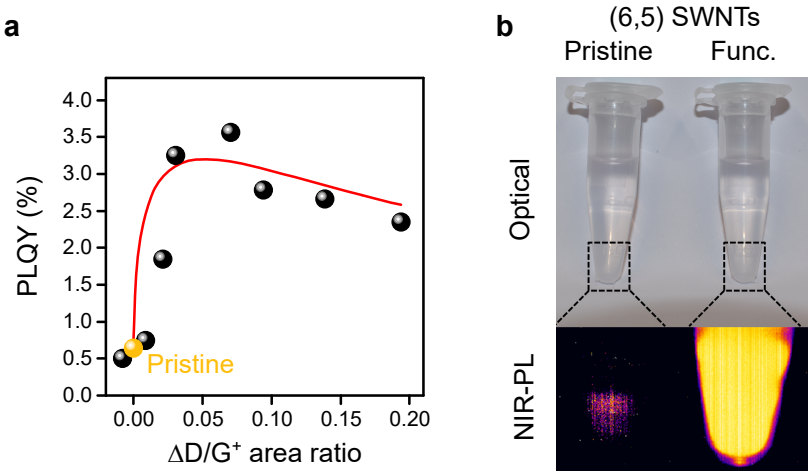

Figure 5.7: a) PLQYs determined from absolute PL measurements in an integrating sphere of functionalized DOC-coated (6,5) SWNTs *versus* the integrated ΔD/G$^+$ area ratio as a metric for the defect density (red line as guide to the eye). The PLQY of pristine DOC-coated (6,5) SWNTs (yellow symbol) represents an average value obtained from multiple measurements. b) White-light images (top) and NIR-PL images (950-1600 nm) of dispersions of pristine (left) and functionalized (right) DOC-coated (6,5) SWNTs. NIR-PL images were obtained by continuous wave excitation at 785 nm under identical excitation conditions and SWNT concentrations. The indicated sections represent the areas shown in the NIR-PL images.

Another typical feature of luminescent defects is their long defect-state lifetime, which is about two orders of magnitude longer than the short E_{11} lifetime (a few ps). Figure 5.8a shows the time-resolved defect-state emission recorded *via* TCSPC at a emission wavelength of 1105 nm and fitted with a biexponential reconvolution fit.

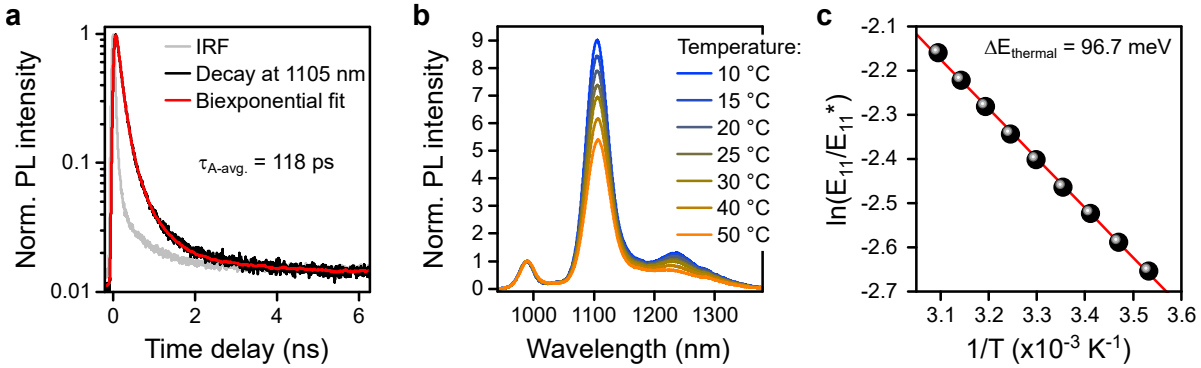

Figure 5.8: Determination of defect-state lifetime and temperature-dependent PL measurements of functionalized DOC-coated (6,5) SWNTs. a) PL decay trace (black) recorded for the spectrally selected E_{11}* emission around 1105 nm. The red line represents a biexponential fit that takes into account the instrument response function (IRF, grey). b) Recorded temperature-dependent normalized PL spectra. c) Computed Van't Hoff plot for the E_{11}* emission band and linear fit to the data (red line). E_{11} and E_{11}* represent integrated PL areas.

The extracted amplitude-averaged PL lifetime ($\tau_{A\text{-avg.}}$) was determined to be 118 ps and is in agreement with previous reports on luminescent oxygen and sp^3 defects.[139] In this context, the aforementioned efficient EVET is expected to be the primary cause for the observed short defect-state lifetime compared to measured and reported values for defect-state emission in *e.g.* D_2O or toluene as seen in Chapter 4.

Table 5.1: Extracted PL lifetime components (τ_{long}, τ_{short}) with the corresponding normalized amplitudes (A_{long}, A_{short}) and the amplitude-averaged PL lifetime ($\tau_{A\text{-avg.}}$).

Sample	τ_{long}	τ_{short}	A_{long}	A_{short}	$\tau_{A\text{-avg.}}$
DOC-coated (6,5) SWNTs functionalized at 63 µM $CuSO_4$ (measured at 1105 nm)	220 ps	86 ps	0.24	0.76	118 ps

Besides EVET, another dominant non-radiative decay pathway for trapped excitons represents reversible thermal trapping, as discussed in detail in Section 4.4. When temperature-dependent PL spectra (see Figure 5.8b) were recorded for (6,5) SWNTs functionalized *via* a Fenton-like reaction, a steep decrease in relative E_{11}* emission can be observed when normalized and thus corrected for the temperature dependence of mobile E_{11} excitons. By construction of the corresponding Van't Hoff plot (Figure 5.8c) a thermal trap depth ($\Delta E_{thermal}$) of 96.7 meV can be extracted which is higher than the value obtained by Ghosh *et al.* (61 meV) and Kim *et al.* (24 meV) for oxygen defects.[11,146] Judging from the reported E_{11}*/E_{11} PL ratios, this discrepancy can be rationalized by an increase in defect density and might be correlated to an increase in a trapping barrier (see discussion Section 4.4). Nevertheless, as the extracted $\Delta E_{thermal}$ is significantly below the optical trap depth ($\Delta E_{optical}$ = 131 meV) and small Stokes shift were observed (see Figure 5.5b) similar to sp^3 defects, significant ground state deformation at the defect site of oxygen defects can be expected.

5.4 Functionalization mechanism

The proposed generation of ROS by Fenton-like copper redox chemistry has important implications for the overall functionalization process and will be investigated in the following. To gain more comprehensive insights into potential changes in the PL spectra, no surfactant transfer from SDS to DOC was performed in these studies. According to Reaction 6 in Figure 5.1, the production of ROS is initiated by the reduction of dissolved oxygen. To test this, the reaction mixture was purged with argon, which greatly reduces the oxygen content. After the addition of $CuSO_4$ (63 µM) and NaAsc (12 eq.), no change in the PL spectra was observed after 16 h (see Figure 5.9a), indicating that no functionalization occurred. This experiment corroborates that covalent functionalization is performed by ROS and suggests that the functionalization process can be controlled by modulating the ROS production. Hence, the degree of functionalization, expressed by the E_{11}^*/E_{11} PL ratio, is expected to show a close correlation with the amount of generated ROS species. Whether the reactive species responsible for the covalent functionalization is actually $OH^\bullet$ remains unclear, but for simplicity this assumption will be made here. The formation of $OH^\bullet$ could be confirmed in the future by adding a spin trap such as 5,5-dimethyl-1-pyrroline *N*-oxide (DMPO).[319] The formed spin adduct could then be detected by electron paramagnetic resonance (EPR) spectroscopy.

The number of $OH^\bullet$ formed in the reaction mixture should correlate strongly with the absolute number of reduction cycles of the Cu(II) catalyst. First, this number was varied by changing the amount of the reducing agent NaAsc at an otherwise constant $CuSO_4$ concentration, which results in an increase in the turn over number (TON) of the Cu(II) catalyst. As shown in Figure 5.9b, no functionalization occurs at low concentrations of NaAsc (3 eq.) with respect to $CuSO_4$, while a high degree of functionalization is observed at high concentrations of NaAsc (24 eq.).

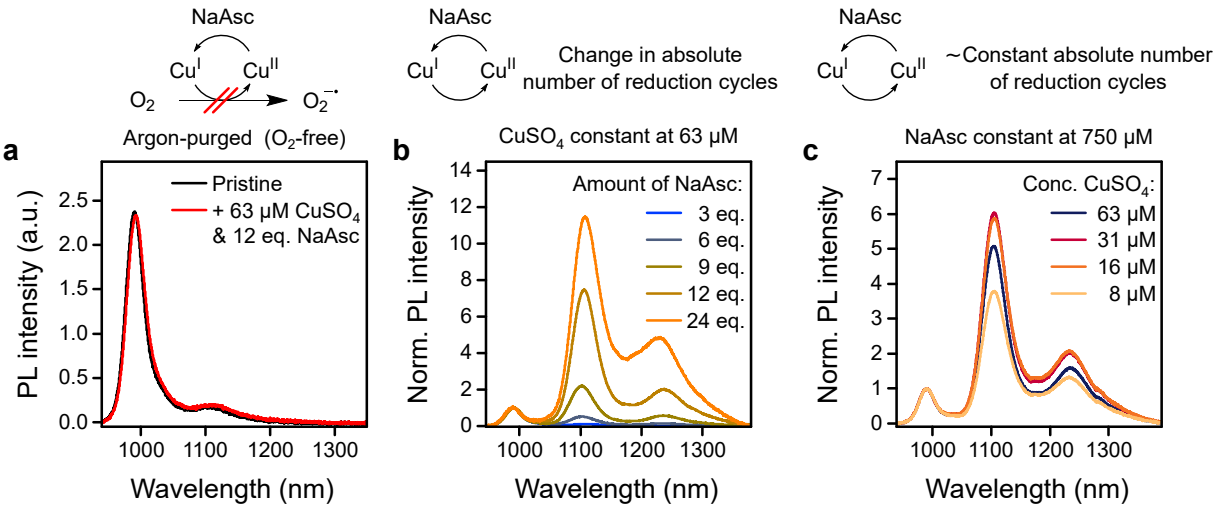

Figure 5.9: a) PL spectra of an argon-purged dispersion of SDS-coated (6,5) SWNTs before and after addition of 63 µM $CuSO_4$ and 12 eq. NaAsc. b) Normalized PL spectra of SDS-coated (6,5) SWNTs after functionalization at a fixed $CuSO_4$ concentration of 63 µM $CuSO_4$ and different concentrations of NaAsc (denoted as eq. with respect to $CuSO_4$). c) Normalized PL spectra of SDS-coated (6,5) SWNTs at a constant NaAsc concentration of 750 µM and varying $CuSO_4$ concentration. Reactions were conducted in the dark, and PL spectra were recorded after ~16 h.

This strong correlation with the absolute number of reduction cycles can also be used to significantly reduce the amount of $CuSO_4$, which could greatly facilitate the removal of copper species after functionalization. When the amount of $CuSO_4$ is reduced while the concentration of NaAsc is kept constant (*e.g.* 750 µM), the total number of generated ROS is expected to remain constant. This is reflected in the approximately equal E_{11}*/E_{11} PL ratio observed in Figure 5.9c. However, this correlation is only expected to be true for high NaAsc/$CuSO_4$ ratios (>12) as shown in Figure 5.9b. In addition, the reduction in $CuSO_4$ concentration is limited because Cu(I) ions partially disproportionate to Cu(II) and inactive Cu(0) species. With decreasing concentrations of Cu(II), the TON of the Cu(I) catalyst increases and thus the probability of disproportionation. This results in a decrease in reactivity for $CuSO_4$ concentrations below 16 µM. Consequently, under the chosen conditions, the $CuSO_4$ concentration could be effectively reduced to 16 µM without loss of reactivity. This high flexibility of the functionalization process may prove particularly advantageous when covalent functionalization is performed at high SWNT concentrations, where high concentrations of $CuSO_4$ and thus the potential production of colloidal copper should be avoided.

The Fenton-like reaction of Cu(I) species with H_2O_2 is expected to show a strong dependence on the pH of the reaction mixture.[308] To investigate this, covalent functionalization was performed at the same reagent concentrations but at varying pH. Recorded PL spectra after 16 h of reaction time are shown in Figure 5.10a. Surprisingly, no significant difference in the PL spectra was observed when functionalization was performed at pH 4.8 (standard conditions) or pH 8. However, a decrease in reactivity was observed at a higher pH of 11.1. This was probably due to the precipitation of insoluble $Cu(OH)_2$ and thus represents an upper limit of the pH at which functionalization should be performed.

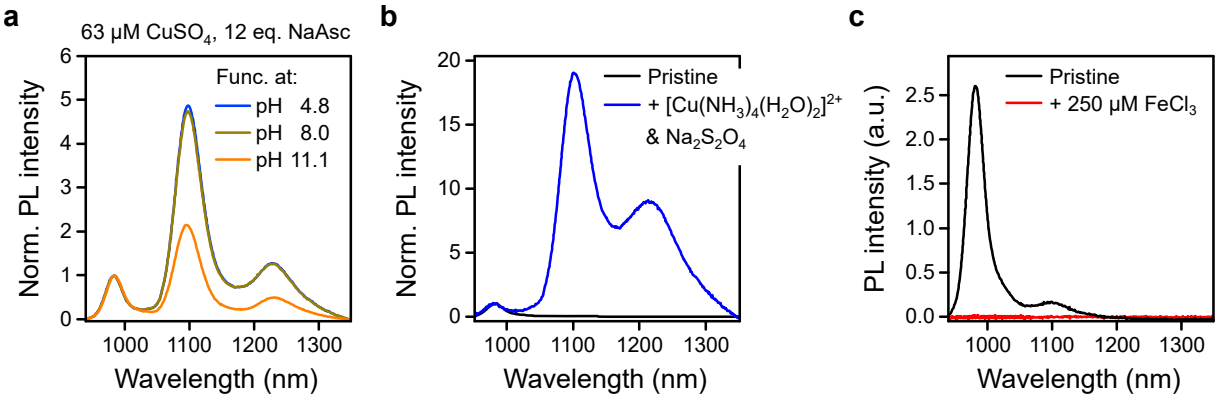

Figure 5.10: a) Normalized PL spectra of SDS-coated (6,5) SWNTs after covalent functionalization *via* Fenton-like reaction at varying pH values. b) Normalized PL spectra of SDS-coated (6,5) SWNTs before and after functionalization with 63 µM $CuSO_4$, which was pre-treated with an excess ammonia and addition of 12 eq. $Na_2S_2O_4$. c) PL spectra of SDS-coated (6,5) SWNTs recorded shortly before and after addition of 250 µM $FeCl_3$.

So far, only $CuSO_4$ and NaAsc have been utilized as Cu(II) precursor and reducing agent, respectively. In principle, however, this approach should be transferable to other combinations of Cu(II) precursors and reducing agents. To test this, tetraamine copper(II) ions were generated by pre-treating $CuSO_4$ with excess ammonia and reduced with sodium dithionite ($Na_2S_2O_4$, 12 eq.). The excess of ammonia serves two purposes. First, it prevents the disproportionation of $Na_2S_2O_4$, and second, it hinders the formation of insoluble $Cu(OH)_2$. Strong defect-induced emission bands were observed after 16 h of reaction in the dark without significant deviation in peak position or shape compared to the $CuSO_4$/NaAsc catalyst system. This indicates that the actual functionalization step by $OH^\bullet$ is independent from its respective generation.
In a next step, the original Fenton reaction was tested using Fe(II/III) salts. However, the use of Fe(III) salts was found to be unsuitable for covalent functionalization with the goal of modulating the optical properties of SWNTs. Strong PL quenching is observed as seen in Figure 5.10c which presumably occurs due to strong *p*-doping of the SWNT by Fe(III).[320] This is also expected to occur when Fe(II) salts are used in combination with excess H_2O_2. However, other metal salts that do not dope the SWNTs could be used in principle. For example, Co(II) salts in combination with NaAsc as reducing agent and H_2O_2 show efficient generation of reactive $OH^\bullet$ as reported by Verma *et al*.[321]

From the investigations performed so far, it is clear that the reaction of, most likely, $OH^\bullet$ with SWNTs leads to the formation of luminescent defects. In this context, the presence of oxygen defects has been assumed, but their formation and chemical structure have not been discussed. As shown in Section 2.2.5, the $E_{11}{}^*$ emission is often associated with a stable ether-d configuration (d-bonds are perpendicular to the SWNT axis) based on TD-DFT calculations.[192] The predicted $\Delta E_{optical}$ (135 meV) for this ether-d configuration agrees very well with the here observed value of 131 meV for the $E_{11}{}^*$ emission band and with previous studies reporting luminescent oxygen defects.[11] In addition, a further red-shifted emission band around 1240 nm ($E_{11}{}^{*-}$) is regularly observed and typically attributed to an epoxide-l configuration (l-bonds are parallel to the SWNT axis).[192] However, this defect species has rarely been observed as a distinct feature in SWNTs that were functionalized in dispersion, due to its expected lower thermodynamic stability.[189,193] Based on this assignment and additional analogy to the atmospheric oxidation of benzene or toluene, the following plausible reaction mechanism can be formulated.[322,323]
In the atmospheric oxidation of benzene or toluene, the first step was postulated to be the reaction of the $OH^\bullet$ with the aromatic compound and subsequent reaction with oxygen. Under the release of $HOO^\bullet$, the corresponding epoxide is formed, which is in equilibrium with its valence isomer, (methyl)oxepine. This reaction mechanism can be transferred to the creation of oxygen defects in SWNTs as sketched in Figure 5.11.

Depending on the position of the initial radical addition of $OH^{\bullet}$ and subsequent oxidation, epoxide-d or epoxide-l configurations are obtained. However, the stabilities of these epoxide configurations are fundamentally different. Due to the high strain induced by the curvature of the SWNT, the epoxide-d configuration is highly unstable and quickly transitions to an ether-d configuration,[189,193] giving rise to the observed E_{11}^* emission. In contrast, the rearrangement of epoxide-l configurations is energetically unfavorable and a potential ether-l configuration has a lower binding energy ($\Delta E = 0.94\,eV$). As a result, E_{11}^{*-} emission is obtained.[192]

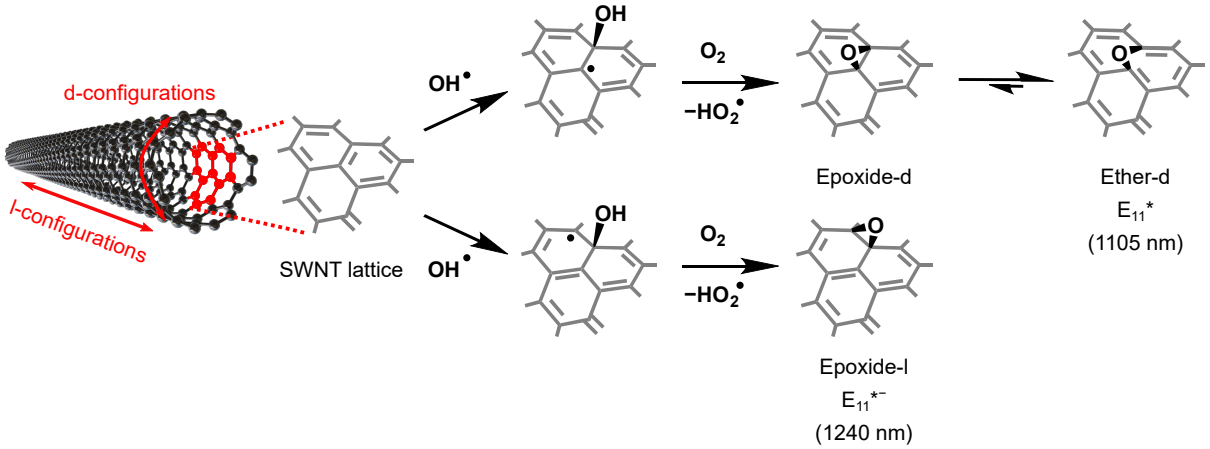

Figure 5.11: Proposed functionalization mechanism for the formation of luminescent E_{11}^* (top reaction path) and E_{11}^{*-} (bottom reaction path) oxygen defects. After initial radical addition of $OH^{\bullet}$, oxidation occurs at the defect sites which leads to the formation of the expoxide-l/d configurations. The epoxide-d rearranges to the stable ether-d configuration which leads to E_{11}^* emission. The epoxide-l shows higher thermodynamic stability and leads to E_{11}^{*-} emission.

5.5 Light-induced effects on functionalized SWNTs

Throughout this study, a striking difference in the contribution of E_{11}^{*-} emission can be observed between samples exposed to light for prolonged periods of time (*e.g.*, E_{22} excitation as shown in Figure 5.3) and those kept in the dark (see Figure 5.9b,c). To investigate this, a series of test reactions were performed in which the reaction mixture was divided into three parts after the addition of $CuSO_4$ and NaAsc to SDS-coated (6,5) SWNTs. Two parts were exposed to E_{22} (570 nm) excitation or UV-light (365 nm) and one part was kept in the dark. The PL spectra recorded after 1 h are displayed in Figure 5.12a and show significant differences in the absolute PL intensity as well as the E_{11}^{*-} contribution. In particular, the E_{11}^{*-} contribution was significantly higher when the covalent functionalization was performed in the absence of light. Simultaneously, the absolute PL intensity of E_{11}^* and/or E_{11} emission was found to be increased when covalent functionalization was performed under light irradiation. This finding would suggest two different reaction pathways and that covalent functionalization should preferably be performed under SWNT (E_{22}) excitation. However, absolute PL measurements show that the PLQYs obtained are similar to previously determined values when functionalization was performed in the dark (see Figure 5.12b), suggesting that the observed effects are not permanent and may change during the workup process or measurement.

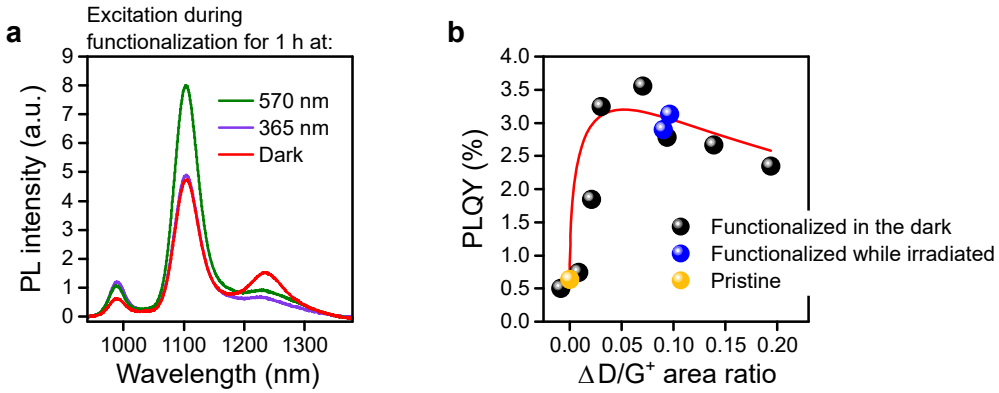

Figure 5.12: a) Covalent functionalization of SDS-coated (6,5) SWNTs at identical reagent concentrations with a 1 h reaction time under E_{22} excitation (570 nm, green), UV-light irradiation (365 nm, purple) and under exclusion of light (dark, red). b) Determined PLQY plotted *versus* the $\Delta D/G^+$ area ratio as metric of the defect density. Previously obtained data points from functionalization in the dark are represented by black dots, data points obtained for functionalization under E_{22} excitation are indicated by blue dots. Red line is a guide to the eye.

To investigate the effect of light irradiation further, covalent functionalization was first performed in the dark, followed by UV-light irradiation. To prevent further functionalization, DOC and EDTA were added to the dispersion prior to irradiation. Surprisingly, a strong increase in E_{11} and E_{11}^* PL intensity was observed upon stepwise UV irradiation, while the E_{11}^{*-} emission completely disappeared for irradiation times >60 min (see Figure 5.13a). This effect was found to be purely light-induced, as no significant change in PL spectra was observed upon heating to 80 °C for 0.5 h in the dark (see Appendix B, Figure B.2). Further light-induced covalent functionalization or detachment of oxygen defects can be ruled out by Raman measurements, where no change of the D mode was observed upon UV irradiation as shown in Figure 5.13b.
A more conclusive picture can be drawn by recording absorption spectra, where a small but significant increase in the E_{11}^* absorption and a simultaneous decrease in the E_{11}^{*-} absorption band was observed (see Figure 5.13c,d). This leads to the conclusion that the epoxide-l (E_{11}^{*-}) defects can partially rearrange to more stable ether-d (E_{11}^*) defects ($\Delta E = 24\,\text{kcal mol}^{-1}$) upon optical excitation of the SWNT,[189] as schematically shown in Figure 5.13e. Most likely, this rearrangement occurs *via* formation of the unstable epoxide-d configuration as shown in Figure 5.11 and is accelerated in acidic media by protonation of the epoxide group.
In light of this observation, it can be assumed that the emission band at ~1200 nm, as observed in Figures 5.3 and 5.5, more likely originates from a different defect species and not from E_{11}^{*-} defects. Espinoza suggested that this defect species could be adjacent di-ether-d defects (E_{11}^{**}),[324] which seems reasonable as the emission band at ~1200 nm is only observed at very high defect densities.
Finally, all of the aforementioned effects that occur under UV-light irradiation can be observed already upon exposure to daylight, *e.g.* during the workup process, and complete reorganization of the defect configurations can be observed after 4 days (see Figure 5.13f). Thus, similar PL properties were obtained for functionalized (6,5) SWNTs even if they were initially functionalized in the dark.

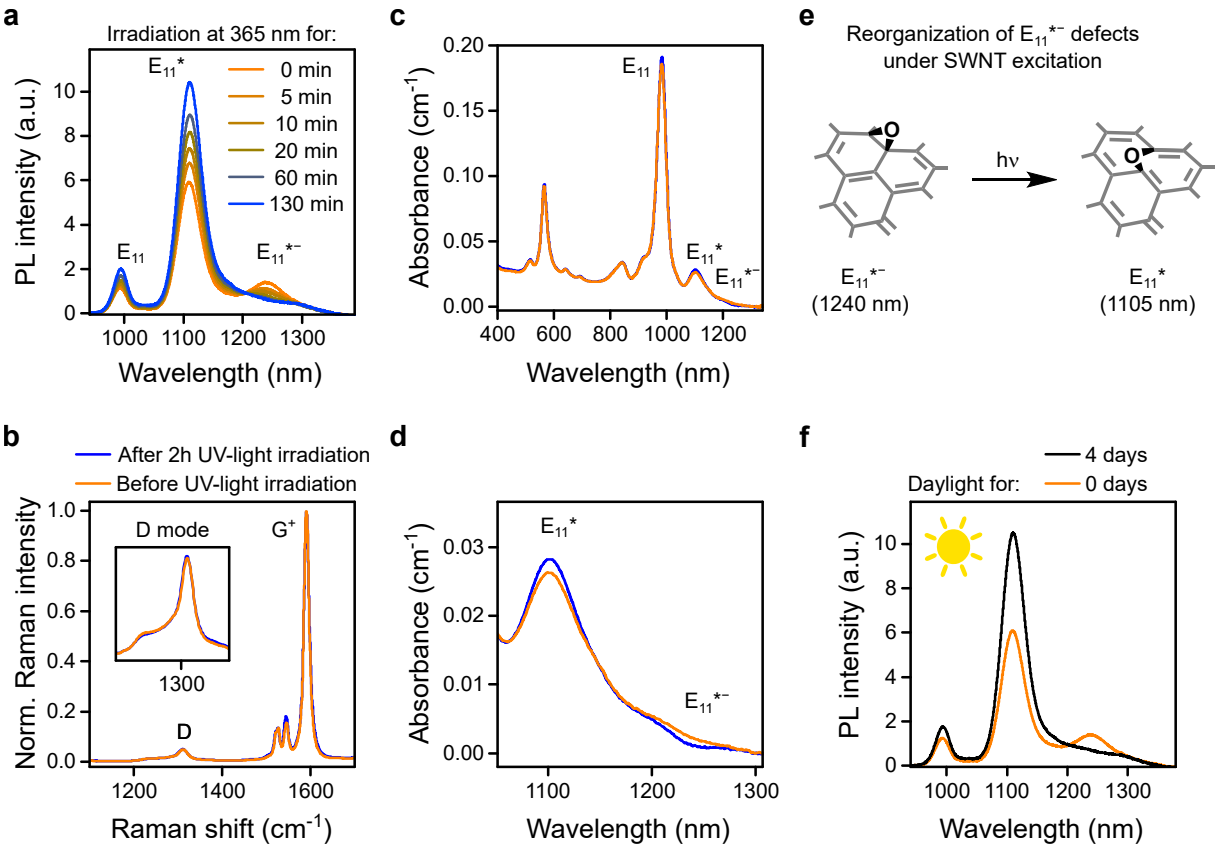

Figure 5.13: a) Stepwise UV-light irradiation (365 nm) of DOC-coated (6,5) SWNTs which were previously functionalized in the dark *via* Fenton-like reaction. b) Raman spectra before and after UV-light irradiation for 2 h of functionalized DOC-coated (6,5) SWNTs. c) Corresponding absorption spectra recorded before and after UV-light irradiation for 2 h. d) Inset on the spectral region of the E_{11}* and E_{11}*$^{-}$ bands. f) PL spectra before and after exposure to daylight for 4 days of functionalized DOC-coated (6,5) SWNTs.

The described light-induced reorganization of oxygen defects sufficiently explains the observed trends in the absorption spectra, but does not adequately account for the disproportional increase in E_{11}* as well as E_{11} PL intensity. Since the E_{11} PL intensity was affected by this phenomenon, the investigated system can be simplified and further reference reactions were performed on pristine SDS-coated (6,5) SWNTs.

First, the effect of UV irradiation and *in situ* generated H_2O_2 was investigated, but only a small decrease in E_{11} PL intensity was observed (Figure 5.14a,b). In sharp contrast to this, strong PL quenching was observed upon the addition of equimolar concentrations of H_2O_2 and $CuSO_4$, which was largely reversed upon irradiation with UV-light (Figure 5.14c). As described in Figure 5.1, the reaction of Cu(II) with H_2O_2 forms $O_2^{-\bullet}$ and $HOO^{\bullet}$ (approximately in equilibrium at standard conditions), which have a longer lifetime than $OH^{\bullet}$ and are not expected to lead to covalent functionalization.[325] Both species potentially interact strongly with the SWNT and induce efficient PL quenching. This is consistent with the observation by Wu and Nißler *et al.* where SWNT PL quenching was observed for Fe(III) ions in the presence of H_2O_2.[326] Upon excitation of the SWNT, $O_2^{-\bullet}$/$HOO^{\bullet}$ that are in direct contact with the SWNT may decompose and thus a reversal of PL quenching is observed. Such strong interactions of $O_2^{-\bullet}$/$HOO^{\bullet}$ with the

ground state of the SWNT are further supported by the observation of a small 2-3 nm blueshift of the E_{11} emission, which is reversed upon UV-light excitation and replicated in the reference sample (see Figure 5.13a and Figure 5.14c).

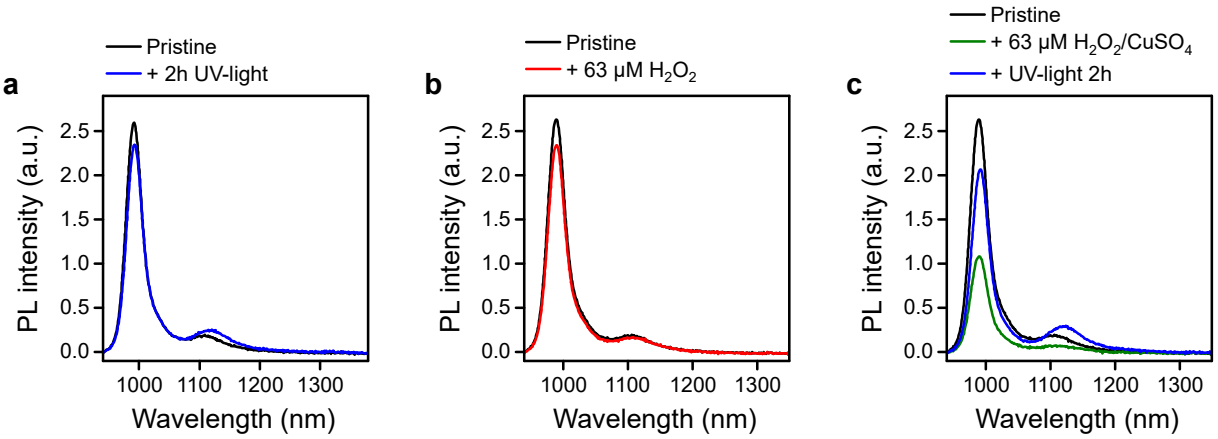

Figure 5.14: a) PL spectra of pristine SDS-coated (6,5) SWNTs recorded before and after 2 h of UV-light irradiation (365 nm). b) PL spectra of pristine SDS-coated (6,5) SWNTs recorded before and after the addition of 63 µM of H_2O_2. c) PL spectra of pristine SDS-coated (6,5) SWNTs recorded before and after addition of 63 µM of H_2O_2 and $CuSO_4$ and subsequent UV-light irradiation for 2 h.

In summary, two effects occur simultaneously upon optical excitation of SWNTs with luminescent oxygen defects. First, E_{11}^{*-} defects are expected to undergo rearrangement to form E_{11}^{*} defects. Second, $O_2^{-\bullet}$/HOO$^{\bullet}$, which are in contact with the SWNT and lead to efficient PL quenching, may decompose. As a result, a decrease in E_{11}^{*-} emission and an overall increase in E_{11} and E_{11}^{*} emission is observed.

5.6 Clustering of luminescent oxygen defects

For sp^3 defects, Sebastian *et al.* reported a linear correlation between the Raman $\Delta D/G^+$ area ratio and the absolute number of defect sites (n_d) extracted from PLQY measurements and application of a diffusion limited contact quenching (DLCQ) model.[144,274] Figure 5.15 shows the results of similar measurements for (6,5) SWNTs functionalized *via* a Fenton-like reaction. Surprisingly, an also linear but ~2.8× steeper increase can be found for oxygen defects in comparison to sp^3 defects. An almost identical correlation is observed for (6,5) SWNTs when functionalized by addition of NaOCl under UV-light irradiation (see Appendix B, Figure B.3 for PL and Raman spectra). This result is surprising, since a higher degree of sp^2 hybridization and thus a smaller relative D mode is expected for ether-d (E_{11}^{*}) oxygen defects compared to sp^3 defects.[327] Its suggests that oxygen defects do not act as independent isolated defect sites. In the applied DLCQ model, a cluster of defects has the same effect as a single isolated sp^3 defect, with both acting as a single defect/quenching site. Such a defect cluster could be formed upon further oxidation of the SWNT lattice in the vicinity of pre-existing oxygen defects, which was found to be favorable in studies by Yang *et al.* and Li *et al.*[197,198]

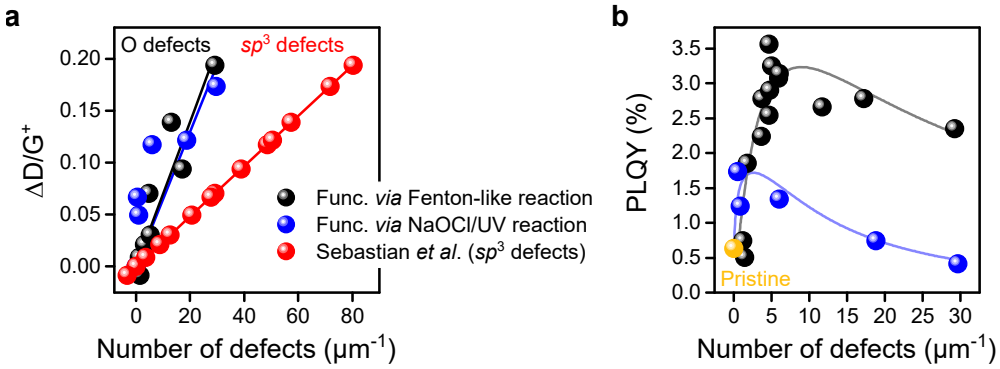

Figure 5.15: a) Differential Raman $\Delta D/G^+$ plotted against the calculated absolute number of defects obtained from PLQY measurements for DOC-coated (6,5) SWNTs that were previously functionalized *via* Fenton-like reaction (black) or in the presence of NaOCl under UV-light irradiation (blue), both labeled as oxygen (O) defects. Hypothetical number of defects for equal $\Delta D/G^+$ for sp^3 defects were calculated according to Sebastian *et al.*[144] b) Determined PLQY plotted against the absolute number of defects. Lines are guides to the eye.

Ma *et al.* suggested that in addition to the previously observed and described luminescent oxygen defects (ether-d, E_{11}^* and epoxide-l_{30}, E_{11}^{*-}), additional ether and epoxide oxygen defects with lower $\Delta E_{optical}$ (> 55 meV) coexist on the same nanotube (labeled as ether-l_{30}, epoxide-l_{30} and ether-l_{30}).[192] All possible oxygen defects are shown in Figure 5.16a, with the number indicating the angle of the respective bond. It is reasonable to assume that several oxygen defects are introduced in close proximity to each other, but only the lowest optical transition can be observed at room temperature, hence the E_{11}^* and E_{11}^{*-} transitions. In contrast, sp^3 defects are expected to act as isolated single defect sites. The deviation in the Raman D mode for the same number of defect sites as extracted from the DLCQ model can therefore be rationalized by the fact that multiple oxygen defects contribute to an overall higher D mode in contrast to isolated sp^3 defects (see Figure 5.16b).

This assumption of clustering of defects is further supported by the fact that the PLQY maximum for luminescent oxygen defects is observed at 4-8 defects per µm (see Figure 5.15b), which is in good agreement with previous observations for sp^3 defects.[144] Hence, in future investigations, the number of clusters containing multiple oxygen defects could be determined by Raman measurements utilizing the integrated Raman signal ratio (I_D/I_{G^+}) according to the following equation:

$$n_d(\text{oxygen-cluster}) = 149\,\mu m^{-1} \cdot \Delta \frac{I_D}{I_{G^+}}, \tag{5.1}$$

which represents the average obtained from the linear fits for oxygen defects created *via* Fenton-like reaction and *via* NaOCl/UV-light irradiation. The presence of luminescent oxygen clusters may be further investigated by comparison to defects introduced *via* ozonolysis or by single-SWNT PL spectroscopy at cryogenic temperatures.

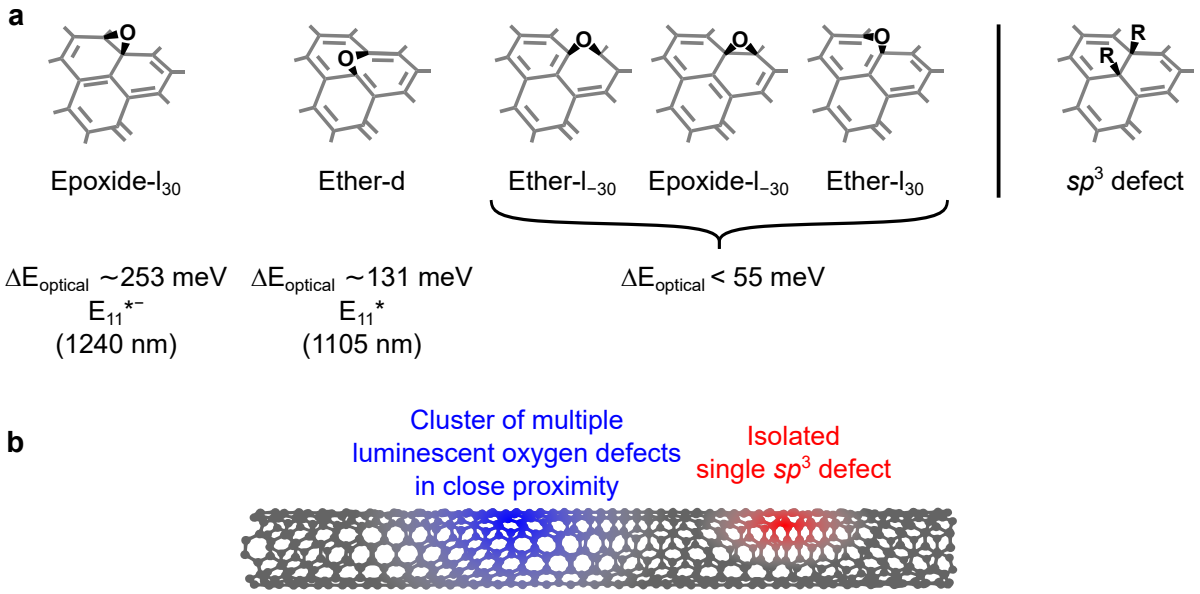

Figure 5.16: a) Possible chemical structures of luminescent oxygen defects as well as exemplary structure of one possible sp^3 defect. Ether-l_{-30}, epoxide-l_{-30} and ether-l_{30} defects were calculated to display $\Delta E_{optical}$ smaller than 55 meV and thus are typically not observed at room temperature.[192] b) Clustering of multiple luminescent oxygen defects leads to a greater disturbance in the SWNT lattice (indicated in blue) while acting as a single defect site for diffusing excitons in contrast to isolated sp^3 defects (red).

5.7 Impact of surfactant choice and SWNT chirality

A prerequisite for covalent functionalization to occur is the molecular accessibility of the SWNT surface, which is largely determined by the adsorbed surfactant or polymer on the SWNT. Consequently, the choice of surfactant has a strong influence on the introduction of luminescent oxygen defects due to the variation of binding affinities to the SWNT surface.[189,328] To investigate the effect of surfactant choice on the functionalization procedure, luminescent oxygen defects were introduced *via* a Fenton-like reaction in (6,5) SWNTs dispersed in different commonly used surfactants. Figure 5.17a shows the normalized PL spectra after covalent functionalization in 0.33% (w/v) SDS, sodium dodecylbenzene sulfonate (SDBS), sodium cholate (SC) or DOC. This concentration is above the critical micelle concentration (CMC) for all surfactants except for SC and successful introduction of luminescent oxygen defects is confirmed in all cases with the exception of DOC.[329–331] SDS remains the preferred surfactant, as the highest absolute PL intensities and well-defined emission features were obtained (see Appendix B, Figure B.4). Notably, SC is suitable for functionalization while DOC efficiently shields the SWNT surface from $OH^{\bullet}$ addition (see also Figure 5.4). While the CMC may play an important role in this case, this observation is more likely connected to the chirality-dependent surface coverage of SC and DOC. SC has been shown to have a higher surface coverage around large-diameter SWNTs compared to small-diameter SWNTs,[332] while the opposite is true for DOC.[333] Combined with the selectivity of SC towards certain chiral angles,[332] this should lead to a SWNT chirality-dependent functionalization for SC-coated SWNTs.

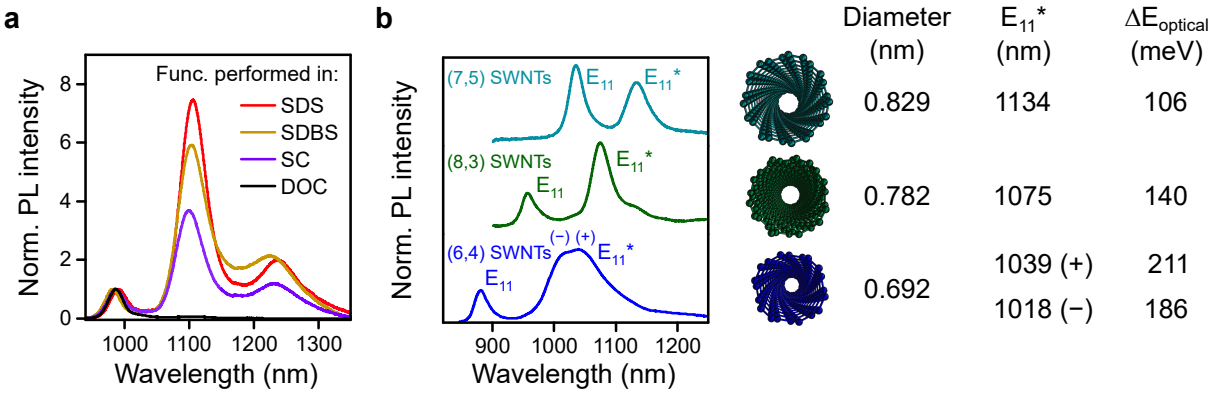

Figure 5.17: a) Normalized PL spectra of (6,5) SWNTs dispersed in SDS (orange), SDBS (ocher), SC (purple) or DOC (black) (0.33% w/v) and functionalized *via* Fenton-like reaction with 63 µM $CuSO_4$ and 12 eq. NaAsc. b) Normalized PL spectra of ATPE-sorted and SDS-coated (7,5) SWNTs (top), (8,3) SWNTs (middle) and (6,4) SWNTs (bottom) functionalized *via* Fenton-like reaction with SWNT diameter, emission band wavelength and $\Delta E_{optical}$.

So far, covalent functionalization has only been performed on (6,5) SWNTs. In contrast to luminescent sp^3 defects, oxygen defects lack tuneability of the functionalization group. To tune the emission wavelength of oxygen defects, it is necessary to shift the emission wavelength of the SWNT itself, hence functionalization of other SWNT chiralities is required. For this purpose, (7,5), (8,3) and (6,4) SWNTs were sorted *via* acid addition ATPE according to a modified protocol by Li *et al.*[257] (see Section 3.1.6 for optical characterization of the obtained dispersions). Upon covalent functionalization *via* Fenton-like reaction, pronounced chirality-dependent defect-induced emission bands are obtained (see Figure 5.17 and Appendix B, Figure B.5 for single PL spectra). With this approach, the defect emission band can be successfully tuned between 1018 nm and 1134 nm, but a reduced optical trap depth $\Delta E_{optical}$ and a decreasing brightening effect (about 2-1.2, see Table 5.2) was observed for increasing SWNT diameter. This is in agreement with the results obtained in Chapter 4 and other reports on luminescent oxygen and sp^3 defects.[11,12] Interestingly, a very broad defect emission is obtained for (6,4) SWNTs and is likely to originate from two enantiomers (labeled as + and −). The splitting of the E_{11} emission was found to be 15-20 nm for (6,4) SWNTs,[334] which closely matches the observed 21 nm shift of the two E_{11}* emission features.

Table 5.2: PLQY values for (7,5), (8,3) and (6,4) SWNTs functionalized *via* Fenton-like reaction.

Sample	$PLQY_{total}$(%)	Increase in PLQY
(7,5) SWNTs	0.24	–
Func-(7,5) SWNTs	0.28	×1.19
(8,3) SWNTs	0.27	–
Func-(8,3) SWNTs	0.48	×1.76
(6,4) SWNTs	0.39	–
Func-(6,4) SWNTs	0.79	× 1.97

5.8 Up-scaling

Despite advances in SWNT-sorting, obtaining large quantities of purified chirality-enriched dispersions remains a challenging and time-consuming task. To make large amounts of bright functionalized SWNTs available to users, unsorted CoMoCAT SWNT raw material was functionalized. After the removal of unexfoliated material such as amorphous carbon by a simple centrifugation step, a dispersion of semiconducting and metallic SWNT chiralities was obtained. This results in multiple emission features as shown in Figure 5.18a (or Appendix A B.6). Functionalization was performed in SDS at a concentration of 125 µM $CuSO_4$ and addition of 12 eq. NaAsc. A strong increase in the overall PL intensity was observed (Figure 5.18b), with the most prominent feature attributed to the E_{11}^* emission originating from the predominantly present (6,5) SWNTs (40% of the raw material's mass). This strong brightening effect was also evident in the NIR-PL images when the pristine and functionalized dispersions were placed in Eppendorf cups and excited under identical conditions and SWNT concentrations (Figure 5.18c).

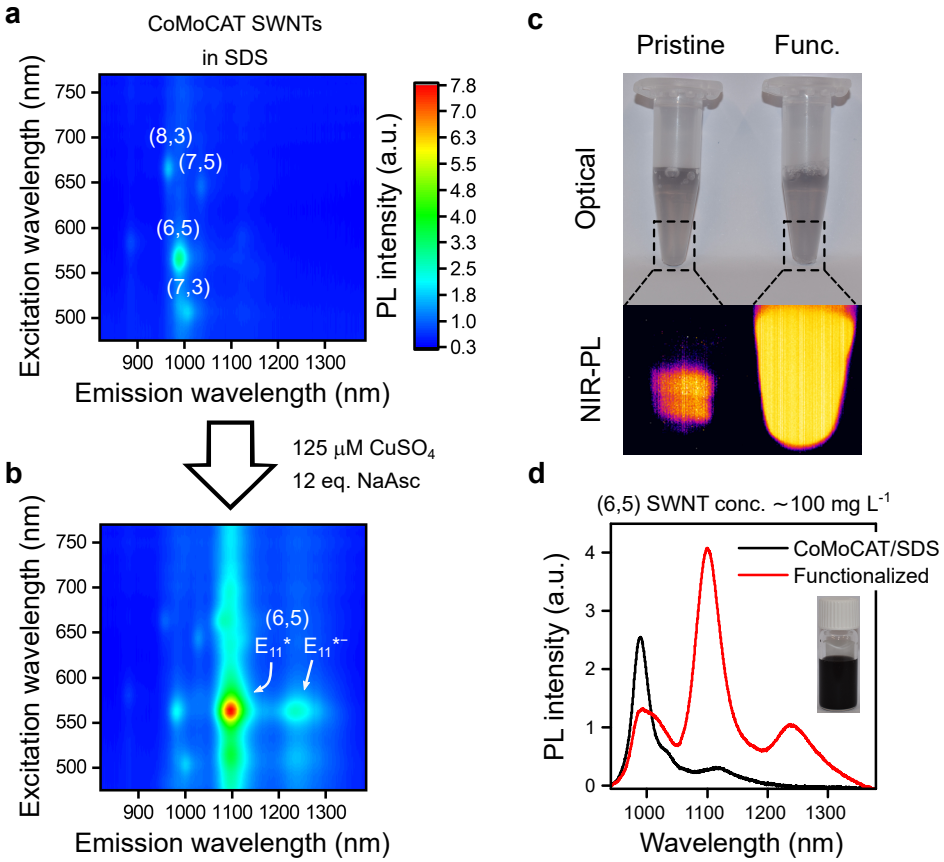

Figure 5.18: PLE map before (a) and after (b) functionalization of unsorted SDS-coated CoMoCAT nanotubes *via* Fenton-like reaction. Covalent functionalization was performed at a concentration of 125 µM $CuSO_4$ and 12 eq. NaAsc. Most dominant SWNT species as well as E_{11}^* and E_{11}^{*-} emission originating from (6,5) SWNTs are labeled. c) White-light images (top) and NIR-PL images (950-1600 nm, bottom) of dispersions of pristine and functionalized SDS-coated CoMoCAT nanotubes. The insets represent the areas displayed in the NIR-PL images. d) PL spectra of a dilute dispersion of unsorted SDS-coated CoMoCAT nanotubes before (black) and after (red) functionalization of a highly concentrated dispersion (~100 mg L^{-1} SWNTs, see optical image).

While the functionalization of the SWNT raw material represents a step towards enhancing the accessibility of this material, the total SWNT concentration remains relatively low (about 0.6 mg L^{-1}, with respect to (6,5) SWNTs). For many applications and potential commercialization, efficient up-scaling is critical. To achieve this, a highly concentrated dispersion of unsorted CoMoCAT SWNTs (100 mg L^{-1}) was transferred from DOC to SDS (0.33% w/v) and covalently functionalized *via* a Fenton-like reaction. The concentration of the highly water soluble $CuSO_4$ and NaAsc was adjusted accordingly. Functionalization was performed for 16 h, after which the dispersion was transferred back to DOC to aid the stability of the dispersion. PL spectra of diluted SDS-coated CoMoCAT SWNTs are shown in Figure 5.18d and show a strong increase in the integrated PL emission, *i.e.* brightening, upon covalent functionalization.

5.9 Making functionalized SWNTs biocompatible

To employ the obtained bright functionalized (6,5) SWNTs as NIR-II fluorescent labels for *in vivo* bioimaging or as optical biosensors, it is essential to provide them with the necessary biocompatibility while maintaining their excellent optical properties. Ultra-short SWNTs (<80 nm) hold great promise for high-resolution bioimaging as they possess molecular emitter properties and can pass through lipid bilayers of cell membranes.[335,336] In addition, they are expected to exhibit greatly reduced biotoxicity and can be easily excreted through the kidney and bile ducts.[337,338] Nonetheless, owing to the highly effective PL quenching at the tube ends, the PL is typically immeasurable. However, the PL can be significantly increased by luminescent defects, as demonstrated by Danné *et al.*[142] To test whether such PL enhancement can be achieved with the developed functionalization procedure, SDS-coated (6,5) SWNTs were shortened by stepwise tip sonication. PL spectra were recorded after each sonication step (see Figure 5.19a) and show the expected dramatic decrease in E_{11} PL intensity, indicating successful shortening.

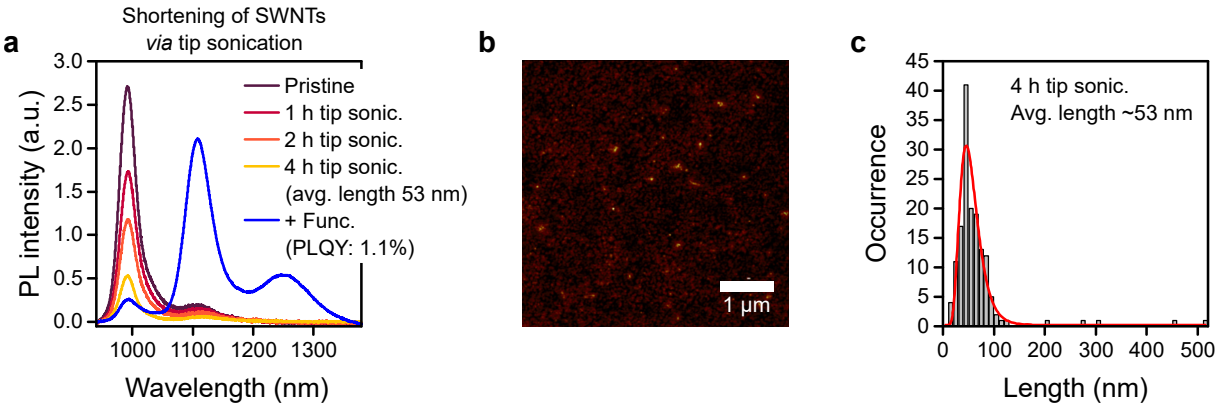

Figure 5.19: a) PL of SDS-coated (6,5) SWNTs upon stepwise tip sonication. After a total 4 h of tip sonication the dispersion was centrifuged and the supernatant subjected to covalent functionalization *via* Fenton-like reaction. A total PLQY of 1.1% was determined. b) Atomic force micrographs of shortened (6,5) SWNTs after 4 h tip sonication deposited on a poly-L-lysine-coated native silicon wafer. c) Histograms of tube lengths and log-normal distribution fit (red line) to the data. The average tube length was ~53 nm.

To determine the tube length distribution atomic force micrographs were taken, which revealed an average tube length of approximately 53 nm after a total of 4 h of tip sonication (Figure 5.19b,c). After covalent functionalization *via* a Fenton-like reaction as described above, a strong brightening effect was observed. Functionalized shortened SDS-coated (6,5) SWNTs exhibited approximately a 7.8× higher integrated PL emission and a total PLQY of 1.1%.
To achieve the required biocompatibility, non-covalent functionalization with pegylated phospholipid (PL-PEG) or single-stranded DNA (ssDNA) was used.[208,262] Transfer of functionalized SDS-coated (6,5) SWNTs (not shortened) to PL-PEG_{5000} and ssDNA-$(GT)_{10}$ in PBS buffer was achieved by kinetic surfactant exchange *via* dialysis for 7 days and 4 days, respectively (see Section 3.3). Successful surfactant exchange is usually indicated by a solvatochromic redshift in the E_{11} emission (here 6 nm for PL-PEG_{5000} and 10 nm for ssDNA-$(GT)_{10}$) resulting from the change in the local dielectric environment of the SWNT surface (see Figure 5.20a,b). Note that during dialysis, the sample was exposed to daylight for several days, so the $E_{11}{}^{*-}$ emission disappeared. Importantly, the PLQY remained high after surfactant exchange with a total PLQY of 2.9% (PL-PEG_{5000}-coated) and 2.4% (ssDNA-wrapped).
Due to its capability to recognize catecholamines such as dopamine with high selectivity and sensitivity, ssDNA-$(GT)_{10}$ was chosen as a biocompatible coating.[245,246,339] In contrast to studies by Spreinat *et al.*,[23] functionalized ssDNA-$(GT)_{10}$-wrapped (6,5) SWNTs showed a strong increase in PL intensity upon addition of 200 µM dopamine (see Figure 5.20c). The increase in PL intensity was larger for $E_{11}{}^{*}$ emission compared to the E_{11} emission, resulting in a slight change in the $E_{11}{}^{*}/E_{11}$ PL intensity ratio from 7.2 to 8.8, which would allow ratiometric detection of dopamine. Here, measuring the defect-state lifetime could help in understanding the effect of dopamine on defect emission in the future.

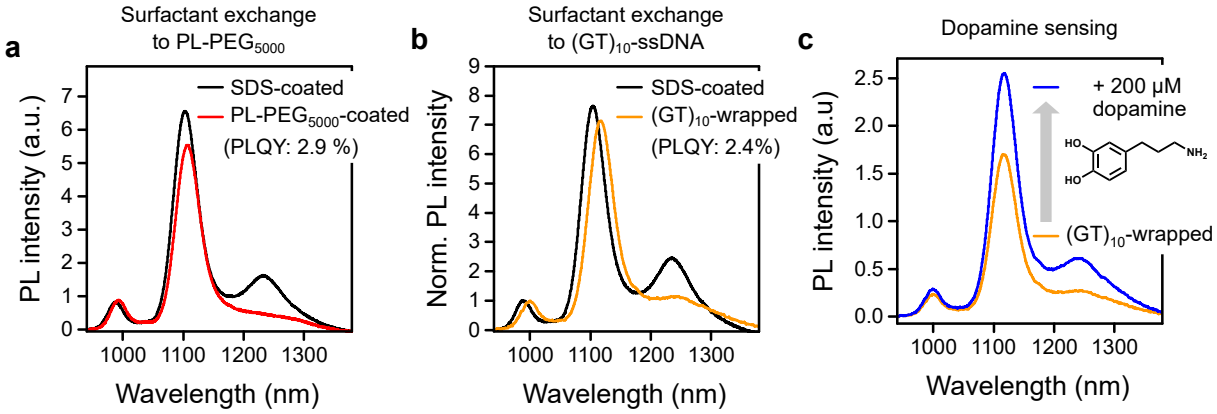

Figure 5.20: a) PL spectra of functionalized (6,5) SWNTs in SDS (black) and after transfer to PL-PEG_{5000} (red) after dialysis for 7 days with a final PLQY of 2.9%. b) Normalized PL spectra of functionalized (6,5) SWNTs in SDS (black) and after transfer to $(GT)_{10}$-ssDNA (orange) after dialysis for 4 days in PBS buffer with a final PLQY of 2.4%. c) PL spectra of functionalized $(GT)_{10}$-wrapped (6,5) SWNTs in PBS buffer before (orange) and after addition of 200 µM dopamine (blue).

Finally, prior to conducting *in vitro* or *in vivo* experiments, it is essential to address the potential metal toxicity of SWNTs functionalized *via* the presented copper-catalyzed Fenton-like reaction. Copper is a naturally occurring essential element found in various tissues, but at elevated concentrations it is associated with many diseases and cellular toxicity.[340] To check its efficient removal, covalent functionalization of SDS-coated (6,5) and CoMoCAT SWNTs was performed in duplicates followed by addition of EDTA and filtration (see also Section 3.6.5). Based on fitted absorption spectra (see Section 3.2), the (6,5) SWNT concentration in pre-selected and unsorted SWNTs was ~0.6 mg L^{-1}, which corresponds to a concentration of SWNT raw material typically used for *in vivo* experiments.[341] Absolute copper concentrations were measured by inductively coupled plasma optical emission spectroscopy (ICP-OES), which requires complete digestion of all dispersed carbon material (hence SWNTs) to correctly measure all copper species present and avoid contamination of the spectrometer. Complete oxidation of the obtained SWNT dispersion was achieved by addition of H_2O_2, and after heating at 80 °C for 3 h, a clear solution was obtained. For reference measurements, the same process was repeated for duplicates of pristine (6,5) and CoMoCAT SWNTs as well as a sample without SWNTs (labeled as reference). In ICP-OES, atomization and ionization of the digested SWNT solution is achieved by argon plasma and the characteristic emission line of copper was detected at $\lambda = 327.395$ nm. The detected signal was calibrated against a copper solution of known concentration and the determined copper concentrations of all samples are presented in Table 5.3. While negligible amounts of copper were found for the pristine SWNT dispersions, slightly elevated concentrations up to 95.8 µg L^{-1} were obtained for functionalized SWNTs. Overall, an average of 51 µg L^{-1} to 59 µg L^{-1} was found, which is about 1% of the initial copper concentration (~4000 µg L^{-1}) used during functionalization. Residual copper concentrations remain well below reported serum concentrations (1000-1500 µg L^{-1}) and the maximum contaminant level established by the United States Environmental Protection Agency (1300 µg L^{-1}).[342] Based on additional reports on cell viability of *e.g.* HeLa cells in the presence of Cu(II) ions and A549 cells for Cu_2O nanoparticles,[343,344] the measured copper concentrations are expected to be harmless. In addition, the Cu(II) concentration, which is used during the functionalization, could be further reduced by a factor of about 8 as outlined in Section 5.4.

Table 5.3: The concentration of copper in the processed reference sample or SWNT dispersion as determined by ICP-OES. All samples were prepared and measured in duplicates.

Sample name	Copper conc. (µg L^{-1})	Avgerage copper conc. (µg L^{-1})	(6,5) SWNT conc. (mg L^{-1})
Reference	4.2 / 3.8	4.0	–
Pristine (6,5) SWNTs	5.9 / 4.4	5.2	0.6
Func. (6,5) SWNTs	6.6 / 95.8	51.2	0.6
Pristine CoMoCAT SWNTs	7.9 / 5.7	6.8	0.6
Func. CoMoCAT SWNTs	73.5 / 45.0	59.3	0.6

5.10 Summary & conclusions

In summary, this Chapter describes a facile and scalable functionalization method for the introduction of bright luminescent oxygen defects into aqueous-dispersed SWNTs. The incorporation of oxygen defects is achieved by covalent functionalization of the SWNT sidewall with ROS generated by Fenton-like copper redox chemistry in the presence of dissolved oxygen. The reaction is initiated by the reduction of Cu(II) ions by the reducing agent NaAsc and can be controlled by the total number of reduction cycles and hence the number of generated ROS. This control can be achieved by adjusting the total reagent concentration or the Cu(II) catalyst loading with appropriate variation of the reducing agent concentration.
Oxygen defects are expected to be formed upon radical addition of $OH^{\bullet}$ to the SWNT lattice and subsequent oxidation, followed by structural rearrangement of epoxide-d defects to an ether-d configuration. This functionalization results in bright E_{11}* emission around 1105 nm and strong brightening with a reproducible PLQY of 3% for (6,5) SWNTs, making it one of the brightest reported ensembles of SWNTs in water.[15,145,345] The observed high brightness strongly implies that the previously assumed existence of a dark state, thought to be energetically below the bright defect state, is unlikely to be the cause of the previously observed low brightness of oxygen defects. It could be either that the lowest state is also bright in the case of oxygen defects, or the energetic difference between the bright and dark state is small and can be easily overcome at room temperature. It is more likely that prior functionalization methods caused unintended damage to the SWNT lattice, reducing the overall PLQY. Due to the high reactivity of ROS, controlling the creation of oxygen defects is considerably more challenging compared to sp^3 defects, and it is preferable to introduce new defects near pre-existing oxygen defects. This assumption is supported by the obtained results when correlating the absolute number of defects with the Raman $\Delta D/G^+$ area ratios. In comparison to luminescent sp^3 defects, a stronger increase in $\Delta D/G^+$ area ratio was observed per defect/quenching site, as estimated by the DLCQ model, suggesting the formation of clusters of luminescent oxygen defects.
Importantly, the introduction of luminescent oxygen defects occurs in the dark and no (UV-)light is necessary during the functionalization process. When functionalization is performed in the dark, significant amounts of epoxide-l defects (E_{11}^{*-}) are introduced into the SWNT lattice, which can reorganize into the more stable ether-d defects (E_{11}*) under SWNT excitation even in daylight. This reorganization effect has been suggested in the literature but was never observed so far, because all functionalization procedures that resulted in luminescent oxygen defects were performed under (UV-)light irradiation. However, it is important to note that light irradiation is still required to achieve maximum brightness, as it efficiently removes presumably adsorbed ROS, which quench SWNT PL. Crucially, this light irradiation step can be performed after the initial functionalization step, and parameters such as irradiation power do not affect the final sample quality.
The developed functionalization method was shown to be insensitive to a variety of reaction parameters such as pH, choice of Cu(II) pre-catalysts, reducing agent, and surfactants. Hence, it was successfully applied to a variety of other SWNT chiralities as well as unsorted CoMoCAT SWNT raw material, for which a strong brightening effect was observed. Therefore, this function-

alization method is well-suited for effective up-scaling, due to its high robustness and the use of non-toxic, readily available, and cheap chemicals. Up-scaling of the initial functionalization step was demonstrated by covalent functionalization at a SWNT concentration of 100 mg L^{-1} (with respect to (6,5) SWNTs). This scalability enables the production of large quantities of bright and biocompatible SWNTs, while retaining their excellent optical properties upon surfactant transfer to PL-PEG_{5000} (PLQY 2.9%). Alternatively, surfactant transfer with ssDNA can be performed. (GT)-$_{10}$-ssDNA-wrapped SWNTs remained bright (PLQY 2.4%) and retained their sensitivity towards dopamine. Even when ultra-short (average length 53 nm) SWNTs were functionalized, sufficient bright PL emission was obtained. The absolute copper concentration after washing was found to be well below harmful concentration, making the obtained samples suitable for application in high-contrast *in vitro* and *in vivo* imaging in the NIR-II.

Overall, the presented functionalization method enables the large-scale production of biocompatible SWNTs with a high PLQY of up to 3% in aqueous dispersion, making them suitable for NIR-II bioimaging. The typically low PLQY (<1%) has been a substantial limitation of SWNTs compared to other inorganic nanomaterials suitable for high-contrast NIR-II bioimaging (see also Table 2.1), such as quantum dots (QDs), lanthanide-doped nanoparticles (LnNPs), and gold nanoparticles (AuNPs).[5] Upon covalent functionalization, the previously existing large gap in PLQY, as compared to AuNPs (up to 4%),[346] LnNPs (up to 10%),[347] and QDs (up to 30%),[222] was significantly reduced.

CHAPTER 6

RATIOMETRIC FLUORESCENT SENSING OF PYROPHOSPHATE WITH sp^3-FUNCTIONALIZED SINGLE-WALLED CARBON NANOTUBES

In this Chapter, a biosensor based on sp^3-functionalized SWNTs is presented for the ratiometric optical detection of pyrophosphate in the near-infrared.

The results of this Chapter are published in Settele *et al.*, *Nat. Commun.* **15**, 706 (2024). Modified reprints are presented with permission of Springer Nature and have been licensed under a Creative Commons CC BY license. Dr. Han Li and Dr. Benjamin S. Flavel (Institute of Nanotechnology, Karlsruhe Institute of Technology) provided ATPE-sorted (6,5) SWNTs. Diazonium salts were synthesized and characterized by Elena Michel under the supervision of Prof. Dr. A. Stephen K. Hashmi (Heidelberg University). The cell-spiking and PCR experiments were performed in collaboration with C. Alexander Schrage and Dr. Sebastian Jung under the supervision of Prof. Dr. Sebastian Kruss at the Department of Chemistry and Biochemistry at the Ruhr University Bochum.

6.1 Introduction

Chapter 5 described a highly efficient functionalization route that introduces bright luminescent oxygen defects into SWNTs, making them attractive as luminescent probes in the NIR-II region for bioimaging and (bio)sensing. However, sensing applications benefit not only from the increased brightness, but also from the introduction of an additional red-shifted emission band at a different wavelength. This defect-induced emission band shows unique responses to changes in both the chemical environment of the SWNT and interactions with the analyte, thus enabling multimodal and ratiometric detection schemes. These unique interactions have been used for the detection of ovarian cancer markers in serum[22] or for the detection of dopamine[23] (see also Section 5.8). In both cases, the strong adsorption of ssDNA *via* π-π stacking of the

nucleic acids to the SWNT surface was used to obtain stable dispersions.[348] Here, ssDNA was not only used to disperse the SWNT, but also served as the recognition unit transmitting changes in the chemical environment to the SWNT. However, the interactions of ssDNA-wrapped SWNTs with the analyte are highly complex. They depend on many variables such as the ssDNA sequence, the length of the nucleic acid backbone, and the chirality of the SWNT.[349–351] This complex structure-function relationship limits the rational design of new analyte binding schemes. Consequently, interpreting the obtained results or enhancing sensitivity and selectivity in this detection approach often requires a large number of datasets. For example, the sensitivity and selectivity of ssDNA interactions with analytes can be improved by screening for new ssDNA sequences *via* directed evolution.[352] Alternatively, Kim *et al.* utilized machine learning algorithms to detect and interpret the analyte "fingerprint" in the PL response of the SWNT sensor.[22] To circumvent these time-consuming approaches, the development of more specific interactions between the target analyte and the SWNT, and ultimately signal transduction, will be the focus here.
In this context, the functional group attached to the luminescence defect may further facilitate such rational design through target analyte-specific interactions. For example boronic acid groups attached to sp^3 defects have been shown to exhibit pronounced blueshifts upon addition of various saccharides,[253] and *N*,*N*-diethyl-4-aminobenzene-functionalized SWNTs exhibit pH-dependent PL shifts.[251] These pH-dependent PL shifts have been used to detect lysosomal acidification, which is closely associated with neurodegenerative diseases and cancers.[254] Attached functional groups can facilitate interactions between analyte and SWNT, enabling the development of new detection systems for the optical identification of biomarkers with structural motifs that were previously unattainable.

A particular biomarker of significance that has attracted substantial attention in biochemistry, molecular biology, and medical diagnostics is inorganic pyrophosphate (PP_i, $P_2O_7^{4-}$). It plays a critical role in cellular energy metabolism and is generated during the biosynthesis of biomacromolecules and metabolites such as amino acids, coenzymes and nucleotides.[353,354] More specifically, it is released during the hydrolysis of adenosine triphosphate (ATP) to adenosine monophosphate (AMP) under cellular conditions, and its exergonic hydrolysis generates inorganic phosphate (P_i), a substrate of ATP synthase.[355] It is also involved in DNA replication and RNA synthesis and is released upon incorporation of nucleotides into a growing DNA or RNA strand by polymerase.[356,357] Hence, monitoring PP_i provides vital information for the assessment of telomerase activity in cancer diagnosis.[358] Furthermore, PP_i is present in blood plasma,[359] urine[360] and synovial fluids,[361] where its levels must be sufficiently high to block calcification. Elevated levels of PP_i are therefore associated with various joint diseases such as osteoarthritis, bone wear and chondrocalcinosis.[362,363] The detection and quantification of PP_i is crucial for the diagnosis of such medical conditions and important for the development of drugs targeting enzymes involved in PP_i metabolism. Consequently, monitoring PP_i in aqueous solutions is highly desirable, prompting extensive research to develop PP_i-sensitive water-soluble luminescent probes.[353,364]

A very powerful tool for PP_i recognition are metal displacement assays, where the coordination of PP_i to (vacant) coordination sites of a metal center is harnessed. In a metal displacement assay, typically, a fluorophore is linked to an acceptor molecule (*e.g.*, a ligand) that can bind reversibly to a metal ion (*e.g.*, Fe^{3+}, Zn^{2+}, Cu^{2+}) and switch the attached fluorophore between an emissive "ON" and non-emissive "OFF" state.[353,364] A typical metal displacement assay, in which metal ion complexation induces an "OFF" state of the fluorophore, is illustrated in Figure 6.1. Crucially for the detection of PP_i, the resulting metal complex must be designed such that PP_i has a stronger affinity for the metal ion than the corresponding acceptor molecule. When PP_i complexes with the metal ion, the metal ion is no longer bound to the acceptor molecule, and the fluorophore switches to an emissive "ON" state. Since the switching of the fluorophore between the emissive "ON" and "OFF" states depends on the exact equilibrium of the competitive complexation between PP_i and the acceptor molecule, it directly correlates with the concentration of PP_i.

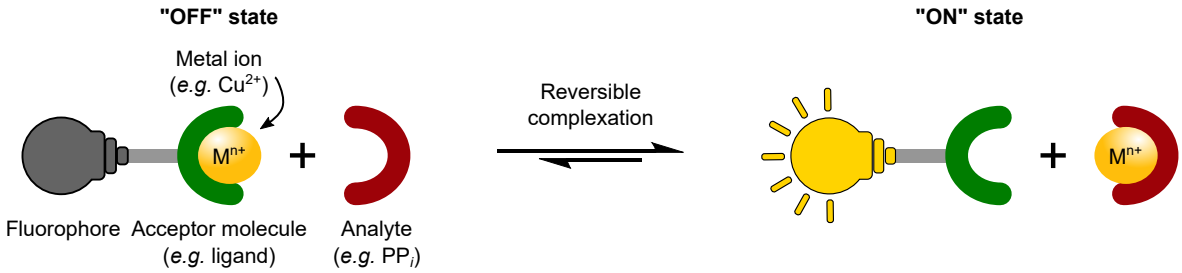

Figure 6.1: Schematic representation of a fluorometric detection scheme in a metal displacement assay: A fluorophore is bound to a metal ion *via* a suitable acceptor molecule, resulting in a non-emissive "OFF" state of the fluorophore. Upon reversible competitive complexation with a metal ion-complexing analyte, the analyte binds the metal ion and counteracts the metal ion-induced changes in the fluorophore. As a result, the fluorophore transitions to its "ON" state.

While previously reported fluorescent PP_i sensors have demonstrated remarkable sensitivity and selectivity towards PP_i, they are confined to emission in the visible range (400-700 nm) and NIR-I (700-1000 nm).[353,365] This Chapter introduces a detection scheme based on a metal displacement assay where sp^3-functionalized SWNTs serve as fluorophores for detecting PP_i in the NIR-II. Comprehensive insights into the sensing mechanism are provided, offering a nuanced understanding for further rational design of nanotube-based biosensors.

6.2 sp^3 functionalization and copper-induced PL quenching

In order to develop a SWNT sensor with luminescent defects capable of detecting PP_i in aqueous media, a functionalization approach was chosen that allows synthetic control over the attached functional group. Specifically, sp^3 functionalization *via* diazonium salt chemistry was adopted. SDS-coated (6,5) SWNTs were selected as a model system and sorted from CoMoCAT raw material by ATPE as outlined in Section 3.1.5. Covalent functionalization (see Figure 6.2a) was performed by adding 4-ethynylbenzene diazonium tetrafluoroborate (Dz-Alkyne) at a concentration of ~0.025-0.005 µg L^{-1} to a dispersion of SDS-coated (6,5) SWNTs. The reaction

mixture was stored under light exclusion for 7 days until complete decomposition of the added diazonium salt was achieved. After successful functionalization, by-products such as the decomposed diazonium salt were removed by spin-filtration. Figure 6.2b shows the normalized PL spectra for this functionalization process, revealing an additional bright red-shifted emission feature (labeled as E_{11}*) around 1135 nm next to the E_{11} emission feature at 988 nm. The E_{11}* emission feature is attributed to defect-induced emission resulting from the trapping of mobile E_{11} excitons at luminescent sp^3 defect sites bearing a 4-ethynyl moiety (also referred to as an alkyne moiety).

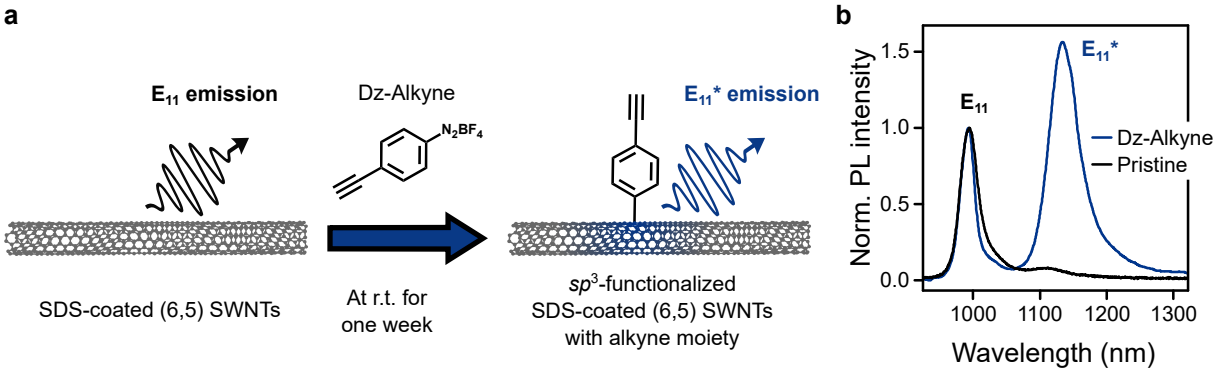

Figure 6.2: a) Covalent functionalization of SDS-coated (6,5) SWNTs through reaction with 4-ethynylbenzene diazonium tetrafluoroborate (Dz-Alkyne) leads to luminescent sp^3 defects bearing an alkyne moiety. b) Normalized PL spectra before and after covalent functionalization, showing a pronounced bright defect-induced E_{11}* emission band around 1135 nm.

An 1:1 mixture of copper(II) sulfate pentahydrate ($CuSO_4(H_2O)_5$) and tris(3-hydroxypropyltriazolylmethyl)amine (THPTA) was added to the obtained dispersion of functionalized (6,5) SWNTs (see Figure 6.3a). THPTA is a well-established water-soluble triazole ligand that efficiently complexes Cu(II) ions and was originally used in click chemistry due to its ability to prevent the swift re-oxidation of *in situ* generated Cu(I) ions to Cu(II).[366] However, in this work, the addition of the aforementioned Cu(II) complex (referred to as [Cu]) leads to a strong decrease in both E_{11} and E_{11}* emission, as shown in Figure 6.3b. This decrease is strongly correlated with the concentration of added [Cu], and PL quenching was observed for [Cu] concentrations above 0.34 µM, reaching an almost constant level of quenching for [Cu] concentrations above >23 µM (see Figure 6.3c). At these concentrations, the E_{11} peak intensity was reduced by a factor of ~2, while the E_{11}* peak intensity was reduced by a factor of ~5.

In addition to PL quenching, Figure 6.3d shows that the E_{11} (not shown) and E_{11}* PL peak positions were red-shifted by up to 7 nm and 5 nm, respectively. PL quenching induced by Cu^{2+} ions was already observed in Chapter 5, but no redshift of the PL peak position was detected. Thus, the Cu^{2+} ion-induced PL quenching observed here is fundamentally stronger and/or operates *via* a different quenching mechanism compared to the PL quenching observed in Chapter 5. Importantly, the PL quenching of defect-induced E_{11}* was more pronounced than that of E_{11} emission, resulting not only in a reduction of the overall PL intensity but also in a reduction of the E_{11}*/E_{11} PL ratio (see Figure 6.3e).

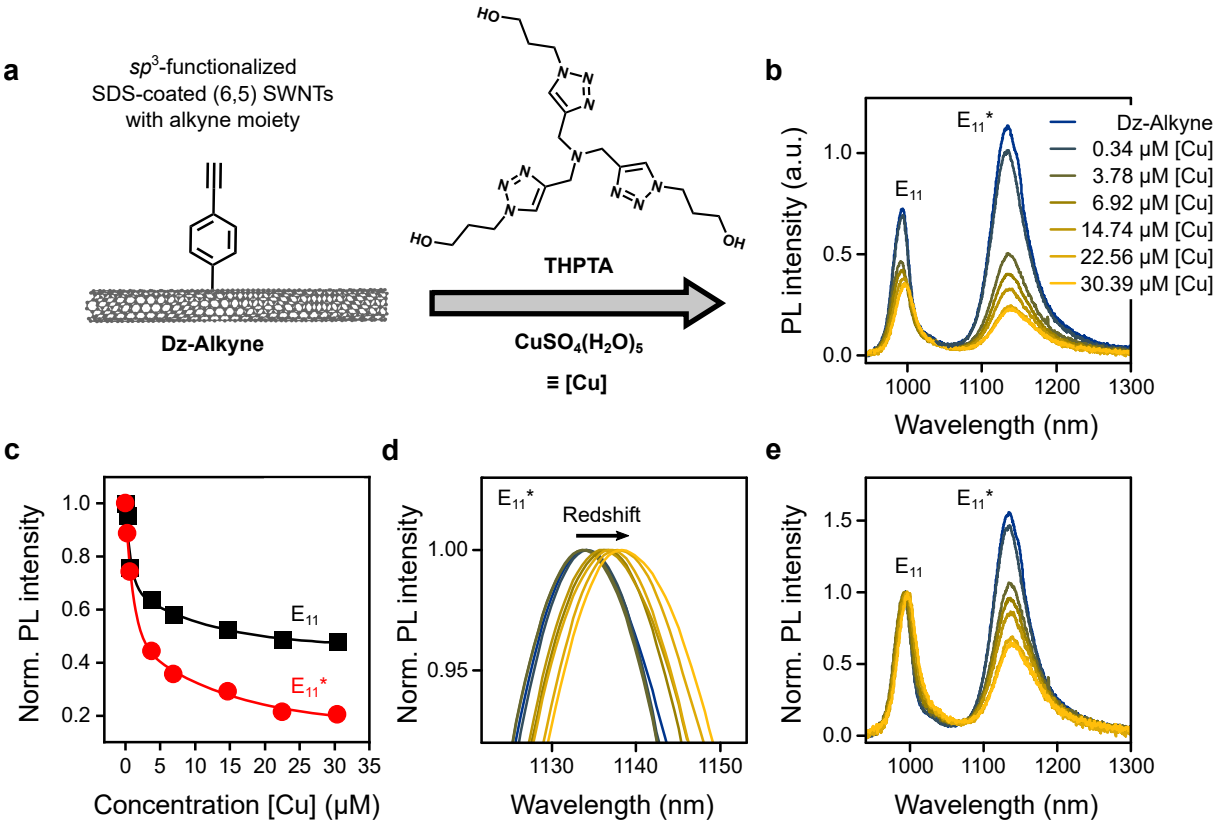

Figure 6.3: a) Schematic illustration of the addition of THPTA and $CuSO_4(H_2O)_5$, also denoted as [Cu], to 4-ethynylbenzene-functionalized SDS-coated (6,5) SWNTs. b) PL spectra recorded after the addition of different concentrations of [Cu], resulting in significant PL quenching. c) Normalized E_{11} and E_{11}* PL intensities plotted against the concentration of [Cu]. d) Zoom-in on the normalized (to E_{11}*) PL spectra after the addition of different concentrations of [Cu]. e) Normalized PL spectra recorded after the addition of different concentrations of [Cu], resulting in a reduction of the E_{11}*/E_{11} PL intensity ratio.

Remarkably, upon the addition of excess EDTA, a strong metal-chelating ligand, to a dispersion of 4-ethynyl-functionalized (6,5) SWNTs quenched with 15 µM [Cu], all induced PL quenching effects and shifts in PL peak position were immediately and completely reversed (Figure 6.4). This observation suggests that the presence of [Cu] leads to changes in the optical properties of 4-ethynyl-functionalized (6,5) SWNTs, that are reversed upon complexation of Cu^{2+} ions with EDTA. It is assumed that the complexation of Cu^{2+} ions by THPTA plays a critical role since EDTA represents a stronger Cu^{2+} ion-chelating complex and breaks up the existing Cu^{2+}/THPTA complex. A thorough investigation of this phenomenon, its implications, and the underlying PL quenching mechanism will be discussed in more detail in Section 6.5.
Crucially, this reversible quenching process establishes the basis for the use of sp^3-functionalized (6,5) SWNTs as luminescent probes in a metal displacement detection scheme. This is particularly important for the identification of small biorelevant molecules with strong copper-complexing capabilities, such as PP_i.

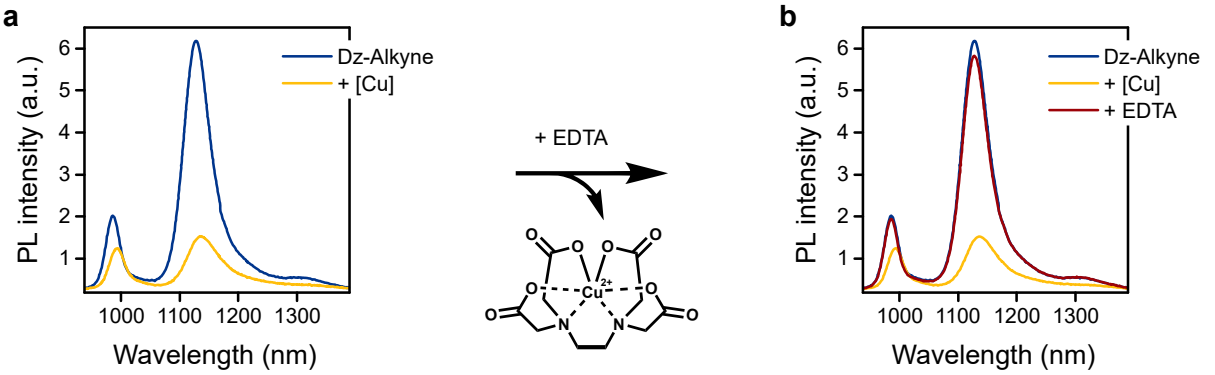

Figure 6.4: a, b) Normalized PL spectra of 4-ethynylbenzene-functionalized (6,5) SWNTs before and after the addition of 30 µM [Cu] (a) and 1 mM EDTA (b).

6.3 Fluorescent probe design and quantitative detection of PP_i

In the envisioned metal displacement detection scheme, the fluorescent probe, *i.e.*, the sp^3-functionalized (6,5) SWNTs, is initially in an "ON" state (Figure 6.5a, b) and switches to its "OFF" state (Figure 6.5c) after the addition of [Cu] due to significant PL quenching. Subsequently, mirroring the effect of EDTA, the addition of PP_i leads to a full recovery of the initial quenching effects, and the sensor returns to its "ON" state (Figure 6.5d).

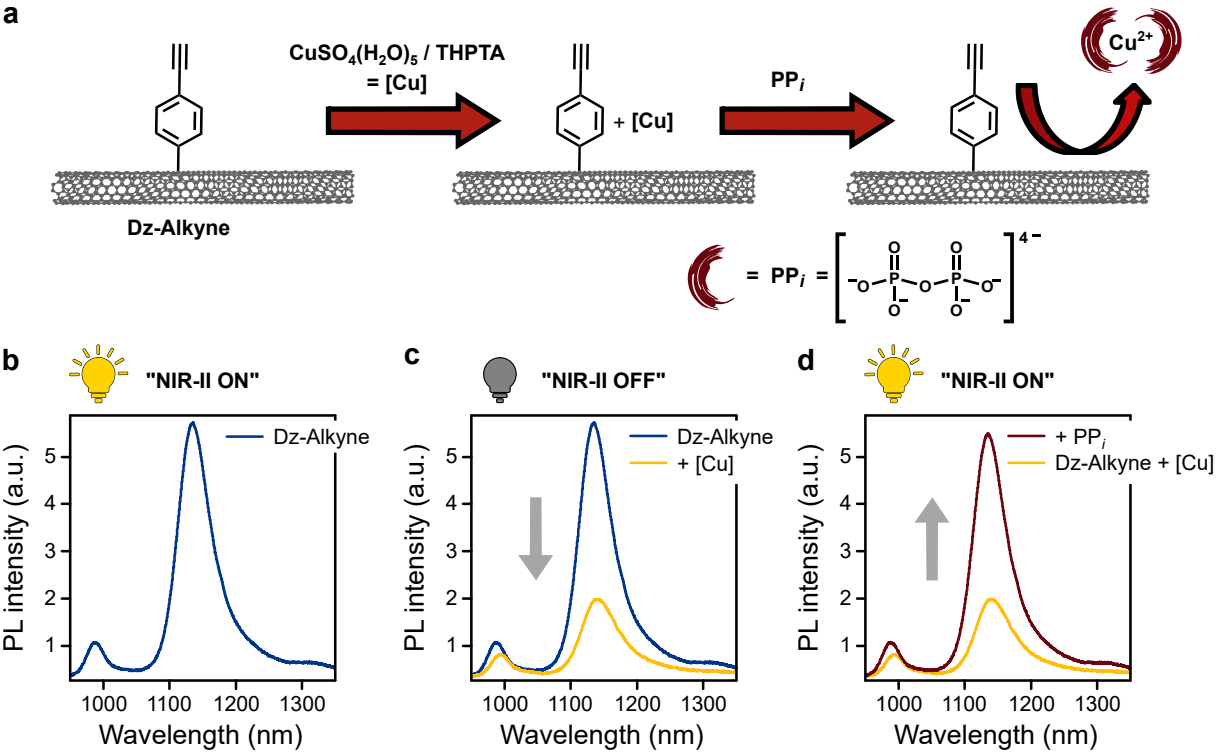

Figure 6.5: a) Overview of the fluorescent probe design. $CuSO_4(H_2O)_5$/THPTA complex ([Cu]) is added to 4-ethynylbenzene-functionalized SDS-coated (6,5) SWNTs, resulting in strong quenching of the E_{11} (988 nm) and E_{11}* (1135 nm) emission. PL quenching is reversed upon addition of PP_i. b) PL spectrum of 4-ethynylbenzene-functionalized SDS-coated (6,5) SWNTs. c) PL spectra before and after the addition of [Cu]. d) PL spectra before and after the addition of PP_i.

This recovery of PL properties serves as the basis for the quantitative detection of PP_i. To investigate its potential, 4-ethynyl-functionalized (6,5) SWNTs were quenched with 15 µM [Cu], unless stated otherwise, to induce substantial PL quenching while maintaining the total [Cu] concentration as low as possible. Following a 15-minute incubation period, small aliquots of PP_i were added to modulate the concentration of PP_i, and PL spectra were recorded (see Figure 6.6). For PP_i concentrations between 12 µM and 10.94 mM, the E_{11} and E_{11}* PL intensities as well as E_{11}*/E_{11} PL ratios gradually recovered allowing for calibration curves to be obtained when plotted on a logarithmic scale. This process inversely mirrors the [Cu]-induced PL quenching shown in Figure 6.3b.

Interestingly, at high PP_i concentrations, a reduction in PL intensity was observed. The observed decrease in PL intensity at very high concentrations of PP_i can be attributed to the aggregation of SDS-coated (6,5) SWNTs in the presence of high salt concentrations. In such conditions, the salt reduces the colloidal stability of the SWNTs by partially shielding the stabilizing negative charges of the SDS sulfate groups. This effect was also observed in the absence of [Cu] for high concentrations of PP_i (see Appendix C, Figure C.1). Analogous results were reported by Niyogi and Koh *et al.*[367,368] Nevertheless, this side-effect has a significantly lower impact on the E_{11}*/E_{11} PL ratio, which remained roughly stable even at elevated PP_i concentrations.

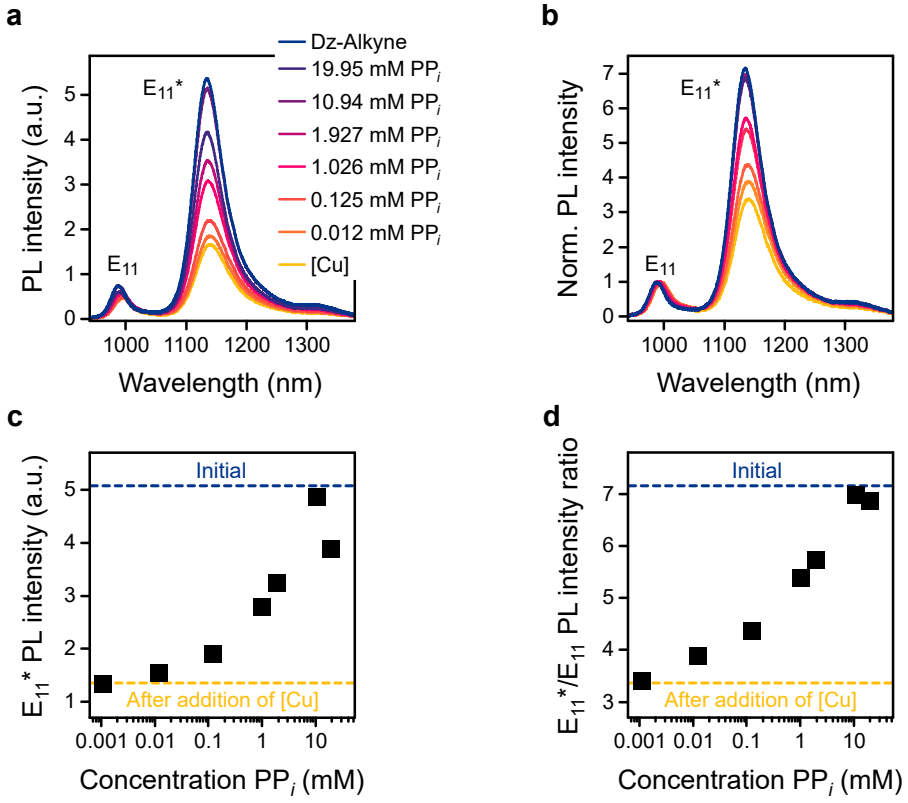

Figure 6.6: a,b) Absolute PL spectra (a) and normalized PL spectra (b) of 4-ethynylbenzene-functionalized (6,5) SWNTs were measured before and after the addition of [Cu] (15 µM) followed by the subsequent adjustment of the PP_i concentration. Extracted E_{11}* PL intensities (c) and E_{11}*/E_{11} PL intensity ratios (d) plotted against the concentration of PP_i. The PL intensity before (labeled as initial) and after the addition of [Cu] are indicated by blue and yellow dashed lines, respectively.

The higher sensitivity of the E_{11}* emission to variations in the chemical environment of the SWNT enables ratiometric detection schemes for PP_i. In such schemes, the E_{11} PL intensity serves as an internal calibration, correcting for changes in the local concentration of SWNTs (*e.g.*, due to aggregation) or fluctuations in the excitation density. Consequently, it removes external effects that affect the E_{11} and E_{11}* emission features to the same extent. Importantly, both emission features are expected to originate from the same fluorophore, further reducing variability from external factors and simplifying the overall experimental design. These inherent properties make ratiometric detection a powerful approach in analytical chemistry, generally providing higher reproducibility and selectivity compared to absolute PL intensity measurements.
Lastly, the suitability of the shifts in E_{11} and E_{11}* PL peak position as a quantification metric is evaluated. Again, the observed redshifts after [Cu] addition are systematically reversed and strongly correlate with the concentration of added PP_i. The initial E_{11} and E_{11}* peak positions of 4-ethynylbenzene-functionalized (6,5) SWNTs are restored for a PP_i concentration of about 10 mM. Shifts in the PL peak position hold great practical relevance due to their ease of read-out. Observed shifts ($\Delta\lambda \approx 6$ nm) are significantly larger than those previously noted for ssDNA-wrapped functionalized SWNTs ($\Delta\lambda < 3$ nm)[22] and occur over a wide concentration window (four orders of magnitude). The combination of such substantial PL shifts with changes in PL intensity (ratio) has the potential to greatly enhance sensor performance.

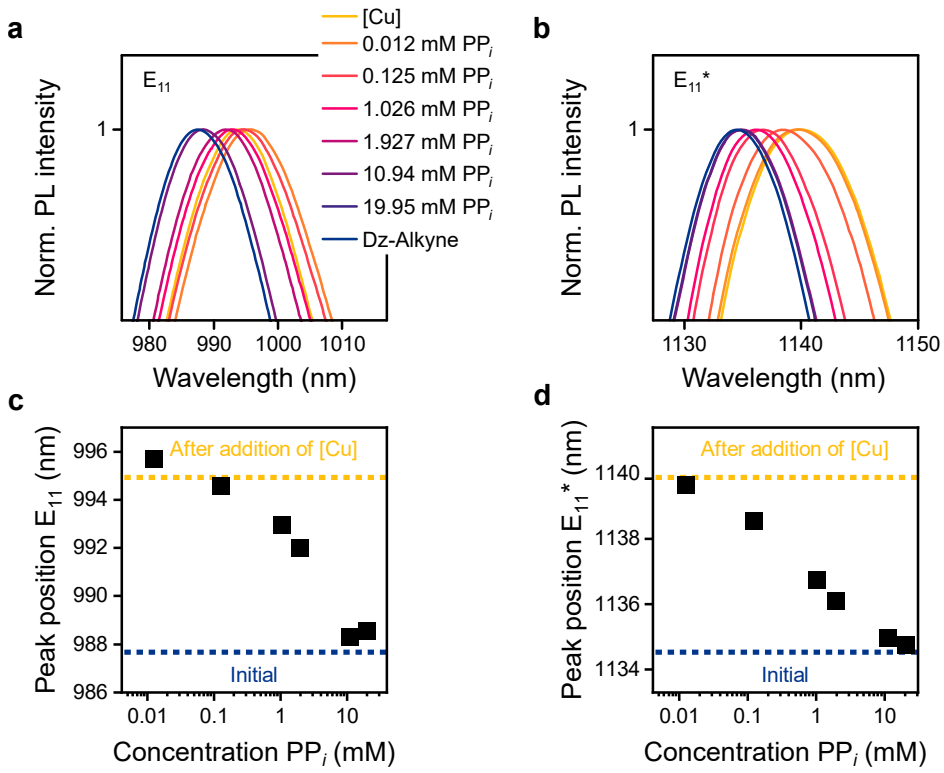

Figure 6.7: a,b) Zoom-in on normalized (to E_{11} (a) and E_{11}* (b)) PL spectra of 4-ethynylbenzene-functionalized SDS-coated (6,5) SWNTs after addition of 15 µM [Cu] and various concentrations of PP_i. c,d) Extracted concentration-dependent E_{11} (c) and E_{11}* (d) PL peak positions. Peak positions before (initial) and after the addition of [Cu] are indicated by blue and yellow dashed lines, respectively.

In summary, all detection metrics show a strong correlation with the concentration of PP_i and enable robust quantification of PP_i within a concentration range from 100 µM to 10 mM. In total, five distinct detection metrics (PL intensities (2x), peak positions (2x) and PL ratio) can be effectively employed. They underscore the potential for the quantitative PP_i detection using sp^3-functionalized SWNTs as fluorescent probes in the NIR-II.

6.4 Selectivity of sp^3-functionalized SWNT probes

In biological environments, ions in general and anions structurally similar to PP_i, such as P_i, are omnipresent. Hence, sensor selectivity is essential in addition to sensitivity. For example, in the case of ssDNA-wrapped SWNTs, it has been shown that fluctuations in ion concentration can significantly impact sensor properties.[369,370] To evaluate the selectivity of the developed SWNT sensor, 4-ethynylbenzene-functionalized SDS-coated (6,5) SWNTs were again quenched with 15 µM [Cu]. Subsequently, 1 mM of potentially interfering anions were added and PL spectra were recorded and displayed in Figure 6.8 (see Appendix C, Figure C.2 for absolute PL spectra). Typically, the concentrations of tested analytes are much lower in biologically relevant systems, yet this depends heavily on the exact biofluid and respective analyte.

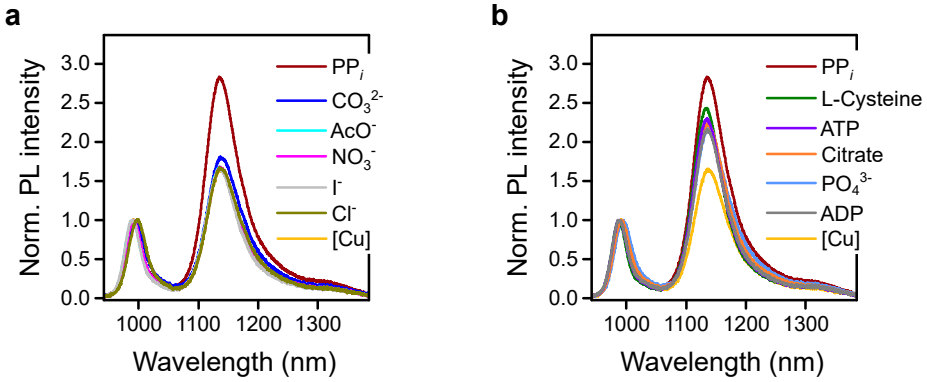

Figure 6.8: a,b) Normalized PL spectra of 4-ethynylbenzene-functionalized SDS-coated (6,5) SWNTs that were previously quenched with 15 µM [Cu] after addition of various strongly (a) or weakly (b) copper-complexing analytes (concentration 1 mM). The normalized PL spectrum after addition of 1 mM PP_i is displayed for comparison.

The ability of each analyte to complex Cu^{2+} ions is expected to correlate directly with the sensor response. Thus, the focus was on the respective anion of the analyte. The analyte can be broadly classified into two categories: Weakly copper-complexing and strongly copper-complexing analytes. In agreement with the employed detection scheme, analytes that weakly complex copper (*i.e.*, CO_3^{2-}, NO_3^-, Cl^-, AcO^-, I^-, see Figure 6.8a) induce only minor changes in the E_{11}^*/E_{11} PL intensity ratio and the E_{11}^* intensity.
Of particular interest is the response to the addition of Cl^- anions in the form of $CaCl_2$. This is the only divalent salt used in this study, and has been shown to have a greater influence on the sensor properties of ssDNA-SWNT sensors than monovalent salts. Pronounced redshifts in the E_{11} peak position have been reported and are also evident in this study ($\Delta\lambda = 6$ nm), but the E_{11}^* peak position is not altered. While in the case of unfunctionalized ssDNA-SWNTs, the influence

of, *e.g.*, Ca^{2+} ions was addressed by increasing the rigidity of the backbone through the use of xenonucleic acids (XNAs),[370] the results obtained here suggest that such a workaround may not be necessary for ssDNA-SWNTs that have been covalently functionalized. Consequently, the influence of ionic strength on the here developed sensor, or on sp^3-functionalized SWNTs in general, should be further investigated.

In clear contrast to weakly copper-complexing analytes, analytes suspected to exhibit high affinity towards Cu^{2+} ions (*i.e.* PO_4^{3-}, citrate, ADP, ATP, L-cysteine, PP_i) led to a significant increase in the PL intensity ratio (see Figure 6.8b). All extracted E_{11}^*/E_{11} PL intensity ratios and E_{11}^* PL intensities after the addition of the respective analytes are shown in Figure 6.9. The categorization into weakly and strongly copper-complexing analytes is especially pronounced for changes in the E_{11}/E_{11} PL intensity ratio, yet weaker for the change in E_{11}^* PL intensity. A combination of both metrics may therefore be useful for discrimination between different analytes.

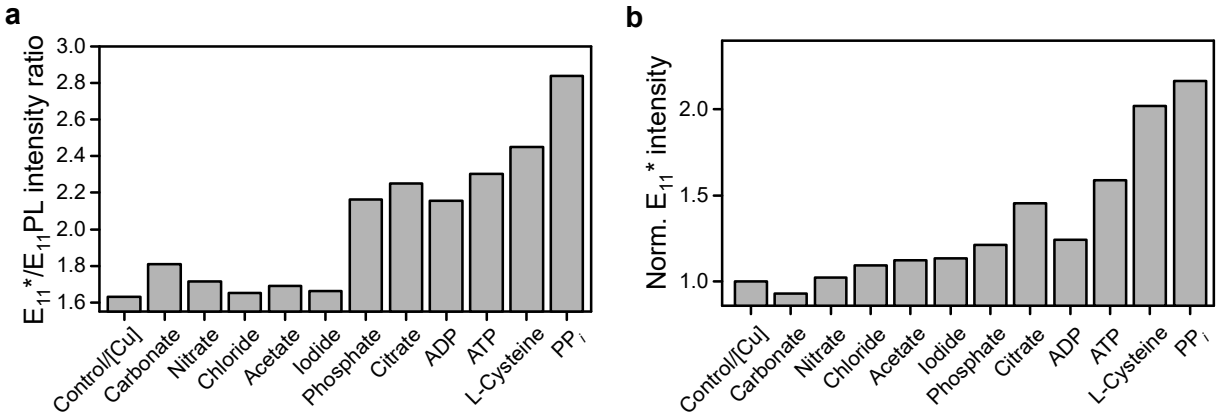

Figure 6.9: a,b) Extracted E_{11}^*/E_{11} PL intensity ratios (a) and normalized E_{11}^* intensities (b) of 4-ethynylbenzene-functionalized SDS-coated (6,5) SWNTs, that were previously quenched with 15 µM [Cu] (control), after the addition of various weakly or strongly copper-complexing analytes (concentration 1 mM).

In addition to the PL intensities and PL intensity ratio, the E_{11} and E_{11}^* PL peak positions offer additional parameters for identification. The PL peak position is expected to correlate with the change in the PL intensity ratio, as indicated in black in Figure 6.10a,b. However, changes in the PL peak positions appear to be unique for each analyte. This finding might be particularly useful to differentiate between PP_i and structurally similar compounds such as ATP and ADP. PP_i differs significantly from ATP and ADP in its shifts of the PL peak positions, showing a much less pronounced blueshifts than what would be expected from the linear correlation between the PL peak position and the PL intensity ratio. The opposite is true for ATP and ADP, and thus, PL peak positions emerge as a valuable analytical tool to differentiate between ATP/ADP and PP_i.

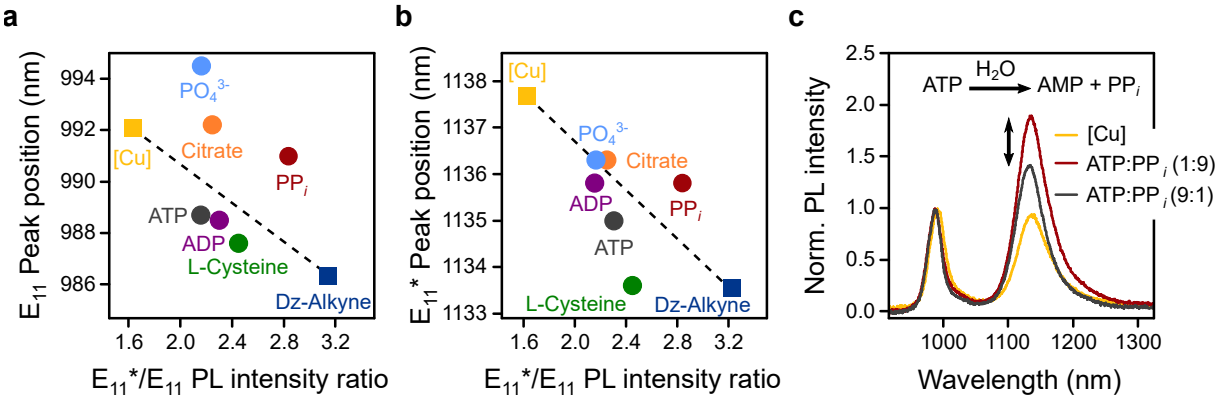

Figure 6.10: a, b) Extracted E_{11} (a) and E_{11}* (b) PL peak positions of 4-ethynylbenzene-functionalized SDS-coated (6,5) SWNTs, previously quenched with 15 µM [Cu] after addition of various strongly copper-complexing analytes (concentration 1 mM), plotted against the E_{11}*/E_{11} PL intensity ratio. The black dotted line is a guide to the eye and represents a linear correlation between the PL peak position and the E_{11}*/E_{11} PL intensity ratio. c) Normalized PL spectra after the addition of different ratios of ATP and PP_i. The total analyte concentration was 1 mM. The black arrow indicates the hypothetical detectable change for the conversion of ATP to PP_i *e.g.*, by a hydrolysis reaction (equation above).

Although the demonstrated selectivity for PP_i may not be sufficient to efficiently detect low concentrations of PP_i in the presence of other Cu^{2+} complexing analytes, it may still be possible to detect dynamic changes in PP_i levels. PP_i not only produces the most significant change in absolute E_{11}* PL intensity and PL intensity ratio but also induces unique changes in PL peak position, exhibiting an opposite response to, for example, ATP. This is particularly useful as the concentrations of PP_i and ATP are closely correlated in living cells due to the generation of PP_i during the hydrolysis of ATP.

To explore the possibility of monitoring this hydrolysis reaction, mixtures of ATP and PP_i were added to a dispersion of 4-ethynylbenzene-functionalized SDS-coated (6,5) SWNTs pre-treated with [Cu]. The total concentration ($C_{total} = C_{ATP} + C_{PP_i}$) was kept constant at 1 mM, but different ATP:PP_i mixing ratios were used (1 : 9 and 9 : 1). Consistent with previous results, an increase in the PL intensity ratio was observed (see Figure 6.10c), but this increase was significantly higher at high PP_i concentrations (ATP:PP_i, 1 : 9). This change in E_{11}*/E_{11} PL intensity ratio, coupled with the observed blueshift at higher PP_i concentrations, suggests the potential of the sensor for real-time monitoring of the hydrolysis of ATP to PP_i. Similar results were obtained at total analyte concentrations of 0.5 mM and 4.0 mM (Appendix C, Figures C.3 and C.4).

Although the presented sensor exhibits good selectivity and sensitivity towards PP_i, even in the presence of other copper-complexing analytes, it is apparent that developing a more selective sensor is essential for quantifying PP_i in a real biological system. Achieving this goal requires a fundamental understanding of the underlying sensing and PL quenching mechanism.

6.5 PP_i sensing & PL quenching mechanism

In the following, the PP_i sensing will be investigated in detail with respect to the ligand THPTA, the functional group, the impact of sp^3 defect density, and the mechanism of PL quenching.
In a metal displacement assay, the acceptor molecule, or more broadly, the linker between the metal center and the fluorophore, plays an essential role. Thus, its role will be discussed first. The acceptor molecule determines how the fluorophore interacts with the metal center (*e.g.*, by distance) and affects the sensors selectivity due to its competitive complexation around the metal center with the target analyte. Two components involved in linking the metal (Cu^{2+} center) to the fluorophore (SWNT) will be discussed: The ligand THPTA and the covalently attached 4-ethynylbenzene moiety.

6.5.1 Impact of the triazole ligand

THPTA itself was found to have a negligible effect on the optical properties of functionalized (6,5) SWNTs, even at elevated concentrations (100 µM), as seen in Figure 6.11a. Consequently, any observed changes in the PL spectra are attributed solely to the presence of Cu^{2+} ions. However, when Cu^{2+} ions were added to functionalized (6,5) SWNTs in the form of $CuSO_4(H_2O)_5$ without THPTA, only moderate PL quenching and no shift in PL peak position was observed (Figure 6.11b).

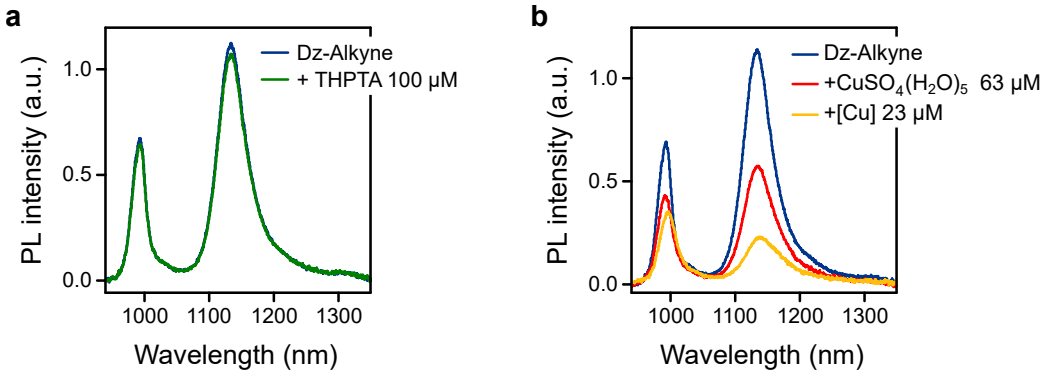

Figure 6.11: a) Absolute PL spectra before and after addition of 100 µM THPTA. b) Absolute PL spectra of 4-ethynylbenzene-functionalized SDS-coated (6,5) SWNTs after addition of 63 µM $CuSO_4(H_2O)_5$ and 23 µM [Cu].

Cu^{2+}-induced PL quenching is expected to correlate closely with the effective concentration of Cu^{2+} ions in close proximity to the SWNT surface or sp^3 defects. The effective concentration, and thus PL quenching, was greatly enhanced when Cu^{2+} ions were added in a pre-complexed form with THPTA. This effect can be rationalized by π-π interactions between the triazole groups of THPTA and the SWNT surface. Adsorption of the Cu^{2+}/THPTA complex ([Cu]) onto the SWNT surface would bring Cu^{2+} ions into direct contact with the SWNT surface and hence increase their effective concentration. In this scenario, the degree of PL quenching should depend on the surface coverage of [Cu] on the SWNT surface. The observed correlation of PL quenching with [Cu] concentration should thus follow a simple Langmuir adsorption isotherm, and the saturation of PL quenching effects at high [Cu] concentration is explained by complete coverage

of the SWNT surface. However, as will be shown later, this is only a simplified picture that can be applied to SWNTs where the functional group is not expected to have an impact on the overall adsorption mechanism.

When [Cu] was added, a significant redshift of the PL peak position occurred besides PL quenching. These observed bathochromic wavelength shifts could be caused by solvatochromism induced by the Cu^{2+} ions at the SWNT surface. Cu^{2+} ions could locally increase the solvent polarity around the SWNT and induce electrostatic stabilization of the photo-excited exciton at the SWNT, resulting in the observed redshift. Alternatively, the SWNT solvation could be altered due to the additional formation of hydration shells around the adsorbed Cu^{2+} ions. Similar solvatochromic shifts that depend on solvent polarity and SWNT solvation have been observed by Larsen *et al.*[123] and were found to influence defect state emission, too, as shown by Shiraki *et al.*[371] Overall, the strong PL quenching and the observed PL shifts can be attributed to the adsorption of [Cu] on the SWNT surface.

6.5.2 Competitive complexation of Cu^{2+} ions

When PP_i is added to a SWNT dispersion containing [Cu], the Cu^{2+}/THPTA complex dissociates, and a $Cu^{2+}/(PP_i)_2$ complex is formed. Since PP_i cannot effectively adsorb to the SWNT surface, the effective concentration of Cu^{2+} ions at the SWNT surface is greatly reduced, and SWNT PL is recovered.

This competitive complexation process can be monitored *in situ* in the absence of SWNTs by tracking the absorption band of [Cu] around 315 nm. The absorption band at this wavelength is ideal for tracking the conversion of Cu^{2+}/THPTA to $Cu^{2+}/(PP_i)_2$ as it is absent in the absorption spectra of the THPTA ligand as well as $CuSO_4(H_2O)_5$ (*i.e.*, solvated Cu^{2+} ions; see Appendix C, Figure C.5). Figure 6.12 shows the titration of 15 µM [Cu] with PP_i, where the absorption feature around 315 nm decreases with increasing PP_i concentration, indicating the complexation of Cu^{2+} ions by PP_i and the release of free THPTA ligand.

Since no absorption feature is expected for the $Cu^{2+}/(PP_i)_2$ complex at this wavelength, the concentration of the Cu/THPTA complex is directly correlated with the absorbance at 315 nm. Furthermore, the previously observed changes in the PL intensity ratio are also directly related to the concentration of the Cu^{2+}/THPTA complex (on the SWNT surface). The values obtained from both, absorbance and PL measurements, are shown in Figure 6.12b and were fitted with a Hill function:

$$Y = \frac{(c_{PP_i})^n}{K_d^n + (c_{PP_i})^n}, \tag{6.1}$$

where c_{PP_i} is the PP_i concentration, K_d is the dissociation constant and n the Hill coefficient. Absorption measurements (in the absence of SWNTs) yield a dissociation constant of $K_d = 20 \cdot 10^{-6}$ M. In contrast, the corresponding K_d derived from PL measurements is 25× higher ($K_d = 516 \cdot 10^{-6}$ M), indicating reduced $Cu^{2+}/(PP_i)_2$ complex formation due to steric shielding of the Cu^{2+} center by adsorption to the SWNT surface. This is reflected in the shift of the calibration curve towards higher concentrations of PP_i (indicated by the grey arrow in Figure 6.12b).

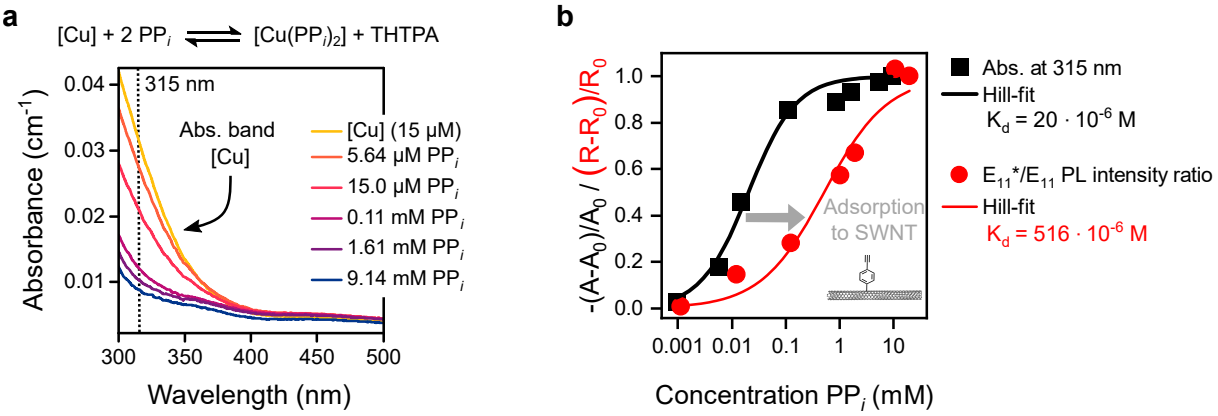

Figure 6.12: a) UV-Vis absorption spectra of pure [Cu] (without SWNTs) measured at various concentrations of PP_i. The absorption band at 315 nm is assigned to the [Cu] complex, which vanishes upon decomplexation due to competitive complexation with PP_i. b) Extracted normalized values obtained from measured absorption spectra (black, A, absorbance at 315 nm for the respective PP_i concentration; A_0, initial absorbance at 315 nm before the addition of PP_i) and PL measurements (red, R, E_{11}/E_{11} PL intensity ratio at the respective PP_i concentration; R_0, initial E_{11}^*/E_{11} PL intensity ratio before the addition of PP_i). Solid lines represent Hill-fits to the data with respective dissociation constants K_d. The grey arrow indicates the impact of the adsorption of [Cu] to the SWNT surface.

Based on this observation, the selectivity as well as the sensitivity of the SWNT sensor towards different analytes can be explained by the competitive complexation of Cu^{2+} ions by THPTA and the respective analyte. To test this hypothesis the complexation equilibrium was shifted by increasing the total concentration of THPTA at a constant Cu^{2+} ion concentration and PP_i-sensing was conducted (Figure 6.13). While only a small increase in PL quenching is observed when the ligand/Cu^{2+} ratio is increased, the complexation equilibrium shifts towards the formation of [Cu] upon the addition of the analyte. Thus, the addition of 1 mM PP_i leads to a reduced response in the PL intensity ratio at higher THPTA:Cu^{2+} ratios, as seen in Figure 6.13b. Consequently, the sensitivity and selectivity of the SWNT sensor can be modified by designing a suitable ligand that exhibits strong physisorption to the SWNT surface and has a suitable complexation strength to achieve higher selectivity towards the desired analyte, such as PP_i. This possibility was tested using a phenantroline ligand as reported by Zhang *et al.*[372] However, the Cu^{2+} ion-induced PL quenching was found to be not fully reversible. Therefore, great care should be taken in designing suitable ligands, and highly planar ligands should be avoided as they may increase the steric shielding effect on the SWNT. Hence, modification of the established Cu^{2+}/triazole complex seems to be a more promising approach for further development of PP_i-sensitive fluorescent SWNT probes.

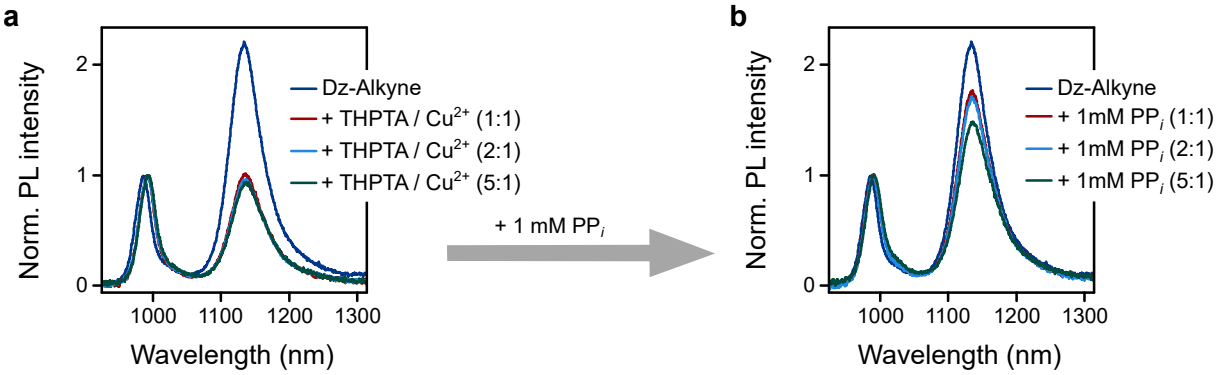

Figure 6.13: a, b) Normalized PL spectra of 4-ethynylbenzene-functionalized SDS-coated (6,5) SWNTs before (a) and after (b) the addition of 1 mM PP_i for different concentrations of THPTA (15, 30, 75 µM) at a fixed concentration of $CuSO_4(H_2O)_5$ (15 µM). Upon the addition of PP_i, high THPTA:$CuSO_4(H_2O)_5$ ratios led to an attenuated response in E_{11}/E_{11} intensity ratio.

6.5.3 Influence of the functional group

Given the importance of [Cu] adsorption on the SWNT surface and thus the binding of the metal center (Cu^{2+}) to the fluorophore (SWNT), the question of the significance of the functional group attached to the sp^3 defect arises. To address this issue, SDS-coated (6,5) SWNTs with simple benzene moieties were synthesized, and their PL quenching was compared to that of functionalized (6,5) SWNTs with a 4-ethynyl motif. Notably, at an equivalent concentration of added [Cu], significantly stronger PL quenching was observed for 4-ethynylbenzene-functionalized SWNTs, as shown in Figure 6.14. This suggests that additional weak coordination of Cu^{2+} ions to the ethynyl group occurs, facilitating SWNT PL quenching. This notion is further supported by the comparable quenching behavior of the E_{11} emission for unfunctionalized (pristine) and benzene-functionalized SWNTs as shown in Figure 6.15.

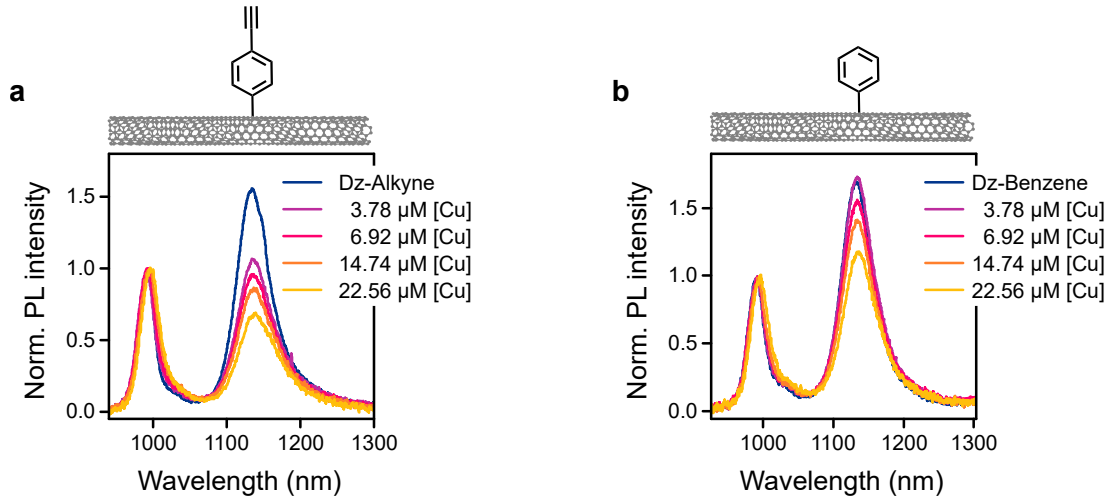

Figure 6.14: a) Normalized PL spectra of 4-ethynylbenzene-functionalized SDS-coated (6,5) SWNTs after the addition of various concentrations of [Cu]. b) Normalized PL spectra of benzene-functionalized SDS-coated (6,5) SWNTs after the addition of various concentrations of [Cu].

The additional weak coordination of Cu^{2+} ions to the ethynyl functional group may affect the PL quenching process in two plausible ways. First, the coordination may increase the presence of Cu^{2+} ions preferentially around sp^3 defect sites, thereby enhancing the quenching of the E_{11}* emission. However, as shown in Figure 6.15b, the quenching of the E_{11} emission is also more pronounced in the presence of ethynyl functional groups. Thus, it is more likely that [Cu] adsorption is accelerated by initial coordination to ethynyl functional groups, resulting in overall stronger PL quenching, including the E_{11} emission.
Consequently, this detection scheme is transferable to other sp^3-functionalized SWNTs, but will greatly benefit from additional interactions of the functional group with the metal center. Functionalization with heterocycle-substituted aryl diazonium salts as reported by Yu *et al.*[187] could offer a valuable approach to further enhance this effect by increasing the coordination strength of the functional group to the metal center.

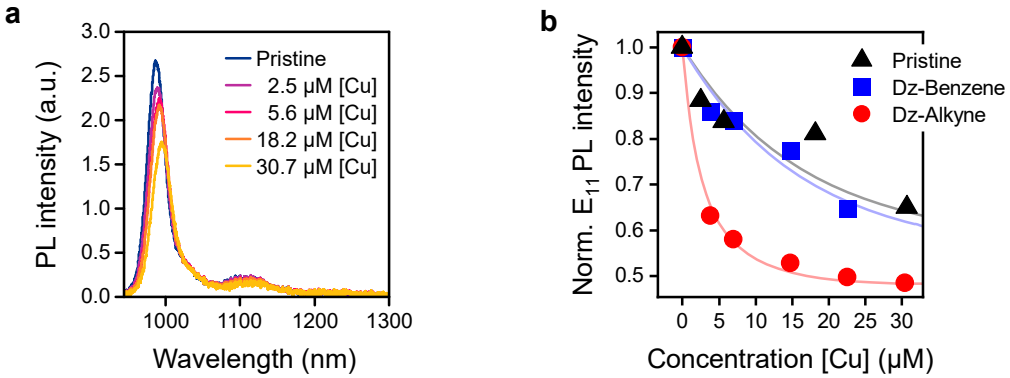

Figure 6.15: a) Absolute PL spectra of pristine SDS-coated (6,5) SWNTs after the addition of various concentrations of [Cu]. b) Extracted E_{11} PL intensities normalized to their initial values before addition of [Cu] for pristine, benzene-functionalized and 4-ethynylbenzene-functionalized SDS-coated (6,5) SWNTs plotted against the added concentration of [Cu].

6.5.4 Influence of the sp^3 defect density

Further in-depth investigations were carried out to evaluate the influence of the defect density of functionalized (6,5) SWNTs on the sensor properties, particularly with respect to quenching by copper ([Cu]) and PP_i sensing. Covalent functionalization was performed at three different concentrations of Dz-Alkyne, yielding functionalized (6,5) SWNTs with varying defect densities. To qualitatively determine the defect density, Raman spectra were recorded for all samples and are displayed in Figure 6.16a. Additionally, the differential Raman $\Delta D/G^+$ area ratios were extracted (see Section 3.6.2). For analysis of the impact of the defect density on the sensor properties, PL spectra were recorded after the addition of 15 µM [Cu] and subsequent addition of 4 mM PP_i (see Appendix C, Figure C.6 for PL spectra).
The quenching factor (QF, $I_{[Cu]}/I_{Ref\text{-}Alkyne}$) of the E_{11}*/E_{11} PL intensity ratio and the relative change of PL before and after the addition of PP_i ($I_{PP_i}/I_{[Cu]}$) were analyzed with respect to the defect density. Figure 6.16b shows that the reduction in the PL intensity ratio upon addition of [Cu] is lower at higher defect densities. This finding can be rationalized by the need for more Cu^{2+} ions in close proximity to the defect sites to achieve an equally strong quenching of the

E_{11}* emission. However, no change in sensitivity was found, as the QF remains approximately constant upon the addition of 4 mM PP_i. Thus, the dynamic range of the sensor, considering the PL intensity ratio, is expected to remain independent of the defect density.

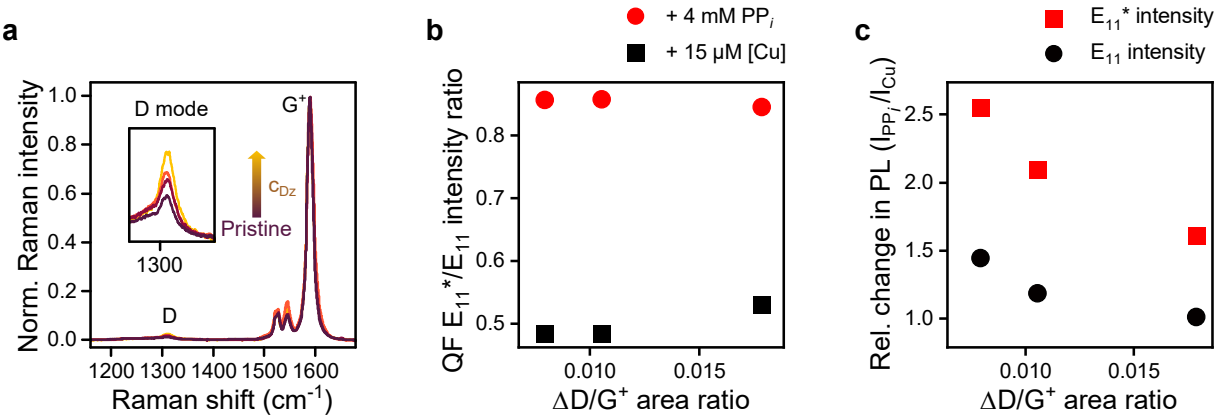

Figure 6.16: a) Normalized Raman spectra of SDS-coated (6,5) SWNTs upon functionalization at different concentrations of Dz-Alkyne. b) Extracted quenching factor (QF) of the E_{11}*/E_{11} intensity ratio *versus* the change in D/G^+ area ratio ($\Delta D/G^+$). c) Relative change in PL intensity ($I_{PP_i}/I_{[Cu]}$) of E_{11} and E_{11}* emission *versus* $\Delta D/G^+$.

In contrast to the PL intensity ratio, a clear dependence was observed in the relative change of absolute PL intensities as shown in Figure 6.16c. The correlation of $\Delta D/G^+$ with the relative intensity change $I_{PP_i}/I_{[Cu]}$ clearly shows an increasing sensitivity to PP_i at lower defect densities. Thus, the dynamic range of the sensor could be tailored by the defect density, with the highest sensitivity expected at extremely low defect densities. However, given the minimal effect on the PL intensity ratio, the advantages of operating the sensor close to the defect density where maximum PLQY is obtained are expected to outweigh the advantages of adjusting the sensitivity in absolute PL intensity to the ideal range.

6.5.5 Origin of PL quenching

From the experiments and analyses performed so far, it is clear that PL quenching occurs due to the adsorption of [Cu] on the SWNT surface, with recovery observed upon complexation of Cu^{2+} ions by the analyte (PP_i). However, the next question that must be addressed is the exact cause of the induced quenching. In the following, possible causes for Cu^{2+}-induced PL quenching shall be discussed, namely SWNT aggregation, bleaching effects, formation of non-emissive ground state complexes, paramagnetic effects, and electron transfer to the metal center. Additional factors, such as the influence of the counterion and the effect of pH, were found to be negligible by Brege *et al.*[373] and Wulf *et al.*[318] and were not investigated here.

To investigate [Cu]-induced SWNT aggregation and bleaching effects, UV-Vis-NIR absorption spectra of 4-ethynylbenzene-functionalized (6,5) SWNTs were recorded after the addition of 15 µM [Cu], and displayed in Figure 6.17. However, both effects can be ruled out, as besides a ~5 nm redshift no reduction in absorption by the E_{11} transition was observed.

To investigate the formation of non-emissive SWNT-Cu^{2+} ground state complexes, the PL decays of the E_{11}* defect-state emission were recorded using TCSPC under pulsed laser excitation, as shown in Figure 6.17b (for normalized PL spectra, see Figure 6.17c). In this context, the extremely fast decay of the E_{11} excitons (few picoseconds) cannot be directly probed, but similar decay dynamics are assumed. Reconvolution fitting of the obtained defect-state PL decay traces revealed a biexponential decay, as commonly found at room temperature,[139] although a substantially shorter amplitude-averaged lifetime ($\tau_{A\text{-}avg.}$) is extracted when [Cu] is added (see Figure 6.17b). Thus, $\tau_{A\text{-}avg.}$ decreases from 151 ps to 79 ps, indicating the presence of new non-radiative decay pathways associated with the Cu^{2+} ions. The quenching process can therefore be considered dynamic rather than static in nature.[374] After the addition of PP_i, the defect-state lifetime recovered to the original level prior to addition of [Cu], as shown in Figure 6.17d.

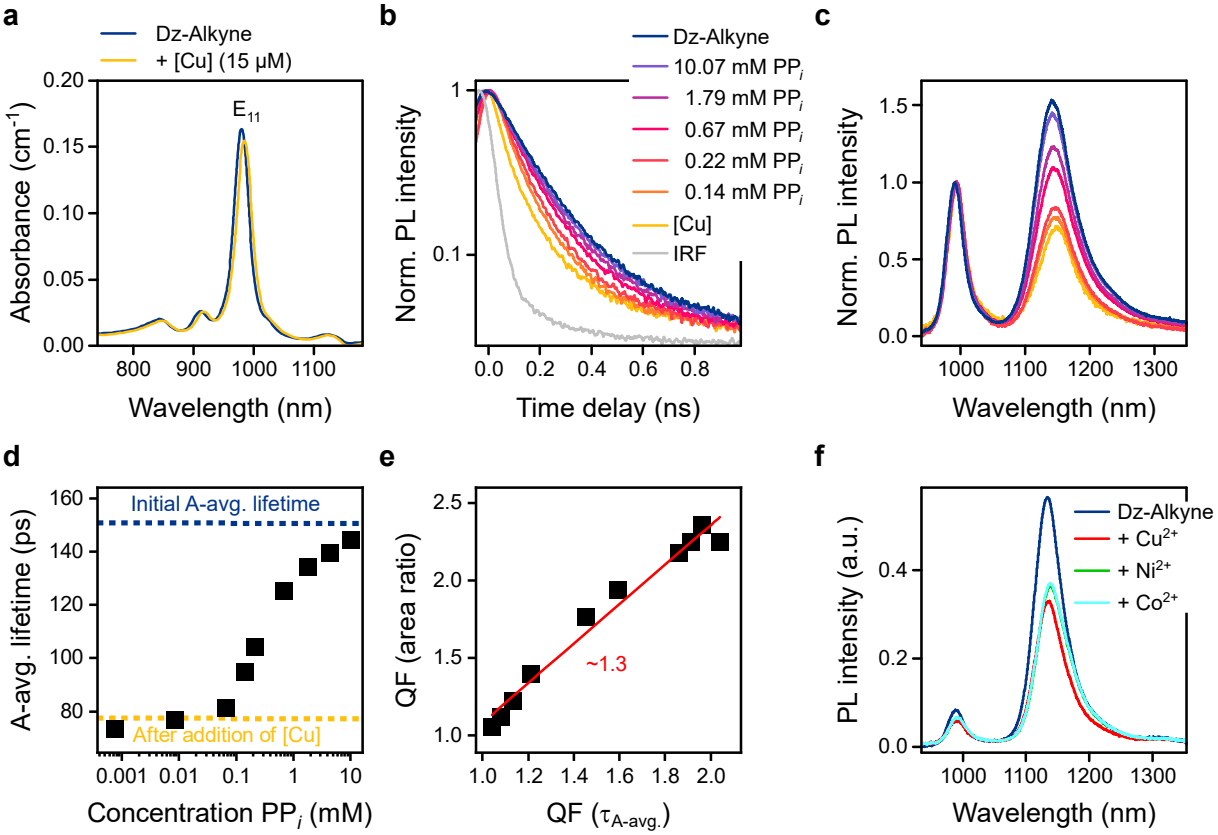

Figure 6.17: a) Absorption spectra of 4-ethynylbenzene-functionalized SDS-coated (6,5) SWNTs before and after addition of 15 µM [Cu]. b) PL decay traces recorded for E_{11}* emission of 4-ethynylbenzene-functionalized SDS-coated (6,5) SWNTs after addition of [Cu] and different concentrations of PP_i. c) Corresponding normalized PL spectra recorded under pulsed laser excitation. d) Extracted $\tau_{A\text{-}avg.}$ lifetimes of E_{11}* emission from biexponential fits plotted against the concentration of PP_i. Initial values before and after addition of [Cu] are indicated by blue and yellow dashed lines, respectively. e) QFs extracted from E_{11}*/E_{11} PL area ratios plotted against the QFs extracted from $\tau_{A\text{-}avg.}$. The red solid line represents a linear fit to the data with a slope of ~ 1.3. f) Absolute PL spectra after addition of $CuSO_4(H_2O)_5$, $NiSO_4(H_2O)_6$ and $CoSO_4(H_2O)_7$ (0.25 mM). Note that PL spectra after addition of $NiSO_4(H_2O)_6$ and $CoSO_4(H_2O)_7$ overlap strongly.

To assess whether ground state quenching and dynamic quenching processes might occur simultaneously, the corresponding QFs were extracted from the defect-state lifetime measurements and the corresponding PL measurements. A linear correlation with a slope of ~1.3 was observed between the two QFs. Consequently, the degree of PL quenching is consistent with the shortening of the PL lifetime, and the observed PL quenching can be fully explained by faster non-radiative relaxation of the defect-state exciton due to the presence of new non-radiative decay pathways in the presence of Cu^{2+} ions. Furthermore, given the close correlation between the E_{11}* lifetime and PP_i concentration, the presented SWNT sensor may serve as a suitable probe for next-generation NIR-II lifetime imaging microscopy (FLIM).[375]

The PL quenching of organic fluorophores by Cu^{2+} ions is typically attributed either to their paramagnetic properties or to fast electron transfer mechanisms. In the case of paramagnetic PL quenching, a strong correlation with the magnetic moment of the metal center is expected. To test this hypothesis, PL quenching induced by Cu^{2+} (d^9) ions was compared to other paramagnetic ions such as Ni^{2+} (d^8) and Co^{2+} (d^7) by addition of the respective sulfates (250 µM). However, the observed quenching efficiencies ($Cu^{2+} > Ni^{2+} = Co^{2+}$) were found to be inconsistent with their order in magnetic moments (μ_{eff}): Co^{2+} ($\mu_{eff} = 3.72$) > Ni^{2+} ($\mu_{eff} = 3.11$) > Cu^{2+} ($\mu_{eff} = 1.83$).[373] Therefore, the observed PL quenching is unlikely to be caused by paramagnetic effects, given the lack of correlation with the magnetic moment. This finding is consistent with studies by Brege *et al.* on SDBS-dispersed SWNTs.[373] Consequently, other non-radiative decay pathways, such as photo-induced electron transfer (PET), must be considered.

PET is an excited state charge transfer in which an electron would be transferred from a trapped exciton at the defect site to the Cu^{2+} center, resulting in its reduction to Cu^{+}. The electron is then transferred back to the SWNT/sp^3 defect, where charge recombination to the E_{11} ground state occurs. To evaluate this process, the Gibbs free energy (ΔG_{PET}) of the initial electron transfer from the sp^3 defect of the SWNT (D, donor) to the Cu^{2+} center (A, acceptor) was calculated according to:[374]

$$\Delta G_{PET} = eE_{red}(D^+/D) - eE_{red}(A/A^-) - \Delta G_{00} - \frac{e^2}{4\pi\varepsilon_r\varepsilon_0 d}\,, \tag{6.2}$$

where E_{red} is the reduction potential, ΔG_{00} is the optical transition energy, ε_r is the relative permittivity of water (ε_r (20 °C) = 80), and d is the assumed distance of about 1.0 nm between the defect site and the metal center. Previously reported redox potential values of Cu(II)/Cu(I) (E^0 (V) = 0.161)[376] and functionalized (6,5) SWNTs (E^{ox} (V) = 0.584 *vs.* Ag/AgCl)[377] were used. For this calculation the shift of the redox potential of Cu(II) upon complexation with THPTA was neglected in this estimation due to its unknown shift upon additional adsorption to the SWNT sidewall. PET from the sp^3 defect to the metal center is thermodynamically favorable, as a large negative ΔG_{PET} of −2.05 eV was calculated (ΔG_{PET} of −2.24 eV for pristine).[374] Furthermore, considering that the rate of PET is expected to decrease exponentially with the distance between the SWNT surface and the metal center, the strong increase in PL quenching upon adsorption to the SWNT surface *via* THPTA complexation can be explained.[378] Thus, equally strong PL quenching by Ni(II) and Co(II) ions is expected to originate from their similar standard reduction potentials (Ni(II/0) E^0 (V) = −0.26 and Co(II/0) E^0 (V) = −0.28),[376] where a negative ΔG_{PET} of −1.61 eV and −1.65 eV was calculated, respectively.

Overall, PET represents a plausible primary cause for PL quenching, and its efficiency is expected to correlate with the standard reduction potential of the metal ion. However, further studies on highly purified SWNTs with different metal ions and ideally a non-coordinating functional group are required to obtain a more conclusive picture.

6.5.6 Summary PP_i sensing & quenching mechanism

In summary, the following mechanism for Cu^{2+} immobilization and PL quenching can be proposed, as schematically shown in Figure 6.18. Upon the addition of [Cu] to 4-ethynylbenzene-functionalized (6,5) SWNTs, strong adsorption occurs *via* π-π interactions between the triazole and the SWNT, immobilizing Cu^{2+} ions on the SWNT surface. This process is facilitated by additional weak coordination of Cu^{2+} ions to the ethynyl functional groups, potentially leading to an increased concentration around defect sites. Dynamic PL quenching likely occurs *via* PET from the SWNT to the Cu^{2+} metal centers, which is stronger for E_{11}* excitons than for E_{11} excitons due to the former's longer lifetime ($\tau_{A\text{-avg.}}$ 151 ps *vs.* 10 ps).[126] Hence, the combination of increased Cu^{2+} ion concentrations around the defect site and stronger quenching of E_{11}* excitons, leads to the observed reduction in the E_{11}*/E_{11} PL ratio. The sensitivity and selectivity of the SWNT sensor are expected to depend on the competitive complexation of Cu^{2+} ions between the ligand (THPTA) and the analyte (PP_i). Hence, when this equilibrium is shifted, the response of the sensor changes. Lastly, the sp^3 defect density was found to have a negligible effect on the E_{11}*/E_{11} intensity ratio but leads to slight shifts in the sensor sensitivity when considering absolute PL intensities. The SWNT sensor was found to exhibit the highest sensitivity towards PP_i at low sp^3 defect densities.

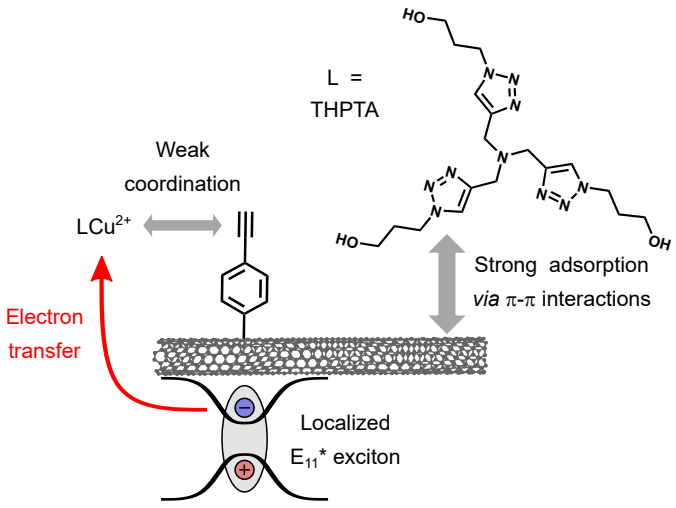

Figure 6.18: Schematic illustration of the suggested adsorption and quenching mechanism. Cu^{2+} ions are immobilized through π-π interactions of the triazole ligand (L = THPTA) with the SWNT sidewall, further facilitated by weak coordination to the ethynyl moieties of the functional groups attached to the sp^3 defects. Following exciton formation and diffusion to defect sites, E_{11}* excitons undergo fast electron transfer to the metal center, resulting in efficient PL quenching.

6.6 Detection of PP_i with PL-PEG_{5000}-stabilized SWNTs in biological environments

In all experiments conducted so far, SWNTs were dispersed in SDS. However, SDS represents an anionic detergent that is toxic to living cells due to its strong denaturing properties, which can disrupt the structure of proteins and cell membranes.[379] Thus, before considering any biomedical application of the developed SWNT sensor, a surfactant with better biocompatibility is required. A potential alternative is the heteropolymer PL-PEG, known for its minimal cytotoxicity and its ability to achieve stable dispersions of SWNTs for extended periods of time.[208] Hence, surfactant exchange, as described in Section 3.3.1, was performed from SDS-coated functionalized SWNTs to PL-PEG_{5000}-coated functionalized SWNTs *via* kinetic exchange dialysis.[208] Figure 6.19a shows the normalized PL spectra for this transfer. Consistent with the observations in Section 5.8, a 6 nm redshift in the E_{11} transition was observed after dialysis, while all other spectroscopic features remained unchanged.

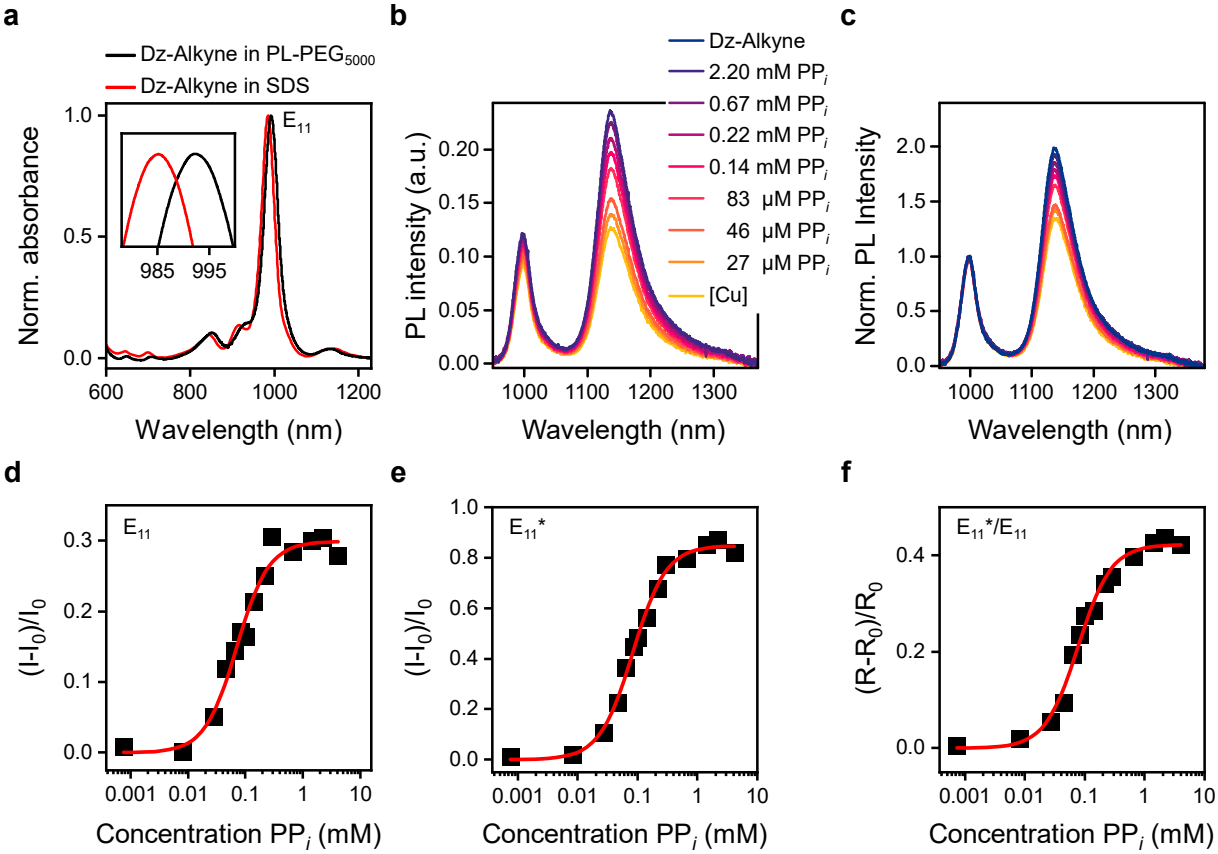

Figure 6.19: a) Normalized absorption spectra with a zoom-in on the E_{11} transition of 4-ethynylbenzene-functionalized (6,5) SWNTs before and after surfactant exchange from SDS to PL-PEG_{5000}. b, c) Absolute (b) and normalized (c) PL spectra of 4-ethynylbenzene-functionalized PL-PEG_{5000}-coated (6,5) SWNTs in 10 mM MOPS buffer after the addition of [Cu] and various concentrations of PP_i. d–f) Concentration-dependent changes of the E_{11} (d), E_{11}* (e) PL intensity, and E_{11}*/E_{11} PL intensity ratio (f) in response to varying PP_i concentrations. I_0 (R_0) represents the PL intensity (ratio) directly after the addition of [Cu], while I (R) represents the PL intensity (ratio) at the respective concentration of PP_i. Red solid lines indicate Hill-fits to the data.

Before PP_i can be detected in a biocompatible environment, efficient PL quenching with [Cu] must occur, and the SWNT sensor should ideally be transferred to a buffer solution close to physiological pH. To achieve this, a modified SWNT sensor preparation procedure was performed, as described in detail in Section 3.4. Briefly, the relative concentration of [Cu] compared to the SWNT concentration was increased, and a THPTA:$CuSO_4(H_2O)_5$ ratio of 5 : 1 was chosen to maximize surface coverage. After an incubation period of 15 min, excess [Cu] was removed by spin filtration (100 kD MWCO), and the concentrated [Cu]-quenched SWNT sensor was re-dispersed in a 10 mM EDTA-free 3-*N*-morpholinopropane sulfonic acid (MOPS) buffer solution. MOPS buffer was chosen due to its low affinity to bind Cu^{2+} ions.[380] The obtained dispersion was further diluted to an absorbance of 0.1 cm^{-1} at the corresponding E_{11} transition of (6,5) SWNTs.

The recorded PL spectra after this processing is shown in Figure 6.19b,c and reveal that while PL quenching was lower compared to SDS-coated (6,5) SWNTs (compare to Figure 6.6), the E_{11}/E_{11} intensity ratio clearly decreased from ~2 to ~1.35. Hence, [Cu] remained physisorbed on the SWNT surface while excess [Cu] was removed during filtration and Cu^{2+} ion-induced PL quenching remains active. The reduced PL quenching is expected to originate from the increased coverage of the SWNT surface by PL-PEG_{5000}. Based on the analysis of solvatochromic shifts, it is estimated that PL-PEG_{5000} results in a very high relative surface coverage compared to SDS.[243,381,382] This notion is further supported by the fact that almost no Cu^{2+}-induced PL quenching was observed for DOC-coated functionalized (6,5) SWNTs due to the known dense packing of DOC on the SWNT surface (see Appendix C, Figure C.7).[76] Other biocompatible polymer coatings such as $(AT)_{15}$-ss-DNA or PL-PEG with lower molecular weight may therefore be more suitable in this detection scheme, as they are reported to exhibit lower surface coverage and similar PL quenching to SDS-coated SWNTs can be expected.

Importantly, the sensor remains fully functional and shows a concentration-dependent PL response of E_{11} and E_{11}* emission as well as E_{11}*/E_{11} intensity ratio upon the addition of PP_i (Figure 6.19b and c). A dose-response curve was computed from the extracted PL intensities (I) and E_{11}/E_{11} PL ratios (R), and fitted with a Hill function according to Equation 6.1 and shown in Figures 6.19d-f. The extracted values from Hill-fits will be discussed later.

Since the overall Cu^{2+}-induced PL changes are attenuated, only small shifts in PL peak position (1-2 nm) were observed for E_{11} and E_{11}* emission (Figure 6.20). Although still significant, the scattering of the data points is significantly increased compared to the PL intensities and PL intensity ratios.

Crucially, when additional concentration-dependent PL spectra were recorded for functionalized (6,5) SWNTs with higher sp^3 defect density, similar PL responses were obtained (see Appendix C, Figures C.8 and C.9). This validates the reproducibility of the sensor and demonstrates effective PP_i detection over multiple batches of functionalized (6,5) SWNTs. However, when comparing the responses in PL intensities as well as PL peak positions for both batches, a noticeable deviation was observed. As already noted in Figure 6.16 and discussed in Section 6.5.4, the defect density has a slight but significant influence on the detection range of the sensor. Figure 6.21a shows that the response is slightly shifted towards lower concentrations of PP_i at low sp^3 defect density compared to sensing at high sp^3 defect density.

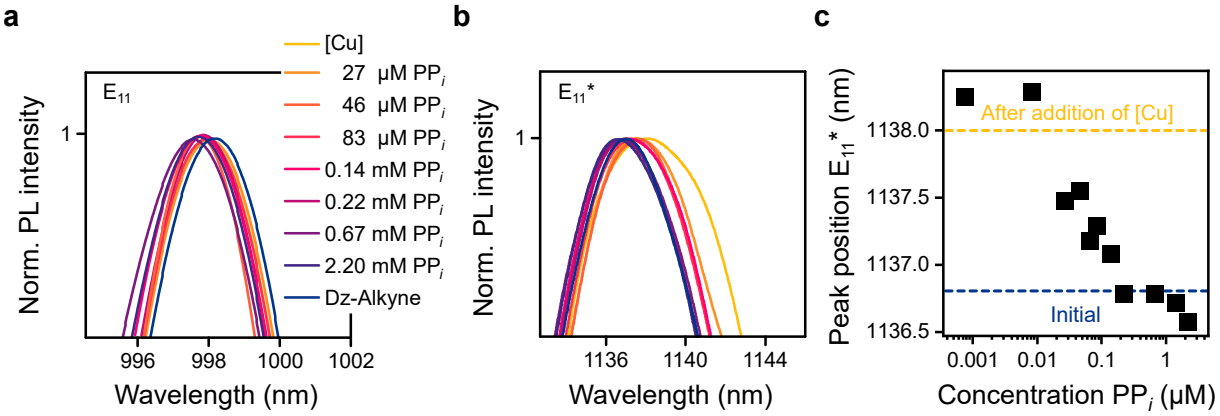

Figure 6.20: a-b) Zoom-in on the normalized E_{11} (a) and E_{11}* (b) PL peaks of 4-ethynylbenzene-functionalized PL-PEG_{5000}-coated (6,5) SWNTs in 10 mM MOPS buffer after the addition of [Cu] and at various concentrations of PP_i. c) Changes in the PP_i concentration-dependent E_{11}* PL peak position.

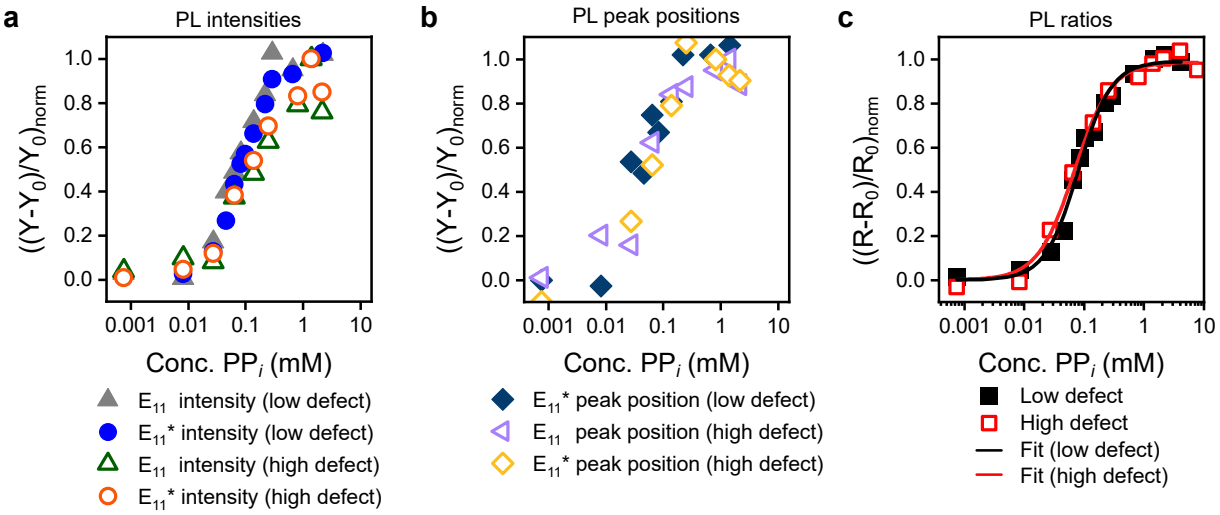

Figure 6.21: a-b) Concentration-dependent changes in the normalized E_{11} and E_{11}* PL intensities (a) and E_{11} and E_{11}* peak positions (b) for 4-ethynylbenzene-functionalized PL-PEG_{5000}-coated (6,5) SWNTs in 10 mM MOPS buffer at high and low sp^3 defect densities. Y represents the normalized PL intensity and peak position, while Y_0 represents the normalized PL intensity and peak position after the addition of [Cu]. c) Concentration-dependent changes in the normalized E_{11}*/E_{11} PL intensity ratio for high and low sp^3 defect densities. R represents the normalized E_{11}*/E_{11} intensity ratio, and R_0 represents the normalized E_{11}*/E_{11} intensity ratio after the addition of [Cu]. Solid lines show Hill-fits according to Equation 6.1.

While defect density-dependent PL shifts are not readily apparent in the PL peak position, as depicted in Figure 6.21b, the observed changes are relatively small and may not allow for the quantification of PP_i with acceptable precision. In clear contrast, nearly identical dose-response curves are obtained when comparing the E_{11}*/E_{11} PL intensity ratios. This demonstrates the superiority of the ratiometric detection approach, which, unlike PL intensities and PL peak positions, provides robust and reproducible values even across different functionalization batches.

When fitted with a Hill function, positive Hill coefficients are obtained, as summarized in Table 6.1. Positive values indicate cooperative binding and can be rationalized by the fact that the coordination of two PP_i molecules per Cu^{2+} site is necessary. Notably, an average K_d value of approximately $74 \cdot 10^{-6}$ M was extracted, which is approximately 7× lower than that for SDS-coated (6,5) SWNTs. This clearly demonstrates the weaker adsorption of [Cu] on the SWNT surface due to higher competition with adsorbed PL-PEG_{5000}.

Table 6.1: Extracted dissociation constants (K_d) and Hill-parameters (n) for normalized E_{11}*/E_{11} PL intensity ratios fit with the Hill-model at low and high sp^3 defect densities.

Sample	K_d (10^{-6} M)	n
Low sp^3 defect density	79.3	1.57
High sp^3 defect density	68.4	1.42

In summary, PP_i can be reproducibly quantified over a concentration range of 17-320 µM. This range considers only changes in PL intensity ratios that exceed 10% and fall below 90% of the maximum response, which is a safe estimate for quantification on a logarithmic scale. The limit of detection (LOD) is the lowest concentration at which the PL response is distinguishable from background noise, and was determined from the standard deviation (SD) of the response after the addition of [Cu] to the SWNT sensor (SD_{blank}; number of blank measurements = 10). Linear regression of the dose-response curve was performed at low PP_i concentrations on a linear (not logarithmic) scale according to:

$$\mathrm{LOD} = \frac{(3 \cdot \mathrm{SD_{blank}})}{\mathrm{m_{linear}}}, \tag{6.3}$$

with a slope (m_{linear}) of the linear fit equal to 0.00381 μM^{-1} and SD_{blank} of 0.0056. A LOD of 4.4 µM was determined when considering E_{11}*/E_{11} intensity ratios (see Appendix C, Figure C.10).

To test the potential application of the PP_i sensor in a complex biological environment, HEK cells were cultured ($2.2 \cdot 10^6$ cells, see Section 3.6.6). The cells were carefully washed with ultra-pure water to remove the phosphate (or other Cu^{2+}-complexing) containing culture media prior to harvesting. Finally, the cells were harvested in a total volume of 200 µL and lysed by pulsed sonication. At this cell concentration, the estimated levels of PP_i and P_i were approximately 3-8 µM and 40-92 µM, respectively.[383–385]

When cell lysate was added to a previously [Cu]-quenched dispersion of PL-PEG_{5000}-coated functionalized (6,5) SWNTs, a small increase in E_{11}* intensity and E_{11}/E_{11} intensity ratio was observed (see Figure 6.22). Upon additional spiking with PP_i (188 µM), the presumably maximum response in E_{11} and E_{11} PL intensity and E_{11}*/E_{11} intensity ratio was observed. This leads to two important findings: First, PP_i can be identified under biological conditions in complex media, suggesting that the developed SWNT sensor may be suitable as a bioanalytical tool. Second, the sensor remains fully reversible under these conditions, as the obtained E_{11}*/E_{11} intensity ratio closely matches the initial ratio before [Cu]-quenching. Additionally, the SWNT concentration used in this experiment was ~5× lower than the typical SWNT concentration employed in this

work. It not only demonstrates that sufficiently high signal-to-noise ratios can be achieved at very low SWNT concentrations due to the high brightness of the sensor, but also indicates that the sensitivity of the sensor scales with the sensor concentration, allowing for fine-tuning of the sensitivity to PP_i.

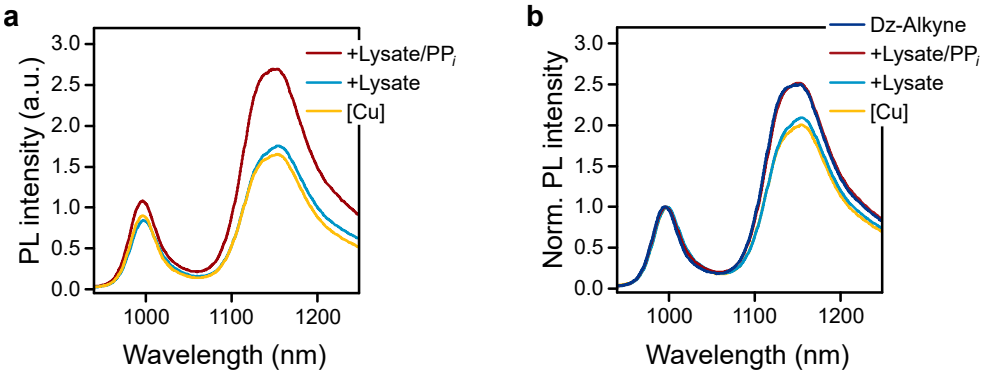

Figure 6.22: a, b) Absolute (a) and normalized (b) PL spectra of 4-ethynylbenzene-functionalized PL-PEG_{5000}-coated (6,5) SWNTs before and after the addition of [Cu], followed by the addition of 0.5 µL cell lysate (to 100 µL SWNT sensor) and subsequent spiking with 188 µM PP_i.

Overall, the developed detection scheme for PP_i with functionalized (6,5) SWNTs was successfully transferred into a biocompatible environment by surfactant exchange to PL-PEG_{5000}. The sensor remained fully operational, allowing for the quantification of PP_i down to 4.4 µM and enabling its use in complex media. Hence, it should be suitable as a bioanalytical tool, for example, in monitoring the evolution of DNA amplification during polymerase chain reaction.

6.7 Detection of PP_i released from PCR

The polymerase chain reaction (PCR) is an indispensable technique for biomedical research and has, for example, become the gold standard for SARS-CoV-2 diagnosis.[386] During PCR, an exponential duplication of a template DNA strand occurs under the release of PP_i. A brief overview of the relevant steps during PCR is provided in Figure 6.23.
After an initial denaturation step of the template DNA and subsequent annealing of the DNA primer to each of the ssDNA templates, DNA extension occurs, during which DNA polymerase synthesizes a new strand of DNA. In this step, nucleotides are incorporated into the DNA strand by hydrolysis of deoxynucleotide triphosphates (dNTP), releasing PP_i. Since each template DNA produces two new elongated DNA strands, exponential duplication occurs with 2^n copies after n PCR cycles.
Most commonly, the amplification of the parent DNA is confirmed by performing agarose gel electrophoresis, but this technique may be too slow when rapid confirmation of DNA amplification is needed. An alternative approach involves fluorescent sensors, with high sensitivity and selectivity towards PP_i over dNTPs, even in the presence of DNA polymerase enzyme, DNA template (plasmid), DNA primers, and PCR buffer. The developed SWNT sensor could hereby represent such fluorescent sensor due to its ability to detect PP_i even in the presence of ATP (see Figure 6.10).

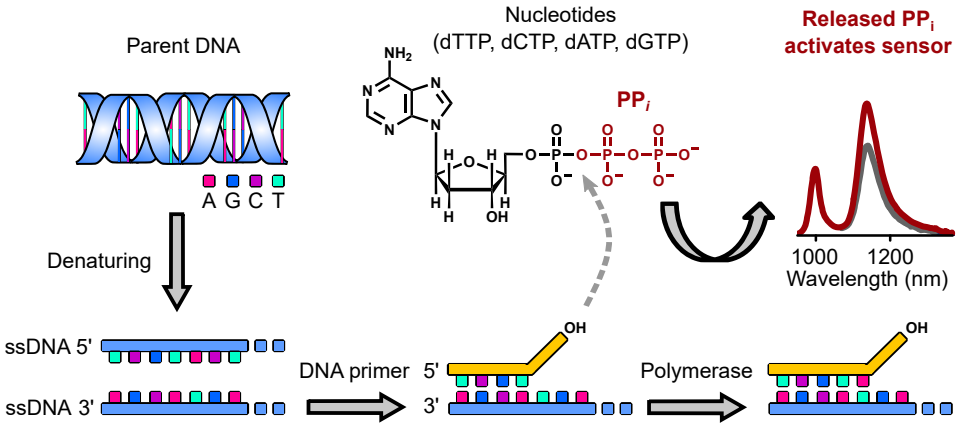

Figure 6.23: Schematic overview of PCR-relevant steps and the concept for measuring PCR cycles by detecting the released PP_i with the SWNT sensor.

To detect PP_i released during PCR, the ready-to-use [Cu]-quenched functionalized SWNT sensor was mixed with the products obtained from different PCR cycles. PCR was performed with 0, 12, and 24 cycles, and PL spectra were recorded after addition of the final PCR product (5 µL too 100 µL of the sensor, see Figure 6.24a,b). The successful amplification of DNA products of the same molecular weight was confirmed and visualized on an 1% agarose gel (Figure 6.24c), indicating different amounts of amplified products corresponding to the number of cycles and indirectly reflecting the released PP_i.
When PCR was performed with zero cycles, high concentrations of dNTPs were present, resulting in a pronounced response in PL intensities and the E_{11}^*/E_{11} PL intensity ratio. Importantly, a stronger response was observed after the addition of PCR cycle products at 12 and 24 cycles. This shows, that the change in PL response was not solely due to the absolute concentration of PP_i but rather to the combined concentration of PP_i and dNTPs. Thus, the difference in the PL response represents the conversion of dNTPs to PP_i and is similar to that demonstrated for different mixing ratios of PP_i and ATP, which has high structural similarity to dNTPs (see Figure 6.10d).
These findings are crucial for understanding the response characteristics of the sensor upon the addition of the PCR product. The sensor's response is significantly smaller when dNTPs are converted to PP_i compared to the direct addition of PP_i in the absence of dNTPs. This allows the sensor to track changes in PP_i concentration over a larger concentration window and can be utilized to monitor PCR over many cycles. However, the response arising from the conversion of dNTPs to PP_i should still exhibit a logarithmic scaling. Due to the logarithmic scaling of both PCR amplification and sensor response, a linear correlation between the number of PCR cycles and the change in the E_{11}^*/E_{11} intensity ratio was observed as shown in Figure 6.24d.
Furthermore, contrary to the previously observed blueshift in E_{11}^* PL peak position for the addition of pure PP_i, a redshift becomes evident with increasing PCR cycles (Figure 6.24e). This observation matches the detected redshift when comparing different ATP:PP_i mixing ratios as described in Section 6.4 and confirms that the originally observed changes in the PL spectra are indeed induced by the presence of dNTPs. Hence, the changed PL response for increasing PCR cycles can be ascribed to the higher relative concentration of PP_i.

In conclusion, these results confirm that the developed SWNT sensor can effectively detect PP_i released during PCR, offering an alternative to agarose gel electrophoresis for real-time monitoring of DNA amplification.

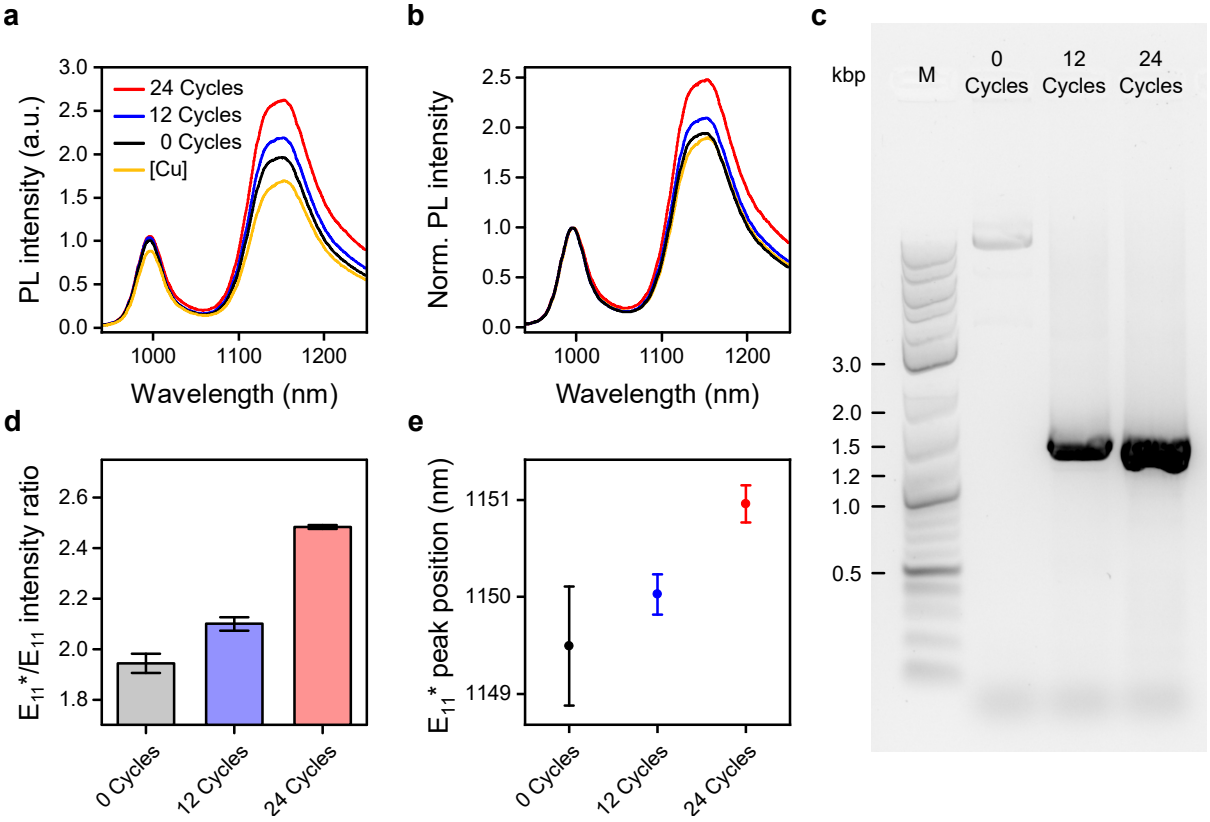

Figure 6.24: a,b) Absolute (a) and normalized PL spectra (averaged over three measurements) of 4-ethynylbenzene-functionalized PL-PEG_{5000}-coated (6,5) SWNTs after addition of 5 µL of PCR product after 0, 12 and 24 cycles. c) Optical image of agarose gel electrophoresis of PCR products after 0, 12 and 24 cycles, M - DNA marker with length of DNA fragments in kilo-base-pair (kbp). d-e) PL E_{11}^*/E_{11} intensity ratio (d) and E_{11}^* PL peak position (e) after addition of 5 µL of PCR product after 0, 12 and 24 cycles, the mean value and standard deviation are given (three measurements).

6.8 Summary & conclusions

In summary, this Chapter describes the first use of SWNTs for the ratiometric optical detection of PP_i in biological environments. The presented detection scheme is based on a metal displacement assay employing reversible Cu^{2+} ion-induced PL quenching of sp^3-functionalized (6,5) SWNTs bearing a 4-ethynyl moiety. A Cu^{2+} complex formed by $CuSO_4(H_2O)_5$ and the triazole derivative THPTA is employed to effectively quench SWNT PL, with the quenching process being fully reversible upon Cu^{2+} ion displacement by the addition of PP_i. Since PL quenching is more enhanced for defect-induced E_{11}* emission (1135 nm) compared to E_{11} emission (988 nm), a change in the E_{11}*/E_{11} intensity ratio occurs. This ratio represents a highly robust sensing metric with greatly reduced sensitivity to external effects such as excitation density and SWNT concentration fluctuations due to internal calibration. In contrast to other multi-signal sensors based on mixed chiralities of SWNTs, PL emission originates from a single chirality and is narrow. Thus, additional PL changes or shifts depending on SWNT chirality can be eliminated, providing a more reliable data readout. In addition to changes in PL intensity (ratio), pronounced shifts of the PL peak positions are observed. All Cu^{2+}-induced changes of the PL properties were recovered as a function of the absolute concentration of PP_i, allowing for precise quantification.

One of the current limitations of this sensor is its selectivity for PP_i because strongly copper-complexing analytes, such as ATP, also lead to significant changes in the PL response. Importantly, PP_i induces the strongest PL response of all tested analytes. This enables the tracking of relative changes in PP_i concentration in biologically relevant processes, such as the hydrolysis of ATP to AMP and PP_i. Furthermore, analyte-specific PL shifts provide an additional analytical tool for distinguishing between ATP and PP_i. These analyte specific PL responses are expected to depend on the chosen ligand (THPTA) and could be altered by screening other suitable triazole ligands.

Mechanistic studies reveal that PL quenching arises from the strong immobilization of Cu^{2+} ions on the SWNT surface and depends on the surface coverage of the SWNT. Here, the immobilization of Cu^{2+} ions was facilitated by strong π-π interactions with the triazole ligand of THPTA. PL quenching was found to be more pronounced in the presence of 4-ethynyl functional groups compared to simple benzene moieties, suggesting that Cu^{2+} adsorption and/or PL quenching is additionally enhanced by weak coordination of the ethynyl moiety to Cu^{2+} ions. Strong immobilization of Cu^{2+} ions enables photo-induced electron transfer, which is proposed to be the primary cause of PL quenching.

The SWNT sensor retains full functionality when rendered biocompatible by coating with PL-PEG in a buffer solution, albeit with a reduced maximum response attributed to the presumed high surface coverage of PL-PEG. Absolute PP_i quantification was possible over a concentration range of 17-320 µM, with a limit of detection of 4.4 µM. Sensitivity can be further increased by reducing the SWNT sensor concentration. In this detection range, various clinical conditions leading to elevated levels of PP_i in urine, intracellular mitochondrial fluids, or synovial fluids can be monitored.[359–361,387–390] For instance, patients diagnosed with hypophosphatasia often exhibit increased PP_i levels, ranging from 5 µM to 17.5 µM in plasma

and 45-234 µM in urine. However, it should be noted that PP_i is typically accompanied by other phosphates and therefore only conditions may be tracked which show an overall increase in PP_i and P_i concentration.[359,360,387]
The detection of PP_i was demonstrated in the presence of cell lysate with high cell count where the SWNT sensor remained fully reversible. This demonstrates its ability to operate under biological conditions and in complex media. Finally, the developed SWNT sensor was employed for the fluorescent detection of PP_i released during DNA synthesis in polymerase chain reaction, indicating its potential applications.

Overall, the functionalized (6,5) SWNT sensor developed in this study is well-suited for ratiometric optical detection of PP_i in the NIR-II range in biological environments. This advancement paves the way for *in vivo* detection of PP_i with low background noise. In comparison to other fluorescent PP_i sensors in the NIR-II, such as lanthanide nanoparticles reported by Su *et al.*,[391] this sensor exhibits similar sensitivity down to the µM level but lower selectivity towards PP_i. However, it offers multiple sensing parameters and internal calibration, thus enabling selective and reliable optical (bio)sensing.

CHAPTER 7

CONCLUSIONS & OUTLOOK

At the outset of this thesis, luminescent defects in SWNTs were already extensively studied and a comprehensive understanding of their photophysics was obtained. Their ability to enhance the photoluminescence (PL) quantum yield of SWNTs was convincingly demonstrated using numerous available synthetic tools for their creation in both aqueous and organic solvents.[15,141] First reports had also demonstrated their potential as single-photon emitters in the near-infrared at room temperature.[18,19] Consequently, research focus started to shift from understanding their fundamental photophysics to more practical applications, such as integrating luminescent defects in photonic structures and light-emitting devices as well as application in bioimaging and biosensing.[22,194,278,290] Despite these pioneering efforts, fundamental problems prevailed in the synthesis of luminescent defects, requiring resolution prior to practical application. More precisely, the optical properties of the majority of introduced luminescent defects did not meet the necessary criteria of emission wavelength, brightness, scalability, or reproducibility. Additionally, biosensing with luminescent defects was largely unexplored and only very few examples were available in literature. This thesis has developed synthetic approaches to address these issues, aiming to provide materials suitable for successful applications (Chapter 4 & 5). It has also introduced a new rational approach for biosensing with luminescent defects (Chapter 6).

Luminescent defects for optoelectronics near telecommunication wavelengths

Due to the geometry of SWNTs, the precise arrangement of the introduced sp^3 carbon atoms plays a crucial role in determining the optical properties of luminescent sp^3 defects.[21] However, there has been little control over the formation of these so-called binding configurations of defects thus far, and the emission from sp^3 defects occurs across a wide spectral range. Specifically, $E_{11}{}^{*-}$ defects, where emission is more red-shifted compared to the commonly obtained $E_{11}{}^{*}$ defects, are desired as they are more suitable for single-photon emission and emit closer to telecommunication wavelengths.[18,19] However, these $E_{11}{}^{*-}$ defects were typically found in only a minority of SWNTs in previous synthetic protocols.

Chapter 4 describes the first functionalization protocol for the selective introduction of luminescent sp^3 defects with strongly red-shifted $E_{11}{}^{*-}$ emission in (6,5) SWNTs (see summary

in Figure 7.1). This was achieved through the covalent functionalization of polymer-wrapped (6,5) SWNTs in organic solvents *via* base-promoted coupling with primarily aniline derivatives. All required reagents are commercially available and the reaction proceeds under ambient conditions. Unlike the commonly employed radical-based chemistry where E_{11}^* defects are obtained, a nucleophilic addition was proposed as the reaction pathway, favoring the formation of sp^3 defects in E_{11}^{*-} configuration. E_{11}^{*-} defects emit further red-shifted (1250 nm) and exhibit longer PL lifetimes and a higher emission efficiency compared to E_{11}^* defects (emission at 1150 nm). In combination with the high quality of long polymer-wrapped (6,5) SWNTs obtained through shear-force mixing, comparatively high PL quantum yields (PLQY) of up to 5% were achieved at optimal defect density. This corresponds to a 2.5-fold enhancement, surpassing reported values for comparable E_{11}^* defects. However, the analysis of wavelength-dependent defect-state lifetimes revealed that the defect-state emission efficiency is likely close to the maximum for E_{11}^{*-} defects in (6,5) SWNTs and cannot be further increased by the modulation of the defect-state emission wavelength. This suggests that an upper limit in the intrinsic PLQY of solution-processed functionalized (6,5) SWNTs has been reached.

Notably, single-photon emission was successfully demonstrated at room temperature with a purity of 93%. Although the observed single-photon purity is lower compared to previous reports,[19] defect emission originates from a narrower wavelength window even on a single-SWNT level, representing an important practical advancement. A narrow emission window allows for improved matching with the finite spectral width of plasmonic nanocavities, which will be necessary to achieve indistinguishability by accelerating the radiative decay.[289,290]

Through the functionalization of larger-diameter (7,5) and (10,5) SWNTs with intrinsic smaller optical band gaps, defect emission could be shifted to 1270 nm and 1474 nm, respectively. While this approach enables reaching the relevant telecommunication O-band, it falls short in the case of the C-band. Achieving further red-shifted defect-state emission represents a significant challenge with the presented functionalization approach as the redshift of defect-state emission decreases with increasing SWNT diameter. Hence, functionalization of even larger-diameter SWNTs will be required.[84] Alternative functionalization approaches that have been reported in literature since then might be more suitable to achieve this goal and defect emission was observed in the C-band.[159] However, these functionalization techniques are limited to aqueous dispersion, which greatly limits their integration in efficient light-emitting devices.

In contrast to this, functionalized polymer-wrapped SWNTs exhibit excellent solution-processability, allowing for the production of large-area thin films using standard deposition techniques such as spin-coating or aerosol-jet printing. Their implementation in ambipolar, light-emitting field-effect transistors has already been realized, achieving narrowband defect-state electroluminescence well within the O-band.[306]

Overall, the presented functionalization technique emerges as a powerful technique to selectively introduce previously inaccessible luminescent defects in polymer-wrapped SWNTs with narrow emission close to telecommunication wavelengths. Due to the processability of polymer-wrapped SWNTs in organic solvents, the obtained functionalized SWNTs are suitable for integration into electrically-driven thin-film devices and quantum-light sources.

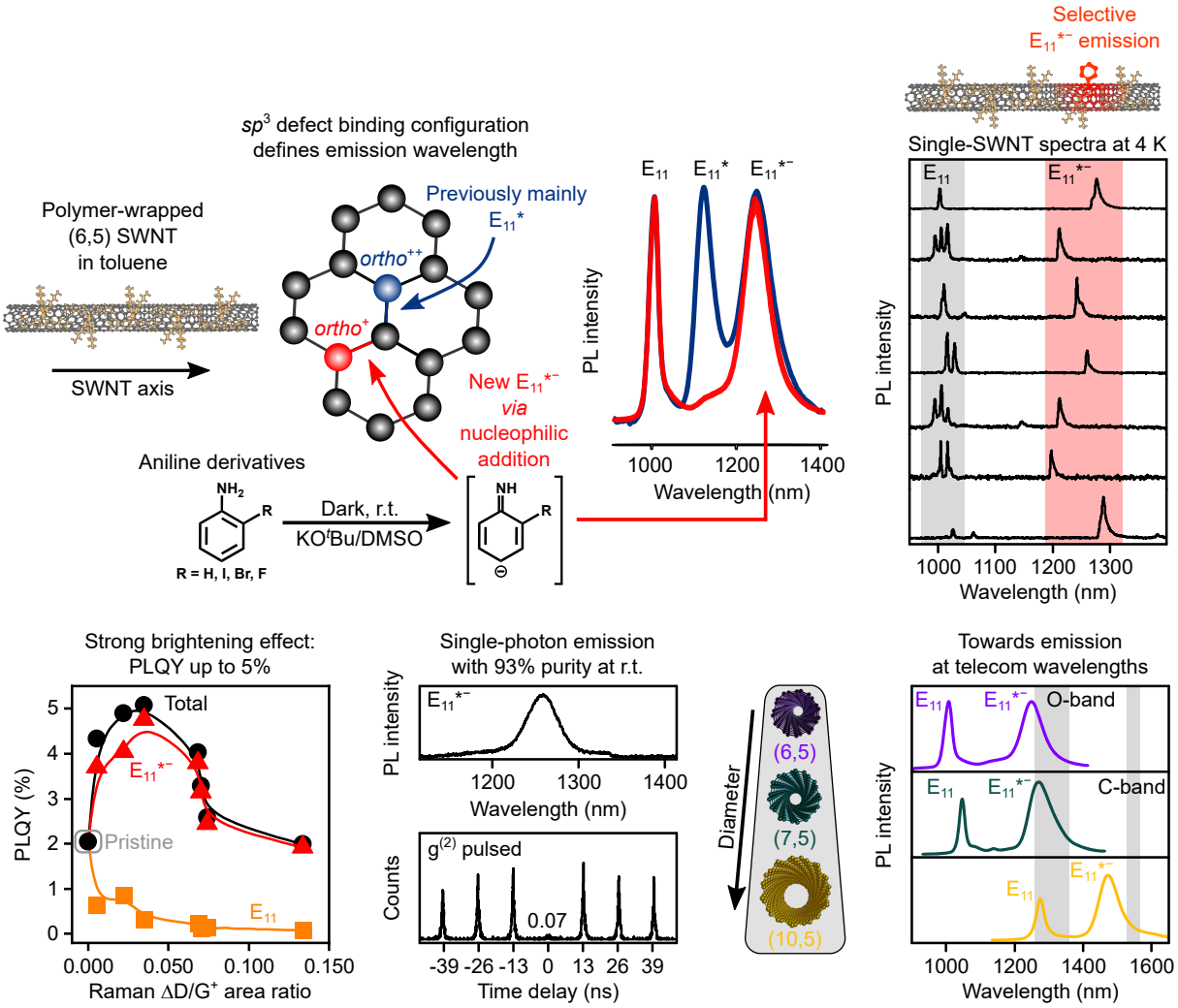

Figure 7.1: Summary of the main results of Chapter 4. The results of this Chapter are published in Settele *et al.*, *Nat. Commun.* **12**, 2119 (2021).

Bright luminescent defects for bioimaging in the near-infrared

For the application of luminescent defects in *in vivo* imaging in the near-infrared, large amounts (mg scale) of functionalized SWNTs in aqueous dispersion with reproducible high brightness are required. This demand cannot be satisfied with the currently available synthetic methods. Luminescent oxygen defects show promise in addressing this issue.[189] Nevertheless, they currently face challenges such as lower brightness when compared to sp^3 defects and the requirement for light/UV-light irradiation during the functionalization process. This complicates the up-scaling process.

Chapter 5 presented an easy, controllable and scalable method for the creation of luminescent oxygen defects in aqueous-dispersed SWNTs (see summary in Figure 7.2). It uses cheap, readily available, and benign chemicals and relies on the generation of reactive oxygen species (ROS) through Fenton-like copper redox chemistry. The reaction is initiated by reducing Cu(II) (added as $CuSO_4(H_2O)_5$) with sodium-L-ascorbate (NaAsc), which leads to the formation of hydroxyl radicals in the presence of dissolved oxygen. Luminescent defects are then formed through radical addition to the SWNT lattice, followed by oxidation and structural rearrangement.

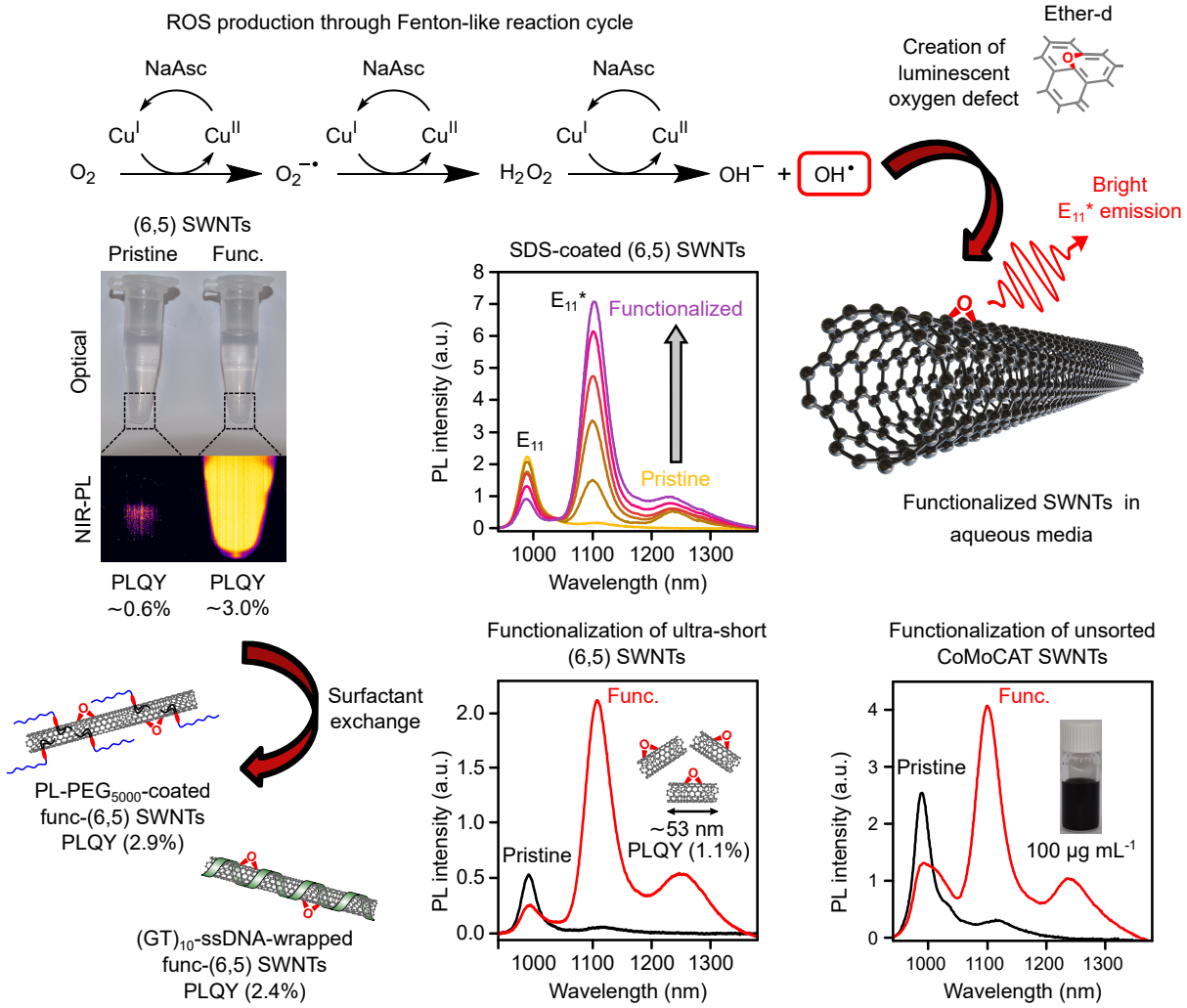

Figure 7.2: Summary of the main results of Chapter 5. The results of this Chapter are subject of a patent application (Settele *et al.* 2024. Method for preparing single-walled carbon nanotubes having luminescent oxygen defects. EP24158317.8).

For pre-selected (6,5) SWNTs, this functionalization results in bright defect emission around 1105 nm and a 5-fold brightening effect with a reproducible PLQY of ~3%. The observed brightening is significantly higher than that reported in previous studies on luminescent oxygen defects,[11,189] suggesting that unintentional oxidation of the SWNT lattice is reduced with this new method. Importantly, the initial functionalization step can be performed in the dark and is applicable to unsorted SWNT raw material. This enables up-scaling by increasing the SWNT concentration up to 0.1 mg mL^{-1} and thus production on larger scale. Functionalized SWNTs can be made biocompatible by coating with single-stranded DNA (ssDNA) or phospholipid-polyethylene glycol (PL-PEG), while maintaining their brightness and sensing capabilities. Even functionalized ultra-short SWNTs showed a PLQY of 1.1%, which may enable their application in super-resolution microscopy, such as mapping the extracellular space in brain tissue when coated with PL-PEG.[235]

One drawback of oxygen defects is their inability to be tuned in their molecular structure. When considering applications as biosensors, they are limited to detection schemes based on

non-covalent functionalization. However, given the large library of small biomolecules that can be detected *via* molecular recognition by adsorbed biomolecules, oxygen-functionalized SWNTs may enhance existing SWNT-based detection schemes.[10,243]
In summary, the developed functionalization protocol has the potential to facilitate large-scale production of luminescent oxygen defects in SWNTs with reproducible brightness, making them suitable for widespread application as near-infrared imaging probes.

Ratiometric detection of pyrophosphates with luminescent defects
Currently, in the majority of optical biosensors utilizing SWNTs, a single emission feature is employed for data readout. The introduction of luminescent defects leads to an additional emission feature (typically E_{11}*) in SWNTs, which can display distinct responses to changes in the SWNT environment. This allows for the implementation of ratiometric schemes, wherein the E_{11} emission serves for self-calibration of the sensor. However, so far SWNT-based biosensors with luminescent defects depend on complex interactions between the target analyte and biopolymers non-covalently bound to the SWNT.[22,23] This limits the rational design of sensors for the optical detection of important biomarkers with novel structural motifs.
In Chapter 6, a new detection scheme is introduced utilizing sp^3-functionalized (6,5) SWNTs bearing an alkyne moiety (see summary in Figure 7.3). This scheme allows for the ratiometric optical detection and quantification of inorganic pyrophosphate (PP_i), an important biomarker which plays a critical role in the cellular energy metabolism and the biosynthesis of biomacromolecules and metabolites.[353,354] The detection scheme relies on a metal displacement assay, where copper ions reversibly quench SWNT emission. When Cu^{2+} ions are complexed by the triazole ligand tris(3-hydroxypropyltriazolylmethyl)amine (THPTA), strong immobilization on the SWNT surface can occur. This immobilization is driven by non-covalent adsorption through π-π interactions and is promoted by coordination to the attached aryl alkyne functional groups. Immobilized Cu^{2+} ions induce dynamic PL quenching *via* photo-induced electron transfer, which can be reversed by addition of copper-complexing analytes such as PP_i. PL quenching is more pronounced for E_{11}* emission than E_{11} emission, resulting in a change in the E_{11}*/E_{11} intensity ratio. Hence, the sensor can function independently from absolute intensities and removes external effects, which affect both emission features. Additionally, significant PL shifts are observed, providing further detection metrics. The manifold of sensing metrics with internal calibration clearly differentiates it from other fluorescent PP_i sensors in the NIR.[391]
The sensor retains its functionality when transferred to a biocompatible environment by coating with PL-PEG in buffer solution. This allows for its application in detecting PP_i released during DNA synthesis in polymerase chain reaction (PCR). Despite the outlined promising results, significant challenges lie ahead in this sensor design. While there is selectivity towards PP_i, other copper-complexing analytes such as adenosine triphosphate (ATP) also induce significant responses in the PL. Sensor sensitivity and selectivity are likely linked to the employed triazole ligand which complexes the Cu^{2+} ions and future work should focus on the development of new suitable ligands,[353] which release Cu^{2+} ions more selectively towards PP_i (or other analytes). Additionally, Cu^{2+} ion immobilization relies partly on non-covalent adsorption to the SWNT surface, making it dependent on the surface coverage by the chosen SWNT

coating/surfactant. Covalent functionalization with stronger Cu^{2+} ion-coordinating functional groups could enable Cu^{2+} ion immobilization at the defect site, which is independent from surface coverage and induces a more selective response in E_{11}* emission. Crucially, to harness the full potential of the sensor, a transfer to blood serum has to be conducted, which may significantly alter the sensor properties. This represents a critical step towards the potential detection of PP_i *in vivo* with low background noise.

Overall, due to its internal calibration and utilization of multiple sensing metrics, this detection scheme significantly expands the currently existing sensor designs for the detection of biomarkers in the NIR-II. Given the high sensitivity of luminescent defects to Cu^{2+} ions, this sensor design may serve as a starting point for the further rational design of SWNT-based biosensors in metal displacement assays.

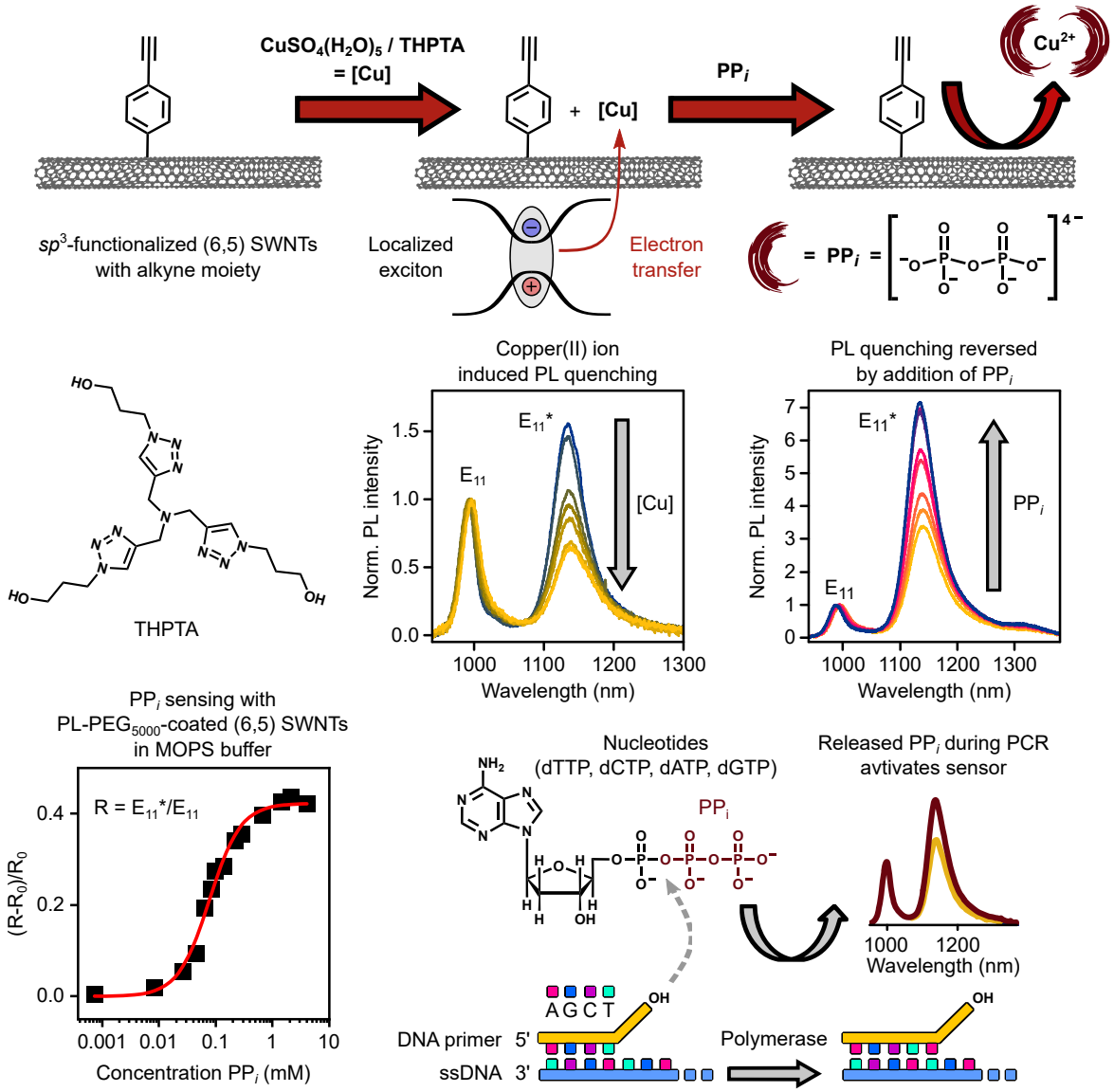

Figure 7.3: Summary of the main results of Chapter 6. The results of this Chapter are published in Settele *et al.*, *Nat. Commun.* **15**, 706 (2024).

Future work

Many of the initial questions and challenges regarding the creation of luminescent defects in SWNTs have been addressed by now. The brightening effect of luminescent defects appears to have reached its limit for small-diameter SWNTs, making it unlikely that new synthetic approaches will significantly enhance the intrinsic PLQY of functionalized SWNTs any further. The narrowing of defect emission bands and covalent functionalization of larger-diameter SWNTs with emission in the desired telecom C-band have been accomplished or are within reach by selecting suitable large-diameter SWNTs. A substantial challenge remains in the deterministic creation and precise placement of individual luminescent defects. The capability to control not only the defect type but also its specific location would represent a significant advancement toward using luminescent defects as a platform for single-photon emission. This achievement might be realized in the future through selective covalent functionalization at photolithographically defined reaction sites on individual SWNTs.[392] Overall, considering that defect-state electroluminescence can be achieved from single-SWNT transistors[393] and the ability of luminescent defects to exhibit high levels of photon indistinguishability when integrated into optical cavities,[290] electrically-pumped, room-temperature single-photon emission at telecommunication wavelengths appears achievable.

Even greater emphasis should be placed on advancing the development of luminescent defects for applications for bioimaging and biosensing in the NIR-II. Here, luminescent defects can help in overcoming current limitations and weaknesses by adding functionality to SWNTs, increase their brightness and give access to ratiometric detection schemes. The benefits of luminescent defects are particularly strong for small-diameter SWNTs, such as the easily accessible (6,5) SWNTs, where PL brightening is large and defect emission already falls well within the NIR-II window. Consequently, luminescent defects in (6,5) SWNTs have the potential to significantly enhance existing sensing methods, which rely on non-covalent functionalization with, *e.g.*, DNA and lipids,[243,246] DNA/aptamers,[394,395] or DNA/proteins.[396,397] However, future research will also need to explore the impact of functionalization on SWNT biocompatibility and potential biotoxicity. So far, the data for functionalized SWNTs with oxygen defects suggest low toxicity when coated with PL-PEG, however more studies will be required.[200]

An exciting prospect lies in the ability of sp^3 defects to act as recognition sites for detecting biomolecules through defect-analyte selective interactions. The challenge here is to bring the recognition event as close to the defect as possible and develop detection schemes where analyte recognition triggers a robust response in the defect-state emission. Further progress in covalent functionalization methods will be essential to explore novel functional groups meeting these requirements. This thesis demonstrates that metal ion-SWNT interactions represent a powerful tool to induce significant changes in defect-state emission which could be further explored by functionalization with small ionophores. Lastly, in addition to tracking the optical response of sp^3 functionalized SWNTs, integration into water-gated transistors could enable the additional monitoring of subtle changes in conductance.[398]

Given the new level of control over SWNT-based fluorescent sensors through luminescent defects, there is the potential for significant conceptual advances in the field of chemical sensors, paving the way for future applications of functionalized SWNTs as sensors for diagnostics.

APPENDIX A

Selective Introduction of Strongly Red-Shifted Luminescent sp^3 Defects in Polymer-Wrapped SWNTs

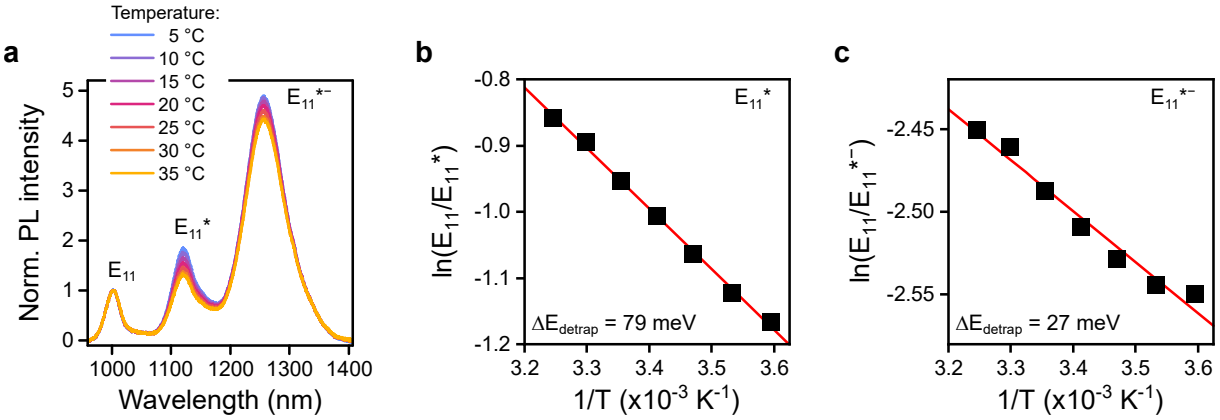

Figure A.1: Temperature dependence of (6,5) SWNTs functionalized with I*o*NH_2 and 0.75 eq. KO^{t}Bu under UV-light illumination. a) Recorded temperature-dependent normalized PL spectra in dispersion between 5 °C and 35 °C. b,c) Computed Van't Hoff plot for the E_{11}* (b) and E_{11}*$^-$ (c) emission band and linear fit to the data (red line). E_{11}, E_{11}* and E_{11}*$^-$ represent integrated PL areas. Note that ΔE_{detrap} is equal to $\Delta E_{thermal}$, as used in other sections or chapters.

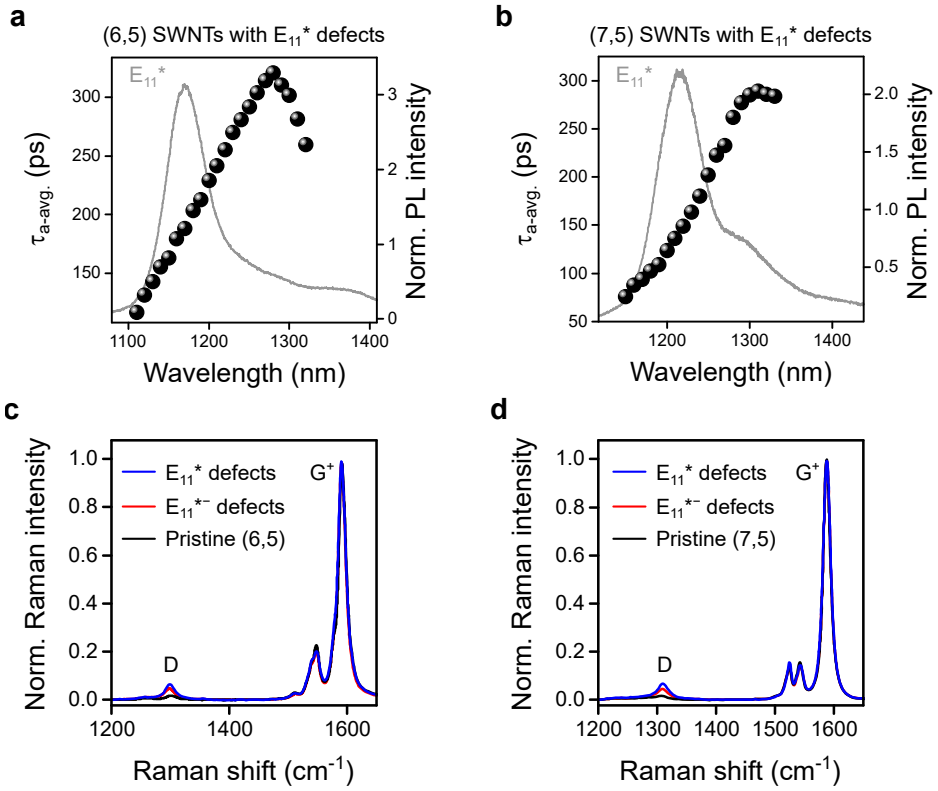

Figure A.2: a,b) A-avg. PL lifetime dependent on defect-state emission wavelength in (6,5) and (7,5) SWNTs. (6,5) and (7,5) SWNTs were functionalized with 4-nitrobenzenediazonium tetrafluoroborate, giving rise to predominantly E_{11}^* emission. The corresponding PL spectra are shown in grey. c,d) Normalized resonant Raman spectra of functionalized (6,5) and (7,5) SWNTs with predominantly E_{11}^* (blue) and E_{11}^{*-} (red) defects. Raman spectra of pristine (6,5) and (7,5) SWNTs are shown in black. The excitation wavelength for (6,5) and (7,5) SWNTs was 523 nm and 633 nm, respectively.

Table A.1: Extracted D/G^+ area ratio, $\Delta D/G^+$ area ratio, and calculated number of defects per µm according to Sebastian *et al.*[144,274]

Sample	D/G^+	$\Delta D/G^+$	n_d (μm^{-1})
Pristine (7,5) SWNTs	0.032	–	–
E_{11}^{*-} in (7,5) SWNTs	0.065	0.033	13.2
E_{11}^* in (7,5) SWNTs	0.100	0.068	27.2
Pristine (6,5) SWNTs	0.055	–	–
E_{11}^{*-} in (6,5) SWNTs	0.149	0.094	38.8
E_{11}^* in (6,5) SWNTs	0.108	0.053	22.1

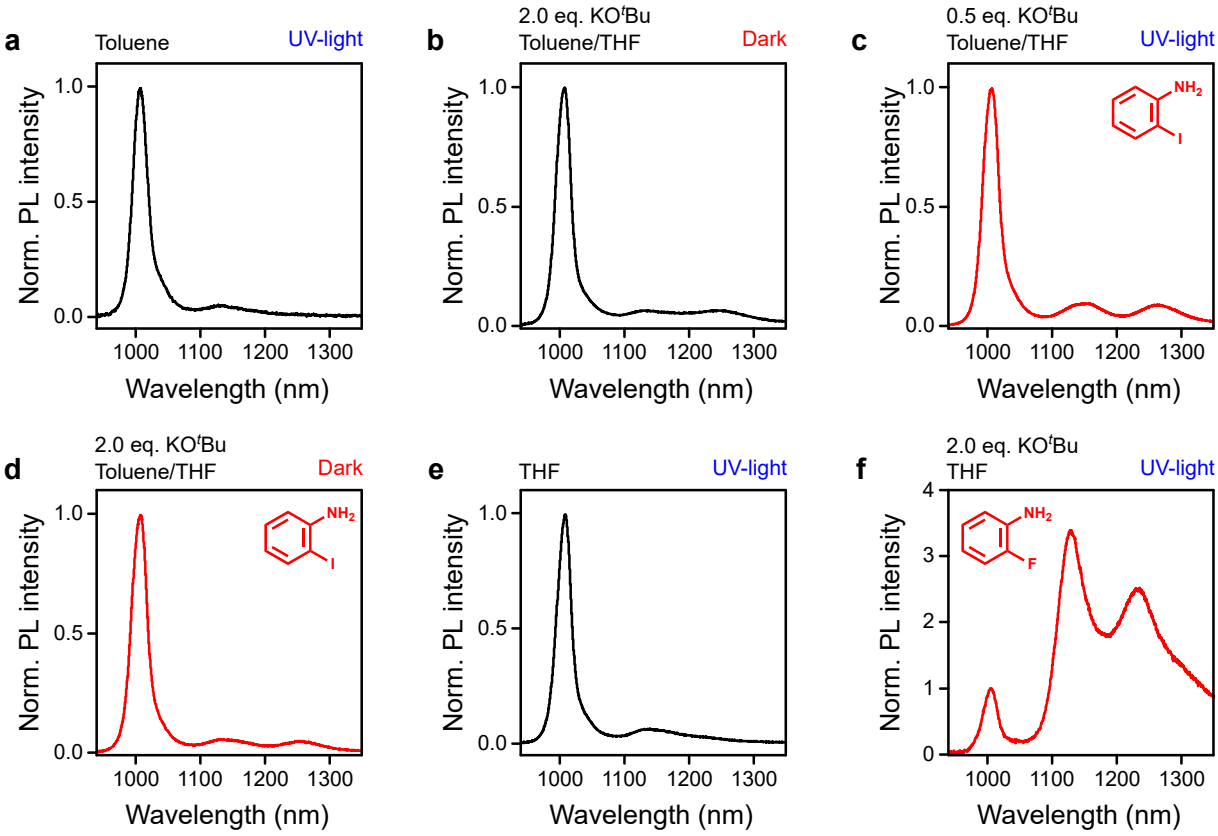

Figure A.3: PL spectra of control and reference reactions (black) performed under various conditions with (6,5) SWNTs in toluene and THF with and without UV-light. Reactions in which 29.30 mM I*o*NH_2 or 2-fluoroaniline was added are shown in red.

APPENDIX B

CREATING BRIGHT OXYGEN DEFECTS IN SINGLE-WALLED CARBON NANOTUBES

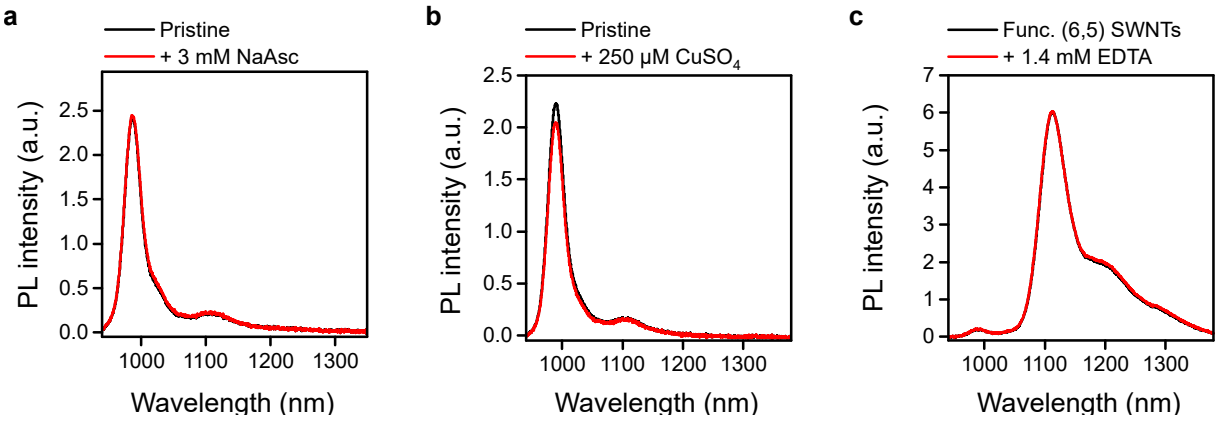

Figure B.1: a,b) PL spectra of SDS-coated (6,5) SWNTs after addition of a) 3 mM NaAsc and b) 250 µM $CuSO_4$. c) PL spectra of functionalized (6,5) SWNTs as shown in Figure 5.3 after addition of 1.4 mM Na_4EDTA.

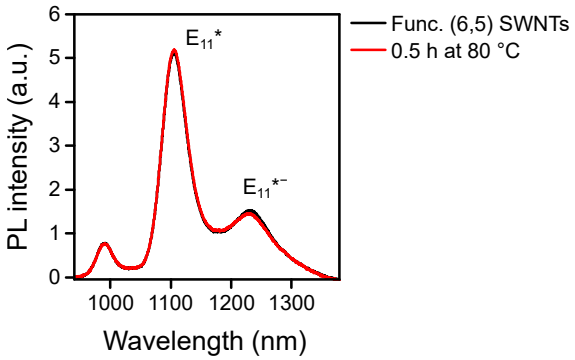

Figure B.2: PL spectra of DOC-coated (6,5) SWNTs, which where previously functionalized at 63 µM $CuSO_4$ and 12 eq. NaAsc in the dark, after heating for 0.5 h at 80 °C. The small decrease in $E_{11}{}^{*-}$ intensity and increase in $E_{11}{}^{*}$ intensity is expected to occur due to E_{22} excitation during the PL measurement.

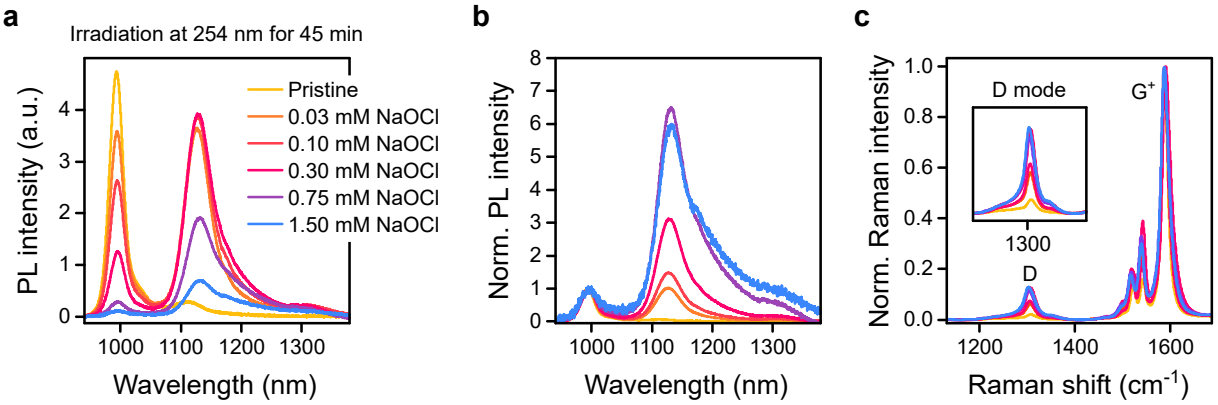

Figure B.3: Covalent functionalization of (6,5) SWNTs as reported by Lin *et al.*[189] Absolute (a) and normalized (b) PL spectra of SDS-coated (6,5) SWNTs functionalized at various concentrations of NaOCl and irradiation at 254 nm for 45 min. Covalent functionalization was performed at a concentration of 0.05% (w/v) SDS and PL spectra measured after addition of DOC to give a final concentration of 0.2% (w/v). c) Corresponding Raman spectra with inset on the D mode.

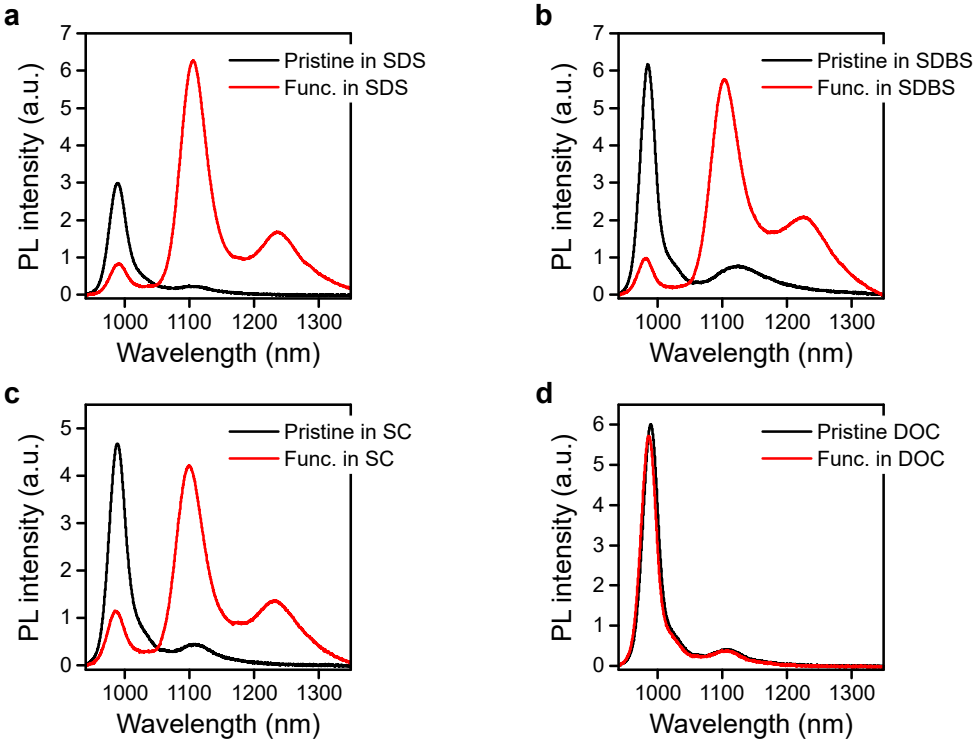

Figure B.4: Absolute PL spectra recorded before (black) and after covalent functionalization with 63 µM $CuSO_4$ and 12 eq. NaAsc. The functionalization was conducted in SDS (a), SDBS (b), SC (c) and DOC (d) at a concentration of 0.33% (w/v).

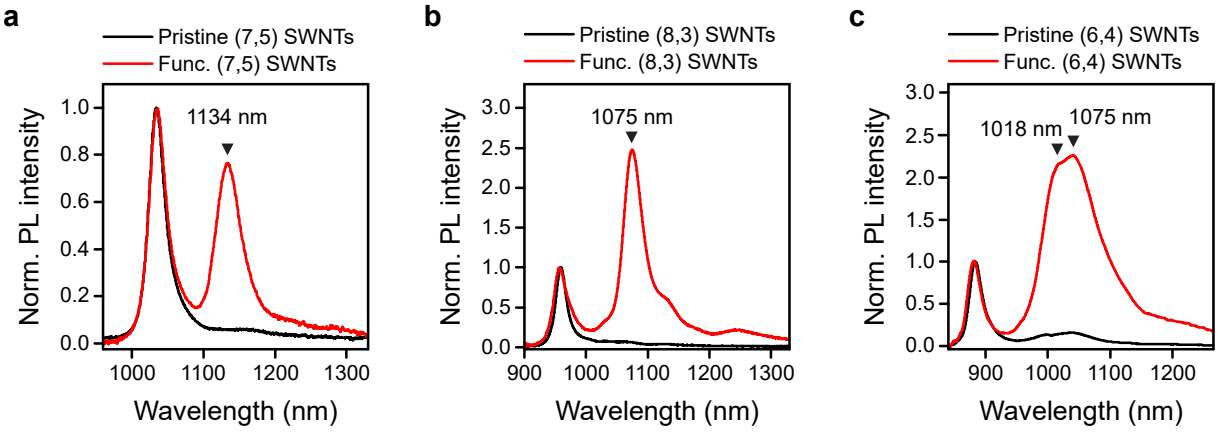

Figure B.5: Normalized PL spectra of functionalized SDS-coated (7,5) SWNTs (a), (8,3) SWNTs (b) and (6,4) SWNTs. The black rectangles indicate the maxima of the E_{11}* emission bands.

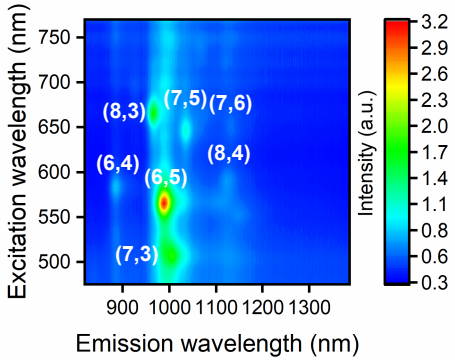

Figure B.6: PLE map of unsorted SDS-coated CoMoCAT nanotubes. SWNT chiralities are assigned according to Weisman *et al.*[6]

APPENDIX C

Ratiometric Fluorescent Sensing of Pyrophosphate with sp^3-Functionalized Single-Walled Carbon Nanotubes

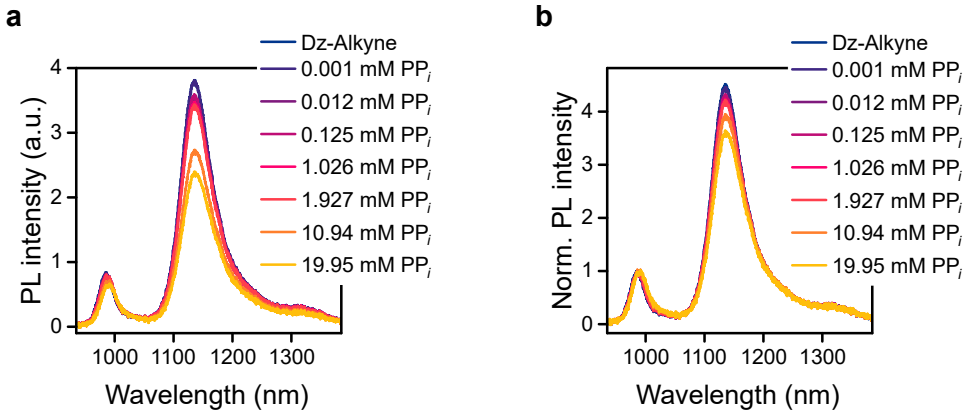

Figure C.1: Absolute (a) and normalized (b) PL spectra of 4-ethynylbenzene-functionalized SDS-coated (6,5) SWNTs after addition of various concentrations of PP_i.

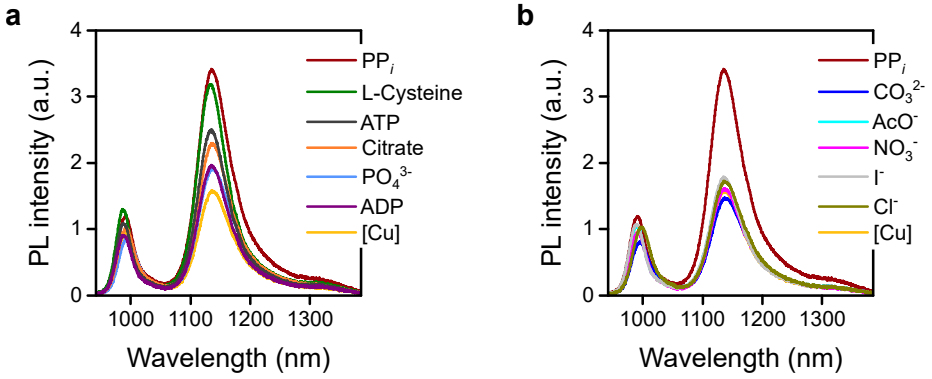

Figure C.2: a,b) Absolute PL spectra of 4-ethynylbenzene-functionalized SDS-coated (6,5) SWNTs which were previously quenched with 15 µM [Cu] (yellow) after addition of various strongly (a) or weakly (b) copper-complexing analytes (concentration 1 mM). Absolute PL spectra after addition of 1 mM PP$_i$ are displayed in a) and b) for comparison.

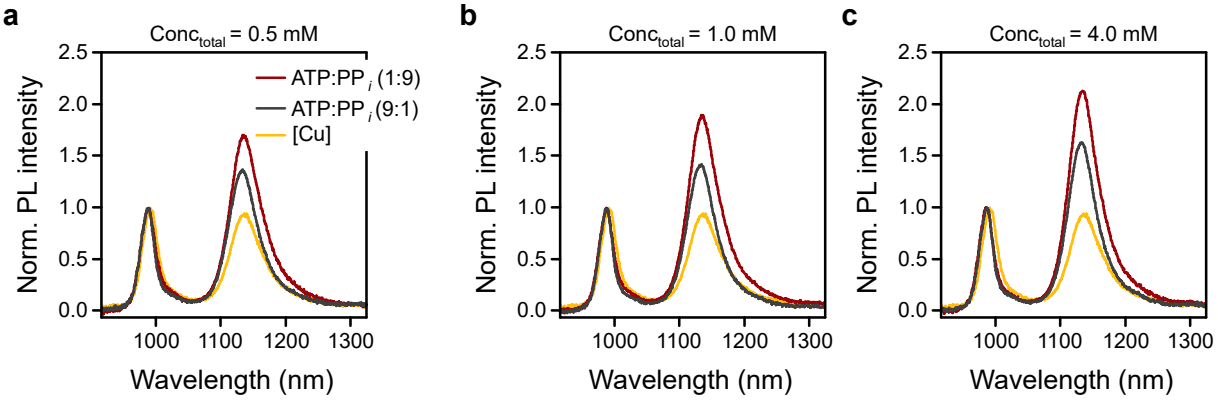

Figure C.3: a-c) Normalized PL spectra of 4-ethynylbenzene-functionalized SDS-coated (6,5) SWNTs after the addition of different ratios of ATP and PP$_i$ with a total analyte concentration of 0.5 mM (a), 1.0 mM (b) and 4.0 mM (c).

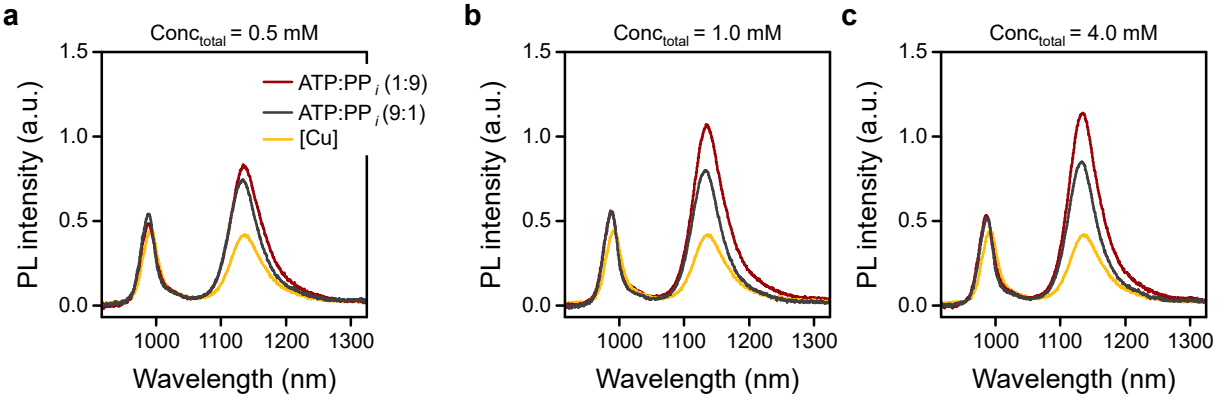

Figure C.4: a-c) Absolute PL spectra of 4-ethynylbenzene-functionalized SDS-coated (6,5) SWNTs after the addition of different ratios of ATP and PP$_i$ with a total analyte concentration of 0.5 mM (a), 1.0 mM (b) and 4.0 mM (c).

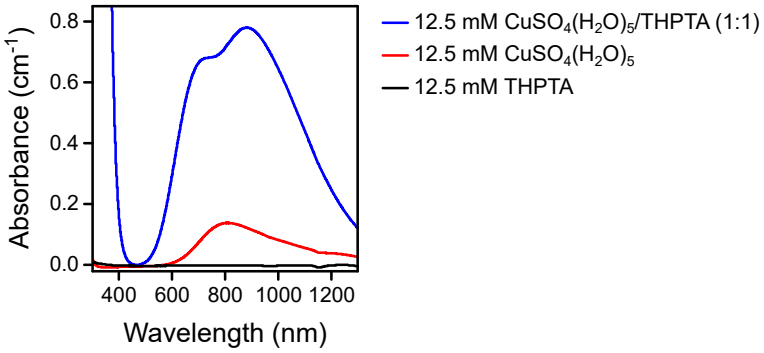

Figure C.5: UV-Vis-NIR absorption spectra of 12.5 mM THPTA (black), $CuSO_4(H_2O)_5$ (red) and [Cu] (blue, $CuSO_4(H_2O)_5$/THPTA in 1:1 ratio).

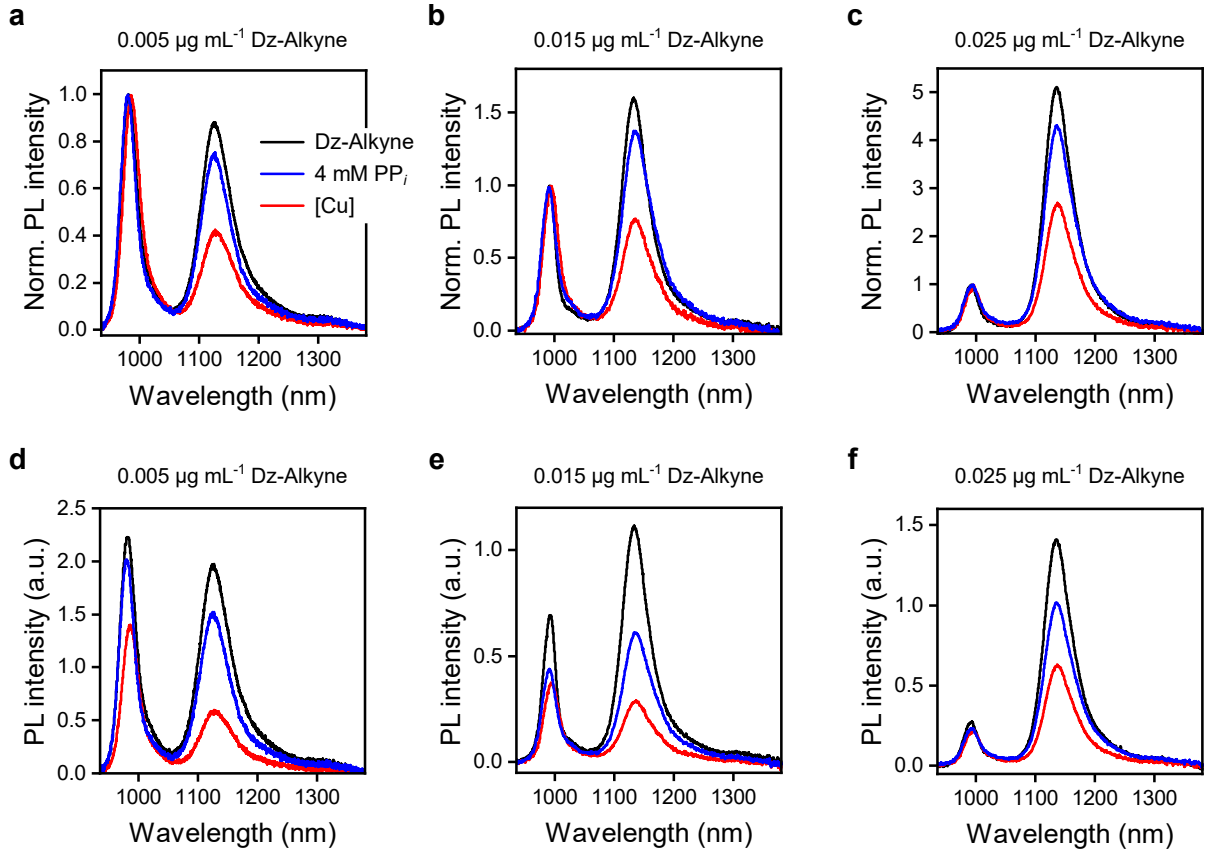

Figure C.6: Normalized (a-c) and absolute (d-f) PL spectra of SDS-coated (6,5) SWNTs functionalized at different concentrations of Dz-Alkyne in SDS after addition of 15 µM [Cu] and 4 mM of PP_i.

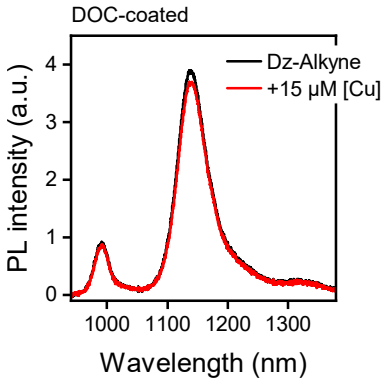

Figure C.7: PL spectra of 4-ethynylbenzene-functionalized DOC-coated (6,5) SWNTs before and after addition of 15 µM [Cu].

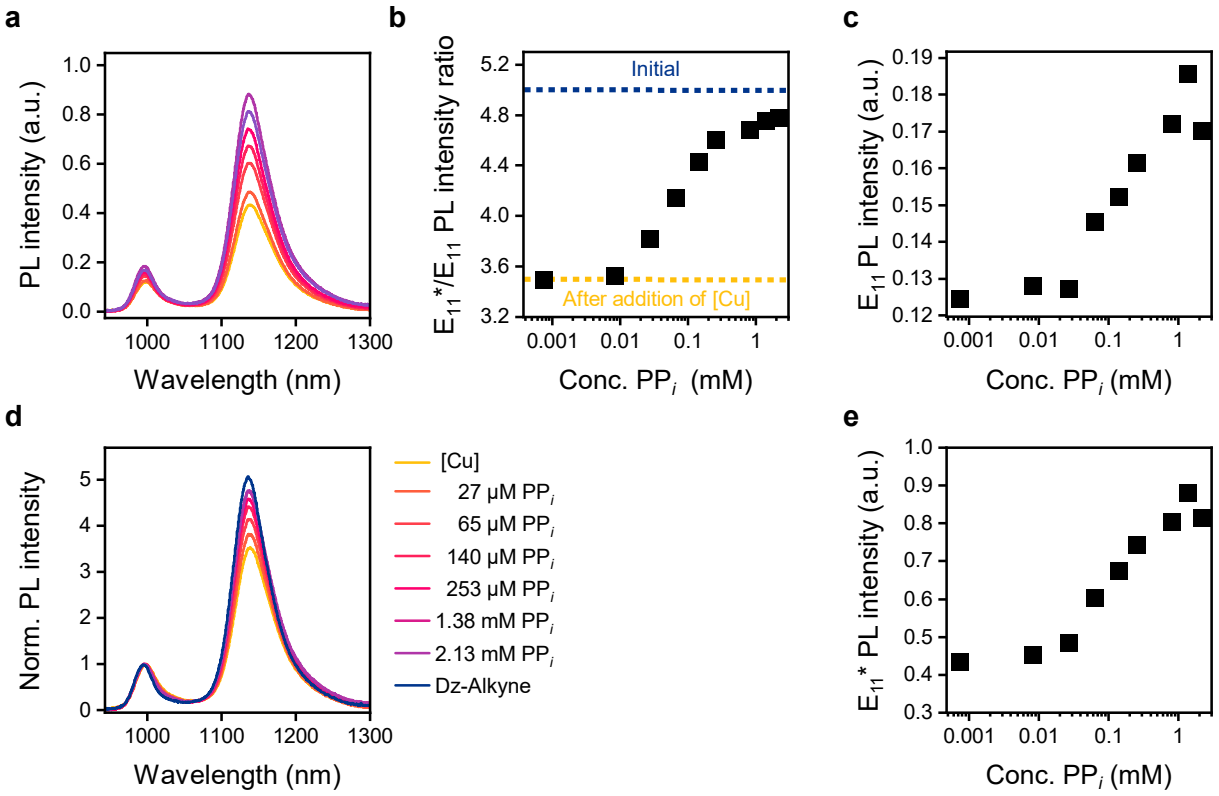

Figure C.8: a,d) Absolute (a) and normalized (d) PL spectra of 4-ethynylbenzene-functionalized PL-PEG$_{5000}$-coated (6,5) SWNTs in 10 mM MOPS buffer at various concentrations of PP$_i$. b) E$_{11}$*/E$_{11}$ PL intensity ratio *vs.* PP$_i$ concentration. c) E$_{11}$ PL intensity *vs.* PP$_i$ concentration. e) E$_{11}$* PL intensity *vs.* PP$_i$ concentration. Initial E$_{11}$*/E$_{11}$ PL intensity ratios before and after the addition of [Cu] are indicated by blue and yellow dotted lines, respectively.

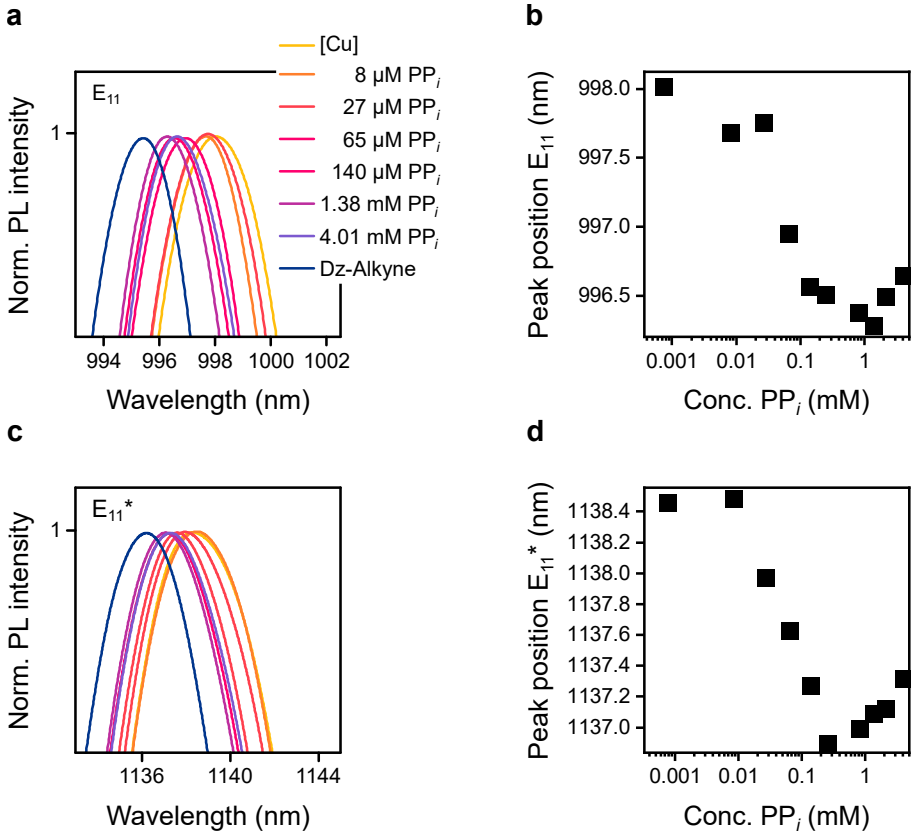

Figure C.9: a,c) Zoom-in on the normalized E_{11} (a) and E_{11}* (c) PL peak of 4-ethynylbenzene-functionalized PL-PEG$_{5000}$-coated (6,5) SWNTs in 10 mM MOPS buffer at various concentrations of PP_i. b,d) PP_i concentration-dependent changes in E_{11} and E_{11}* PL peak position.

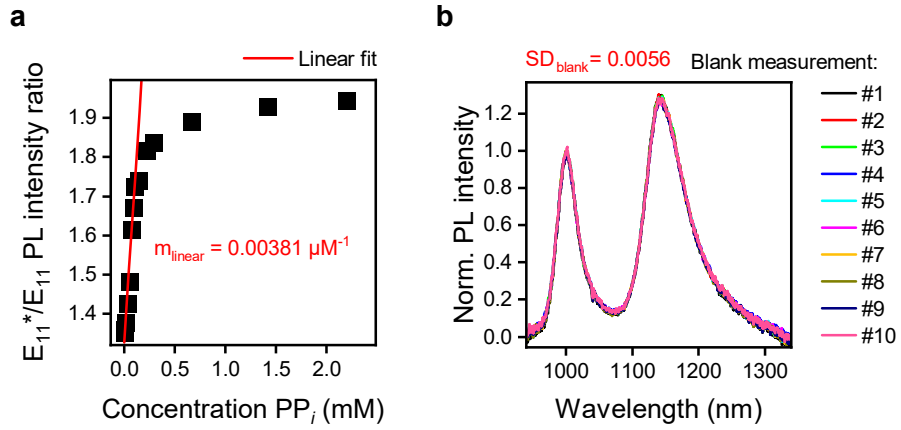

Figure C.10: a) PP_i concentration-dependent changes of the E_{11}*/E_{11} PL intensity ratio of 4-ethynylbenzene-functionalized PL-PEG$_{5000}$-coated (6,5) SWNTs in 10 mM MOPS buffer at low sp^3 defect density with linear fit to data at low concentrations of PP_i ($m_{linear} = 0.00381\ \mu M^{-1}$). b) Normalized PL spectra after addition of [Cu]. The standard deviation of the E_{11}*/E_{11} PL intensity ratio was $SD_{blank} = 0.0056$ (number of blank measurements = 10).

BIBLIOGRAPHY

1. Sillard, P. & Molin, D. in *Fibre Optic Communication*: *Key Devices* (eds Venghaus, H. & Grote, N.) 49–102 (Springer, Cham, 2017) (cit. on p. 1).
2. Grote, N., Möhrle, M. & Ortsiefer, M. in *Fibre Optic Communication: Key Devices* (eds Venghaus, H. & Grote, N.) 103–149 (Springer, Cham, 2017) (cit. on p. 1).
3. Aharonovich, I., Englund, D. & Toth, M. Solid-state single-photon emitters. *Nat. Photonics* **10,** 631–641 (2016) (cit. on p. 1).
4. Nathan, A. *et al.* Flexible electronics: The next ubiquitous platform. *Proc. IEEE* **100,** 1486–1517 (2012) (cit. on p. 1).
5. Chen, Y., Wang, S. & Zhang, F. Near-infrared luminescence high-contrast *in vivo* biomedical imaging. *Nat. Rev. Bioeng.* **1,** 60–78 (2023) (cit. on pp. 1, 31, 89, 113).
6. Weisman, R. B. & Bachilo, S. M. Dependence of optical transition energies on structure for single-walled carbon nanotubes in aqueous suspension: An empirical Kataura plot. *Nano Lett.* **3,** 1235–1238 (2003) (cit. on pp. 1, 5, 13, 56, 159).
7. Zaumseil, J. Single-walled carbon nanotube networks for flexible and printed electronics. *Semicond. Sci. Technol.* **30,** 074001 (2015) (cit. on p. 1).
8. Zaumseil, J. Semiconducting single-walled carbon nanotubes or very rigid conjugated polymers: A comparison. *Adv. Electron. Mater.* **5,** 1800514 (2019) (cit. on p. 1).
9. Barone, P. W., Baik, S., Heller, D. A. & Strano, M. S. Near-infrared optical sensors based on single-walled carbon nanotubes. *Nat. Mater.* **4,** 86–92 (2005) (cit. on p. 1).
10. Ackermann, J., Metternich, J. T., Herbertz, S. & Kruss, S. Biosensing with fluorescent carbon nanotubes. *Angew. Chem. Int. Ed.* **61,** e202112372 (2022) (cit. on pp. 1, 32, 33, 35, 149).
11. Ghosh, S., Bachilo, S. M., Simonette, R. A., Beckingham, K. M. & Weisman, R. B. Oxygen doping modifies near-infrared band gaps in fluorescent single-walled carbon nanotubes. *Science* **330,** 1656–1659 (2010) (cit. on pp. 2, 17–19, 29, 30, 62, 71, 90, 97, 100, 107, 148).
12. Brozena, A. H., Kim, M., Powell, L. R. & Wang, Y. Controlling the optical properties of carbon nanotubes with organic colour-centre quantum defects. *Nat. Rev. Chem.* **3,** 375–392 (2019) (cit. on pp. 2, 17, 24, 31, 80, 107).
13. Zaumseil, J. Luminescent defects in single-walled carbon nanotubes for applications. *Adv. Optical Mater.* **10,** 2101576 (2022) (cit. on pp. 2, 17, 35).

14. Shiraki, T., Miyauchi, Y., Matsuda, K. & Nakashima, N. Carbon nanotube photoluminescence modulation by local chemical and supramolecular chemical functionalization. *Acc. Chem. Res.* **53,** 1846–1859 (2020) (cit. on pp. 2, 17, 35).

15. Piao, Y. *et al.* Brightening of carbon nanotube photoluminescence through the incorporation of sp^3 defects. *Nat. Chem.* **5,** 840–5 (2013) (cit. on pp. 2, 5, 17, 19, 24, 25, 45, 61, 62, 67, 82, 94, 95, 112, 145).

16. Mandal, A. K. *et al.* Fluorescent sp^3 defect-tailored carbon nanotubes enable NIR-II single particle imaging in live brain slices at ultra-low excitation doses. *Sci. Rep.* **10,** 5286 (2020) (cit. on pp. 2, 32).

17. Mann, F. A., Herrmann, N., Opazo, F. & Kruss, S. Quantum defects as a toolbox for the covalent functionalization of carbon nanotubes with peptides and proteins. *Angew. Chem. Int. Ed.* **59,** 17732–17738 (2020) (cit. on pp. 2, 35, 36, 88).

18. Ma, X., Hartmann, N. F., Baldwin, J. K. S., Doorn, S. K. & Htoon, H. Room-temperature single-photon generation from solitary dopants of carbon nanotubes. *Nat. Nanotechnol.* **10,** 671–675 (2015) (cit. on pp. 2, 17, 27, 30, 62, 72, 145).

19. He, X. *et al.* Tunable room-temperature single-photon emission at telecom wavelengths from sp^3 defects in carbon nanotubes. *Nat. Photonics* **11,** 577–582 (2017) (cit. on pp. 2, 17, 21, 62, 76, 78, 145, 146).

20. Lounis, B. & Orrit, M. Single-photon sources. *Rep. Prog. Phys.* **68,** 1129 (2005) (cit. on p. 2).

21. Gifford, B. J., Kilina, S., Htoon, H., Doorn, S. K. & Tretiak, S. Controlling defect-state photophysics in covalently functionalized single-walled carbon nanotubes. *Acc. Chem. Res.* **53,** 1791–1801 (2020) (cit. on pp. 2, 17, 22, 27, 62, 145).

22. Kim, M. *et al.* Detection of ovarian cancer *via* the spectral fingerprinting of quantum-defect-modified carbon nanotubes in serum by machine learning. *Nat. Biomed. Eng.* **6,** 267–275 (2022) (cit. on pp. 2, 33, 34, 115, 116, 122, 145, 149).

23. Spreinat, A. *et al.* Quantum defects in fluorescent carbon nanotubes for sensing and mechanistic studies. *J. Phys. Chem. C* **125,** 18341–18351 (2021) (cit. on pp. 2, 33, 34, 110, 115, 149).

24. Hirsch, A. The era of carbon allotropes. *Nat. Mater.* **9,** 868–871 (2010) (cit. on p. 5).

25. Tanaka, K. in *Carbon Nanotubes and Graphene* (eds Tanaka, K. & Iijima, S.) (Elsevier, Oxford, 2014) (cit. on p. 5).

26. Collavini, S. & Delgado, J. L. Fullerenes: The stars of photovoltaics. *Sustain. Energy Fuels* **2,** 2480–2493 (2018) (cit. on p. 5).

27. Nelson, J. Polymer: Fullerene bulk heterojunction solar cells. *Mater. Today* **14,** 462–470 (2011) (cit. on p. 5).

28. Partha, R. & Conyers, J. L. Biomedical applications of functionalized fullerene-based nanomaterials. *Int. J. Nanomedicine.* **4,** 261–275 (2009) (cit. on p. 5).

29. Balandin, A. A. Thermal properties of graphene and nanostructured carbon materials. *Nat. Mater.* **10,** 569–581 (2011) (cit. on p. 5).

30. Bonaccorso, F., Sun, Z., Hasan, T. & Ferrari, A. C. Graphene photonics and optoelectronics. *Nat. Photonics* **4,** 611–622 (2010) (cit. on p. 5).

31. Geim, A. K. & Novoselov, K. S. The rise of graphene. *Nat. Mater.* **6,** 183–191 (2007) (cit. on p. 5).

32. Iijima, S. Helical microtubules of graphitic carbon. *Nature* **354,** 56–58 (1991) (cit. on p. 5).

33. Bethune, D. S. *et al.* Cobalt-catalysed growth of carbon nanotubes with single-atomic-layer walls. *Nature* **363,** 605–607 (1993) (cit. on p. 5).

34. Wang, X. *et al.* Fabrication of ultralong and electrically uniform single-walled carbon nanotubes on clean substrates. *Nano Lett.* **9,** 3137–3141 (2009) (cit. on p. 5).

35. Takakura, A. *et al.* Strength of carbon nanotubes depends on their chemical structures. *Nat. Commun.* **10,** 3040 (2019) (cit. on pp. 5, 10).

36. White, C. T. & Todorov, T. N. Carbon nanotubes as long ballistic conductors. *Nature* **393,** 240–242 (1998) (cit. on p. 5).

37. Javey, A., Guo, J., Wang, Q., Lundstrom, M. & Dai, H. Ballistic carbon nanotube field-effect transistors. *Nature* **424,** 654–657 (2003) (cit. on p. 5).

38. Bachilo, S. M. *et al.* Structure-assigned optical spectra of single-walled carbon nanotubes. *Science* **298,** 2361–2366 (2002) (cit. on pp. 5, 31).

39. Yang, F. *et al.* Chirality-specific growth of single-walled carbon nanotubes on solid alloy catalysts. *Nature* **510,** 522–524 (2014) (cit. on pp. 5, 7).

40. Zhang, S. *et al.* Arrays of horizontal carbon nanotubes of controlled chirality grown using designed catalysts. *Nature* **543,** 234–238 (2017) (cit. on p. 5).

41. Liu, B., Wu, F., Gui, H., Zheng, M. & Zhou, C. Chirality-controlled synthesis and applications of single-wall carbon nanotubes. *ACS Nano* **11,** 31–53 (2017) (cit. on pp. 5, 8).

42. Tu, X., Manohar, S., Jagota, A. & Zheng, M. DNA sequence motifs for structure-specific recognition and separation of carbon nanotubes. *Nature* **460,** 250–253 (2009) (cit. on pp. 5, 8).

43. Fagan, J. A. Aqueous two-polymer phase extraction of single-wall carbon nanotubes using surfactants. *Nanoscale Adv.* **1,** 3307–3324 (2019) (cit. on pp. 5, 8–10, 39, 91).

44. Samanta, S. K. *et al.* Conjugated polymer-assisted dispersion of single-wall carbon nanotubes: The power of polymer wrapping. *Acc. Chem. Res.* **47,** 2446–2456 (2014) (cit. on pp. 5, 10, 63).

45. Setaro, A. *et al.* Preserving π-conjugation in covalently functionalized carbon nanotubes for optoelectronic applications. *Nat. Commun.* **8,** 14281 (2017) (cit. on pp. 5, 18, 26).

46. Akinwande, D. & Wong, H. S. P. *Carbon Nanotube and Graphene Device Physics* (Cambridge University Press, Cambridge, 2010) (cit. on pp. 6, 7, 12, 13).

47. Dresselhaus, M. S., Dresselhaus, G. & Saito, R. Physics of carbon nanotubes. *Carbon* **33,** 883–891 (1995) (cit. on p. 6).

48. Charlier, J.-C., Blase, X. & Roche, S. Electronic and transport properties of nanotubes. *Rev. Mod. Phys.* **79,** 677–732 (2007) (cit. on pp. 6, 11, 12).

49. Odom, T. W., Huang, J.-L., Kim, P. & Lieber, C. M. Structure and electronic properties of carbon nanotubes. *J. Phys. Chem. B* **104,** 2794–2809 (2000) (cit. on p. 6).

50. Ao, G., Streit, J. K., Fagan, J. A. & Zheng, M. Differentiating left- and right-handed carbon nanotubes by DNA. *J. Am. Chem. Soc.* **138,** 16677–16685 (2016) (cit. on p. 6).

51. Kataura, H. *et al.* Diameter control of single-walled carbon nanotubes. *Carbon* **38,** 1691–1697 (2000) (cit. on p. 7).

52. Guo, T., Nikolaev, P., Thess, A., Colbert, D. T. & Smalley, R. E. Catalytic growth of single-walled manotubes by laser vaporization. *Chem. Phys. Lett.* **243,** 49–54 (1995) (cit. on p. 7).

53. Ando, Y. *et al.* Mass production of single-wall carbon nanotubes by the arc plasma jet method. *Chem. Phys. Lett.* **323,** 580–585 (2000) (cit. on p. 7).

54. Su Kim, K. *et al.* Large-scale production of single-walled carbon nanotubes by induction thermal plasma. *J. Phys. D*: *Appl. Phys.* **40,** 2375 (2007) (cit. on p. 7).

55. Prasek, J. *et al.* Methods for carbon nanotubes synthesis-review. *J. Mater. Chem.* **21,** 15872–15884 (2011) (cit. on p. 7).

56. Bati, A. S. R., Yu, L., Batmunkh, M. & Shapter, J. G. Synthesis, purification, properties and characterization of sorted single-walled carbon nanotubes. *Nanoscale* **10,** 22087–22139 (2018) (cit. on p. 7).

57. Hofmann, S. *et al. In situ* observations of catalyst dynamics during surface-bound carbon nanotube nucleation. *Nano Lett.* **7,** 602–608 (2007) (cit. on p. 7).

58. Kitiyanan, B., Alvarez, W. E., Harwell, J. H. & Resasco, D. E. Controlled production of single-wall carbon nanotubes by catalytic decomposition of CO on bimetallic Co-Mo catalysts. *Chem. Phys. Lett.* **317,** 497–503 (2000) (cit. on p. 7).

59. Bachilo, S. M. *et al.* Narrow (n,m)-distribution of single-walled carbon nanotubes grown using a solid supported catalyst. *J. Am. Chem. Soc.* **125,** 11186–11187 (2003) (cit. on p. 7).

60. Lolli, G. *et al.* Tailoring (n,m) structure of single-walled carbon nanotubes by modifying reaction conditions and the nature of the support of CoMo catalysts. *J. Phys. Chem. B* **110,** 2108–2115 (2006) (cit. on p. 7).

61. Resasco, D. E. *et al.* A scalable process for production of single-walled carbon nanotubes (SWNTs) by catalytic disproportionation of CO on a solid catalyst. *J. Nanoparticle Res.* **4,** 131–136 (2002) (cit. on p. 7).

62. Nikolaev, P. *et al.* Gas-phase catalytic growth of single-walled carbon nanotubes from carbon monoxide. *Chem. Phys. Lett.* **313,** 91–97 (1999) (cit. on p. 7).

63. Bronikowski, M. J., Willis, P. A., Colbert, D. T., Smith, K. A. & Smalley, R. E. Gas-phase production of carbon single-walled nanotubes from carbon monoxide *via* the HiPco process: A parametric study. *J. Vac. Sci. Technol. A* **19,** 1800–1805 (2001) (cit. on p. 7).

64. Nadeem, A. *et al.* Enhancing intracellular optical performance and stability of engineered nanomaterials *via* aqueous two-phase purification. *Nano Lett.* **23,** 6588–6595 (2023) (cit. on p. 8).

65. Coleman, J. N. Liquid-phase exfoliation of nanotubes and graphene. *Adv. Funct. Mater.* **19,** 3680–3695 (2009) (cit. on p. 8).

66. Chiou, K., Byun, S., Kim, J. & Huang, J. Additive-free carbon nanotube dispersions, pastes, gels, and doughs in cresols. *Proc. Natl. Acad. Sci.* **115,** 5703–5708 (2018) (cit. on p. 8).

67. Arnold, M. S., Green, A. A., Hulvat, J. F., Stupp, S. I. & Hersam, M. C. Sorting carbon nanotubes by electronic structure using density differentiation. *Nat. Nanotechnol.* **1,** 60–65 (2006) (cit. on pp. 8, 9).

68. Ghosh, S., Bachilo, S. M. & Weisman, R. B. Advanced sorting of single-walled carbon nanotubes by nonlinear density-gradient ultracentrifugation. *Nat. Nanotechnol.* **5,** 443–450 (2010) (cit. on p. 8).

69. Ihara, K., Endoh, H., Saito, T. & Nihey, F. Separation of metallic and semiconducting single-wall carbon nanotube solution by vertical electric field. *J. Phys. Chem. C* **115,** 22827–22832 (2011) (cit. on p. 8).

70. Liu, H., Nishide, D., Tanaka, T. & Kataura, H. Large-scale single-chirality separation of single-wall carbon nanotubes by simple gel chromatography. *Nat. Commun.* **2,** 309 (2011) (cit. on p. 8).

71. Khripin, C. Y., Fagan, J. A. & Zheng, M. Spontaneous partition of carbon nanotubes in polymer-modified aqueous ühases. *J. Am. Chem. Soc.* **135,** 6822–6825 (2013) (cit. on p. 8).

72. Nish, A., Hwang, J.-Y., Doig, J. & Nicholas, R. J. Highly selective dispersion of single-walled carbon nanotubes using aromatic polymers. *Nat. Nanotechnol.* **2,** 640–646 (2007) (cit. on pp. 8, 10).

73. Ao, G., Khripin, C. Y. & Zheng, M. DNA-controlled partition of carbon nanotubes in polymer aqueous two-phase systems. *J. Am. Chem. Soc.* **136,** 10383–10392 (2014) (cit. on p. 8).

74. Lin, Z., Yang, Y., Jagota, A. & Zheng, M. Machine learning-guided systematic search of DNA sequences for sorting carbon nanotubes. *ACS Nano* **16,** 4705–4713 (2022) (cit. on p. 8).

75. Yang, H., Neal, L., Flores, E. E., Adronov, A. & Kim, N. Y. Role and impact of surfactants in carbon nanotube dispersions and sorting. *J. Surfact. Deterg.* **26,** 607–622 (2023) (cit. on p. 9).

76. Blanch, A. J. & Shapter, J. G. Surfactant concentration dependent spectral effects of oxygen and depletion interactions in sodium dodecyl sulfate dispersions of carbon nanotubes. *J. Phys. Chem. B* **118,** 6288–6296 (2014) (cit. on pp. 9, 94, 136).

77. Zeng, X. *et al.* Detecting and tuning the interactions between surfactants and carbon nanotubes for their high-efficiency structure separation. *Adv. Mater. Interfaces* **5,** 1700727 (2018) (cit. on p. 9).

78. Tummala, N. R. & Striolo, A. SDS surfactants on carbon nanotubes: Aggregate morphology. *ACS Nano* **3,** 595–602 (2009) (cit. on pp. 9, 10, 24, 91).

79. Richard, C., Balavoine, F., Schultz, P., Ebbesen, T. W. & Mioskowski, C. Supramolecular self-assembly of lipid derivatives on carbon nanotubes. *Science* **300,** 775–778 (2003) (cit. on p. 10).

80. Li, H. *et al.* Separation of specific single-enantiomer single-wall carbon nanotubes in the large-diameter regime. *ACS Nano* **14,** 948–963 (2020) (cit. on p. 10).

81. Wei, L., Flavel, B. S., Li, W., Krupke, R. & Chen, Y. Exploring the upper limit of single-walled carbon nanotube purity by multiple-cycle aqueous two-phase separation. *Nanoscale* **9,** 11640–11646 (2017) (cit. on p. 10).

82. Hennrich, F. *et al.* Length-sorted, large-diameter, polyfluorene-wrapped semiconducting single-walled carbon nanotubes for high-density, short-channel transistors. *ACS Nano* **10,** 1888–1895 (2016) (cit. on p. 10).

83. Graf, A. *et al.* Large scale, selective dispersion of long single-walled carbon nanotubes with high photoluminescence quantum yield by shear force mixing. *Carbon* **105,** 593–599 (2016) (cit. on pp. 10, 11, 37, 52, 56, 63).

84. Stürzl, N., Hennrich, F., Lebedkin, S. & Kappes, M. M. Near monochiral single-walled carbon nanotube dispersions in organic solvents. *J. Phys. Chem. C* **113,** 14628–14632 (2009) (cit. on pp. 10, 11, 88, 146).

85. Jakubka, F. *et al.* Effect of polymer molecular weight and solution parameters on selective dispersion of single-walled carbon nanotubes. *ACS Macro Lett.* **1,** 815–819 (2012) (cit. on pp. 10, 11).

86. Kang, Y. K. *et al.* Helical wrapping of single-walled carbon nanotubes by water soluble poly(*p*-phenyleneethynylene). *Nano Lett.* **9,** 1414–1418 (2009) (cit. on p. 10).

87. Deria, P. *et al.* Single-handed helical wrapping of single-walled carbon nanotubes by chiral, ionic, semiconducting polymers. *J. Am. Chem. Soc.* **135,** 16220–16234 (2013) (cit. on p. 10).

88. Gomulya, W. *et al.* Semiconducting single-walled carbon nanotubes on demand by polymer wrapping. *Adv. Mater.* **25,** 2948–2956 (2013) (cit. on p. 10).

89. Gao, J., Loi, M. A., de Carvalho, E. J. F. & dos Santos, M. C. Selective wrapping and supramolecular structures of polyfluorene–carbon nanotube hybrids. *ACS Nano* **5,** 3993–3999 (2011) (cit. on p. 10).

90. Joo, Y. *et al.* Isolation of pristine electronics grade semiconducting carbon nanotubes by switching the rigidity of the wrapping polymer backbone on demand. *ACS Nano* **9,** 10203–10213 (2015) (cit. on p. 10).

91. Salazar-Rios, J. M. *et al.* Understanding the selection mechanism of the polymer wrapping technique toward semiconducting carbon nanotubes. *Small Methods* **2,** 1700335 (2018) (cit. on p. 10).

92. Imin, P., Cheng, F. & Adronov, A. The effect of molecular weight on the supramolecular interaction between a conjugated polymer and single-walled carbon nanotubes. *Polym. Chem.* **2,** 1404–1408 (2011) (cit. on p. 10).

93. Hwang, J.-Y. *et al.* Polymer structure and solvent effects on the selective dispersion of single-walled carbon nanotubes. *J. Am. Chem. Soc.* **130,** 3543–3553 (2008) (cit. on p. 10).

94. Sun, Z., O'Connor, I., Bergin, S. D. & Coleman, J. N. Effects of ambient conditions on solvent-nanotube dispersions: Exposure to water and temperature variation. *J. Phys. Chem. C* **113,** 1260–1266 (2009) (cit. on p. 10).

95. Fong, D. & Adronov, A. Recent developments in the selective dispersion of single-walled carbon nanotubes using conjugated polymers. *Chem. Sci.* **8,** 7292–7305 (2017) (cit. on p. 10).

96. Ozawa, H., Ide, N., Fujigaya, T., Niidome, Y. & Nakashima, N. One-pot separation of highly enriched (6,5)-single-walled carbon nanotubes using a fluorene-based copolymer. *Chem. Lett.* **40,** 239–241 (2011) (cit. on p. 11).

97. Naumov, A. V., Tsyboulski, D. A., Bachilo, S. M. & Weisman, R. B. Length-dependent optical properties of single-walled carbon nanotube samples. *Chem. Phys.* **422,** 255–263 (2013) (cit. on p. 11).

98. Cambré, S. *et al.* Luminescence properties of individual empty and water-filled single-walled carbon nanotubes. *ACS Nano* **6,** 2649–2655 (2012) (cit. on p. 11).

99. Lindenthal, S., Settele, S., Hellmann, J., Schmitt, K. & Zaumseil, J. A hands-on guide to shear force mixing of single-walled carbon nanotubes with conjugated polymers, https://doi.org/10.11588/heidok.00033977 (2023) (cit. on pp. 11, 37).

100. Reich, S., Maultzsch, J., Thomsen, C. & Ordejón, P. Tight-binding description of graphene. *Phys. Rev. B* **66,** 035412 (2002) (cit. on p. 11).

101. Saito, R., Dresselhaus, G. & Dresselhaus, M. S. Trigonal warping effect of carbon nanotubes. *Phys. Rev. B* **61,** 2981–2990 (2000) (cit. on pp. 12, 13).

102. Sato, K., Saito, R., Jiang, J., Dresselhaus, G. & Dresselhaus, M. S. Discontinuity in the family pattern of single-wall carbon nanotubes. *Phys. Rev. B* **76,** 195446 (2007) (cit. on p. 13).

103. Yu, P. Y. & Cardona, M. *Fundamentals of Semiconductors* (Springer, Berlin, 2005) (cit. on pp. 13, 14).

104. Katsutani, F. *et al.* Direct observation of cross-polarized excitons in aligned single-chirality single-wall carbon nanotubes. *Phys. Rev. B* **99,** 035426 (2019) (cit. on p. 13).

105. Amori, A. R., Hou, Z. & Krauss, T. D. Excitons in single-walled carbon nanotubes and their dynamics. *Annu. Rev. Phys. Chem.* **69,** 81–99 (2018) (cit. on pp. 13, 16).

106. Blancon, J.-C. *et al.* Direct measurement of the absolute absorption spectrum of individual semiconducting single-wall carbon nanotubes. *Nat. Commun.* **4,** 2542 (2013) (cit. on p. 13).

107. Spataru, C. D., Ismail-Beigi, S., Benedict, L. X. & Louie, S. G. Excitonic effects and optical spectra of single-walled carbon nanotubes. *Phys. Rev. Lett* **92,** 077402 (2004) (cit. on pp. 13, 14).

108. Dresselhaus, M. S., Dresselhaus, G., Saito, R. & Jorio, A. Exciton photophysics of carbon nanotubes. *Annu. Rev. Phys. Chem.* **58,** 719–747 (2007) (cit. on pp. 13, 14).

109. Chernikov, A. *et al.* Exciton binding energy and nonhydrogenic rydberg series in monolayer WS_2. *Phys. Rev. Lett.* **113,** 076802 (2014) (cit. on p. 14).

110. Wang, F., Dukovic, G., Brus, L. E. & Heinz, T. F. The optical resonances in carbon nanotubes arise from excitons. *Science* **308,** 838–841 (2005) (cit. on p. 14).

111. Maultzsch, J. *et al.* Exciton binding energies in carbon nanotubes from two-photon photoluminescence. *Phys. Rev. B* **72,** 241402 (2005) (cit. on p. 14).

112. Zhao, H. & Mazumdar, S. Electron-electron interaction effects on the optical excitations of semiconducting single-walled carbon nanotubes. *Phys. Rev. Lett.* **93,** 157402 (2004) (cit. on pp. 15, 16).

113. Perebeinos, V., Tersoff, J. & Avouris, P. Scaling of excitons in carbon nanotubes. *Phys. Rev. Lett.* **92,** 257402 (2004) (cit. on p. 15).

114. Mortimer, I. B. & Nicholas, R. J. Role of bright and dark excitons in the temperature-dependent photoluminescence of carbon nanotubes. *Phys. Rev. Lett.* **98,** 027404 (2007) (cit. on pp. 15, 18).

115. Blackburn, J. L., Holt, J. M., Irurzun, V. M., Resasco, D. E. & Rumbles, G. Confirmation of K-momentum dark exciton vibronic sidebands using ^{13}C-labeled, highly enriched (6,5) single-walled carbon nanotubes. *Nano Lett.* **12,** 1398–1403 (2012) (cit. on pp. 15, 16).

116. Kadria-Vili, Y., Bachilo, S. M., Blackburn, J. L. & Weisman, R. B. Photoluminescence side band spectroscopy of individual single-walled carbon nanotubes. *J. Phys. Chem. C* **120,** 23898–23904 (2016) (cit. on pp. 15, 16, 77).

117. Amori, A. R., Rossi, J. E., Landi, B. J. & Krauss, T. D. Defects enable dark exciton photoluminescence in single-walled carbon nanotubes. *J. Phys. Chem. C* **122,** 3599–3607 (2018) (cit. on p. 15).

118. Perebeinos, V., Tersoff, J. & Avouris, P. Radiative lifetime of excitons in carbon nanotubes. *Nano Lett.* **5,** 2495–2499 (2005) (cit. on pp. 15, 19, 69).

119. Soavi, G., Scotognella, F., Lanzani, G. & Cerullo, G. Ultrafast photophysics of single-walled carbon nanotubes. *Adv. Opt. Mater.* **4,** 1670–1688 (2016) (cit. on p. 15).

120. Jones, M. *et al.* Analysis of photoluminescence from solubilized single-walled carbon nanotubes. *Phys. Rev. B* **71,** 115426 (2005) (cit. on p. 16).

121. Zorn, N. F. *et al.* Near-intrinsic photo- and electroluminescence from single-walled carbon nanotube thin films on BCB-passivated surfaces. *Adv. Optical Mater.* **11,** 2300236 (2023) (cit. on pp. 16, 77).

122. Englman, R. & Jortner, J. The energy gap law for radiationless transitions in large molecules. *Mol. Phys.* **18,** 145–164 (1970) (cit. on p. 16).

123. Larsen, B. A. *et al.* Effect of solvent polarity and electrophilicity on quantum yields and solvatochromic shifts of single-walled carbon nanotube photoluminescence. *J. Am. Chem. Soc.* **134,** 12485–12491 (2012) (cit. on pp. 16, 32, 127).

124. Silvera-Batista, C. A., Wang, R. K., Weinberg, P. & Ziegler, K. J. Solvatochromic shifts of single-walled carbon nanotubes in nonpolar microenvironments. *Phys. Chem. Chem. Phys.* **12,** 6990–6998 (2010) (cit. on pp. 16, 32).

125. Ju, S.-Y., Kopcha, W. P. & Papadimitrakopoulos, F. Brightly fluorescent single-walled carbon nanotubes *via* an oxygen-excluding surfactant organization. *Science* **323,** 1319–1323 (2009) (cit. on p. 16).

126. Hertel, T., Himmelein, S., Ackermann, T., Stich, D. & Crochet, J. Diffusion limited photoluminescence quantum yields in 1-D semiconductors: Single-wall carbon nanotubes. *ACS Nano* **4,** 7161–7168 (2010) (cit. on pp. 16, 17, 19, 21, 31, 69, 134).

127. Birkmeier, K., Hertel, T. & Hartschuh, A. Probing the ultrafast dynamics of excitons in single semiconducting carbon nanotubes. *Nat. Commun.* **13,** 6290 (2022) (cit. on p. 16).

128. Avouris, P., Freitag, M. & Perebeinos, V. Carbon-nanotube photonics and optoelectronics. *Nat. Photonics* **2,** 341–350 (2008) (cit. on p. 16).

129. Cole, M. W. *et al.* Structural, electronic, optical and vibrational properties of nanoscale carbons and nanowires: A colloquial review. *J. Condens. Matter Phys.* **22,** 334201 (2010) (cit. on p. 16).

130. Cognet, L. *et al.* Stepwise quenching of exciton fluorescence in carbon nanotubes by single-molecule reactions. *Science* **316,** 1465–1468 (2007) (cit. on pp. 16, 17, 24).

131. O'Connell, M. J. *et al.* Band gap fluorescence from individual single-walled carbon nanotubes. *Science* **297,** 593–596 (2002) (cit. on p. 17).

132. Tasis, D., Tagmatarchis, N., Bianco, A. & Prato, M. Chemistry of carbon nanotubes. *Chem. Rev.* **106,** 1105–1136 (2006) (cit. on pp. 17, 24, 85).

133. Hartmann, N. F. *et al.* Photoluminescence dynamics of aryl sp^3 defect states in single-walled carbon nanotubes. *ACS Nano* **10,** 8355–8365 (2016) (cit. on pp. 17, 19, 20, 75, 80).

134. Hartmann, N. F. *et al.* Photoluminescence imaging of solitary dopant sites in covalently doped single-wall carbon nanotubes. *Nanoscale* **7,** 20521–20530 (2015) (cit. on pp. 17, 18).

135. Janas, D. Perfectly imperfect: A review of chemical tools for exciton engineering in single-walled carbon nanotubes. *Mater. Horiz.* **7,** 2860–2881 (2020) (cit. on pp. 17, 24, 30).

136. Kilina, S., Ramirez, J. & Tretiak, S. Brightening of the lowest exciton in carbon nanotubes *via* chemical functionalization. *Nano Lett.* **12,** 2306–2312 (2012) (cit. on pp. 18, 22).

137. Gifford, B. J. *et al.* Optical effects of divalent functionalization of carbon nanotubes. *Chem. Mater.* **31,** 6950–6961 (2019) (cit. on pp. 18, 22, 27, 84).

138. Spataru, C. D., Ismail-Beigi, S., Capaz, R. B. & Louie, S. G. Theory and *ab initio* calculation of radiative lifetime of excitons in semiconducting carbon nanotubes. *Phys. Rev. Lett.* **95,** 247402 (2005) (cit. on pp. 19, 69).

139. He, X. *et al.* Solvent- and wavelength-dependent photoluminescence relaxation dynamics of carbon nanotube sp^3 defect states. *ACS Nano* **12,** 8060–8070 (2018) (cit. on pp. 19–21, 31, 61, 68–70, 74, 96, 97, 132).

140. Sykes, M. E. *et al.* Ultrafast exciton trapping at sp^3 quantum defects in carbon nanotubes. *ACS Nano* **13,** 13264–13270 (2019) (cit. on p. 19).

141. Berger, F. J. *et al.* Brightening of long, polymer-wrapped carbon nanotubes by sp^3 functionalization in organic solvents. *ACS Nano* **13,** 9259–9269 (2019) (cit. on pp. 19, 24–26, 42, 61, 62, 67, 68, 70, 71, 96, 145).

142. Danné, N. *et al.* Ultrashort carbon nanotubes that fluoresce brightly in the near-infrared. *ACS Nano* **12,** 6059–6065 (2018) (cit. on pp. 19, 26, 32, 71, 72, 109).

143. Kozawa, D. *et al.* Formation of organic color centers in air-suspended carbon nanotubes using vapor-phase reaction. *Nat. Commun.* **13,** 2814 (2022) (cit. on pp. 19, 26).

144. Sebastian, F. L. *et al.* Absolute quantification of sp^3 defects in semiconducting single-wall carbon nanotubes by Raman spectroscopy. *J. Phys. Chem. Lett.* **13,** 3542–3548 (2022) (cit. on pp. 19, 32, 39, 58, 66, 68, 80, 104, 105, 154).

145. Yu, B. *et al. ortho*-substituted aryldiazonium design for the defect configuration-controlled photoluminescent functionalization of chiral single-walled carbon nanotubes. *ACS Nano* **16,** 21452–21461 (2022) (cit. on pp. 19, 27, 31, 32, 36, 62, 88, 112).

146. Kim, M. *et al.* Fluorescent carbon nanotube defects manifest substantial vibrational reorganization. *J. Phys. Chem. C* **120,** 11268–11276 (2016) (cit. on pp. 19, 30, 70, 72, 90, 94, 97).

147. Perebeinos, V. & Avouris, P. Phonon and electronic nonradiative decay mechanisms of excitons in carbon nanotubes. *Phys. Rev. Lett.* **101,** 057401 (2008) (cit. on pp. 20, 74).

148. Aharoni, A., Oron, D., Banin, U., Rabani, E. & Jortner, J. Long-range electronic-to-vibrational energy transfer from nanocrystals to their surrounding matrix environment. *Phys. Rev. Lett.* **100,** 057404 (2008) (cit. on p. 20).

149. Wen, Q. *et al.* Impact of D_2O /H_2O solvent exchange on the emission of HgTe and CdTe quantum dots: Polaron and energy transfer effects. *ACS Nano* **10,** 4301–4311 (2016) (cit. on p. 20).

150. Gifford, B. J., Kilina, S., Htoon, H., Doorn, S. K. & Tretiak, S. Exciton localization and optical emission in aryl-functionalized carbon nanotubes. *J. Phys. Chem. C* **122,** 1828–1838 (2018) (cit. on pp. 21, 62, 66).

151. Kwon, H. *et al.* Probing trions at chemically tailored trapping defects. *ACS Cent. Sci.* **5,** 1786–1794 (2019) (cit. on p. 21).

152. Castelletto, S. & Boretti, A. Perspective on solid-state single-photon sources in the infrared for quantum technology. *Adv. Quantum Technol.* **6,** 2300145 (2023) (cit. on pp. 21, 87).

153. Iwamura, M. *et al.* Nonlinear photoluminescence spectroscopy of carbon nanotubes with localized exciton states. *ACS Nano* **8,** 11254–11260 (2014) (cit. on pp. 21, 69).

154. Kwon, H. *et al.* Molecularly tunable fluorescent quantum defects. *J. Am. Chem. Soc.* **138,** 6878–6885 (2016) (cit. on pp. 22, 25, 26, 62, 82).

155. Maeda, Y. *et al.* Influence of local strain caused by cycloaddition on the band gap control of functionalized single-walled carbon nanotubes. *RSC Adv.* **9,** 13998–14003 (2019) (cit. on p. 22).

156. Hayashi, K. *et al.* Azide modification forming luminescent sp^2 defects on single-walled carbon nanotubes for near-infrared defect photoluminescence. *Chem. Commun.* **58,** 11422–11425 (2022) (cit. on pp. 22, 26).

157. He, X. *et al.* Low-temperature single carbon nanotube spectroscopy of sp^3 quantum defects. *ACS Nano* **11,** 10785–10796 (2017) (cit. on p. 22).

158. Saha, A. *et al.* Narrow-band single-photon emission through selective aryl functionalization of zigzag carbon nanotubes. *Nat. Chem.* **10,** 1089–1095 (2018) (cit. on pp. 23, 24, 27, 28, 62, 66, 76).

159. Wang, P. *et al.* Quantum defects: What pairs with the aryl group when bonding to the sp^2 carbon lattice of single-wall carbon nanotubes? *J. Am. Chem. Soc.* **144,** 13234–13241 (2022) (cit. on pp. 23, 27, 62, 80, 81, 146).

160. Zheng, Y. *et al.* Photochemical spin-state control of binding configuration for tailoring organic color center emission in carbon nanotubes. *Nat. Commun.* **13,** 4439 (2022) (cit. on pp. 23, 28, 62, 80, 84).

161. Gifford, B. J. *et al.* Mod(n-m,3) dependence of defect-state emission bands in aryl-functionalized carbon nanotubes. *Nano Lett.* **19,** 8503–8509 (2019) (cit. on p. 23).

162. Hirsch, A. Functionalization of single-walled carbon nanotubes. *Angew. Chem. Int. Ed.* **41,** 1853–1859 (2002) (cit. on p. 24).

163. Banerjee, S., Hemraj-Benny, T. & Wong, S. S. Covalent surface chemistry of single-walled carbon nanotubes. *Adv. Mater.* **17,** 17–29 (2005) (cit. on p. 24).

164. Doyle, C. D., Rocha, J.-D. R., Weisman, R. B. & Tour, J. M. Structure-dependent reactivity of semiconducting single-walled carbon nanotubes with benzenediazonium salts. *J. Am. Chem. Soc.* **130,** 6795–6800 (2008) (cit. on p. 24).

165. Niyogi, S. *et al.* Chemistry of single-walled carbon nanotubes. *Acc. Chem. Res.* **35,** 1105–1113 (2002) (cit. on pp. 24, 80).

166. Dou, Q., Xu, B., Wu, X., Mo, J. & Wang, Y. Tunable photo-patterning of organic color-centers. *Mater. Des.* **212,** 110252 (2021) (cit. on p. 24).

167. Huang, Z. *et al.* Photolithographic patterning of organic color-centers. *Adv. Mater.* **32,** 1906517 (2020) (cit. on p. 24).

168. Usrey, M. L., Lippmann, E. S. & Strano, M. S. Evidence for a two-step mechanism in electronically selective single-walled carbon nanotube reactions. *J. Am. Chem. Soc.* **127,** 16129–16135 (2005) (cit. on p. 24).

169. Schmidt, G., Gallon, S., Esnouf, S., Bourgoin, J.-P. & Chenevier, P. Mechanism of the coupling of diazonium to single-walled carbon nanotubes and its consequences. *Chem. Eur. J.* **15,** 2101–2110 (2009) (cit. on p. 24).

170. Gomberg, M. & Bachmann, W. E. The synthesis of biaryl compounds by means of the diazo reaction. *J. Am. Chem. Soc.* **46,** 2339–2343 (1924) (cit. on p. 24).

171. Ma, C. *et al.* Stochastic formation of quantum defects in carbon nanotubes. *ACS Nano* **17,** 15989–15998 (2023) (cit. on p. 24).

172. Powell, L. R., Piao, Y. & Wang, Y. Optical excitation of carbon nanotubes drives localized diazonium reactions. *J. Phys. Chem. Lett.* **7,** 3690–3694 (2016) (cit. on p. 24).

173. Powell, L. R., Kim, M. & Wang, Y. Chirality-selective functionalization of semiconducting carbon nanotubes with a reactivity-switchable molecule. *J. Am. Chem. Soc.* **139,** 12533–12540 (2017) (cit. on p. 24).

174. Luo, H.-B. *et al.* One-pot, large-scale synthesis of organic color center-tailored semiconducting carbon nanotubes. *ACS Nano* **13,** 8417–8424 (2019) (cit. on pp. 24, 25, 90).

175. Bensghaïer, A., Mousli, F., Lamouri, A., Postnikov, P. S. & Chehimi, M. M. The molecular and macromolecular level of carbon nanotube modification *via* diazonium chemistry: Emphasis on the 2010s years. *Chem. Afr.* **3,** 535–569 (2020) (cit. on p. 24).

176. Wu, X., Kim, M., Kwon, H. & Wang, Y. Photochemical creation of fluorescent quantum defects in semiconducting carbon nanotube hosts. *Angew. Chem. Int. Ed.* **57,** 648–653 (2018) (cit. on pp. 25, 26, 62, 81, 82).

177. Przypis, L. *et al.* Enhancing near-infrared photoluminescence from single-walled carbon nanotubes by defect-engineering using benzoyl peroxide. *Sci. Rep.* **10,** 19877 (2020) (cit. on pp. 25, 26).

178. Maeda, Y., Takehana, Y., Yamada, M., Suzuki, M. & Murakami, T. Control of the photoluminescence properties of single-walled carbon nanotubes by alkylation and subsequent thermal treatment. *Chem. Commun.* **51,** 13462–13465 (2015) (cit. on pp. 25, 26).

179. Zhang, Y. *et al.* Propagative sidewall alkylcarboxylation that induces red-shifted near-IR photoluminescence in single-walled carbon nanotubes. *J. Phys. Chem. Lett.* **4,** 826–830 (2013) (cit. on pp. 25, 62).

180. Liang, F. *et al.* A convenient route to functionalized carbon nanotubes. *Nano Lett.* **4,** 1257–1260 (2004) (cit. on p. 25).

181. Deng, S. *et al.* Confined propagation of covalent chemical reactions on single-walled carbon nanotubes. *Nat. Commun.* **2,** 382 (2011) (cit. on p. 25).

182. Maeda, Y., Zhao, P. & Ehara, M. Recent progress in controlling the photoluminescence properties of single-walled carbon nanotubes by oxidation and alkylation. *Chem. Commun.* **59,** 14497–14508 (2023) (cit. on p. 25).

183. Nagai, Y., Nakamura, K., Yudasaka, M., Shiraki, T. & Fujigaya, T. Radical polymer grafting on the surface of single-walled carbon nanotubes enhances photoluminescence in the near-infrared region: Implications for bioimaging and biosensing. *ACS Appl. Nano Mater.* **3,** 8840–8847 (2020) (cit. on pp. 26, 82).

184. Zheng, Y., Bachilo, S. M. & Weisman, R. B. Controlled patterning of carbon nanotube energy levels by covalent DNA functionalization. *ACS Nano* **13,** 8222–8228 (2019) (cit. on p. 26).

185. Artyukhov, V. I., Penev, E. S. & Yakobson, B. I. Why nanotubes grow chiral. *Nat. Commun.* **5,** 4892 (2014) (cit. on pp. 27, 62).

186. Shiraki, T., Shiraishi, T., Juhász, G. & Nakashima, N. Emergence of new red-shifted carbon nanotube photoluminescence based on proximal doped-site design. *Sci. Rep.* **6,** 28393 (2016) (cit. on pp. 27, 62, 90).

187. Yu, B., Fujigaya, T. & Shiraki, T. Wavelength modulation of defect photoluminescence from locally functionalized single-walled carbon nanotubes using heterocycle-substituted aryldiazonium salts. *Bull. Chem. Soc. Jpn.* **96,** 127–132 (2023) (cit. on pp. 27, 36, 90, 130).

188. Zheng, Y., Bachilo, S. M. & Weisman, R. B. Photoexcited aromatic reactants give multicolor carbon nanotube fluorescence from quantum defects. *ACS Nano* **14,** 715–723 (2020) (cit. on pp. 28, 84).

189. Lin, C.-W. *et al.* Creating fluorescent quantum defects in carbon nanotubes using hypochlorite and light. *Nat. Commun.* **10,** 2874 (2019) (cit. on pp. 29, 30, 47, 90, 95, 100–102, 106, 147, 148, 158).

190. Ma, X., Baldwin, J. K. S., Hartmann, N. F., Doorn, S. K. & Htoon, H. Solid-state approach for fabrication of photostable, oxygen-doped carbon nanotubes. *Adv. Funct. Mater.* **25,** 6157–6164 (2015) (cit. on p. 29).

191. Chiu, C. F., Saidi, W. A., Kagan, V. E. & Star, A. Defect-induced near-infrared photoluminescence of single-walled carbon nanotubes treated with polyunsaturated fatty acids. *J. Am. Chem. Soc.* **139,** 4859–4865 (2017) (cit. on pp. 29, 90).

192. Ma, X. *et al.* Electronic structure and chemical nature of oxygen dopant states in carbon nanotubes. *ACS Nano* **8,** 10782–10789 (2014) (cit. on pp. 30, 100, 101, 105, 106).

193. Yim, W.-L. & Johnson, J. K. Ozone oxidation of single walled carbon nanotubes from density functional theory. *J. Phys. Chem. C* **113,** 17636–17642 (2009) (cit. on pp. 30, 100, 101).

194. Iizumi, Y. *et al.* Oxygen-doped carbon nanotubes for near-infrared fluorescent labels and imaging probes. *Sci. Rep.* **8,** 6272 (2018) (cit. on pp. 30, 90, 145).

195. Wieland, S., El Yumin, A. A., Settele, S. & Zaumseil, J. Photo-activated, solid-state introduction of luminescent oxygen defects into semiconducting single-walled carbon nanotubes. *J. Phys. Chem. C* **128,** 2012–2021 (2024) (cit. on p. 30).

196. Miyauchi, Y. *et al.* Brightening of excitons in carbon nanotubes on dimensionality modification. *Nat. Photonics* **7,** 715–719 (2013) (cit. on pp. 30, 90).

197. Yang, M. *et al.* Rapid room temperature degradation of carbon nanotubes by sodium hypochlorite and UV-light irradiation. *Carbon* **208,** 238–246 (2023) (cit. on pp. 30, 104).

198. Li, Y. *et al.* Fluorescent ultrashort nanotubes from defect-induced chemical cutting. *Chem. Mater.* **31,** 4536–4544 (2019) (cit. on pp. 30, 104).

199. Eremin, T., Eremina, V., Svirko, Y. & Obraztsov, P. Over two-fold photoluminescence enhancement from single-walled carbon nanotubes induced by oxygen doping. *Nanomaterials* **13,** 2079–4991 (2023) (cit. on pp. 30, 90, 95).

200. Takeuchi, T., Iizumi, Y., Yudasaka, M., Kizaka-Kondoh, S. & Okazaki, T. Characterization and biodistribution analysis of oxygen-doped single-walled carbon nanotubes used as *in vivo* fluorescence imaging probes. *Bioconjugate Chem.* **30,** 1323–1330 (2019) (cit. on pp. 30, 90, 151).

201. Clement, M., Daniel, G. & Trelles, M. Optimising the design of a broad-band light source for the treatment of skin. *J. Cosmet. Laser Ther.* **7,** 177–189 (2005) (cit. on p. 30).

202. Cao, J. *et al.* Recent progress in NIR-II contrast agent for biological imaging. *Front. Bioeng. Biotechnol.* **7** (2020) (cit. on p. 30).

203. Wang, F. *et al.* Light-sheet microscopy in the near-infrared II window. *Nat. Methods* **16,** 545–552 (2019) (cit. on p. 30).

204. Hong, G., Antaris, A. L. & Dai, H. Near-infrared fluorophores for biomedical imaging. *Nat. Biomed. Eng.* **1,** 0010 (2017) (cit. on pp. 30, 31, 89).

205. Jacques, S. L. Optical properties of biological tissues: A review. *Phys. Med. Biol.* **58,** R37 (2013) (cit. on p. 30).

206. Aubin, J. E. Autofluorescence of viable cultured mammalian cells. *J. Histochem. Cytochem.* **27,** 36–43 (1979) (cit. on p. 30).

207. He, S., Song, J., Qu, J. & Cheng, Z. Crucial breakthrough of second near-infrared biological window fluorophores: Design and synthesis toward multimodal imaging and theranostics. *Chem. Soc. Rev.* **47,** 4258–4278 (2018) (cit. on p. 31).

208. Welsher, K. *et al.* A route to brightly fluorescent carbon nanotubes for near-infrared imaging in mice. *Nat. Nanotechnol.* **4,** 773–780 (2009) (cit. on pp. 31, 32, 48, 110, 135).

209. Lu, L. *et al.* NIR-II bioluminescence for *in vivo* high contrast imaging and *in situ* ATP-mediated metastases tracing. *Nat. Commun.* **11,** 4192 (2020) (cit. on p. 31).

210. Saxena, V., Sadoqi, M. & Shao, J. Degradation kinetics of indocyanine green in aqueous solution. *J. Pharm. Sci.* **92,** 2090–2097 (2003) (cit. on p. 31).

211. Heller, D. A., Baik, S., Eurell, T. E. & Strano, M. S. Single-walled carbon nanotube spectroscopy in live cells: Towards long-term labels and optical sensors. *Adv. Mater.* **17,** 2793–2799 (2005) (cit. on p. 31).

212. Boghossian, A. A. *et al.* Near-infrared fluorescent sensors based on single-walled carbon nanotubes for life sciences applications. *ChemSusChem* **4,** 848–863 (2011) (cit. on pp. 31, 32).

213. Nadort, A., Zhao, J. & Goldys, E. M. Lanthanide upconversion luminescence at the nanoscale: Fundamentals and optical properties. *Nanoscale* **8,** 13099–13130 (2016) (cit. on p. 31).

214. Lei, X. *et al.* Intense near-infrared-II luminescence from $NaCeF_4$:Er/Yb nanoprobes for *in vitro* bioassay and *in vivo* bioimaging. *Chem. Sci.* **9,** 4682–4688 (2018) (cit. on p. 31).

215. Kim, H. N., Ren, W. X., Kim, J. S. & Yoon, J. Fluorescent and colorimetric sensors for detection of lead, cadmium, and mercury ions. *Chem. Soc. Rev.* **41,** 3210–3244 (2012) (cit. on p. 31).

216. Gidwani, B. *et al.* Quantum dots: Prospectives, toxicity, advances and applications. *J. Drug Deliv. Sci. Technol.* **61,** 102308 (2021) (cit. on p. 31).

217. Jackson, C. T., Jeong, S., Dorlhiac, G. F. & Landry, M. P. Advances in engineering near-infrared luminescent materials. *iScience* **24,** 102156 (2021) (cit. on p. 31).

218. Lei, Z. & Zhang, F. Molecular engineering of NIR-II fluorophores for improved biomedical detection. *Angew. Chem. Int. Ed.* **60,** 16294–16308 (2021) (cit. on p. 31).

219. Naczynski, D. J. *et al.* Rare-earth-doped biological composites as *in vivo* shortwave infrared reporters. *Nat. Commun.* **4,** 2199 (2013) (cit. on p. 31).

220. Zhang, M. *et al.* A new class of blue-LED-excitable NIR-II luminescent nanoprobes based on lanthanide-doped CaS nanoparticles. *Angew. Chem. Int. Ed.* **58,** 9556–9560 (2019) (cit. on p. 31).

221. Fan, Y. *et al.* Lifetime-engineered NIR-II nanoparticles unlock multiplexed *in vivo* imaging. *Nat. Nanotechnol.* **13,** 941–946 (2018) (cit. on p. 31).

222. Bruns, O. T. *et al.* Next-generation *in vivo* optical imaging with short-wave infrared quantum dots. *Nat. Biomed. Eng.* **1,** 0056 (2017) (cit. on pp. 31, 113).

223. Dong, B. *et al.* Facile synthesis of highly photoluminescent Ag_2Se quantum dots as a new fluorescent probe in the second near-infrared window for *in vivo* imaging. *Chem. Mater.* **25,** 2503–2509 (2013) (cit. on p. 31).

224. Zhang, Y. *et al.* Ag_2S quantum dot: A bright and biocompatible fluorescent nanoprobe in the second near-infrared window. *ACS Nano* **6,** 3695–3702 (2012) (cit. on p. 31).

225. Zhang, Y., Liu, Y., Li, C., Chen, X. & Wang, Q. Controlled synthesis of Ag_2S quantum dots and experimental determination of the exciton bohr radius. *J. Phys. Chem. C* **118,** 4918–4923 (2014) (cit. on p. 31).

226. Chen, Y. *et al.* Shortwave infrared *in vivo* imaging with gold nanoclusters. *Nano Lett.* **17,** 6330–6334 (2017) (cit. on p. 31).

227. Pramanik, G. *et al.* Gold nanoclusters with bright near-infrared photoluminescence. *Nanoscale* **10,** 3792–3798 (2018) (cit. on p. 31).

228. Antaris, A. L. *et al.* A small-molecule dye for NIR-II imaging. *Nat. Mater.* **15,** 235–242 (2016) (cit. on p. 31).

229. Yang, Q. *et al.* Donor engineering for NIR-II molecular fluorophores with enhanced fluorescent performance. *J. Am. Chem. Soc.* **140,** 1715–1724 (2018) (cit. on p. 31).

230. Bai, L. *et al.* Novel aza-BODIPY based small molecular NIR-II fluorophores for *in vivo* imaging. *Chem. Commun.* **55,** 10920–10923 (2019) (cit. on p. 31).

231. Jena, P. V. *et al.* A carbon nanotube optical reporter maps endolysosomal lipid flux. *ACS Nano* **11,** 10689–10703 (2017) (cit. on p. 32).

232. Galassi, T. V. *et al.* Long-term *in vivo* biocompatibility of single-walled carbon nanotubes. *PLOS ONE* **15,** e0226791 (2020) (cit. on p. 32).

233. Kim, M. *et al.* Human and environmental safety of carbon nanotubes across their life cycle. *Nat. Rev. Mater.* **9,** 63–81 (2024) (cit. on p. 32).

234. Harvey, J. D. *et al.* A carbon nanotube reporter of microRNA hybridization events *in vivo*. *Nat. Biomed. Eng.* **1,** 0041 (2017) (cit. on pp. 32, 33).

235. Godin, A. G. *et al.* Single-nanotube tracking reveals the nanoscale organization of the extracellular space in the live brain. *Nat. Nanotechnol.* **12,** 238–243 (2017) (cit. on pp. 32, 148).

236. Paviolo, C. *et al.* Nanoscale exploration of the extracellular space in the live brain by combining single carbon nanotube tracking and super-resolution imaging analysis. *Methods* **174,** 91–99 (2020) (cit. on p. 32).

237. Howes, P. D., Chandrawati, R. & Stevens, M. M. Colloidal nanoparticles as advanced biological sensors. *Science* **346,** 1247390 (2014) (cit. on p. 32).

238. Kruss, S. *et al.* Carbon nanotubes as optical biomedical sensors. *Adv. Drug Deliv. Rev.* **65,** 1933–1950 (2013) (cit. on p. 32).

239. Gillen, A. J. & Boghossian, A. A. Non-covalent methods of engineering optical sensors based on single-walled carbon nanotubes. *Front. Chem.* **7** (2019) (cit. on p. 32).

240. Pan, J., Li, F. & Choi, J. H. Single-walled carbon nanotubes as optical probes for bio-sensing and imaging. *J. Mater. Chem. B* **5,** 6511–6522 (2017) (cit. on pp. 32, 34).

241. Liu, Z., Yang, K. & Lee, S.-T. Single-walled carbon nanotubes in biomedical imaging. *J. Mater. Chem.* **21,** 586–598 (2011) (cit. on p. 32).

242. Zhang, J. *et al.* Molecular recognition using corona phase complexes made of synthetic polymers adsorbed on carbon nanotubes. *Nat. Nanotechnol.* **8,** 959–968 (2013) (cit. on p. 32).

243. Bisker, G. *et al.* Protein-targeted corona phase molecular recognition. *Nat. Commun.* **7,** 10241 (2016) (cit. on pp. 32, 136, 149, 151).

244. Zheng, M. *et al.* DNA-assisted dispersion and separation of carbon nanotubes. *Nat. Mater.* **2,** 338–342 (2003) (cit. on p. 33).

245. Yang, S. J., Del Bonis-O'Donnell, J. T., Beyene, A. G. & Landry, M. P. Near-infrared catecholamine nanosensors for high spatiotemporal dopamine imaging. *Nat. Protoc.* **16,** 3026–3048 (2021) (cit. on pp. 34, 110).

246. Kruss, S. *et al.* Neurotransmitter detection using corona phase molecular recognition on fluorescent single-walled carbon nanotube sensors. *J. Am. Chem. Soc.* **136,** 713–724 (2014) (cit. on pp. 34, 110, 151).

247. Kruss, S. *et al.* High-resolution imaging of cellular dopamine efflux using a fluorescent nanosensor array. *Proc. Natl. Acad. Sci. USA* **114,** 1789–1794 (2017) (cit. on p. 34).

248. Raja, A. *et al.* Dielectric disorder in two-dimensional materials. *Nat. Nanotechnol.* **14,** 832–837 (2019) (cit. on p. 34).

249. Siitonen, A. J., Tsyboulski, D. A., Bachilo, S. M. & Weisman, R. B. Surfactant-dependent exciton mobility in single-walled carbon nanotubes studied by single-molecule reactions. *Nano Lett.* **10,** 1595–1599 (2010) (cit. on p. 34).

250. Wang, H. & Boghossian, A. A. Covalent conjugation of proteins onto fluorescent single-walled carbon nanotubes for biological and medical applications. *Mater. Adv.* **4,** 823–834 (2023) (cit. on p. 35).

251. Kwon, H. *et al.* Optical probing of local pH and temperature in complex fluids with covalently functionalized, semiconducting carbon nanotubes. *J. Phys. Chem. C* **119,** 3733–3739 (2015) (cit. on pp. 35, 36, 116).

252. Onitsuka, H., Fujigaya, T., Nakashima, N. & Shiraki, T. Control of the near infrared photoluminescence of locally functionalized single-walled carbon nanotubes *via* doping by azacrown-ether modification. *Chem. Eur. J.* **24,** 9393–9398 (2018) (cit. on pp. 35, 36).

253. Shiraki, T., Onitsuka, H., Shiraishi, T. & Nakashima, N. Near infrared photoluminescence modulation of single-walled carbon nanotubes based on a molecular recognition approach. *Chem. Commun.* **52,** 12972–12975 (2016) (cit. on pp. 35, 36, 116).

254. Kim, M. *et al.* Nanosensor-based monitoring of autophagy-associated lysosomal acidification *in vivo*. *Nat. Chem. Biol.* **19,** 1448–1457 (2023) (cit. on pp. 36, 116).

255. Ioannidis, M., Gentleman, A. S., Ho, L., Lincoln, S. F. & Sumby, C. J. Complexation and structural studies of a sulfonamide aza-15-crown-5 derivative. *Inorg. Chem. Commun.* **13,** 593–598 (2010) (cit. on p. 36).

256. Niidome, Y. *et al.* Near-infrared photoluminescent detection of serum albumin using single-walled carbon nanotubes locally functionalized with a long-chain fatty acid. *Carbon* **216,** 118533 (2024) (cit. on p. 36).

257. Li, H., Gordeev, G., Garrity, O., Reich, S. & Flavel, B. S. Separation of small-diameter single-walled carbon nanotubes in one to three steps with aqueous two-phase extraction. *ACS Nano* **13,** 2567–2578 (2019) (cit. on pp. 40, 91, 107).

258. Pfohl, M. *et al.* Fitting single-walled carbon nanotube optical spectra. *ACS Omega* **2,** 1163–1171 (2017) (cit. on pp. 42, 56).

259. Streit, J. K., Bachilo, S. M., Ghosh, S., Lin, C.-W. & Weisman, R. B. Directly measured optical absorption cross sections for structure-selected single-walled carbon nanotubes. *Nano Lett.* **14,** 1530–1536 (2014) (cit. on p. 42).

260. Sanchez, S. R., Bachilo, S. M., Kadria-Vili, Y., Lin, C.-W. & Weisman, R. B. (n,m)-specific absorption cross sections of single-walled carbon nanotubes measured by variance spectroscopy. *Nano Lett.* **16,** 6903–6909 (2016) (cit. on p. 42).

261. Zhang, K., Xu, X.-H. & Qing, F.-L. Copper-promoted Ritter-type trifluoroethoxylation of (hetero)arenediazonium tetrafluoroborates: A method for the preparation of trifluoroethyl Imidates. *Eur. J. Org. Chem.* **2016,** 5088–5090 (2016) (cit. on p. 45).

262. Ackermann, J. *et al.* High sensitivity near-infrared imaging of fluorescent nanosensors. *Small* **19,** 2206856 (2023) (cit. on pp. 48, 110).

263. De Mello, J. C., Wittmann, H. F. & Friend, R. H. An improved experimental determination of external photoluminescence quantum efficiency. *Adv. Mater.* **9,** 230–232 (1997) (cit. on p. 52).

264. Wei, X. *et al.* Photoluminescence quantum yield of single-wall carbon nanotubes corrected for the photon reabsorption effect. *Nano Lett.* **20,** 410–417 (2020) (cit. on p. 52).

265. Naumov, A. V., Ghosh, S., Tsyboulski, D. A., Bachilo, S. M. & Weisman, R. B. Analyzing absorption backgrounds in single-walled carbon nanotube spectra. *ACS Nano* **5,** 1639–1648 (2011) (cit. on p. 56).

266. Nair, N., Usrey, M. L., Kim, W.-J., Braatz, R. D. & Strano, M. S. Estimation of the (n,m) concentration distribution of single-walled carbon nanotubes from photoabsorption spectra. *Anal. Chem.* **78,** 7689–7696 (2006) (cit. on p. 56).

267. Dresselhaus, M. S., Jorio, A., Hofmann, M., Dresselhaus, G. & Saito, R. Perspectives on carbon nanotubes and graphene Raman spectroscopy. *Nano Lett.* **10,** 751–758 (2010) (cit. on p. 57).

268. Jorio, A. *et al.* Characterizing carbon nanotube samples with resonance Raman scattering. *New J. Phys.* **5,** 139 (2003) (cit. on p. 57).

269. Dresselhaus, M. S., Jorio, A., Souza Filho, A. G. & Saito, R. Defect characterization in graphene and carbon nanotubes using Raman spectroscopy. *Philos. Trans. R. Soc. A* **368,** 5355–5377 (2010) (cit. on pp. 57, 58).

270. Grimm, S. *et al.* Doping-dependent G-mode shifts of small diameter semiconducting single-walled carbon nanotubes. *Carbon* **118,** 261–267 (2017) (cit. on p. 57).

271. Jorio, A. *et al.* Polarized Raman study of single-wall semiconducting carbon nanotubes. *Phys. Rev. Lett.* **85,** 2617–2620 (2000) (cit. on p. 57).

272. Magg, M., Kadria-Vili, Y., Oulevey, P., Weisman, R. B. & Bürgi, T. Resonance Raman optical activity spectra of single-walled carbon nanotube enantiomers. *J. Phys. Chem. Lett.* **7,** 221–225 (2016) (cit. on p. 57).

273. Zaumseil, J., Jakubka, F., Wang, M. & Gannott, F. *In situ* Raman mapping of charge carrier distribution in electrolyte-gated carbon nanotube network field-effect transistors. *J. Phys. Chem. C* **117,** 26361–26370 (2013) (cit. on p. 57).

274. Sebastian, F. L. *et al.* Unified quantification of quantum defects in small-diameter single-walled carbon nanotubes by Raman spectroscopy. *ACS Nano* **17,** 21771–21781 (2023) (cit. on pp. 58, 80, 104, 154).

275. Brozena, A. H., Leeds, J. D., Zhang, Y., Fourkas, J. T. & Wang, Y. Controlled defects in semiconducting carbon nanotubes promote efficient generation and luminescence of trions. *ACS Nano* **8,** 4239–4247 (2014) (cit. on p. 62).

276. Wei, L., Flavel, B. S., Li, W., Krupke, R. & Chen, Y. Exploring the upper limit of single-walled carbon nanotube purity by multiple-cycle aqueous two-phase separation. *Nanoscale* **9,** 11640–11646 (2017) (cit. on p. 63).

277. Hennrich, F. *et al.* Length-sorted, large-diameter, polyfluorene-wrapped semiconducting single-walled carbon nanotubes for high-density, short-channel transistors. *ACS Nano* **10,** 1888–1895 (2016) (cit. on p. 63).

278. Zorn, N. F., Berger, F. J. & Zaumseil, J. Charge transport in and electroluminescence from sp^3-functionalized carbon nanotube networks. *ACS Nano* **15,** 10451–10463 (2021) (cit. on pp. 63, 145).

279. Settele, S. Photoenhanced functionalization of polymer-wrapped carbon nanotubes by aryl halides, Master thesis, Heidelberg University (2020) (cit. on pp. 63, 64).

280. Budén, M. E., Bardagí, J. I., Puiatti, M. & Rossi, R. A. Initiation in photoredox C–H functionalization reactions. Is dimsyl anion a key ingredient? *J. Org. Chem.* **82,** 8325–8333 (2017) (cit. on pp. 63, 82).

281. Chen, J.-S. *et al.* Room temperature lasing from semiconducting single-walled carbon nanotubes. *ACS Nano* **16,** 16776–16783 (2022) (cit. on p. 69).

282. Wang, F., Dukovic, G., Knoesel, E., Brus, L. E. & Heinz, T. F. Observation of rapid Auger recombination in optically excited semiconducting carbon nanotubes. *Phys. Rev. B* **70,** 241403 (2004) (cit. on p. 69).

283. Ishii, A., Yoshida, M. & Kato, Y. K. Exciton diffusion, end quenching, and exciton-exciton annihilation in individual air-suspended carbon nanotubes. *Phys. Rev. B* **91,** 125427 (2015) (cit. on p. 69).

284. Kim, Y. *et al.* Photoluminescence intensity fluctuations and temperature-dependent decay dynamics of individual carbon nanotube sp^3 defects. *J. Phys. Chem. Lett.* **10,** 1423–1430 (2019) (cit. on pp. 71–73).

285. Shiraishi, T. *et al.* Determination of precise redox properties of oxygen-doped single-walled carbon nanotubes based on *in situ* photoluminescence electrochemistry. *J. Phys. Chem. C* **120,** 15632–15639 (2016) (cit. on p. 73).

286. Sarpkaya, I. *et al.* Strong acoustic phonon localization in copolymer-wrapped carbon nanotubes. *ACS Nano* **9,** 6383–6393 (2015) (cit. on p. 76).

287. Raynaud, C. *et al.* Superlocalization of excitons in carbon nanotubes at cryogenic temperature. *Nano Lett.* **19,** 7210–7216 (2019) (cit. on p. 76).

288. Hofmann, M. S., Noé, J., Kneer, A., Crochet, J. J. & Högele, A. Ubiquity of exciton localization in cryogenic carbon nanotubes. *Nano Lett.* **16,** 2958–2962 (2016) (cit. on p. 76).

289. He, X. *et al.* Carbon nanotubes as emerging quantum-light sources. *Nat. Mater.* **17,** 663–670 (2018) (cit. on pp. 78, 146).

290. Luo, Y. *et al.* Carbon nanotube color centers in plasmonic nanocavities: A path to photon indistinguishability at telecom bands. *Nano Lett.* **19,** 9037–9044 (2019) (cit. on pp. 79, 87, 145, 146, 151).

291. Borel, A. *et al.* Telecom band single-photon source using a grafted carbon nanotube coupled to a fiber Fabry-Perot cavity in the Purcell regime. *ACS Photonics* **10,** 2839–2845 (2023) (cit. on pp. 79, 87).

292. Settele, S. *et al.* Synthetic control over the binding configuration of luminescent sp^3-defects in single-walled carbon nanotubes. *Nat. Commun.* **12,** 2119 (2021) (cit. on p. 80).

293. O'Hagan, D. Understanding organofluorine chemistry. An introduction to the C–F bond. *Chem. Soc. Rev.* **37,** 308–319 (2008) (cit. on p. 81).

294. Deimel, P. S., Feulner, P., Barth, J. V. & Allegretti, F. Spatial decoupling of macrocyclic metal–organic complexes from a metal support: A 4-fluorothiophenol self-assembled monolayer as a thermally removable spacer. *Phys. Chem. Chem. Phys.* **21,** 10992–11003 (2019) (cit. on p. 82).

295. Lu, H., Zeysing, D., Kind, M., Terfort, A. & Zharnikov, M. Structure of self-assembled monolayers of partially fluorinated alkanethiols with a fluorocarbon part of variable length on gold substrate. *J. Phys. Chem. C* **117,** 18967–18979 (2013) (cit. on p. 82).

296. Barham, J. P. *et al.* KO^{t}Bu: A privileged reagent for electron transfer reactions? *J. Am. Chem. Soc.* **138,** 7402–7410 (2016) (cit. on p. 82).

297. Olmstead, W. N., Margolin, Z. & Bordwell, F. G. Acidities of water and simple alcohols in dimethyl sulfoxide solution. *J. Org. Chem.* **45,** 3295–3299 (1980) (cit. on p. 82).

298. Raczyńska, E. D., Stępniewski, T. M. & Kolczyńska, K. Consequence of one-electron oxidation and one-electron reduction for aniline. *J. Mol. Model.* **17,** 3229–3239 (2011) (cit. on p. 84).

299. Bordwell, F. G. & Algrim, D. J. Acidities of anilines in dimethyl sulfoxide solution. *J. Am. Chem. Soc.* **110,** 2964–2968 (1988) (cit. on p. 85).

300. Alsharif, M. A., Khan, D., Mukhtar, S., Alahmdi, M. I. & Ahmed, N. KO^{t}Bu-mediated aza-Michael addition of aromatic amines or *N*-phenylurea to 3-nitro-2-phenyl-2*H*-chromenes and sequential aerobic dehydrogenation. *Eur. J. Org. Chem.* **2018,** 3454–3463 (2018) (cit. on p. 85).

301. Holzinger, M. *et al.* Sidewall functionalization of carbon nanotubes. *Angew. Chem. Int. Ed.* **40,** 4002–4005 (2001) (cit. on p. 85).

302. Li, F. *et al.* KO^{t}Bu-mediated, three-component coupling reaction of indoles,[60]fullerene, and haloalkanes: One-pot, transition-metal-free synthesis of various 1,4-(3-indole)(organo)[60]fullerenes. *Org. Lett.* **19,** 1192–1195 (2017) (cit. on p. 86).

303. Li, F. *et al.* KO^{t}Bu-promoted C4 selective coupling reaction of phenols and [60] fullerene: One-pot synthesis of 4-[60] fullerephenols under transition-metal-free conditions. *J. Org. Chem.* **83,** 5431–5437 (2018) (cit. on p. 86).

304. Wang, J.-F. *et al.* Experimental optical properties of single nitrogen vacancy centers in silicon carbide at room temperature. *ACS Photonics* **7,** 1611–1616 (2020) (cit. on p. 87).

305. Alfieri, A., Anantharaman, S. B., Zhang, H. & Jariwala, D. Nanomaterials for quantum information science and engineering. *Adv. Mater* **35,** 2109621 (2023) (cit. on p. 87).

306. Zorn, N. F., Settele, S., Sebastian, F. L., Lindenthal, S. & Zaumseil, J. Tuning electroluminescence from functionalized SWCNT networks further into the near-infrared. *ACS Appl. Opt. Mater.* **1,** 1706–1714 (2023) (cit. on pp. 87, 146).

307. Berger, F. J. *et al.* Interaction of luminescent defects in carbon nanotubes with covalently attached stable organic radicals. *ACS Nano* **15,** 5147–5157 (2021) (cit. on p. 90).

308. Babuponnusami, A. & Muthukumar, K. A review on Fenton and improvements to the Fenton process for wastewater treatment. *J. Environ. Chem. Eng.* **2,** 557–572 (2014) (cit. on pp. 90, 99).

309. Fenton, H. J. H. Oxidation of tartaric acid in presence of iron. *J. Chem. Soc., Trans.* **65,** 899–910 (1894) (cit. on p. 90).

310. Haber, F. & Weiss, J. Über die Katalyse des Hydroperoxydes. *Naturwissenschaften* **20,** 948–950 (1932) (cit. on p. 90).

311. Fridovich, I. Superoxide dismutases. *Annu. Rev. Biochem.* **44,** 147–159 (1975) (cit. on p. 90).

312. Meyerstein, D. Re-examining Fenton and Fenton-like reactions. *Nat. Rev. Chem.* **5,** 595–597 (2021) (cit. on p. 90).

313. Pham, A. N., Xing, G., Miller, C. J. & Waite, T. D. Fenton-like copper redox chemistry revisited: Hydrogen peroxide and superoxide mediation of copper-catalyzed oxidant production. *J. Catal.* **301,** 54–64 (2013) (cit. on p. 90).

314. Almkhelfe, H., Li, X., Thapa, P., Hohn, K. L. & Amama, P. B. Carbon nanotube-supported catalysts prepared by a modified photo-Fenton process for Fischer–Tropsch synthesis. *J. Catal.* **361,** 278–289 (2018) (cit. on p. 90).

315. Fan, C. *et al.* Efficient photo-assisted Fenton oxidation treatment of multi-walled carbon nanotubes. *Chin. Sci. Bull.* **52,** 2054–2062 (2007) (cit. on p. 90).

316. Grey, A. D. N. J. d. $HO_2\cdot$: The forgotten radical. *DNA Cell Biol.* **21,** 251–257 (2002) (cit. on p. 90).

317. Yin, X. *et al.* Chemical stability of ascorbic acid integrated into commercial products: A review on bioactivity and delivery technology. *Antioxidants* **11,** 153 (2022) (cit. on p. 90).

318. Wulf, V. *et al.* Multicomponent system of single-walled carbon nanotubes functionalized with a melanin-inspired material for optical detection and scavenging of metals. *Adv. Funct. Mater.* **32,** 2209688 (2022) (cit. on pp. 93, 131).

319. Eberson, L. Formation of hydroxyl spin adducts *via* nucleophilic addition to 5,5-dimethyl-1-pyrroline *N*-oxide (DMPO). *Acta Chim. Scand.* **53,** 584–593 (1999) (cit. on p. 98).

320. Park, N.-H. *et al.* High performance carbon nanotubes thin film transistors by selective ferric chloride doping. *J. Inf. Disp.* **24,** 109–118 (2023) (cit. on p. 100).

321. Verma, P., Baldrian, P. & Nerud, F. Decolorization of structurally different synthetic dyes using cobalt(II)/ascorbic acid/hydrogen peroxide system. *Chemosphere* **50,** 975–979 (2003) (cit. on p. 100).

322. Klotz, B., Barnes, I., Golding, B. T. & Becker, K.-H. Atmospheric chemistry of toluene-1,2-oxide/2-methyloxepin. *Phys. Chem. Chem. Phys.* **2,** 227–235 (2000) (cit. on p. 100).

323. Klotz, B., Barnes, I., H. Becker, K. & T. Golding, B. Atmospheric chemistry of benzene oxide/oxepin. *J. Chem. Soc., Faraday Trans.* **93,** 1507–1516 (1997) (cit. on p. 100).

324. Espinoza, V. B. Photochemical tailoring of single-wall carbon nanotubes by photoexcited sodium hypochlorite, Dissertation, Rice University. https://hdl.handle.net/1911/113278 (2022) (cit. on p. 102).

325. Kehrer, J. P., Robertson, J. D. & Smith, C. V. in *Comprehensive Toxicology* (ed McQueen, C. A.) 2nd ed., 277–307 (Elsevier, Oxford, 2010) (cit. on p. 103).

326. Wu, H. *et al.* Monitoring plant health with near-infrared fluorescent H_2O_2 nanosensors. *Nano Lett.* **20,** 2432–2442 (2020) (cit. on p. 103).

327. Zhang, K., Wang, J., Zou, J., Cai, W. & Zhang, Q. Low excitation of Raman D-band in $[2+1]$ cycloaddition functionalized single-walled carbon nanotubes. *Carbon* **138,** 188–196 (2018) (cit. on p. 104).

328. Oh, H., Sim, J. & Ju, S.-Y. Binding affinities and thermodynamics of noncovalent functionalization of carbon nanotubes with surfactants. *Langmuir* **29,** 11154–11162 (2013) (cit. on p. 106).

329. Rharbi, Y. & Winnik, M. A. Salt effects on solute exchange in sodium dodecyl sulfate micelles. *J. Am. Chem. Soc.* **124,** 2082–2083 (2002) (cit. on p. 106).

330. Bakshi, M. *et al.* Mixed-micelle formation by strongly interacting surfactant binary mixtures: Effect of head-group modification. *Colloid Polym. Sci.* **280,** 990–1000 (2002) (cit. on p. 106).

331. Hebling, C. M. *et al.* Sodium cholate aggregation and chiral recognition of the probe molecule (R,S)-1,1′-binaphthyl-2,2′-diylhydrogenphosphate (BNDHP) observed by ^{1}H and ^{31}P NMR spectroscopy. *Langmuir* **24,** 13866–13874 (2008) (cit. on p. 106).

332. Zeng, X. *et al.* Detecting and tuning the interactions between surfactants and carbon nanotubes for their high-efficiency structure separation. *Adv. Mater. Interfaces* **5,** 1700727 (2018) (cit. on p. 106).

333. Shih, C.-J., Lin, S., Strano, M. S. & Blankschtein, D. Understanding the stabilization of single-walled carbon nanotubes and graphene in ionic surfactant aqueous solutions: Large-scale coarse-grained molecular dynamics simulation-assisted DLVO theory. *J. Phys. Chem. C* **119,** 1047–1060 (2015) (cit. on p. 106).

334. Podlesny, B. *et al.* Highly-selective harvesting of (6,4) SWCNTs using the aqueous two-phase extraction method and nonionic surfactants. *Adv. Sci.* **10,** 2207218 (2023) (cit. on p. 107).

335. Paviolo, C. & Cognet, L. Near-infrared nanoscopy with carbon-based nanoparticles for the exploration of the brain extracellular space. *Neurobiol. Dis.* **153,** 105328 (2021) (cit. on p. 109).

336. Liu, L., Yang, C., Zhao, K., Li, J. & Wu, H.-C. Ultrashort single-walled carbon nanotubes in a lipid bilayer as a new nanopore sensor. *Nat. Commun.* **4,** 2989 (2013) (cit. on p. 109).

337. Kolosnjaj-Tabi, J. *et al. In vivo* behavior of large doses of ultrashort and full-length single-walled carbon nanotubes after oral and intraperitoneal administration to swiss mice. *ACS Nano* **4,** 1481–1492 (2010) (cit. on p. 109).

338. Kostarelos, K. The long and short of carbon nanotube toxicity. *Nat. Biotechnol.* **26,** 774–776 (2008) (cit. on p. 109).

339. Mann, F. A., Herrmann, N., Meyer, D. & Kruss, S. Tuning selectivity of fluorescent carbon nanotube-based neurotransmitter sensors. *Sensors* **17,** 1521 (2017) (cit. on p. 110).

340. Gaetke, L. M., Chow-Johnson, H. S. & Chow, C. K. Copper: Toxicological relevance and mechanisms. *Arch. Toxicol.* **88,** 1929–1938 (2014) (cit. on p. 111).

341. Hendler-Neumark, A., Wulf, V. & Bisker, G. *In vivo* imaging of fluorescent single-walled carbon nanotubes within *C. elegans* nematodes in the near-infrared window. *Materials Today Bio* **12,** 100175 (2021) (cit. on p. 111).

342. Barceloux, D. G. & Barceloux, D. Copper. *J. Toxicol. Clin. Toxicol.* **37,** 217–230 (1999) (cit. on p. 111).

343. Chen, S.-Y., Liu, S.-T., Lin, W.-R., Lin, C.-K. & Huang, S.-M. The mechanisms underlying the cytotoxic effects of copper *via* differentiated embryonic chondrocyte gene 1. *Int. J. Mol. Sci.* **20,** 5225 (2019) (cit. on p. 111).

344. Wang, Z. *et al.* CuO nanoparticle interaction with human epithelial cells: Cellular uptake, location, export, and genotoxicity. *Chem. Res. Toxicol.* **25,** 1512–1521 (2012) (cit. on p. 111).

345. Crochet, J., Clemens, M. & Hertel, T. Quantum yield heterogeneities of aqueous single-wall carbon nanotube suspensions. *J. Am. Chem. Soc.* **129,** 8058–8059 (2007) (cit. on p. 112).

346. Chen, Y. *et al.* Shortwave infrared *in vivo* imaging with gold nanoclusters. *Nano Lett.* **17,** 6330–6334 (2017) (cit. on p. 113).

347. Guo, Y. *et al. In vivo* NIR-II fuorescence lifetime imaging of whole-body vascular using high quantum yield lanthanide-doped nanoparticles. *Small* **19,** 2300392 (2023) (cit. on p. 113).

348. Zheng, M. *et al.* DNA-assisted dispersion and separation of carbon nanotubes. *Nat. Mater.* **2,** 338–342 (2003) (cit. on p. 116).

349. Albertorio, F., Hughes, M. E., Golovchenko, J. A. & Branton, D. Base dependent DNA–carbon nanotube interactions: Activation enthalpies and assembly–disassembly control. *Nanotechnology* **20,** 395101 (2009) (cit. on p. 116).

350. Landry, M. P. *et al.* Comparative dynamics and sequence dependence of DNA and RNA binding to single walled carbon nanotubes. *J. Phys. Chem. C* **119,** 10048–10058 (2015) (cit. on p. 116).

351. Roxbury, D., Mittal, J. & Jagota, A. Molecular-basis of single-walled carbon nanotube recognition by single-stranded DNA. *Nano Lett.* **12,** 1464–1469 (2012) (cit. on p. 116).

352. Lambert, B., Gillen, A. J., Schuergers, N., Wu, S.-J. & Boghossian, A. A. Directed evolution of the optoelectronic properties of synthetic nanomaterials. *Chem. Commun.* **55,** 3239–3242 (2019) (cit. on p. 116).

353. Anbu, S., Paul, A., Stasiuk, G. J. & Pombeiro, A. J. L. Recent developments in molecular sensor designs for inorganic pyrophosphate detection and biological imaging. *Coord. Chem. Rev.* **431** (2021) (cit. on pp. 116, 117, 149).

354. Mansurova, S. E. Inorganic pyrophosphate in mitochondrial metabolism. *Biochim. Biophys. Acta - Bioenerg.* **977,** 237–247 (1989) (cit. on pp. 116, 149).

355. Nelson, D. L., Cox, M. M. & Hoskins, A. A. *Lehninger Principles of Biochemistry* 8th ed. (Macmillan International, Higher Education, New York, 2021) (cit. on p. 116).

356. Kim, S. K., Lee, D. H., Hong, J.-I. & Yoon, J. Chemosensors for pyrophosphate. *Acc. Chem. Res.* **42,** 23–31 (2009) (cit. on p. 116).

357. Burke, C. R. & Lupták, A. DNA synthesis from diphosphate substrates by DNA polymerases. *PNAS* **115,** 980–985 (2018) (cit. on p. 116).

358. Xu, S. *et al.* A quantitative method to measure telomerase activity by bioluminescence connected with telomeric repeat amplification protocol. *Anal. Biochem.* **299,** 188–93 (2001) (cit. on p. 116).

359. Russell, R. G. G., Bisaz, S., Donath, A., Morgan, D. B. & Fleisch, H. Inorganic pyrophosphate in plasma in normal persons and in patients with hypophosphatasia, osteogenesis imperfecta, and other disorders of bone. *J. Clin. Invest.* **50,** 961–969 (1971) (cit. on pp. 116, 142, 143).

360. Russell, R. G. G. Excretion of inorganic pyrophosphate in hypophosphatasia. *Lancet* **286,** 461–464 (1965) (cit. on pp. 116, 142, 143).

361. Rachow, J. W., Ryan, L. M., Mccarty, D. J. & Halverson, P. C. Synovial fluid inorganic pyrophosphate concentration and nucleotide pyrophosphohydrolase activity in basic calcium phosphate deposition arthropathy and milwaukee shoulder syndrome. *Arthritis & Rheumatism* **31,** 408–413 (1988) (cit. on pp. 116, 142).

362. Wright, G. D. & Doherty, M. Calcium pyrophosphate crystal deposition is not always 'wear and tear' or aging. *Ann. Rheum. Dis.* **56,** 586–588 (1997) (cit. on p. 116).

363. Rosenthal, A. K. & Ryan, L. M. Calcium pyrophosphate deposition disease. *N. Engl. J. Med.* **374,** 2575–2584 (2016) (cit. on p. 116).

364. Wongkongkatep, J., Ojida, A. & Hamachi, I. Fluorescence sensing of inorganic phosphate and pyrophosphate using small molecular sensors and their applications. *Top. Curr. Chem.* **375,** 30 (2017) (cit. on pp. 116, 117).

365. Zhu, W. *et al.* A novel NIR fluorescent turn-on sensor for the detection of pyrophosphate anion in complete water system. *Chem. Commun.* **48,** 1784–6 (2012) (cit. on p. 117).

366. Chan, T. R., Hilgraf, R., Sharpless, K. B. & Fokin, V. V. Polytriazoles as copper(I)-stabilizing ligands in catalysis. *Org. Lett.* **6,** 2853–2855 (2004) (cit. on p. 118).

367. Niyogi, S. *et al.* Selective aggregation of single-walled carbon nanotubes *via* salt addition. *J. Am. Chem. Soc.* **129,** 1898–1899 (2007) (cit. on p. 121).

368. Koh, B. & Cheng, W. Mechanisms of carbon nanotube aggregation and the reversion of carbon nanotube aggregates in aqueous medium. *Langmuir* **30,** 10899–10909 (2014) (cit. on p. 121).

369. Heller, D. A. *et al.* Optical detection of DNA conformational polymorphism on single-walled carbon nanotubes. *Science* **311,** 508–511 (2006) (cit. on p. 123).

370. Gillen, A. J., Kupis-Rozmysłowicz, J., Gigli, C., Schuergers, N. & Boghossian, A. A. Xeno nucleic acid nanosensors for enhanced stability against ion-induced perturbations. *J. Phys. Chem. Lett.* **9,** 4336–4343 (2018) (cit. on pp. 123, 124).

371. Shiraki, T. *et al.* Solvatochromism of near infrared photoluminescence from doped sites of locally functionalized single-walled carbon nanotubes. *Chem. Commun.* **55,** 3662–3665 (2019) (cit. on p. 127).

372. Zhang, S.-T., Li, P., Kou, X. & Xiao, D. Highly selective and sensitive luminescent turn-on probe for pyrophosphate detection in aqueous solution. *ChemistrySelect* **3,** 10057–10063 (2018) (cit. on p. 128).

373. Brege, J. J., Gallaway, C. & Barron, A. R. Fluorescence quenching of single-walled carbon nanotubes with transition-metal ions. *J. Phys. Chem. C* **113,** 4270–4276 (2009) (cit. on pp. 131, 133).

374. Lakowicz, J. R. *Principles of Fluorescence Spectroscopy* 3rd ed. (Springer, New York, 2006) (cit. on pp. 132, 133).

375. Sistemich, L., Galonska, P., Stegemann, J., Ackermann, J. & Kruss, S. Near-infrared fluorescence lifetime imaging of biomolecules with carbon nanotubes. *Angew. Chem. Int. Ed.* **62,** e202300682 (2023) (cit. on p. 133).

376. Bratsch, S. G. Standard electrode potentials and temperature coefficients in water at 298.15 K. *J. Phys. Chem. Ref. Data* **18,** 1–21 (1989) (cit. on p. 133).

377. Shiraishi, T., Shiraki, T. & Nakashima, N. Substituent effects on the redox states of locally functionalized single-walled carbon nanotubes revealed by *in situ* photoluminescence spectroelectrochemistry. *Nanoscale* **9,** 16900–16907 (2017) (cit. on p. 133).

378. Lewis, F. D. *et al.* Distance-dependent electron transfer in DNA hairpins. *Science* **277,** 673–676 (1997) (cit. on p. 133).

379. Brown, R. B. & Audet, J. Current techniques for single-cell lysis. *J. R. Soc. Interface.* **5,** S131–S138 (2008) (cit. on p. 135).

380. Mash, H. E., Chin, Y.-P., Sigg, L., Hari, R. & Xue, H. Complexation of copper by zwitterionic aminosulfonic (Good) buffers. *Anal. Chem.* **75,** 671–677 (2003) (cit. on p. 136).

381. Polo, E. & Kruss, S. Impact of redox-active molecules on the fluorescence of polymer-wrapped carbon nanotubes. *J. Phys. Chem. C* **120,** 3061–3070 (2016) (cit. on p. 136).

382. Park, M. *et al.* Measuring the accessible surface area within the nanoparticle corona using molecular probe adsorption. *Nano Lett.* **19,** 7712–7724 (2019) (cit. on p. 136).

383. Lust, G. & Seegmiller, J. E. A rapid, enzymatic assay for measurement of inorganic pyrophosphate in biological samples. *Clin. Chim. Acta* **66,** 241–249 (1976) (cit. on p. 138).

384. Lust, G., Faure, G., Netter, P., Gaucher, A. & Seegmiller, J. E. Evidence of a generalized metabolic defect in patients with hereditary chondrocalcinosis. *Arthritis & Rheumatism* **24,** 1517–1521 (1981) (cit. on p. 138).

385. Xu, H., Yang, D., Jiang, D. & Chen, H.-Y. Phosphate assay kit in one cell for electrochemical detection of intracellular phosphate ions at single cells. *Front. Chem.* **7** (2019) (cit. on p. 138).

386. Zhu, H. *et al.* PCR past, present and future. *BioTechniques* **69,** 317–325 (2020) (cit. on p. 139).

387. Caballero, D. *et al.* Intraperitoneal pyrophosphate treatment reduces renal calcifications in *Npt2a* null mice. *PLOS ONE* **12,** e0180098 (2017) (cit. on pp. 142, 143).

388. March, J. G., Simonet, B. M. & Grases, F. Determination of pyrophosphate in renal calculi and urine by means of an enzymatic method. *Clin. Chim. Acta* **314,** 187–194 (2001) (cit. on p. 142).

389. Terkeltaub, R. A. Inorganic pyrophosphate generation and disposition in pathophysiology. *Am. J. Physiol. Cell Physiol.* **281,** C1–C11 (2001) (cit. on p. 142).

390. Johnson, K. *et al.* Mitochondrial oxidative phosphorylation is a downstream regulator of nitric oxide effects on chondrocyte matrix synthesis and mineralization. *Arthritis & Rheumatism* **43,** 1560–1570 (2000) (cit. on p. 142).

391. Su, Y. *et al.* Sensing and imaging of PP_i *in vivo* using lanthanide-based second near-infrared luminescent probes. *J. Mater. Chem. B* **10,** 1055–1062 (2022) (cit. on pp. 143, 149).

392. Bouilly, D. *et al.* Single-molecule reaction chemistry in patterned nanowells. *Nano Lett.* **16,** 4679–4685 (2016) (cit. on p. 151).

393. Li, M.-K. *et al.* Electroluminescence from single-walled carbon nanotubes with quantum defects. *ACS Nano* **16,** 11742–11754 (2022) (cit. on p. 151).

394. Landry, M. P. *et al.* Single-molecule detection of protein efflux from microorganisms using fluorescent single-walled carbon nanotube sensor arrays. *Nat. Nanotechnol.* **12,** 368–377 (2017) (cit. on p. 151).

395. Nißler, R. *et al.* Remote near infrared identification of pathogens with multiplexed nanosensors. *Nat. Commun.* **11,** 5995 (2020) (cit. on p. 151).

396. Pinals, R. L. *et al.* Rapid SARS-CoV-2 spike protein detection by carbon nanotube-based near-infrared nanosensors. *Nano Lett.* **21,** 2272–2280 (2021) (cit. on p. 151).

397. Mann, F. A., Lv, Z., Großhans, J., Opazo, F. & Kruss, S. Nanobody-conjugated nanotubes for targeted near-infrared *in vivo* imaging and sensing. *Angew. Chem. Int. Ed.* **58,** 11469–11473 (2019) (cit. on p. 151).

398. Balcı Leinen, M., Lindenthal, S., Heimfarth, D. & Zaumseil, J. Networks of as-dispersed, polymer-wrapped (6,5) single-walled carbon nanotubes for selective Cu^{2+} and glyphosate sensing. *Nanoscale* **14,** 13542–13550 (2022) (cit. on p. 151).

Abbreviations

0D	Zero-dimensional
1D	One-dimensional
2D	Two-dimensional
A	Adenine
ADP	Adenosine 5′-diphosphat
AFM	Atomic force microscopy
AMP	Adenosine monophosphate
ATP	Adenosine 5′-triphosphate
ATPE	Aqueous two-phase extraction
AuNP	Gold nanoparticles
BHAS	Base-promoted homolytic aromatic substitution
C	Cytosine
CMC	Critical micelle concentration
CoMoCAT	Cobalt-molybdenum catalyst
CVD	Chemical vapor deposition
DFT	Density functional theory
DGU	Density gradient ultracentrifugation
DLCQ	Diffusion-limited contact quenching
DMSO	Dimethyl sulfoxide
DNA	Deoxyribonucleic acid
dNTPs	Deoxynucleotide triphosphates
DOC	Sodium deoxycholate
DOS	Density of states
DzAlkyne	4-Ethynyl benzene diazonium tetrafluoroborate

DzBenzene	Benzene diazonium tetrafluoroborate
DzNO_2	4-Nitrobenzenediazonium tetrafluoroborate
EPR	Electron paramagnetic resonance
EVET	Electronic-to-vibrational energy transfer
F8BT	Poly-[(9,9-di-*n*-octylfluorenyl-2,7-diyl)-*alt*-(benzo[2,1,3]thiadiazol-4,8-diyl)]
FWHM	Full width at half maximum
G	Guanine
HiPCO	High-pressure carbon monoxide
ICP-OES	Inductively coupled plasma optical emission spectroscopy
I*o*NH_2	2-Iodoaniline
IRF	Instrument response function
LaNPs	Lanthanide nanoparticles
LED	Light-emitting diode
LOD	Limit of detection
MD	Molecular dynamics
MOPS	Morpholinopropane sulfonic acid
MPD	Multi-phonon decay
MWCO	Molecular weight cut-off
NaAsc	Sodium-L-ascorbate
NIR	Near-infrared
OD	Optical density
PSB	Phosphate buffered saline
PCR	Polymerase chain reaction
PEG	Polyethylene glycol
PET	Photo-induced electron transfer
PFO	Poly(9,9-dioctylfluorene)
PFO-BPy	Poly[(9,9-dioctylfluorenyl-2,7-diyl)-*alt*-(6,6′-2,2′-bipyridine)]
PL	Photoluminescence
PLE	Photoluminescence excitation-emission
PL-PEG	Phospholipid–polyethylene glycol
PLQY	Photoluminescence quantum yield

PP_i	Inorganic pyrophosphate
PLL	Poly-L-lysine
PS	Polystyrene
PSB	Phonon sideband
PTFE	Poly(tetrafluoroethylene)
QDs	Quantum dots
r.t.	Room temperature
RBM	Radial breathing mode
ROS	Reactive oxygen species
SC	Sodium cholate
SDBS	Sodium dodecyl benzene sulfonate
SDS	Sodium dodecyl sulfate
SFM	Shear force mixing
SPE	Single-photon emission
ssDNA	Single-stranded DNA
SWNTs	Single-walled carbon nanotubes
T	Thymine
TCSPC	Time-correlated single-photon counting
TD	Thermal detrapping
TD-DFT	Time-dependent DFT
THF	Tetrahydrofuran
THPTA	Tris(3-hydroxypropyltriazolylmethyl)amine
TON	Turn over number
UV	Ultraviolet
vH	van Hove
Vis	Visible
XPS	X-ray photoemission spectroscopy

Eidesstattliche Erklärung

Eidesstattliche Versicherung gemäß § 8 der Promotionsordnung für die Gesamtfakultät für Mathematik, Ingenieur- und Naturwissenschaften der Universität Heidelberg.

1. Bei der eingereichten Dissertation zu dem Thema "Creating Luminescent Defects in Carbon Nanotubes for Optoelectronics and Biomedical Applications" handelt es sich um meine eigenständig erbrachte Leistung.

2. Ich habe nur die angegebenen Quellen und Hilfsmittel benutzt und mich keiner unzulässigen Hilfe Dritter bedient. Insbesondere habe ich wörtlich oder sinngemäß aus anderen Werken übernommene Inhalte als solche kenntlich gemacht.

3. Die Arbeit oder Teile davon habe ich bislang nicht an einer Hochschule des In- oder Auslands als Bestandteil einer Prüfungs- oder Qualifikationsleistung vorgelegt.

4. Die Richtigkeit der vorstehenden Erklärungen bestätige ich.

5. Die Bedeutung der eidesstattlichen Versicherung und die strafrechtlichen Folgen einer unrichtigen oder unvollständigen eidesstattlichen Versicherung sind mir bekannt.

Ich versichere an Eides statt, dass ich nach bestem Wissen die reine Wahrheit erklärt und nichts verschwiegen habe.

Heidelberg, 07.03.2024 Unterschrift: .....

Simon Johannes Settele